DEVELOPMENT OF METAL & METAL OXIDES DECORATED GRAPHENE-BASED ELECTRODE MATERIALS FOR NEXT GENERATION LI-ION AND LI-O_2 BATTERIES

by

ADNAN TAŞDEMİR

Submitted to the Graduate School of Engineering and Natural Sciences
in partial fulfillment of
the requirements for the degree of
Doctor of Philosophy

Sabanci University
September 2020

METAL & METAL OXIDES DECORATED GRAPHENE-BASED ELECTRODE MATERIALS FOR NEXT GENERATION LI-ION AND LI-O_2 BATTERIES

APPROVED BY:

Prof. Dr. Selmiye Alkan Gürsel (Thesis Supervisor)

Asst. Prof. Dr. Alp Yürüm (Thesis Co-advisor)

Prof. Dr. Ayşe Gül Gürek

Assoc. Prof. Dr. Fevzi Çakmak Cebeci

Assoc. Prof. Dr. Önder Metin

Asst. Prof. Dr. Mustafa Kemal Bayazıt

DATE OF APPROVAL:03.09.2020

Development of Metal & Metal Oxides Decorated Graphene-Based electrode Materials for Next Generation Li-ion and Li-O_2 Batteries

Adnan Taşdemir

Ph.D. Dissertation, September 2020

Supervisor: Prof. Dr. Selmiye Alkan Gürsel

Co-advisor: Asst. Prof. Alp Yürüm

ABSTRACT

Keywords: Lithium-oxygen batteries, Li-ion batteries, air cathode, anode, CeO_2 nanorods, silicon, TiO_2-B, lithium iodide, nitrogen doped reduced graphene oxide, high cycle performance

Batteries are the global solution for the future energy crisis emerging from depleting fossil fuels and environmental issues. Even though lithium-ion batteries are widely commercialized for powering portable electronics, materials development for their electrodes has never stopped. In this Ph.D. thesis, metal and metal oxides decorated graphene-based electrode materials were developed to sustain long term operation and enhance Li-ion storage capacity. Moreover, Li-O_2 as the next-generation batteries were studied to compensate for immense energy demand in the automotive and aerospace industry. A new catalyst material was developed to be used as their porous air cathode partaking in oxygen evolution reactions (OER) and oxygen reduction reactions (ORR).

The graphene oxide (GO) utilized in this study was synthesized by the improved Hummers' method. Then a straightforward, one-step thermal route has been established to fabricate reduced- (rGO) and nitrogen-doped reduced graphene oxide (NrGO) electrodes with remarkable lithium-ion storage properties. The electrochemical properties of the rGO and NrGO electrodes have been extensively compared in a Li-ion half-cell. The NrGO electrodes exhibited a reversible capacity of 240 $mAhg^{-1}$ at a high current of 10 Ag^{-1} after 500 cycles of operation with 90 % capacity retention.

Further, we have investigated the synergistic effect of NrGO and nanotubular TiO_2 to achieve high rate capabilities with high discharge capacities through a simple, one-step and scalable method. First, hydrogen titanate nanotubes were hydrothermally grown on

the surface of NrGO sheets and then converted to a mixed phase of TiO_2-B and anatase by thermal annealing. The prepared anode showed a stable discharge capacity of 150 $mAhg^{-1}$ at 1C current rate after 50 cycles.

Moreover, we introduced a simple and cost-effective spray-drying method to fabricate a layered (sandwich-like) anode structure using Si nanoparticles (NPs) and rGO. The Si NPs were synthesized by the magnesiothermic reduction of SiO_2 nanoparticles. By a scalable and straightforward spraying/drying method, we embedded Si NPs between two layers of rGO sheets. The sandwich-like structure, which successfully contains the expansion of Si particles, protected the anode from detrimental conditions. With this new and uncomplicated production technique, the rGO-Si-rGO anode after 50 cycles, showed a high specific capacity of 1089 $mAhg^{-1}$ at 1C with 97% coulombic efficiency and a stable cycling performance at current densities up to 5C.

Lastly, cerium (IV) oxide (CeO_2) nanorods were synthesized by hydrothermal treatment and supported on NrGO by another hydrothermal step. Herein, CeO_2/NrGO catalyst materials were studied as a Li-O_2 cathode using an aprotic electrolyte, which includes lithium iodide (LiI) as a redox mediator. The results showed that the novel catalyst hybrid of CeO_2 and NrGO with LiI directly increased the electrochemical performance of Li-O_2 battery. Their synergetic effect improved the kinetics of OER and ORR. The impact of LiI on CeO_2/NrGO by comparing bare NrGO air cathode was investigated for the first time in this study. The addition of LiI decreased the overpotential up to 0.78 V in CeO_2/NrGO air cathode. CeO_2/NrGO were tested at the different current densities and revealed a maximum capacity of 5040 $mAhg^{-1}$ at 25 mAg^{-1} current density.

Yeni Nesil Li-iyon ve Li-O_2 Pilleri İçin Metal ve Metal Oksit Dekore Edilmiş Grafen Esaslı Elektrot Malzemelerinin Geliştirilmesi

Adnan Taşdemir

Doktora Tezi, Eylül 2020

Tez Danışmanı: Prof. Dr. Selmiye Alkan Gürsel
Tez eş danışmanı: Dr. Öğr. Üyesi Alp Yürüm

ÖZET

Anahtar kelimeler: Li-oksijen pilleri, Li-iyon pilleri, hava katotu, anot, CeO_2 nano çubuklar, silisyum, TiO_2-B, lityum iyodur, azot katkılanmış indirgenmiş grafen oksit, yüksek çevirim performansı

Piller fosil yakıtların tükenmesi ve çevresel faktörlerden kaynaklanan gelecekteki enerji krizi için evrensel çözümdür. Lityum iyon piller taşınabilir elektronik cihazlar güç verebilmek için geniş çapta ticarileşmesine rağmen, elektrot malzemelerinin gelişimi asla durmamıştır. Bu doktora tezinde metal ve metal oksitler ile dekore edilmiş grafen esaslı elektrot malzemeleri uzun çalışma süresinin sürdürmesi ve Li iyonu depolama kapasitesini artırması için geliştirilmiştir. Dahası otomobil ve havacılık endüstrisindeki yüksek enerji talebini karşılamak için yeni nesil piller olarak Li-O_2 çalışılmıştır. Oksijen oluşum ve indirgenme reaksiyonlarında görev alan gözenekli hava katodu olarak kullanılmamak üzere yeni bir katalizör malzemesi geliştirildi.

Bu çalışmada kullanılan grafen oksit (GO), Hummers'ın geliştirilmiş yöntemiyle sentezlendi. Ardından, olağanüstü lityum iyon depolama özelliklerine sahip indirgenmiş (rGO) ve azot katkılı indirgenmiş grafen oksit (NrGO) elektrotları üretmek için basit ve tek adımlı bir termal yöntem oluşturuldu. RGO ve NrGO elektrotlarının elektrokimyasal özellikleri Li-iyon yarı hücesi kullanılarak kapsamlı bir şekilde karşılaştırıldı. NrGO elektrotları,% 90 kapasite tutma ile 500 çalışma döngüsünden sonra 10 Ag^{-1}'lik yüksek bir akımda 240 $mAhg^{-1}$'lik tersine çevrilebilir bir kapasite sergiledi.

Ayrıca, basit, tek adımlı ve ölçeklenebilir bir yöntemle yüksek akım oranı kullanarak yüksek deşarj kapasiteleri elde etmek için NrGO ve nanotübüler TiO_2'nin sinerjik etkisini araştırdık. İlk olarak, hidrojen titanat nanotüpler, NrGO tabakalarının yüzeyinde hidrotermal yöntemiyle büyütüldü ve daha sonra bu ürün ısıl tavlama ile TiO_2-B ve anataz

karışık fazlarına dönüştürüldü. Hazırlanan anot, 50 çevirimden sonra 1C akım hızında 150 $mAhg^{-1}$ sabit deşarj kapasitesi gösterdi.

Ayrıca, Si nanoparçacıklar (NP'ler) ve rGO kullanarak katmanlı (sandviç benzeri) bir anot yapısı üretmek için basit ve uygun maliyetli bir püskürtmeli kurutma yöntemini tanıttık. Si NP'ler, SiO_2 nanoparçacıklarının magneziyotermik indirgenmesiyle sentezlendi. Ölçeklenebilir ve basit bir püskürtme/kurutma yöntemiyle, Si NP'lerini iki rGO katmanın arasına yerleştirdik. Si partiküllerinin genişlemesini başarıyla engelleyen sandviç benzeri yapı, anodu zararlı koşullardan korudu. Bu yeni ve karmaşık olmayan üretim tekniğiyle, 50 döngüden sonra rGO-Si-rGO anodu, 1C'de % 97 kulombik verimlilikle 1089 $mAhg^{-1}$'lik yüksek spesifik kapasite ve 5C'ye kadar akım yoğunluklarında kararlı bir döngü performansı gösterdi.

Son olarak, seryum (IV) oksit (CeO_2) nano çubuklar hidrotermal işlemle sentezlendi ve başka bir hidrotermal aracılığıyla NrGO ile desteklendi. Burada CeO_2/NrGO katalizör malzemeleri, lityum iyodür (LiI) redoks mediatörü içeren aprotik bir elektrolit kullanılarak Li-O_2 katodu olarak incelenmiştir. Sonuçlar, LiI ile CeO_2 ve NrGO'nun yeni katalizör hibritinin Li-O_2 pilin elektrokimyasal performansını doğrudan artırdığını gösterdi. Onların sinerjik etkileri, OER ve ORR kinetiğini geliştirdi. LiI'nin etkisi salt NrGO hava katodunu CeO_2/NrGO katotuyla karşılaştırılarak ilk kez bu çalışmada araştırıldı. LiI eklenmesi, aşırı potansiyeli CeO_2/NrGO hava katodunda 0,78 V'a kadar düşürdü. CeO_2/NrGO farklı akım yoğunluklarında test edildi ve 25 mAg^{-1} akım yoğunluğunda maksimum 5040 $mAhg^{-1}$ kapasite ortaya çıkardı.

To my elder brother, Sinan Taşdemir;

who always supported me to have this education, passed away at his 28 due to lung cancer, always will be remembered and loved.

I kept my promise…

ACKNOWLEDGEMENT

Foremost, I would like to express my deep gratitude to my supervisor, Prof. Dr. Selmiye Alkan Gürsel. for her continuous support, enthusiasm and encouragement throughout my Ph.D. education. She was there whenever I stated the problem and she removed all the obstacles through my study. I extend my gratefulness to my co-advisor, Dr. Alp Yürüm for his guidance and constructive criticism at any time of my research. I would not go that further without his expertise in chemistry and batteries. I would like to thank my committee members, Prof. Dr. Ayşe Gül Gürek, Assoc. Prof. Dr. Fevzi Çakmak Cebeci, Assoc. Prof. Dr. Önder Metin and Asst. Prof. Dr. Mustafa Kemal Bayazıt for their valuable time, interest, and constructive suggestions.

I must thank the faculty members of department of Materials Science and Nanoengineering for their valuable and educative lectures throughout my Ph.D. which helps me shape my profession in materials science. I thank to Prof. Dr. Mehmet Ali Gülgün, Prof. Dr. Cleva W. Ow-Yang, Prof. Dr. İbrahim Burç Mısırlıoğlu, Prof. Dr. Melih Papilla, Assoc. Prof. Dr. Gözde İnce and Daniel Lee Calvey for their guidance.

In addition, my sincere thanks go to Dr. Begüm Yarar Kaplan, Dr. Emre Biçer, Dr. Dilek Çakıroğlu, Dr. Aysu Yurduşen Öztürk, Dr. Ali Tufani, Dr. Özlem Karahan, Dr. E. Billur Seviniş Özbulut, Dr. Esin Ateş Güvel, Dr. Mine Altunbek, Dr. Serap Hayat Saytaş and Dr. Meral Yüce for their inexhaustible discussion and problem solution debates about my academic problems.

I am pleased to Ertuğrul Sadıkoğlu, Serkan Bostan, Nursel Karakaya, Bülent Köroğlu, Onur Serbest, Mehmet Karahan, Süleyman Tutkun and Turgay Gönül for technical support and help.

I am also grateful to my colleagues and collaborators Buse Bulut Köpüklü, Ahmet Can Kırlıoğlu, Emre Burak Boz, Sezer Seçkin, Bilal Sayyed Said Iskandarani, Naimeh Rajabalizadeh, Navid Haghmoradi, Esaam Jamil, Shayan Mehraeen, Yousuf Rahman Azemi for having mutual studies and dedicated studies in mutual publications. Buse and Sezer earned special thanks since we suffer from the all pain together in all time whenever we faced experimental problems.

I would like to thank my current and former lab-mates, Hamed Salimkhani, Vahid Charkhesht, Golnaz Nasari, Osman Burak Seymen, Anagüli Abulizi, Ece Arıcı, Miad Yarali, Rıdvan Erğün, Bahareh Bakhtiari, Ayça Yiğitalp, Alp Duman, Faisal Jamil, Sahl

Sadeghi, Vildan Bayram, Sahand Saeidi and Mirsajjad Mousavi for making laboratory work productive, efficient and also enjoyable. I am very happy to be a member of SU-ESC research group since they have been my second family during my Ph.D life.

I am also thankful to SUNUM-Grad students Abdurrahim Can Eğil, Milad Torabfam, Onur Zırhlı, Araz Sheibani, Sirous Khabbazabkenar, Zeki Semih Pehlivan, Dilek Sezer, Mehmet Can Zeybek, Yelda Yorulmaz and Ali Ansari. I will always feel gratitude to Ali for his time to discuss about electrochemistry and batteries based on his deep knowledge.

I will always remember the time I spent in the dorm with my best flat mates İsa Emami Tabrizi, Ebru Özer, Hümeyra Nur Kaleli, Kaveh Rahimzadeh Berenji, and Pouya Yousefi, Farzaneh Jalalypour, Pouya Zoghipour, Sara Atito, Wael Ali Saeed Aldulaimi for their cheerful activities.

I feel very lucky to know my previous lab mates Cem Turkay, Mutlu Devran Yaman, Şebnem Yazıcı, Mehmet Ali Olğar, Öykü Tanışman, and Serkan Duyar in IZTECH and they will be my friend to the end of my life for making life bearable and enjoyable.

I will never forget the joyful memories my friends from Koç's group, Cem Balda Dayan, Ezgi Bakırcı, Burak Toprakhisar, Ferdows Afghah, Ali Nadernezhad and Navid Khani. I thank to them for all the greater goods they made me gain to my vision and I will always remember joyful memories with them as well.

Melike Barak earned most special thanks for endless support during my Ph.D. life not only for correcting my writings in the thesis, but also for delicious cooking's and unique friendship. She was always ready to help me anytime I need.

Last but not least, I would like to thank my family all their support they could give to me. My sister Dilek ASLAN earned my gratitude for supporting me all time. Especially, my deepest appreciation is to my brother, Sinan Taşdemir. His vision and personality made me a better person with love and strength at every moment in my life. He will be never forgotten, and his memories will live with me always.

Li-O_2 battery research project was funded by Scientific and Technological Research Council of Turkey (TUBITAK) under the grant agreement number 115M659. Lastly, I would like to show my appreciation for all the support received from Sabanci University Nanotechnology Research and Application Center (SUNUM) and Faculty of Engineering and Natural Science in Sabanci University.

ABBREVIATIONS

BET	Brunauer-Emmett-Teller
CB	Carbon Black
CNT	Carbon Nanotube
CV	Cyclic Voltammograms
DBBQ	5-Di-Tert-Butyl-1,4-Benzoquinone
DBG	Diethylene Glycol Dibutyl Ether
DEC	Diethyl Carbonate
DEMS	Differential Electrochemical Mass Spectrometry
DFT	Density Functional Theory
DG	Dimethyl Ether
DMC	Dimethyl Carbonate
DME	1,2-Dimethoxyethane
DMPZ	Dimethylphenazine
DMSO	Dimethyl Sulfoxide
DN	Donor Number
DW	Distilled Water
EC	Ethylene Carbonate
EIS	Electrochemical Impedance Spectroscopy
EV	Electric Vehicles
FEC	Fluoroethylene Carbonate
FEC	Fluoroethylene Carbonate
FESEM	Field Emission Scanning Electron Microscopy
GBAs	Graphene-Based Aerogels
GO	Graphene Oxide
HSAB	Pearson’s Hard Soft Acid Base
LiB	Lithium İon Batteries
LiTF	Lithium Trifluoromethanesulfonate
LiTFSI	Lithium Bis(Fluorosulfonyl)İmide
MRRs	Metallothermic Reduction Reactions
MWNTs	Multi-Walled Nanotubes
NCA	Lithium Nickel Cobalt Aluminum Oxides
NCO	Lithium Nickel Cobalt Oxides

NMC	Lithium Nickel Manganese Cobalt Oxides
NMP	N-Methyl Pyrrolidone
NrGO	Nitrogen Doped Reduced Graphene Oxide
OER	Oxygen Evolution Reaction
ORR	Oxygen Reduction Reaction
ox-GNRs	Oxidized Graphene Nanoribbons
PAS	Polyacenic Semiconductors
PC	Propylene Carbonate
PV	Photovoltaic
PVDF	Polyvinylidene Fluoride
RF	Resorcinol-Formaldehyde
rGNS	reduced Graphene Nanosheets
rGO	reduced GO
RM	Redox Mediator
RTIL	Room Temperature Ionic Liquid
SEI	Solid Electrolyte Interface
SWNTs	Single-Walled Nanotubes
TEGDME	Tetraethylene Glycol Dimethyl Ether
TEM	Transmission Electron Spectroscopy
TEMPO	2,2,6,6-Tetramethylpiperidinyloxy
TEPa	Triethyl Phosphate
TGA	Thermogravimetric Analyzer
TTF	Tetrathiafulvalene
UGF	Ultrathin Graphite Foam
XPS	X-Ray Photoelectron Spectrometer
XRD	X-Ray Diffraction

TABLE OF CONTENT

LIST OF FIGURES

LIST OF TABLES

CHAPTER 1. INTRODUCTION

1.1.The Motivations of This Thesis

The main aim of this dissertation is to develop anode materials for Li-ion batteries and to synthesize a novel catalyst material in air cathode for Li-O_2 batteries. Based on this motivation, we established a strait forward method to dope N and reduce improved Hummers GO by thermal annealing method in a single step. A long-term operability at high current density was achieved by employing NrGO as anode material in which high capacity not only sustained but also increased by cycling due to pyridinic N defects enhancing Li storage capacity (Chapter 2-part 1). Moreover, titanate nanotubes were decorated on the NrGO and converted to TiO_2 B by an annealing step. A very stable capacity was obtained with high cycling (Chapter 2-part 2). Furthermore, a simple spraying system were used to establish a sandwich like structure of rGO-Si-rGO as anode materials yielding high capacity at high current rate upon cycling (Chapter 2-part 3). Lastly, a novel catalyst material developed in air cathode for Li-O_2 batteries as future battery technology. CeO_2 decorated NrGO used as catalyst in cathode and LiI used as soluble catalyst in electrolyte in which cell provided high capacity and low overpotential enhancing electrochemical performance of the battery (Chapter 3).

1.2. Energy Concerns for The Future

Recently energy became the biggest problem of the society due to the gradual depletion of fossil fuels which confronts the challenges to sustain power sources within the next 100 years. To overcome these demands, renewable energy sources have been invested to develop systems offering solutions for energy consumption crisis. These sources can be classified as hydroelectricity energy, wind energy, solar energy (Photovoltaic (PV) systems), geothermal energy, ocean or tidal energy, biofuels energy systems which are covert to electricity to overcome energy shortage. However, these solutions are deficient due to geographically limitations and natural intermittencies lacking a stable and efficient power delivery system. In other word, these system needs other system to store energy and keep delivery system working continuously for longer lifetimes [1]. Lithium batteries and supercapacitors are widely commercialized systems to convert and store energy from

renewable energy sources. Additionally, fuel cells are similarly energy conversion system which can power portable electronic devices and internal combustion machine in automobiles.

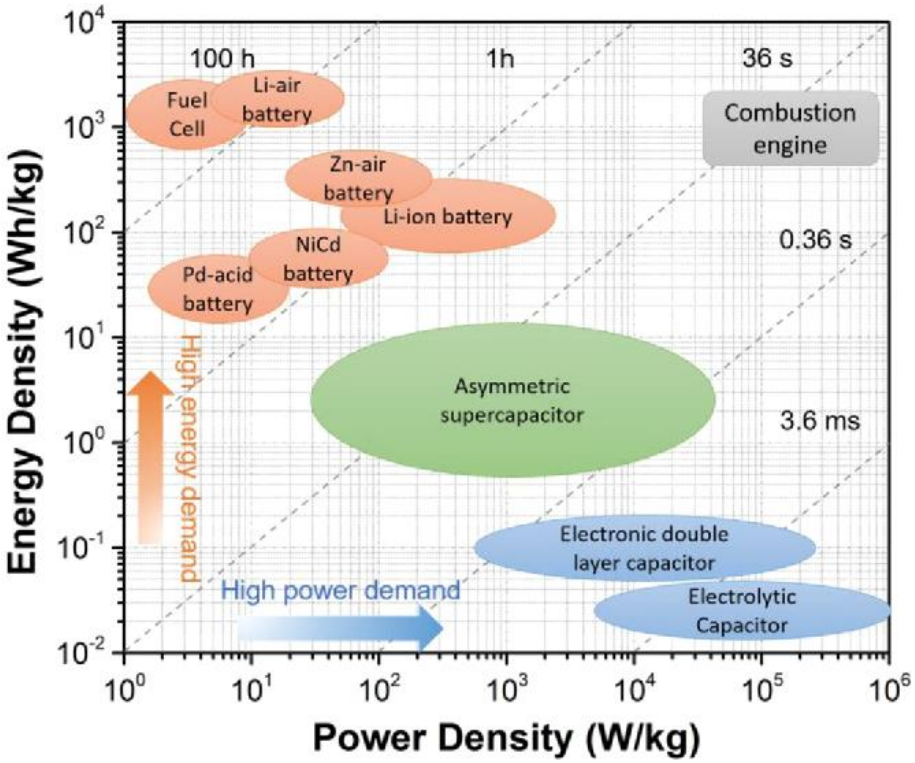

Figure 1. 1. Ragone plot for batteries, supercapacitors, fuel cell and internal combustion engine

Figure 1. 1 demonstrates energy and power densities of various energy storage and conversion device with respect to internal combustion engines[2]. Even though fuel cells match with the demand on energy and power densities for vehicle electrification in theory, they have low practical efficiency, high cost catalyst materials and difficulty in usage. Followingly, supercapacitors have enough power density to initialize vehicle transportation, but they suffer from low energy density to sustain long range utilities. On the other hand, rechargeable (secondary) lithium ion batteries (LiBs) are most widely used energy systems for past two decades to compensate low scale energy demands. However, there are still various problems to be solved, and several limitations to overcome for the electrode materials of the batteries. Moreover, LiBs are restricted candidates for next generation energy applications such as electrical vehicle due to their low energy and power densities. As alternative, metal air batteries can theoretically supply energy density 10 times bigger than conventional LiBs. The development of metal air batteries can be the solution as being future battery technology to replace internal

combustion engines and to counterbalance energy demand long after depletion of fossil fuels [3]. Therefore, such electrochemical energy systems will be widely used in future.

1.3. Thermodynamic View of Energy Storage and Conversion Materials

Electrochemical energy systems exploit the chemical reaction harvesting electrical current in a range of potential and time. The chemical reactions occur spontaneously within these devices like batteries or supercapacitors which are also called galvanic or voltaic systems. Conversely, electrolytic systems first consume electrical current to initiate nonspontaneous chemical reactions such as electrodepositions. These systems contain two different terminals (electrodes) within the electrolyte solution in which electrodes are connected via an external circuit. During the operation of the system cell, the electron flow forces the substance to dissolve or to be deposited that the processes are dictated by chemical activity of reactants. Some metals tend to lose electrons more compare to their chemical rection potentials with other metals. Chemical potential can be described as how much a substance tends to transform or how spontaneously Gibbs energy will change when substance interacts another species. In another word, chemical potential is determined by substance fermi energy level based on available electron state density and lattice properties of the substance yielding as final phenomena which is called electronegativity and electron affiliations as well. The difference between fermi levels of the substance directs the reaction kinetics by electron or charge flow. In an electrochemical cell, the sum of the chemical potentials and electrostatic potential of all species is called electrochemical potential. In summary, chemical reactions within the electrochemical system is generated by reactions Gibbs free energy which is the sum of the electrochemical potential of the species involved in reaction. The difference between electrochemical potential creates a driving force to mobile charge carriers until the difference between electrochemical potential diminished. The materials for electrochemical system are chosen based on their thermodynamic characteristic compared to each other and electrolyte to process both electrodes selected based on the optimum kinetics to the electrode chemistry. The electrochemical application dictates the selectivity according to reaction mechanism. Charge storage capacity, lower electrochemical potential for the reaction and reversibility of the reaction are three main factors to sustain the working mechanism of energy storage and conversion devices.

Materials research and development are carried out to enhance these parameters for next generation energy technology.

1.4. Li-ion Batteries

Although battery research starts from primary battery, rechargeable batteries also called secondary batteries- become increasingly popular owing to its economic efficiency, and environment awareness. The rechargeable batteries are usually portable and light energy storage devices that convert the stored chemical energy in its active materials into the electrical energy via several chemical oxidation-reduction reactions leading this conversion [4]. By having a large application area, lithium-ion batteries (LIBs) are the most preferred energy storage sources in terms of not only their lower weight, high energy capacity, and performance but also longer lifetime, higher operation voltage and greater reliability when compared to previously commercialized batteries such as lead acid, nickel cadmium and nickel-metal hydride batteries. Still, research on LIBs never stopped to enhance their electrochemical performance, and inquiry in best version of batteries are still under investigation by trying newer upgraded refinements. Features of LIBs as high volumetric (range from 250 to 300 Wh/L, maximum about 400 Wh/L in theory) and gravimetric energy density (range from 100 to 125 Wh/kg, theoretically up to 150 Wh/kg) with light weight and good shape versatility make it as a very promising candidate for numerous of practical application on electronic devices. Even though anode in LiBS gained a lot of upgrades in terms of high capacity and cyclability without capacity fading, cathode still is the limiting part due to their low capacity and overall cycling performance. Lithium is generally preferred alkali metal but other metals like Na, Mg, Al, etc. also being employed as ion source of batteries due to their greatly negative redox potentials with low equivalent weights. As the lightest and the most electropositive one among alkali metal, lithium has lowest density as 0.534 g/cc which leads to specific capacity value as high as 3.86 Ah/g, the highest among others so far [5, 6].

1.5. Working Principle of Li-ion Batteries

Batteries are able to store energy by hosting formation or decomposition of chemical reactants producing electrical charges. An electrochemical-cell such as a battery-consists of three main components which are a positive and negative terminal, or cathode and

anode, and electrolyte. The cathode is originated from Greek as kathodos word which is a combination of kata “down” and hodos “way” standing for “a way down”. The anode is anodos in Greek as well and it is the combination of ana “up” and hodos “way” representing “a way up”. The electrolyte is an ionically conductive solution that provides the environment in which electrons are transformed as ions inside between the anode and the cathode electrodes within the cell [7]. Briefly, the current is flowed by the ionic motion between electrodes and terminals in an electrolyte media (Figure 1. 2).

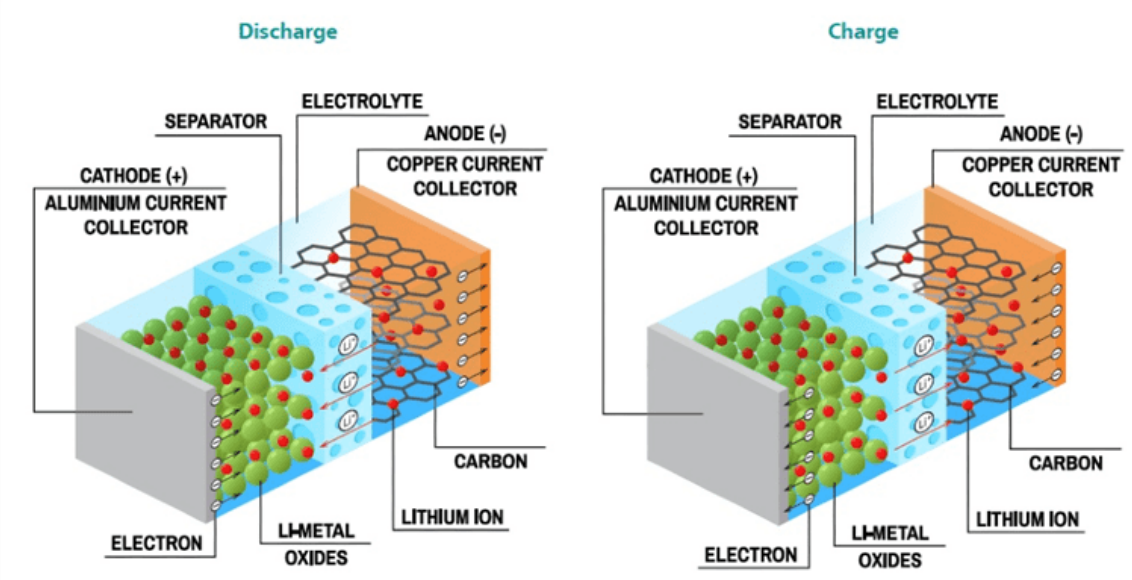

Figure 1. 2. Charge and discharge process of Li-ion batteries. Image Credit: Metrohm AG

Moreover, the electrolyte is one of the most critical component in Li-ion batteries to maintain chemical stability during the ion flow, ionic conductivity during the charge transfer, non-flammability due to electrochemical heat liberation and non-polarizability due to large potential window during the cell operation via chemical reactions. Several types of electrolyte were established for li-ion batteries which are aqueous, room temperature ionic liquid (RTIL), jel-like (polymeric), solid and nan-aqueous (organic liquid) based electrolytes. So far, organic liquid electrolytes including organic carbonates such as propylene carbonate (PC), ethylene carbonate (EC) , diethyl carbonate (DEC), dimethyl carbonate (DMC), fluoroethylene carbonate (FEC) are the most compatible solvent with Li salts to maintain stable operability in Li-ion batteries [8, 9] In general, 1 M lithium hexafluorophosphate (LiF_6P) in EC/DEC: 50/50 (v/v) or EC/DMC: 50/50 (v/v) is used as a standard electrolyte for fabrication of Li-ion batteries. This electrolyte

is.widely used as commercial electrolyte which includes doped polymers with some plasticizers to reduce crosslinking, side reactions and to avoid explosive flammability. Another phenomenon to be stated here is solid electrolyte interface (SEI). The SEI is a passivating and protecting layer on the electrode surface as a result of precipitation of Li products arising from spontaneous decomposition of electrolyte during charge discharge process. It is an electrically insulative and selective film that permits Li as an active charge carrier, but it prevents reactive electrolyte components to the lithium.

In summary, Li storage mechanism differs from material to material dictated by their physical and chemical properties. There are mainly three different Li storage mechanism to summarize the working principle of LiBs as presented in Figure 1. 4. They are namely intercalation, alloying and conversion type of reactions to Li that will be explained in following sections.

1.5.1. Intercalation Mechanism

The active materials in Li-ion cells work by reversibly incorporating lithium in an insertion process in which lithium ions are reversibly extracted or inserted into anode/cathode without a significant structural change to the anode/cathode, which is called the intercalation and de- intercalation. The anode or negative electrode is defined as oxidizing electrode which gives up the electrons to the external load by oxidation during the overall redox reaction. The cathode is defined as positive electrode or reducing electrode which accept electrons from the external load by reduction during the overall redox reaction. To describe the logic in terms of ion movements, Li-ions move during discharge from anode to cathode, and from cathode to anode when charging [4]. When a charger removes electrons from cathode, the cathode stays with a net positive charge, so those electrons are pushed into anode that gives negative charge to anode. The energy that is pumped into the cell transforms the active chemicals back into their original states. Electrode materials accommodate Li in ionic forms not in atomic form. The electro-insertion reaction of Li to the carbon materials is maintained by Li^+ ions sliding throughout the sheets of layered structure.

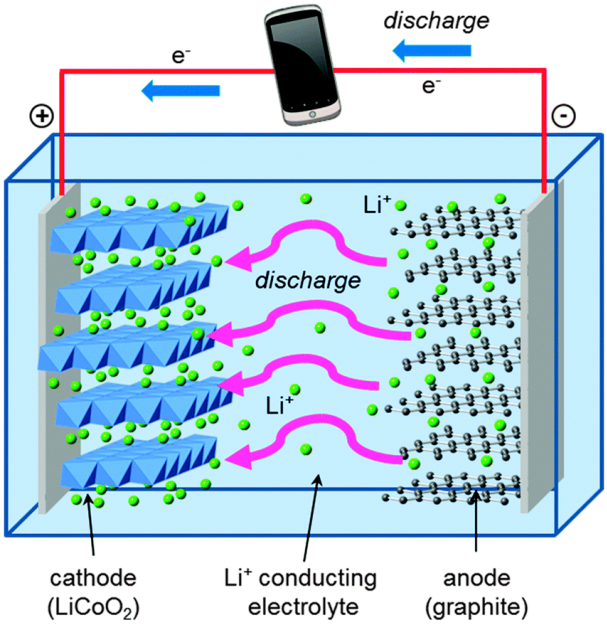

Figure 1. 3. Schematic of the electrochemical process in Li-ion cell [5].

As shown in the Figure 1. 3, $LiMO_2$ represents the lithium metal oxide positive material, such as $LiCoO_2$, and C the carbonaceous negative material, such as graphite in which combinations are being used in commercialized Li-ion batteries.

$$\textbf{\textit{Cathode reaction}}: Li_{1-x}CoO_2 + xLi^+ + xe \leftrightarrow LiCoO_2$$

$$\textbf{\textit{Anode reaction}}: Li_xC \leftrightarrow C + xLi^+ + xe^-$$

$$\textbf{\textit{Overall reaction}}: Li_xC + Li_{1-x}CoO_2 \leftrightarrow C + LiCoO_2$$

During the charging process, Li ion is removed from the cathode, left out $Li_{1-x}CoO_2$ and inserted into graphite layers to form Li_xC_6. The ion displacement and insertion are maintained by electromotive force sourced from external circuit. In other word, electric current applied to process chemical reaction that electrical energy converted to chemical energy. During discharge process, Li ions spontaneously moved back to cathode by delivering stored chemical energy back to the external circuit that electrical energy produced through chemical energy.

1.5.2. Alloying Mechanism

The Li ions stored in anode by alloying with anode element such as Si, Ge, Sn, P and Sb. However, huge structural expansion takes place during lithiation and de-lithiation process due to mechanical instability of active material. The volume expansion can be listed as follow; 4, 3.7, 2.6 and 3 folds for Si, Ge, Sn, and P respectively. They have de-lithiation

potential 0.45, 0.6 and 0.9 V for Si, Sn and Pb respectively. Si is the most popular alloying metal for Li storage, and it yield specific capacity up to 4200 $mAhg^{-1}$ which is 11 folds higher than graphite.

$$\textbf{\textit{Anode reaction:}}\ xLi^+ + xe^- + M_y \leftrightarrow Li_xM_y$$

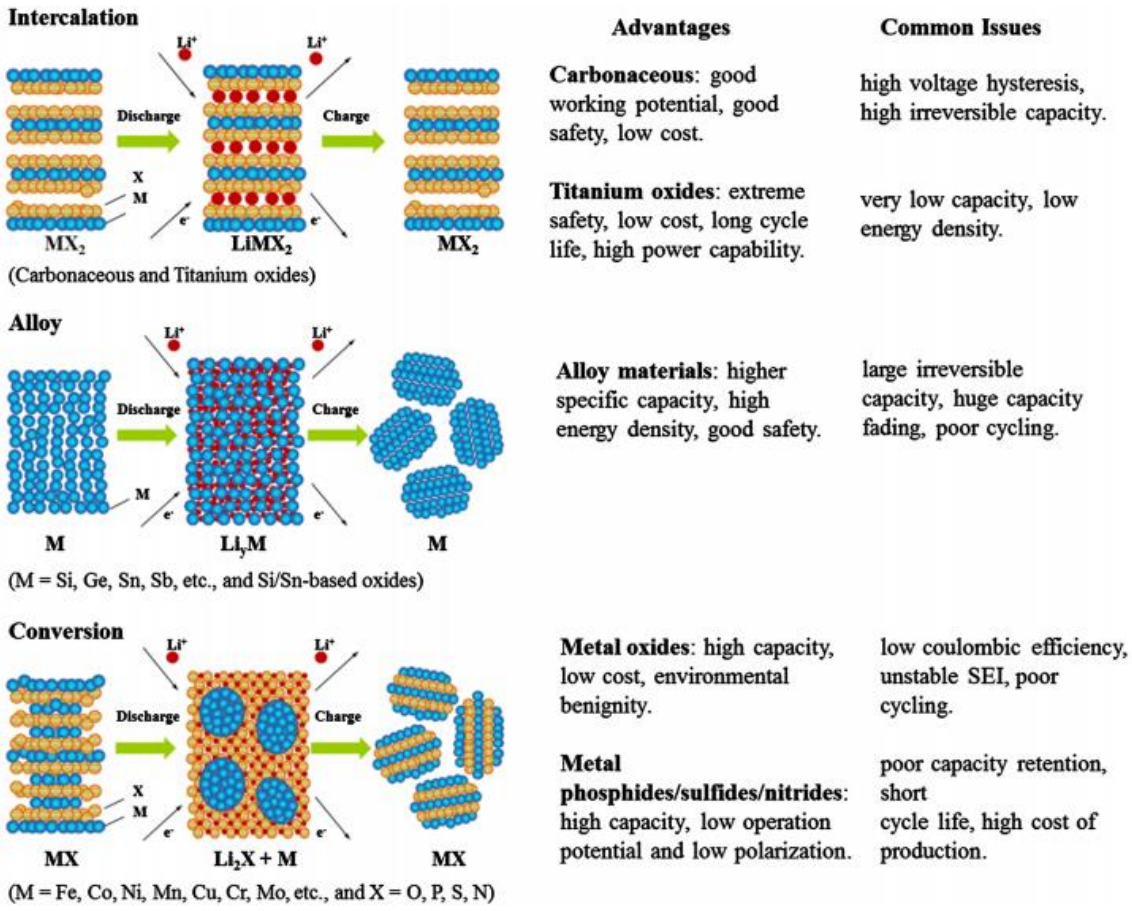

Figure 1. 4. Li storage process via intercalation, alloying and conversion [10]

1.5.3. Conversion Mechanism

Conversion type of Li storage mechanism is observed in transition metal fluorides/oxides/sulfides/phosphides anode materials employing metals such as Fe, Mn, Co, Ni, Cu, etc. They offer specific capacity within the range of 700 to 1200 $mAhg^{-1}$ and de-lithiation potential in a range of 1 to 2 V. Redox reactions are established based on formation and decomposition of Li binary compounds by displacement reaction which requires diffusion of anion and cation within a long distance and active Li exchanges the inactive transition metal during the conversion reaction. Multi elections are transferred during the chemical reaction and smaller spinel polymorphs of transition metal oxides are formed. Resulting that, high capacity and energy density were revealed but low

coulombic efficiency, large hysteresis and poor cyclability were also the issue. Briefly, their nanostructures are exposed pulverization or morphological distortions which lead to SEI instability [11].

Anode reaction: $M_xO_y + 2yLi^+ + 2ye^- \leftrightarrow yLi_2O + xM$

1.6. Energy Merits for Li-ion Batteries

The qualitative properties of a battery are reported by theoretical capacity, specific capacity, its current bearing ability, energy density and power density. The theoretical energy capacity of a substance is calculated by following formula:

$$\textbf{\textit{Theoretical capacity (mAhg}}^{\textbf{-1}}\textbf{\textit{)}} = \frac{nF}{3.6 \times M_w}$$

To explain the formula members; n represent the number of electron transferred during the redox reaction, F stands for the Faraday constant (96485 C/mol), 1/3.6 is due to the conversion A·s to mAh, and lastly Mw (g/mol) depicts the molar weight of active substance.

The specific capacity is calculated by formula below:

$$\boldsymbol{Specific\ Capacity\ (mAhg^{-1})} = \frac{Time\ (h) \times Current(mA)}{W}$$

Formula express the duration of the discharge process (time in hours) at a constant current (in mA) withdrawn from the cell over the exploited weight (W in g) of the active materials on the electrode.

C rate determines the time to fully charge a battery. 1 C rate for Si battery with the nominal capacity 4200 mAh would be 4.2 A current implying that if 4.2A current is applied to the cell, cell will be fully charged in 1 hour. C/2 rate (2.1 A) will charge it in 2 hours. Current is applied by the merit of gravimetric current density as well which is determined by the active materials load in the cell. A cell utilizing 1.7 mg of active material will need to apply 1.7 mA constant current to test cell at 1 Ag^{-1} current density.

Energy and power density merits are used to compare the batteries with supercapacitors or internal combustion engine to express how much powerful the cell is. Energy density is the amount of energy that the cell can store, and power density is how long the battery can supply that stored energy. The comparison of these merits leads researchers to the

directions of which part of cell chemistry to be developed either in materials wise or engineering wise.

$$\boldsymbol{Energy\ density}\left(\frac{\boldsymbol{Wh}}{\boldsymbol{kg}}\right) = Capacity\left(\frac{Ah}{kg}\right) \times Voltage(V)$$

$$\boldsymbol{Power\ density}\left(\frac{\boldsymbol{W}}{\boldsymbol{kg}}\right) = Energy\ density\ \left(\frac{Wh}{kg}\right)/Time(h)$$

Where V is the average potential (mid potential) of the potential window and the time is discharge time in hours.

1.7. Cathode Materials for Li-ion Battery

Cathode as positive electrode in LiBs has a lot of limitation to overcome for fabricating the next-generation battery technology. Cell properties require upgrades in terms of cell voltage and stable capacity and long cyclability. Li reaction within the cathode is rather depends how much to comprehend the constituents and components involve in reaction mechanism according to their crystal and electronic structure. The enhancement crystal forms of the cathode materials are briefly associated with understanding the principles to control elemental and microstructural changes via crystallite size and surface modification where it confronts the main challenges and Li reaction limitations. The enhancements can upgrade the phase stability, rate capability, capacity retention and charge carrier transport as well as they can prevent agglomeration, metal dissolution, thickening of SEI formation and instability in anionic redox reactions. There are several types of cathode materials classified according to their constituents and crystal structures. Briefly, cathode materials are listed as nickel-rich layered oxide materials, lithium-rich layered oxide materials, spinel oxide materials, polyanion materials, cation disordered rock-salt oxide materials and conversion materials. As listed above, all of the cathode materials have their distinctive challenges to overcome [12].

In recent years, ternary metal oxide incorporated with lithium is being employed as cathode such as lithium nickel manganese cobalt oxides (NMC), lithium nickel cobalt oxides (NCO) and lithium nickel cobalt aluminum oxides (NCA) to provide safer and more affordable layered oxides with high reversible capacity [13]. On the anode part, derivatives of graphite, Si, Sb, Sn, Fe_3O_4, SnO_2, MnO_2, NiO, TiO_2 and composition of these metal oxides with carbon-based materials were employed as anode in recent studies.

1.8.Anode Materials for Li-ion Battery

Carbon and carbon derivatives had been utilized vastly in the anode electrode of lithium-ion batteries prior to the discovery of graphene. Carbon is a versatile material with numerous allotropes and a wide range of electrical conductivity based on its allotropes from fullerene to graphite as displayed in Figure 1. 5. A number of studies have focused on carbon as anode materials in lithium batteries, and graphene has been one of the most widely studied carbon-based anodes in the field. Briefly, the structural order and inter-coordination of carbon lattice vary the adsorption mechanism of lithium and de-lithiation potential. Carbon based materials are discussed in the following section by comparing their structural forms from exfoliated graphite to reduced GO (rGO) or via unzipping carbon nanotubes to provide graphene nanoribbons. (GNRs).

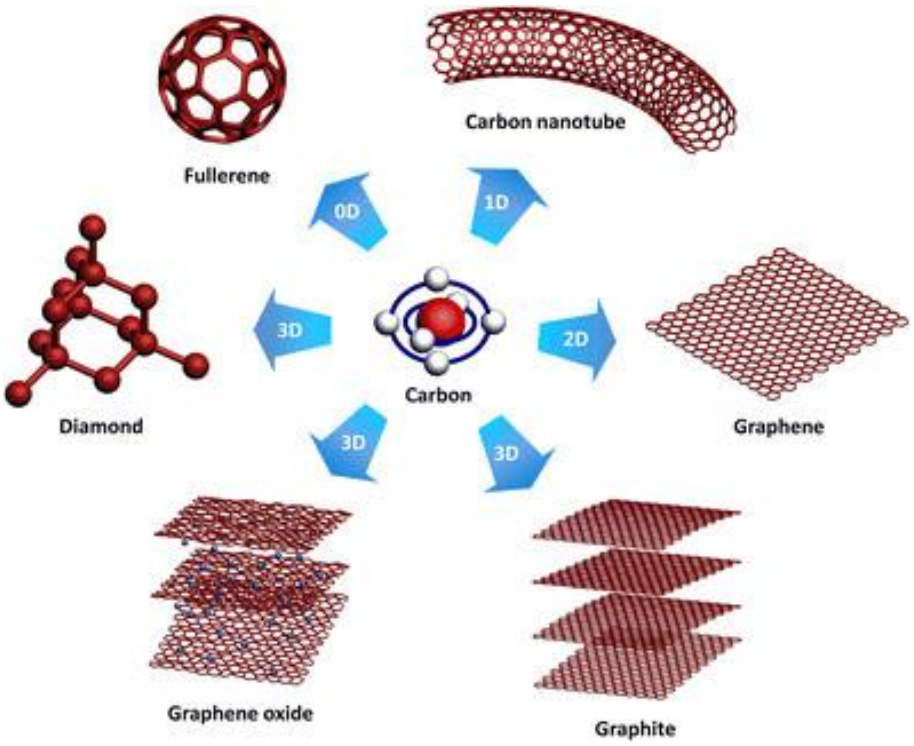

Figure 1. 5. Forms of carbon [14].

1.8.1. Graphite

Natural graphite is generally in the form of discrete flakes steaking on each other by van der Waals bond and their size is in the range of 5 to 80 micrometer. It is fabricated by heat treatment of petroleum coke at 2800 °C and higher. The flakes have large anisotropy since they have very crystalline and electrically conductive layer in the tangential plane, but these values are far different by 100 times than their normal direction. Graphite

demonstrates excellent chemical stability due to its carbon nature. The properties such as, surface texture, morphology, microstructural form and the crystallinity of carbon materials prepare ground for the high quantity of electrochemically active sites to store Li ion, and low de-lithiation potential for intercalation reaction. Carbon based anodes undergo redox reaction with highly low potentials according to Li/Li^+ that reveals high cell potentials and high energy density. Graphite has lithiation reaction around 0.2 V and reveals specific capacity of 372 $mAhg^{-1}$ based on graphite mass. The theoretical specific capacity of graphite is higher than theoretical capacity of almost all of the cathode materials in use. Since the cathode part is the rate determining factor for commercial Li-ion batteries, graphite is conserving its role as an anode material in Li-ion batteries even though there are a lot of enhanced alternative anode materials yielding better performance than graphite. Open crystal structures of graphitic materials can allow the insertion or extraction of lithium ions in between layers without changing its crystal structure. The open and porous structure of anode materials makes an increase in the amount of the electrolyte interacting with the electrode and it improves the discharge performance. Furthermore, it remains stable and preserves their energy capacities in high current values due to the enhanced Li^+ ion and electron mobility. Therefore, the graphene-based composites are the perfect fit for anode materials of lithium-ion batteries [15]. As a conclusion, graphite as anode materials still provides great advantages in terms of adequate reversible capacity, excellent cyclicity, enhanced energy and power density, and low de-lithiation potential due to its layered and open structure hosting large number of lithium-ions [16].

1.8.2. Graphene

Andre Geim and Konstantin Novoselov were awarded the Nobel Prize in Physics in 2010 for their groundbreaking works on graphene which is a 2D material form of sp^2 hybridized carbon atoms [8]. The 2D graphene sheets can create a 3D graphitic form by stacking layer on themselves, whereas the 2D rolled form provides nanotubes and lastly it can also be wrapped up into the buckyballs (Fullerenes, 0D). The electrical and thermal properties of graphene are very impressive, reported as 104 Scm^{-1} for the electrical conductivity and 3000 WmK^{-1} for the thermal conductivity. The diffusion coefficient of lithium-ion to graphene is between 10^{-7} to 10^{-10} cm^2s^{-1}, which nominates it a potentially wonderful material for the negative electrodes in lithium-ion batteries. In addition to these properties, the mechanical properties of graphene are also exciting to form composite

with better integrity. Moreover, the stacked sheets of graphene derived from exfoliated graphite provide a modular approach to increase surface for lithium storage in layered carbon forms (Figure 1. 5) as well as layered carbon/metal nanocomposites (Figure 1. 6)[17].

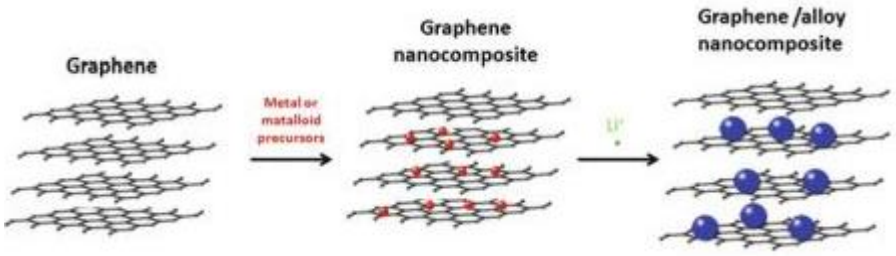

Figure 1. 6. Graphene-metal/oxide nanocomposite electrodes [14].

Graphene has many application areas with wide range technology field and lithium-ion batteries have lots of ongoing research focused on usage of the distinctive properties of graphene and its derivatives. Until now, a limited number of results have been published using bare graphene as the active anode material, and mostly reports have been published on graphene/metal or graphene/metal oxide nanocomposites [14]. An interesting approach was taken by Yoo et al. to investigate graphene as an anode active material for lithium storage [18]. Graphene platelets was prepared using scalable processes starting from abundantly available graphite in which the graphene sheets provide high surface layered carbon electrode material. Furthermore, Gue et al. performed oxidation, rapid expansion, and ultrasonic treatment to the artificial graphite to obtain graphene. They tested these obtained graphene samples in half-cells. For irreversible capacity, 1250 $mAhg^{-1}$ was obtained for the first cycle and 672 $mAhg^{-1}$ was measured for reversible capacity up to 30 cycles [19]. Moreover, Wang et al. showed that a discharge capacity of 680 $mAhg^{-1}$ can be achieved by using graphene paper as an anode made from reduced GO dispersions, but at the time of the second cycle, capacity dramatically dropped to 84 $mAhg^{-1}$ [20]. An annealing procedure was applied to the graphene paper at 800 ^{0}C under the flow of N_2 gases for 1 h; thus, oxygen functional groups were removed which provided 301 $mAhg^{-1}$ of reversible discharge capacities after 10 cycles. The result yielded a capacity higher than that of the commercial graphite anode and better performance in cell kinetics [21]. The lithium-ion mobility is enhanced by functional graphitic oxides as well. Graphene nanoplatelet, graphene oxide, carbon nanotube (CNT) and reduced or

functionalized nanocomposites forms of graphene are employed support material in electrode for batteries, fuel cell, and supercapacitors [22]. Functionalized graphene oxide (GO) also has been exploited vastly as an electrode for supercapacitors and it yielded high capacitive performance [23-26]. Pre-reduced GO with fewer oxygen groups by thermal annealing in H_2 exhibits greatly reduced reactivity with NH_3 and lower N-doping level [27, 28].

The methods to process graphene-based materials are important since they strongly alter the capacity for lithium-ion storage. Defect density, surface area, and other critical properties such as electrical conductivity all depend on processing methods. Through the oxidation of graphite followed by rapid thermal expansion, prepared graphene sheets also have high capacity values. The reversible capacity was maintained at 848 mAg^{-1} at current densities from 100 to 1000 mAg^{-1} even after 40 cycles. Moreover, at a high current density of 500 mAg^{-1}, the rate capability of graphene with a reversible specific capacity remained at 718 $mAhg^{-1}$. Wan et al. studied the influence of the temperature of the graphene oxide reduction. The results showed that the irreversible capacities of the graphene nanosheets in the first cycle decrease by increasing annealing temperatures (2137 $mAhg^{-1}$ for 300 ℃, 1523 $mAhg^{-1}$ for 600 ℃, and 1167 $mAhg^{-1}$ for 800 ℃) [29]. The reason for this is potentially the larger number of lithium insertion active sites in larger surface area graphene obtained with lower annealing temperature. The capacity differences of three cells were much closer to each other after 100 cycles. They varied 478 $mAhg^{-1}$ for the graphene prepared at 300 ℃ to approximately 350 $mAhg^{-1}$ for the sample prepared at 800 ℃. Nitrogen doped graphene oxide and its reduced (NrGO) form has been used as an anode material for LiBs. Its fabrication starts with the synthesis of GO using the Hummers method and annealing it at elevated temperature in ammonia media to process the doping step. Decreasing of the functional group and using nitrogen doping process to obtain a more porous structure serves ideally as an ideal electrode for batteries. Zheng, et al synthesized nitrogen-doped graphene in one-pot by hydrothermal method as high-performance anode materials for lithium ion batteries. The results showed that the N-doped graphene exhibits outstanding electrochemical properties such as high reversible capacity, superior rate capability and long-term cycling stability [30]. Additionally, Changjing, et al. successfully obtained N-rGO during GO synthesis by using the Hummers method without annealing but using freeze drying [31]. However, they obtained better results in LiBs such as higher reversible specific capacity of 332 $mAhg^{-1}$

during 600 cycles at 500 mAg^{-1}. Graphene foam. The critical point of preparing GO is the selection of suitable oxidizing agents to oxidize graphite [32]. Al in all, graphene-based composites is ideal fit for anode materials of lithium-ion batteries. Their open structure forms with the high surface area can accommodate lithium reversibly and offer high capacity, good electronic conductivity and low electrochemical potential [7]. Zhou et al. [33] reported an rGO sponge prepared via thermal annealing and followingly freeze-drying route. The initial cycle capacity of this material was as high as 1059 $mAhg^{-1}$ at 50 mAg^{-1} current density. However, the large surface area of this material resulted in an increased irreversible capacity, indicated by a retaining capacity of only 400 $mAhg^{-1}$ (500 mAg^{-1}) after a few cycles and the capacity dropping to 230 $mAhg^{-1}$ (1000 mAg^{-1}) at higher discharge rates. Hengxing, et al. prepared ultrathin graphite foam (UGF) by precipitation of a very thin layer of graphite on Ni foam and subsequent removal of the Ni template. They demonstrated a general method for creating high-rate capability rechargeable lithium ion batteries using a 3D interconnected network of UGF [34].

The characteristic voltage curves of lithium insertion into the graphene/CNT was different from the lithium insertion to the graphene/fullerene devices. Moreover, the reversible capacity was obtained of 540 $mAhg^{-1}$ for graphene, 730 $mAhg^{-1}$ for graphene/CNT, and lastly 784 $mAhg^{-1}$ for graphene/fullerene. These are high values, but as observed previously, the rate at which these devices degrade is significant, and data was only shown for 20 cycles. It is unclear at this juncture if the increased d-spacing obtained with CNTs and fullerenes can yield enhanced lithium accommodation as observed with polyacenic semiconductors. In addition, the derivation of GNRs from MWNTs was explored by Bhardwaj et al., in which the tubes are unzipped to yield narrow strips of GNRs. The reason for using GNRs instead of MWNTs was the exhibition of higher capacity in first charge and discharge cycle. On the other hand, for the oxidized graphene nanoribbons (ox-GNRs), high irreversible charge capacity was 1400 $mAhg^{-1}$ with a discharge capacity of 820 $mAhg^{-1}$. However, only 14 cycles were observed in their cycling capability results due to gradual capacity fading by 3 % loss of capacity per cycle. In order to obtain GNRs, the ox-GNR were annealed at 900 ^{0}C in an H_2/Ar environment for nearly 15 minutes. These ribbons yielded cells with an irreversible capacity of approximately 200 $mAhg^{-1}$ after 14 cycles, a capacity still much lower than graphite [35, 36].

Apart from the promising claims on graphene, the pure form of graphene has large irreversible capacity since graphene sheets restack on each other after cycling. Researchers showed that it can be used with other active materials as a part of composite in anode to provide better irreversible capacity results [37]. Zhang et al reported a graphene oxide composite as a high capacity and binder-free anode with reversible capacity exceeding 690 $mAhg^{-1}$ at 0.5 C which exhibits excellent cycle performance and rate capability [38]. In another investigation, the same researchers successfully synthesized a novel composite of graphene oxide, graphite, and CNTs and used them as a binder-free anode material for LiBs [39]. Based on electrochemical measurements, the composite exhibited superior performance and stable properties, with a capacity of 1050.3 $mAhg^{-1}$ after 60 cycles at a rate of 0.5C. Wang et al. prepared a graphene network supported H-Fe_3O_4 electrodes, in which graphene formed a 3D conductive network with hollow Fe_3O_4 spindles encapsulated between graphene sheets. Similar Fe_3O_4/graphene sheet/GF integrated electrodes were reported by Wei et al. and showed a high capacity of ~ 850 $mAhg^{-1}$ at 150 $mAhg^{-1}$, much higher than the pure Fe_3O_4 on graphene sheet counterpart (~ 620 $mAhg^{-1}$). In another study, researchers dispersed a nanoarchitecture of LiV_3O_8 nanoparticle on reduced graphene oxide and claimed to obtain lithium-ion battery cathodes with high capacity and long-life [40]. Graphene/SnO_2 paper integrated electrodes were also synthesized with a similar laminate structure [41]. This paper electrode showed a higher capacity and better cycling stability than the pure graphene paper and SnO_2 nanoparticles. Similar performance enhancement has also been observed in other 3D graphene network supported metal oxides such as graphene/MnO_2 [42], graphene/Co_3O_4 [43] and graphene/Si [44].

1.8.2.1. Synthesis Methods for Graphene-based Materials

There are several strategies to fabricate graphene-based materials. To start with mechanical approach, scotch tape was used to detach single layer graphene from graphite stacks since stakes were connected by weak van der Waals bonds. Another method can be ball milling or solution/surfactant assisted ball milling of graphite to detach the graphene layer. The final product is washed filtered and dried to obtain graphene. Moreover, liquid phase exfoliation is used to separate graphene layers from graphite or graphitic oxide by using sonic wave trough graphitic materials dispersion. The oxidization of graphite will be explained in following paragraph. Lastly, Chemical vapor

deposition (CVD) method is employed to produce high quality graphene by depositing a gaseous source on to a substrate to obtain single layer graphene deposition.

The oxidizing graphite is highly preferred to obtain graphitic oxide as a starting material for electrochemical application. There is a main method as called Hummers' method to fabricate GO; however, great many modifications were applied to method as well. Pioneering to GO synthesis, Brodie was the first to chemically oxidize graphite in 1859 by adding $KClO_3$ to graphite slurry in fuming HNO_3 [40]. Then, the Brodie method was altered via using concentrated H_2SO_4 and fuming HNO_3 as the oxidizing agents by Staudenmaier [45]. In 1958, Hummers and Offeman reported an alternative method in which graphite is oxidized in a mixture of $NaNO_3$, $KMnO_4$ and concentrated H_2SO_4 for only a few hours experimental procedure. The method was called Hummers' method and it has been used to fabricate GO for a long time [32]. However, this method has flaws such as releasing toxic gas, precipitating nitrate and yielding low amount of GO. Since then, lots of modification was applied to the Hummers' experimental procedure to eliminate these problems. The graphitic oxide is achieved by processing graphite via mixture of concentrated H_2SO_4, $NaNO_3$ and $KMnO_4$ in various reactant and solvent ratio. Kovtyukhova et al. introduced several modifications in the Hummers' method providing pre-oxidized treatment with H_2SO_4, $K_2S_2O_8$, and P_2O_5 molecules and rendering NO_x and ClO_2. The C/O ratio of the oxidation product was 4.0/3.1 which implies much more oxygen contained than the Hummers' method [46]. In 2010, the new method reported by Marcano et al. bringing a different approach to Hummers' method which is called improved Hummers' method. The usage of $KMnO_4$, H_2SO_4, and H_3PO_4 as the oxidizing agents in the improved Hummers' method prevents release of NO and leads in higher amount of hydrophilic oxidized graphite content relative to the Hummers' method. The improved Hummers' method is advantageous for preparation of GO in massive amount because of its easy protocol and equivalent conductivity through reduction. Aii results showed that GO produced by improved Hummers' method yielded highest degree of oxidation that efficient oxidation provokes great numbers of available sites for metal or metal oxides nanoparticles to bond with or higher degree of reduction and increase in electrical conductivity. Recently, GOs that was produced using the improved Hummers method revealed to gain a strong poly-grafting rate at an average condition [47, 48]. In conclusion, the hydrothermal and annealing processes of GO or GO and metal oxide composites are conducted to obtain an ideal electrochemically active material [49].

1.8.3. Titanium Dioxide (TiO_2)

The TiO_2 is a functional metal oxide with high abundancy, non-toxic and highly catalytic activity. Moreover, TiO_2 have received so much attention due to its good chemical stability, low volume change without structural distortion and low-cost preparation. TiO_2 has various polymorphs (Figure 1. 7) such as anatase, rutile, brookite, titanates and bronze, and they all have been studided for Li-ion batteries. Anatase TiO_2 is the most popular witihin these polymorphs due to its layered structure allowing stable capacity after its a few initial cycles even though it has capacity less than graphite. Among them, titanate and bronze-phase titanium dioxide (TiO_2–B) have drawn more attantion due to posession of a greater theoretical capacity and lower density. In this regard, titanium dioxide with versatile crystalline forms and diverse morphologies demonstrate excellent electrochemical performance due to the short diffusion path and numerous available sites for hosting Li ions. Furthermore, it prevents the formation of solid-electrolyte interphase layer by avoiding Li decomposition at the electrode surface, thereby yielding in a high coulombic efficiency and safer operability in Li-ion battery applications. Despite all benefits, TiO_2 has some disadvantages as well, including low solid-state diffusion rate of Li^+ and low electronic conductivity which results in low rate capabilities. Yang et al. discussed TiO_2 nanostructures based on their crystalline forms and morphologies, and their reactions to lithium for Li-ion batteries. their results reveal that the abundant active crystal planes and their directions dictate Li insertion and diffusion which results in shorter pathway and higher capacity [50]. Yarali et al. devised titanate nanotubes with high surface area and expanded interlayer spacing which revealed superior capacity up to 1017 $mAhg^{-1}$ and enhanced electrochemical performance [51, 52]. Dylla et al. studied mesoporous TiO_2(B) nanoparticles for Li^+ insertion capacity and found out that mesoporous structure establishes higher capacity at high charge rates due to the effcient electrode/electrolyte ineraction [53]. In another study, TiO_2–B microflowers were tested for Li-ion batteries and revealed 205 $mAhg^{-1}$ at 10 C as reported by Etacheri et al [54].

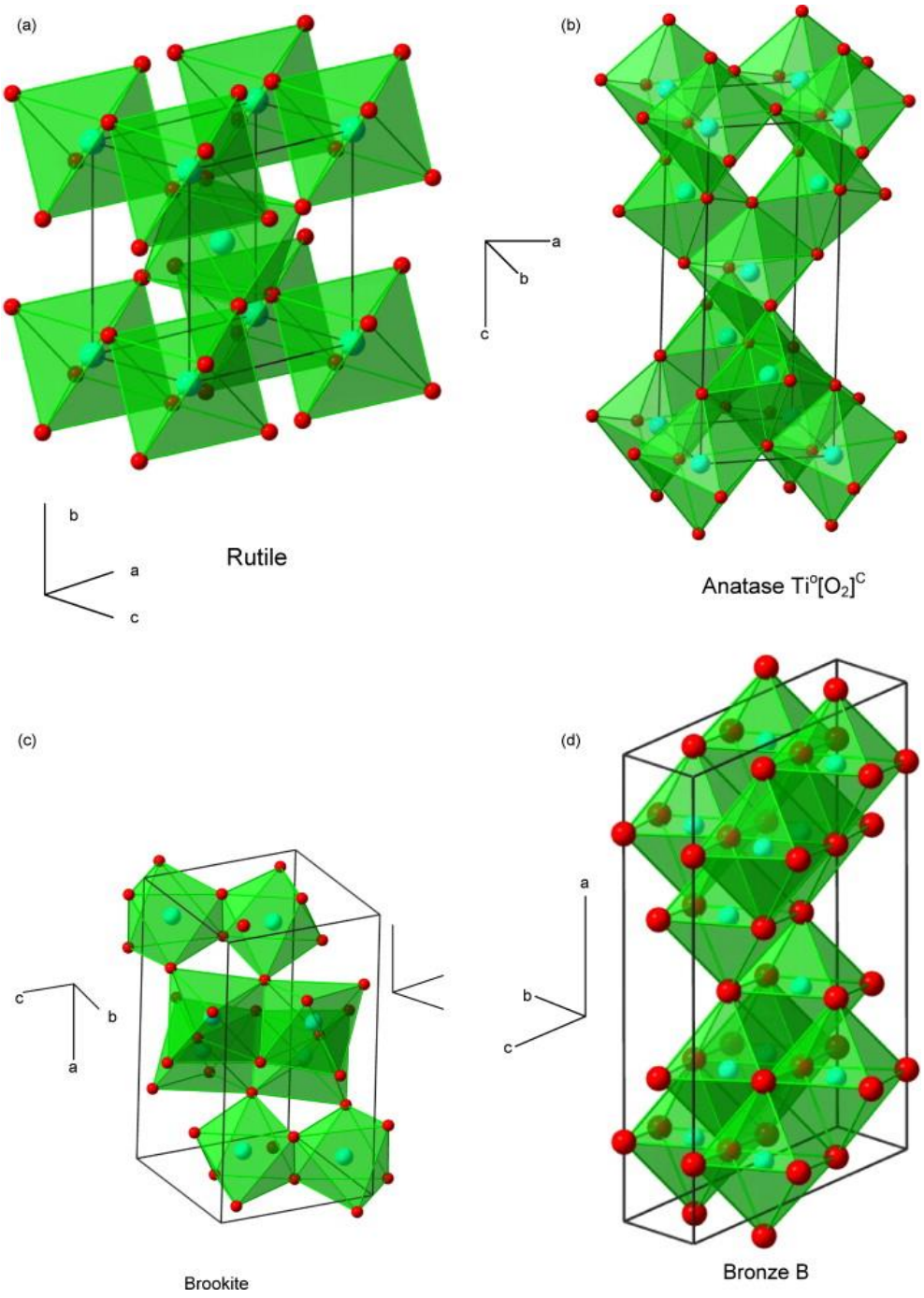

Figure 1. 7. Polymorphs of TiO_2 (a) Rutile, (b) anatase, (c) brookite, and (d) bronze(B) [50]

Besides, its bare crystalline forms reveal low discharge capacity, carbon-based materials used as support for TiO_2-based electrode to enhance its practical use. Overall, numerous researches conducted as carbon and TiO_2 hybrid anode electrode for li-ion batteries. Hu et al. [55] fabricated a free standing graphene–TiO_2 paper using a simple fabrication route which reveled 122 $mAhg^{-1}$ specific capacity at 2 Ag^{-1} current rate after 100 cycles. The titania nanotubes deposited graphene film were fabricated by electrochemical anodization

which showed a capacity of 300 $mAhg^{-1}$ after 100 cycles as reported by Menéndez et al. [56]. Hou et al. fabricated graphene–TiO_2 (B) nanowires hybrid composite by hydrothermal reaction and their electrochemical results displayed a capacity of 304 $mAhg^{-1}$ at 30 mAg^{-1} current density with good cyclability and only 7 % capacity loss after 60 cycles at 150 mAg^{-1} [57]. Moreover, The homogenously dispersed TiO_2 nanoparticles–graphene nanosheets (GNS) anode material synthesized by Tao et al. using an in situ chemical synthesis method which delivered 60 mAh g^{-1} at 5 A g^{-1} current density with negligible fading at its 400^{th} cycle [58]. Wang et al. prepared a TiO_2 nanotube/graphene composite by a one-step hydrothermal method showing excellent electrochemical performance such as 150 mAh g^{-1} capacity at 4 A g^{-1} current density after 50 cycles [59]. Further, TiO_2 nanoparticles dispersed nitrogen-doped reduced graphene oxide anode manufacture by using a hydrothermal method revealing a capacity of 118.4 $mAhg^{-1}$ at 10 C after 100 cycles [60]. The graphene supported TiO_2 (B) nanosheets were used as anode material by Zhang et al. and their results showed 189 $mAhg^{-1}$ after 100 cycles [61]. Cai et al. pprepared TiO_2 nanoparticles and nitrogen-doped graphene nanocomposite which were synthesized by a gas/liquid interface reaction exhibiting 136 $mAhg^{-1}$ capacity at a current density of 1 Ag^{-1} after 80 cycles [62]. A rutile TiO_2 nanoneedle/graphene composite was obtained by Gan et al. via hydrothermal method and it showed 94% capacity retention of 49 $mAhg^{-1}$ capacity at a 5 C rate [63]. Dong et al. synthesized nano-rod TiO_2 and TiO_2 nanoparticles on reduced graphene to compare their Li-ion capacity according to their specific surface area [64]. Furthermore, graphene nanoscrolls surrounded TiO_2 (B) nanowires were prepared by Li et al., which resulted in 153 $mAhg^{-1}$ capacity at 10 C current rate after 300 cycles with 6 % capacity loss [65]. A TiO_2 and nitrogen doped graphene anode constructed by Qin et al. via hydrothermal and calcination synthesis displayed a reversible capacity over 288.6 $mAhg^{-1}$ at 30 C after 1000 cycles [66]. Xiu et al wrapped graphene on TiO_2 microspheres and their results showed a capacity of 170 $mAhg^{-1}$ at 10 C current rate [67].

1.8.3.1. Hydrothermal Method

The hydrothermal synthesis method is used to synthesize high crystalline nanoparticles at high vapor pressure and using high temperature in an aqueous solution. Basically, it uses a cylindrical teflon container and stainless-steel autoclave reactor with hermetic sealing which has to be suitable at high pressure and temperature operation without any

corrosion. Generally, PTFE vessel is filled up to 2/3 of volume limit and synthesis temperature is kept below 250 ^{o}C to maintain the safety of synthesis set-up. This procedure is an effective wet-chemical synthesis method that enables fabrication of various morphologies of materials or their composites for specific applications by lowering their chemical reaction temperature at high pressure. The crystallinity degree, elemental composition and morphology of resulting samples are mainly altered by the duration of synthesis, the solvent to solute ratio, the concentration of the starters, the volume of the solvent, the temperature, the final pH, and the surfactant in use [68, 69].

1.8.4. Silicon (Si)

The pure metal nanostructures have been investigated to be used as anode materials without further treatment. The choice of active metal for Li-ion batteries was discussed by Larcher et al. based on electrochemical capacity, cost, voltage, toxicity, capacity retention and the adaptability of the active mass [70]. Silicon is the most attractive metal to be employed in anode for LiBs due to its low Li insertion potential (0.1 V vs. Li/Li^{+}) and highest theoretical Li storage capacity among all materials. Si has the theoretical specific capacity as 3580 $mAhg^{-1}$ of its $Li_{15}Si_4$ phase at room temperature. However, its structural volume expands more than 300 % upon intercalation process which results in pulverization and huge capacity fading after initial cycle. Furthermore, the poor cycling stability was originated by gradual loss of electrical contact, and unstable solid electrolyte interphase (SEI). Even though it demonstrates discharge capacity up to its theoretical capacity of 4200 mAhg-1 (for its $Li_{4.4}Si$ form), several morphologies like its nanowires form tried out to prevent capacity fading [71]. The smaller nanoparticle size has been proved to prevent the capacity fading up to 4 % according to study conducted by Kim et al.'s [72]. FeSi-embedded ion permeable Si/SiO_x anode yielded long term operability with a 14 % capacity loss as reported by He et al [73]. Carbon based materials were employed as support to tolerate the volume change of Si during the cycle operation. A graphene encapsulated silicon nanocomposite was fabricated by Chabot et al. via freeze-drying and thermal processes demonstrating a capacity of 1200 $mAhg^{-1}$ [74]. Fan et al. fabricated CNT–silicon core shell anode which showed a constant capacity retention up 90 % after 100 cycles at 0.2 C current rate [75]. Reduced graphene oxide wrapped Si nanoparticles were synthesized by Luo et al. via one-step aerosol-induced capillary assembly technique and their results proved that graphene shell hosts volume change of the Si particles and tailors stable cyclicity and rate capability with coulombic efficiency

[76]. A freestanding Si nanoparticles embedded graphene composite membrane was proved to be an anode material with stable cyclicity upon 1000 cycles with a capacity loss of 0.57 $mAhg^{-1}$ per cycle [77]. Liu, Lu et al. fabricated pomegranate-like surrounded ample Si nanoparticles resulting excellent cycling with only 3 % capacity loss after 1,000 cycles [78]. Si/C Yolk−Shell nanostructures were established to engineer the stability in cycling with high capacity and coulombic efficiency by several research groups [79, 80] [81-83]. Entwistle et al. discussed the fabrication of porous Si for LiBs by using magnesiothermic reduction as a facile bulk synthesis route [84]. Moreover, Huang et al. prepared porous silicon/carbon (pSi/C) composite nanosheets by CVD, topochemical reaction, and templating method resulting a capacity up to 1837 using 4 Ag^{-1} current density operable at 500 cycle [85]. Carbon coated porous silicon was synthesized by Gao, Tang et al. via magnesiothermic reaction delivering capacity of 1045 $mAhg^{-1}$ at 1 Ag^{-1} current density [86]. Having high technological capacities, metals like silicon and tin can also be used as active anode materials to replace graphite. On the other hand, there are some negative effects of these materials such as the failure of the batteries because of large volume changes during cycling Which can be compensated by using graphene as support materials.

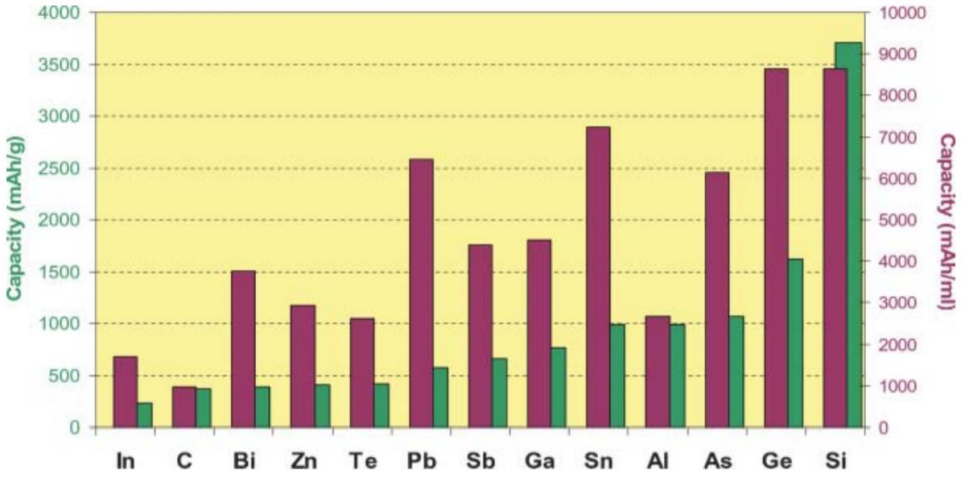

Figure 1. 8. A comparison of metals for Li-ion batteries based on their capacities via alloying [70].

1.8.4.1. Magnesiothermic Reduction Reactions

Magnesiothermic reduction reactions is a subsection title of metallothermic reduction reactions (MRRs) by establishing displacement reactions to reduce compounds by a reactive metal. MRRs are exploited to fabricate metals, alloys, nanoporous silicon, nanoporous carbon by using reactive metals, such as Li, Mg, Al, Ti, Mn, Zn, Fe, Co, Ni, Sn, Pt and Au. The properties of resulting materials in MRRs are varied by controlling temperatures, durations, and using different grain sizes for the reactive metals. Porous and nanostructured Si are prepared by performing magnesiothermic or aluminothermic reduction reactions where magnesium and aluminum are used as the reductants. The magnesiothermic reduction reactions employ Mg metal to reduce SiO_2 by exchanging oxygen anions between silicon oxide and magnesium under a thermally activated environment. The reaction is operated at the temperature range of 500-800 ℃ under the Ar flow in a furnace [84, 87].

$$4Mg(g) + SiO_2 \rightarrow 2MgO + Mg_2Si$$

$$Mg_2Si + O_2 \rightarrow 2MgO + Si$$

1.9. Metal Air Batteries

Metal air batteries are basically composed of a metal as anode, a cathode and a separator that separate anode and cathode within an electrolyte. LiBs operate based on intercalation of Li^+ ions but this type of battery works based on formation of metal peroxide (Me_2O_2) or metal hydroxide (Me-OH) after exposing cathode to oxygen from air. As a matter fact that, metal air batteries were designed to employ air as source of oxygen, however, pure oxygen gas was started to involve as oxygen source due to challenges coming from air content, such as 78 % N_2, 21 % O_2, ~0.04 % CO_2, and ~0.4 % water vapor. The extra contents of air force cell chemistry to have a lot of side products and numerous challenges lowering the cell performance. The consequence of open architecture cell is highly problematic since number of side product increased and they are irreversible. Li_3N, LiOH and $LiCO_3$ are the main irreversible side products and require to be decomposed at every cycle operating under the air ambient. Several pieces of research were reported to prevent corrosion of Li metal anode using a protective layer for the anode surface as a composite protective layer on Li metal to obtain high cyclic stability and round-trip efficiency [36].

As a result of that, trends turned to Li-O_2 to operate cell in pure O_2 flow to control the ambient and side products.

General electrochemical reaction occurs based on kinetics of electrolyte-electrode interface meeting oxygen-metal species. Metallic anode material has been studied as Li, Na, Zn, Mg, Al, etc. with different type of electrolyte and various cathode materials as detailed in Table 1. 1 [88]. Li is the lightest alkali metal among all in table donating lowest reduction potential vs SHE. In addition, it has the highest volumetric and gravimetric theoretical capacity. Since magnesium and aluminum are highly reactive, Zn and Na are the other closest alternative metals employing in metal-air batteries in future.

Table 1. 1. Reduction potentials and energy merits of various metals for metal air batteries [88]

Metal	**ρ (gcm^{-3})**	**n-electrons**	**Theoretical capacity**		**E^0(V) vs SHE**
			$mAhcm^{-3}$	**$mAhg^{-1}$**	
Li	0.53	1	2060	3860	-3.04
Zn	7.14	2	5850	820	-0.76
Mg	1.74	2	3830	2210	-2.37
Na	0.97	1	1120	1170	-2.71
Al	2.70	3	8040	3820	-1.66

1.10. Lithium-O_2 Batteries

Lithium oxygen (Li-O_2) battery also called lithium air battery is a type of rechargeable metal air battery. They exhibit ultra-high energy density to power electrical vehicles and compete with gasoline power. The oxygen as cathode material is provided from outside environment of battery rather than already stored inside which vastly reduce the battery weight. Additionally, great specific capacity is obtained at discharge process and high operation voltage window. As an outcome of these reasons, Li-O_2 batteries exhibit high energy density.

The first prototype of Li-O_2 was first introduced by Semkow and Sammells [89]. Most importantly, Li-O_2 was first reported in 1996 by Abraham and Jiang [90]. The figured out a hole in their cell composed of polymer-based electrolyte and carbon cathode but still

revealing high capacity. Many of researchers were started to report Li-O_2 battery studies for beginning of new hope as future battery technology. Then, scientist in this field were claiming non-rechargeability for this type of battery based on their results after following years. Yet, many like Read et al were also revealed good results likewise Abraham, and Bruce showed the solid results of rechargeable Li-O_2 batteries [91-93]. Then, Li-O_2 became one of the most promising alternatives for electrifying electrical vehicles.

1.10.1. Li_2O_2 formation

Like silicon or graphite being active material in Li-ion batteries, Li_2O_2 is the main material in Li-O_2 batteries account for electrochemical energy storage and conversion. Li_2O_2 electrochemically forms during the discharge process and decomposes during the charge process as the standard operation mechanism of Li-O_2 battery. On one hand, oxygen undergoes reduction in the cathode and Li oxidizes at the anode during the discharge process. The oxygen reduction reaction (ORR) forms O_2^-, O_2^{2-}, and O^{2-} yielding LiO_2, Li_2O_2 and Li_2O as shown in charge and discharge reactions below. On the other hand, Li_2O_2 decomposes into Li and O_2, and lithium reduced back to its solid form at anode during the charging process. The thermodynamically formation energy of Li_2O_2 corresponds to 2.96V with respect to Li^+/Li derived from the standard Gibss free energy (Δ_rG=−570.18 kJ mol^{-1}) [94].

Discharge:

Anode:

$$2Li \rightarrow 2Li^+ + 2e^-$$

Cathode:

$$Li^+ + e^- + O_2 \rightarrow LiO_2$$

$$2LiO_2 \rightarrow Li_2O + O_2$$

$$Li^+ + e^- + LiO_2 \rightarrow Li_2O_2$$

$$2Li^+ + e^- + Li_2O_2 \rightarrow 2LiO_2$$

Charge:

Anode:

$$2Li^+ + 2e^- \rightarrow 2Li$$

Cathode:

$$Li_2O_2 \rightarrow O_2 + 2e^- + 2Li^+$$

Overall reaction:

$$2Li + O_2 \leftrightarrow Li_2O_2 \qquad E^0 = 2.96V\ (V\ vs\ Li^+/Li)$$

However, the growth mechanism of Li_2O_2 is not one step process chemistry, but various types of additional chemical reactions with intermediate steps which is rather cumbersome.

The crystalline Li_2O_2 as final product has poor electronic conductivity to sustain the electrochemical reaction within the batteries, so that, catalyst materials must be employed to promote generation of amorphous Li_2O_2. The study conducted by Zhong et al confirmed [95] that amorphous Li_2O_2 provided greater Li^+ mobility and higher density of O_2^- defects than crystalline Li_2O_2. They observed via in situ transmission electron spectroscopy (TEM) that Li_2O_2 initially decomposed at cathode interface rather than solid electrolyte interface giving clue as Li^+ transports faster than electrons and electronic conductivity retards OER process. Similar results were reported by Kushima et al. using oxygenated liquid electrolyte to analyze Li_2O_2 at three-phase interface. In this respect, Gallant[96], presented several aspect like surface delithiation and bulk oxidation of Li_2O_2 and the promoted one-electron charge reactions [97]. It is significant that these achievements are inadequate to explain the intrinsic mechanism that includes charge and discharge.

Besides having problems with the formation of Li_2O_2 and not have a stable electrolyte, they have been suffering from several challenges disallowing from commercialization. Firstly, high charge overpotential is required due to their dully problematic reaction kinetics during oxygen evaluation reaction yielding decomposition of electrolyte [98]. The overpotential is simply the potential difference between charging and discharging platue which potential for formation and decomposition of Li_2O_2 requires merits more/lower than their thermodynamic values happening due to practical kinetic resistance

during the cell operation. Secondly, reduced oxygen species such as superoxide radical anions ($O_2^{\bullet-}$) produced on discharge step tend to attract with electrolyte, air electrode, and Li metal anode partaking side products and corrosion respectively [99]. Lastly for now, the oxidative nature of reaction products initiates parasitic side product such as $LiCO_3$ by degrading the cathode and electrolyte resulting passivation of active sites on cathode surface [100]. There is a great deal of research from last three decades to find solutions for these aforementioned problems such as electrochemically active air cathode materials, a stable electrolyte and a compatible catalyst to overcome overpotential for formation of Li_2O_2.

In addition, formation of side products during OER stage makes it even more obscure enough to be confused in electrochemical intermediate steps and kinetic details. According to Lewis definition, bases donate electron (electron donor) whereas, acids accept electrons (electron acceptors) to form a chemical bond. The Pearson's Hard Soft Acid Base (HSAB) theory expresses that hard bases tend to react with hard acids and soft bases to soft acids. Donor number (DN, basicity) of solvent in electrolyte is a measure for electrolyte to solvate Li-O_2 battery reactants as Li^+, O_2^- and LiO_2. Li^+ ions fit the hard acid definition because of having high charge state and weak polarizability. On the other hand, O_2^- possesses low charge states and firm polarizability thus it states as soft base. Briefly, LiO_2 as overall product is not stable when a hard Lewis acid (Li^+ cation) reacts with soft base (O_2^- anion). In ORR process, oxygen (O_2) is reduced by cathode active materials to generate O_2^- anion by one electron reduction process and dissolved in electrolyte to form LiO_2 [101]. After this step, LiO_2 could disproportionated to Li_2O_2 and O_2 or reveled another Li^+ cation to form Li_2O_2. The equilibrium is maintained in between solvated LiO_2 within the electrolyte and adsorbed LiO_2 on cathode surface controlled by solvation capability and kinetic of electrolyte solvent. So that, the basicity of electrolyte solvent determines the coordination of Li^+ (strong Lewis acid) and $O_2^{\bullet-}$ (soft base) assigning stability of electrolyte and Li_2O_2 growth pathway during discharge process.

1.10.2. Electrolytes for Li-O_2 batteries

To find a proper electrolyte, there have been reposted four different types of electrolyte such as aprotic, aqueous, hybrid, and all solid-state based on their chemical constitutes. A typical Li-O_2 battery is constructed with Lithium metal as anode, a carbon-based air cathode and finally one of these electrolytes as seen in Figure 1. 9 [102]. Ionic liquid-

based electrolyte has several desirable properties such as safer electrolytes in terms of very low vapor pressure, thermal stability, low flammability, high operation liquid temperature ranges, broad electrochemical potential windows. However, lithium hydroxide (LiOH) or lithium hydroxide monohydrate ($LiOH.H_2O$) is the main product in the case of utilizing aqueous or hybrid aprotic/aqueous as electrolyte. Thus, reaction between water and Li metal is unavoidable in these electrolyte systems so that, protection layers on lithium metals or impermeable membrane as separator were purposed in literature as solution. On the other hand, there is lack of study in literature for all solid electrolyte with high ionic conductivity to be performed in Li-O_2 research. Although solid electrolyte brings solutions to limited potential window, dendritic formation on Li surface, evaporation of solvents and leakage problem, they have low ionic conductivity and sluggish kinetic during electrochemical process. As will be discussed in next line, aporetic based electrolyte have been widely studied for Li-O_2 batteries.

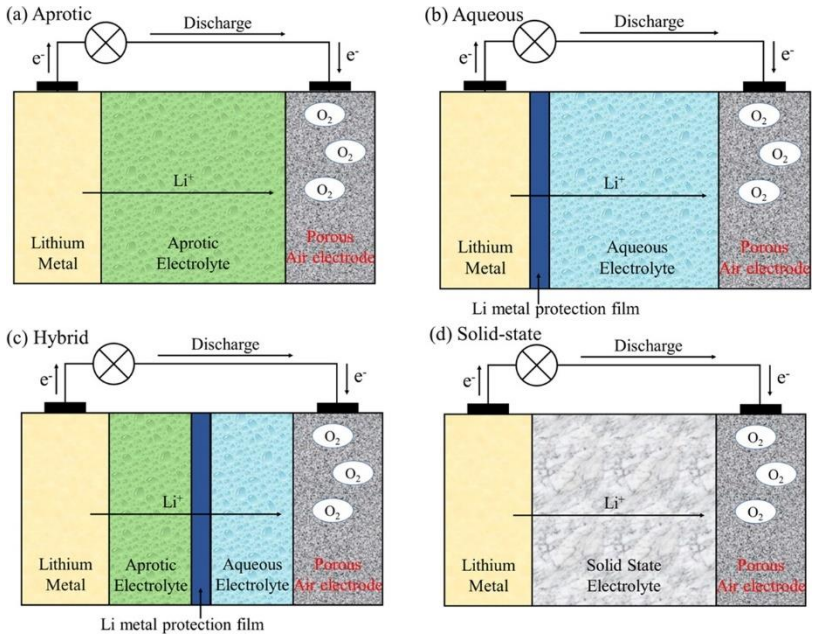

Figure 1. 9. Four different electrolytes for Li-O_2 batteries; a) aprotic, b) aqueous, c) hybrid and d) solid-state electrolytes [103]

The selection of Li salts and electrolyte solution is able to construct a stable electrolyte for Li-O_2 cell throughout the electrochemical process. Literature suggests several lithium salts such as hexafluorophosphate ($[PF6]^-$), tetrafluoroborate ($[BF4]^-$), perchlorate ($[ClO4]^-$), nitrate ($[NO3]^-$), bis(oxalato)borate ($[BOB]^-$), trifluoromethanesulfonate ($[OTF]^-$ or $[TF]^-$), bis[(trifluoromethyl)sulfonyl] imide ($[TFSI]^-$), bis(fluorosulfonyl)imide ($[FSI]^-$), and bis((perfluoroethane) sulfonyl)imide ($[BETI]^-$) to

be used in electrolyte for Li-O_2 battery [104, 105]. Li[PF_6] as salt for electrolyte in conventual Li-ion batteries is found to be not applicable for Li-O_2 batteries due to its moisture sensitivities, thermally instability and dissociation to $[PF_5]^{2-}$ at high polarization. Li[TF] and Li[TFSI] are more stable salts that utilized in TEGME giving less capacity fading. $[TF]^-$and $[TFSI]^-$ via high electron donor capability of Li salts anions successfully establish coordination between Li^+ to O_2^- to promote lifetime of stability and solubility discharge intermediates within the proper electrolyte solvent. In addition, numerous solution were employed such as organic carbonates (i.e. propylene carbonate (PC), ethylene carbonate (EC)), ethers (i.e. 1,2-dimethoxyethane (DME), diethylene glycol dimethyl ether (diglyme or DG), diethylene glycol dibutyl ether (DBG), triethylene glycol dimethyl ether (triglyme), tetraethylene glycol dimethyl ether (TEGDME or tetraglyme)), dimethyl sulfoxide (DMSO), phosphates (i.e. triethyl phosphate (TEPa)), nitriles (i.e. acetonitrile, sebaconitrile), and ionic liquids (i.e. 1-butyl-1-methylpyrrolidium bis(trifluoromethanesulfonyl)imide (Pyr_{14}TFSI)) as electrolyte solvents in Li–O_2 batteries [106-110]. Alternatively, DME proved to be good candidate as Li-O_2 batteries electrolyte solvents according to the recent researches. Dimethyl Sulfoxide (DMSO) containing Li-O_2 battery was also reported as yielding high capacity however there is also contradiction from many researches as well claiming instability of DMSO due to formation of $DMSO_2$ at high polarization [111]. Acetonitrile (MeCN) and methylimidazole earned credibility to be studied as convenient Li-O_2 battery electrolyte solvent according to recent reports.

1.10.3. Redox mediator

Effect on battery performance in terms of accelerating ionic conductivity and reaction kinetic. Using a redox mediator is another solution to refine problematic reaction kinetics during oxygen evaluation reaction [98] of Li-O_2 battery. As a soluble catalyst within the electrolyte, redox mediator repairs low round-trip efficiency and low reversibility by decreasing high overpotential during charging process. Redox mediators can block the parasitic reaction normally occurring at high potential via their charge transfer between their oxidized and reduced forms. However, redox mediator must sustain their compatibility with electrolyte/cathode interface and stability of their organic structure during the transformation between their oxidized-reduced forms. General formulation of

the effect of redox mediators to decomposition reaction of Li_2O_2 can be summarized as following in Figure 1. 10.

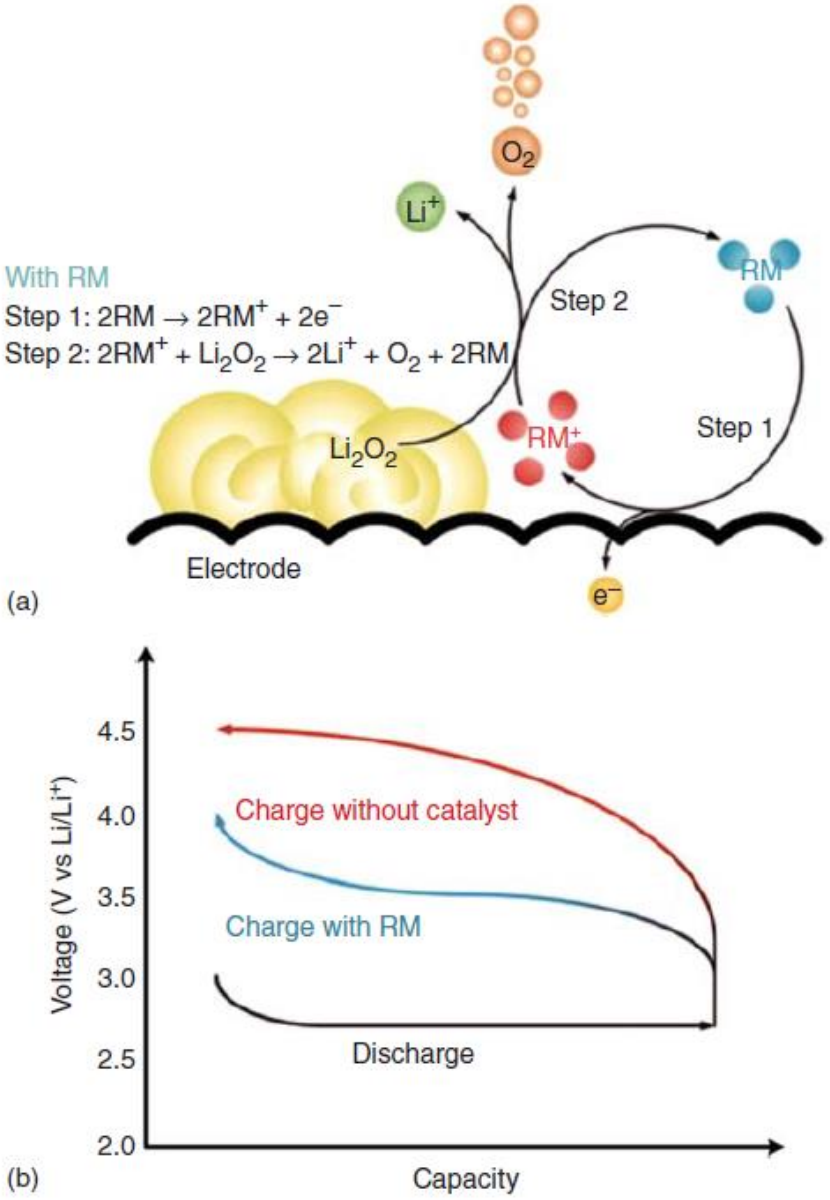

Figure 1. 10. Working principle of redox mediators illustrated by Lim et al [112].

Benjamin J. Bergner et al showed 2,2,6,6-tetramethylpiperidinyloxy (TEMPO) can be used as redox mediator combined with solid electrolyte which yielded higher stability and prolonged cycling [113]. In addition, Hee-Dae Lim and coworkers compared RM-assisted charging process in their study and showed DMPZ performing remarkably low overpotential and high stability in the Li-O_2 cell [114]. Moreover, Li-O_2 cells containing

TTF were cycled 100 times with complete reversibility of Li_2O_2 formation/decomposition on each cycle reported by Yuhui Chen et al [115]. Lastly, LiI is proved to be a good redox mediator presented by Won-Jin Kwak and Tao Liu claiming high efficiency and rechargeability of Li-O_2 battery with extremely large capacities [116]. According to Aetukuri et al., a ppm fraction of H_2O can act as redox mediator to promote solution growth mechanism and enhance the solubility of O_2^- and LiO_2[117].

1.10.4. Lithium as anode material

The open-cell structure of Li-O_2 battery permits oxygen or even moisture/CO_2 to the cell ambient, and Li anode is corroded, eventually ending up with capacity fading as presented by Shui et al. [118]. In contrast to intercalation mechanism of Li-ion batteries, Li^+ ions are plated and striped during the charge and discharge process which expose Li metal anode to volumetric and morphological changes. Unlike the process in Li-ion batteries, SEI forms and decompose on the lithium metal anode surface upon cycling. Several pieces of research were reported to prevent corrosion of Li metal anode using a protective layer for the anode surface as a composite protective layer on Li metal to obtain high cyclic stability and round-trip efficiency similarly reported by lee et al. [99]. Liu et al. reported that using fluoroethylene carbonate (FEC) as additive to 1M LiF_3SO_3/TEGDME formed protection layer on Li metal and increased cyclability [119]. Lee et al. suggested to use Al_2O_3/PVdF-HFP as a composite protective layer on Li metal to obtain high cyclic stability and round-trip efficiency [99].

1.10.5. Cathode materials

Li-air batteries are generally composed of lithium anode, electrolyte and porous carbon based O_2-cathode. As remind the main concept, -during discharge- O_2 is reduced on the cathode by the help of catalyst within the pores structure and lithium is oxidized to Li^+ cation in the anode. Carbon materials are widely preferred cathode materials for Li-air batteries due to efficient oxygen diffusion channels and facilitative electrolyte wettability for ionic transport within their forms. Researchers investigate carbon materials due to lightness and high conductivity. Super P, Super S, Ketjen Black, et al. carbon materials were used in Li-air batteries so far to optimize their early stage developments [92, 120-125].

The two-dimensional (2D) monolayer structure of graphene and the very high surface area create both a large surface for the reaction and it helps the oxygen to reach the Li^+

ions [126]. On the other hand, graphene is an important potential support material for Li-air battery applications due to its lightness and high electrical conductivity. A very high capacity values which is 15000 mAh/g were obtained by using graphene in an important study of Xiao et al. [127]. Graphene is used as a main compound in Li-air batteries instead of other carbon-based materials. Li et al. reported that they obtained 8705 $mAhg^{-1}$ capacity by using only graphene. That value is pretty high by comparison with other carbon types such as BP-2000 (1909 mAh g^{-1}) Vulcan XC-72 (1053 $mAhg^{-1}$)[128]. It demonstrates the catalytic behavior to reduce oxygen due to its defectous structure. A study showed that using graphene in air cathode increased the capacity and decreased the overpotential as a good catalyst compared to Vulcan XC-72. [129]. As the characteristic of carbon materials, graphene is used as support material for catalysts like MnO_2, Co_3O_4, SnO_2 ve Mn_3O_4 yielding superior Li-air performance results [130-137]. The catalysts were either dispersed onto graphene physically or synthesizing on the graphene. Binding of metal oxide onto graphene surface is possible via coordination's with carbonyl (C=O), hydroxyl (-OH) and carboxylic acid (-COOH) groups. As an exaample, graphene supported MOx catalysts provided high catalytic activity [138]. In addition to it, nano structured $CoMn_2O_4$/graphene catalyst exhibited high activity both ORR and OER [131, 139].

Another important point with the catalyst is accumulation of Li_2O_2 on the cathode that clogs the pores and prevents the O_2 input/output decreasing the capacity and cycle life of the battery [123]. The most perceptible work is published on this topic by Freunberger et al. [120]. In their study of Li-air batteries, Li_2O_2 formation was investigated using various carbon materials (Super P, Ketjen Black, Black Pearls, etc.). Carbon compounds with different surface area are published by Cheng and Scott [140], and Xiao et al. [121] and it has been shown that increasing the surface of the carbon redounds the reaction surfaces and consequently enhances the capacity. However, the high surface area is not adequate by itself but porous network along the structure. When the pores are too small, i.e. the micro-porous structure, the pore inlet is obstructed, and reaction cannot occur in the interior of the pores. Yang et al. determined the effect having different pore size and surface area by using carbon materials [141]. They reported that energy density decreases when the pores are very large [142]. In this case, an optimum pore structure and high surface area are required. Graphene foams seem appealing due to its ability to provide more host space for catalyst particles, higher accommodation sites Li-ions, the faster

migration rate of Li ions, the stability of high electron conductivity, high surface area, more open structure, accessibility of more pore volume, high strength, relatively large specific capacity and good cycle stability at high current density properties. Recently, Wang et al. [143] fabricated a resorcinol-formaldehyde (RF) crosslinked rGO sponge on a Ni foam template to create a loosely packed, highly conductive cathode composite. The microsize pore structures enable better O_2 transport throughout the electrode channels revealing 2020 mAg^{-1} capacity at a high current density of 2.8 mAg^{-1}. Therefore, freestanding graphene foams are excellent porous air cathodes to enhance the rate and capacity of next generation Li-O_2 batteries. In another investigation, Sergeev et al. evaluated the optimal cathode thickness taking into account oxygen transport parameters and a proper design of porous cathode materials that is able to shorten the oxygen diffusion path [144]. Storm, et al. investigated the variation of the performance of Li-O_2 batteries due to differences in functional groups of reduced graphene oxide (rGO) and synthesis method. Moreover, they concluded that rGO based cathodes in Li–air batteries can yield high capacity with the ability to cycle [145] .

The freeze drying is a unique drying process to generate free-standing graphene and graphene oxide sponges. In this method, already frozen oxidized graphene sheets entangle and bind each other by lowering the pressure at lower temperature where water molecules evaporated, and active binding sites left behind. In addition, mechanical strength, specific surface area and pore size are tailored by modifying the hydrophilic character during GO reduction as a starting material for freeze drying. Chemically modified GO is a type of amphiphilic material with distinct hydrophilic and hydrophobic sections from edge to center by altering functional groups and surfactants. Another technique to form 3D graphene is using gelator molecules during the solution-based synthesis. Gelator molecules are responsible for maintaining the 3D structure as physical or chemical crosslinking agents thereby offering integrity for the final product. Cross-linking agents typically contain amides, peptides, ureas, saccharides, nucleobases, large alkyl chains molecules and steroid compounds. [146]. Such steps can be combined to produce graphene hydrogel via hydrothermal treatment. The size and shape of pores in hydrogel are determined by the amount of trapped water in hydrophobic and hydrophilic sites of functional groups on graphene surface. Freze drying is used to remove water molecules from hydrogel where it converted to aerogel as final product. Graphene-based aerogel is a kind of carbon based monolithic materials with 3D micro- and nano-structures that air

entrapped in the voids where water removed.[147, 148]. Graphene/oxide foam is produced via chemical vapor deposition techniques. Nickel foam with micron size porosity is utilized as a substrate in order to deposit the carbon-based materials by CVD method, followed by etching the nickel foam with a high concentration of acidic solvent. After drying procedure, a free-standing graphene foam is obtained which can be oxidized in order to produce graphene oxide foam. [149].

Apart from their promising results, carbon was claimed to be non-stable beyond 3.5 V (vs. Li^+/Li) and precipitate irreversible Li_2CO_3 by promoting electrolyte decomposition during the oxidation of Li_2O_2 [150]. As the main reason, the synthesis of Li_2CO_3 is highly possible since the reaction of Li_2O_2 and C is spontaneous. Li_2CO_3 causes capacity loss since it is precipitated in the electrolyte or deposited on the carbon surface, which leads to blocking of Li^+ transport within the electrolyte/electrode and loss of catalytic activity of electrode, respectively. Moreover, decomposition of Li_2CO_3 requires a potential higher than the decomposition of Li_2O_2. High charge overpotential (>4V vs. Li^+/Li) increases the possibility of additional parasitic reactions, lowering the faradic efficiency, and limiting cyclic performance. McCloskey et al. presented that 36 % of the total Li_2CO_3 stems from the carbon electrode via the study carried with the help of differential electrochemical mass spectrometry (DEMS). Due to this reason carbon free or metal oxide and carbon nanocomposites were studied by many researchers to eliminate electrode surface passivation and corrosion. Pt and Pt-alloys are the well-known electrocatalysts for ORR including electrochemical applications [151]. Since Pt is a costly material, other catalysts have been studied as alternatives; however, the alternatives display generally lesser activity during the operation [150, 152-155]. Studies which are to develop different catalysts such as Pt and Au instead of highly active metal oxides and alloys proceed in Li-air batteries [156]. Gold (Au) /carbon has drawn attention as a good catalyst for the OER reaction, but the use of Au is not considered economically feasible as well [157]. Oh et al. reported the mesoporous metal oxide compounds can yield high catalytic effect on oxygen reduction and oxidation reactions by reaching a capacity of approximately 10000 mAh/g [158]. Further, MnO_2 earned its place as one of the most studied metal oxide compounds among these catalysts for reducing the overpotential during charging according to recent regarding studies [159]. Truong et al. reported that the nanostructured MnO_2 compounds with different morphologies reduce the activation energy and thus they achieve better performance in Li-air batteries [160, 161]. Black et

al. (2013) studied Co_3O_4 and reduced graphene oxide nanocomposite to reduce the charge and discharge voltage difference. A Co nanoparticles dispersed on N-rich carbon were prepared via sol–gel method Zhang et al. [162] as a cathode which yielded low overpotential, high cyclability and enhanced performance. Kim et al. employed Co nanoparticles and carbon nanofiber composite as cathode for Li-O_2 batteres to reduce discharge and charge polarization and improve cycling stability [163].

1.10.5.1. Ceria

Another effective catalyst is CeO_2. Besides being the most abundant element in earth's crust among the rare earth class, cerium is one of the most studied rare earth elements based on its versatile properties and wide application areas. Ceria has been studied as a catalyst for the oxidation reactions of several organic compounds and CO with diesel soot to purify automobile exhaust from toxic gasses in catalytic converters [164-168]. The other applications of ceria are dry reforming [169], combustion of organic compounds [170], oxygen sensors [171], Sabatier reaction [172] and chemical valorisation of CO_2 [173]. Ceria is an attractive material by yielding a fast redox change in oxidation states and oxygen vacancy defects by very small activation energy.

There are too many factors partaking in the enhancement of cerium redox property and its catalytic efficiency such as composition, shape, size, morphology, temperature, and doping. Catalytic performance of ceria nanomaterials depends on surface oxygen composition properties implying surface geometric and electronic structure, and nanocrystal morphology implying high-density crystal planes [174, 175]. Higher surface to volume ratio, smaller particle size, and high temperatures increases the oxygen vacancy mobility thus enhancing the catalytic properties. Smaller surface to volume ratio regarding to shape and particle size, and temperature increases the oxygen vacancy mobility to increase aforementioned properties.

Studies have shown that the activity of the cathode is directly related to the structure, morphology and pore size of the used catalyst. Morphology-dependent surface chemistry and catalytic performance of ceria are directly related to the majority of oxygen vacancies within the ceria structure. Oxygen vacancy formation is a direct result of Ce^{4+} to Ce^{3+} transition. This transition can be obtained by the loss of oxygen or electrons which can be induced by temperature, oxygen partial pressure, desorption or adsorption of other

atoms, electric field, and surface stress. When a neutral oxygen atom extracted from the CeO_2 lattice accommodating Ce^{4+} atoms, lattice gains two reduced new Ce^{3+} atoms, one oxygen vacancy defect and 2 electrons. The vacancy can be easily replenished in an oxygen rich ambient which is an excellent property for the catalytic reactions. The oxygen vacancy formation is calculated by Ce^{3+} concentration over total existing cerium (Ce^{3+} /(Ce^{3+} + Ce^{4+})). Ce^{4+} to Ce^{3+} transition is achieved by a very slight energy due to the similar energy levels of 4f and 5d electronic states and low potential energy barrier they have [176, 177].

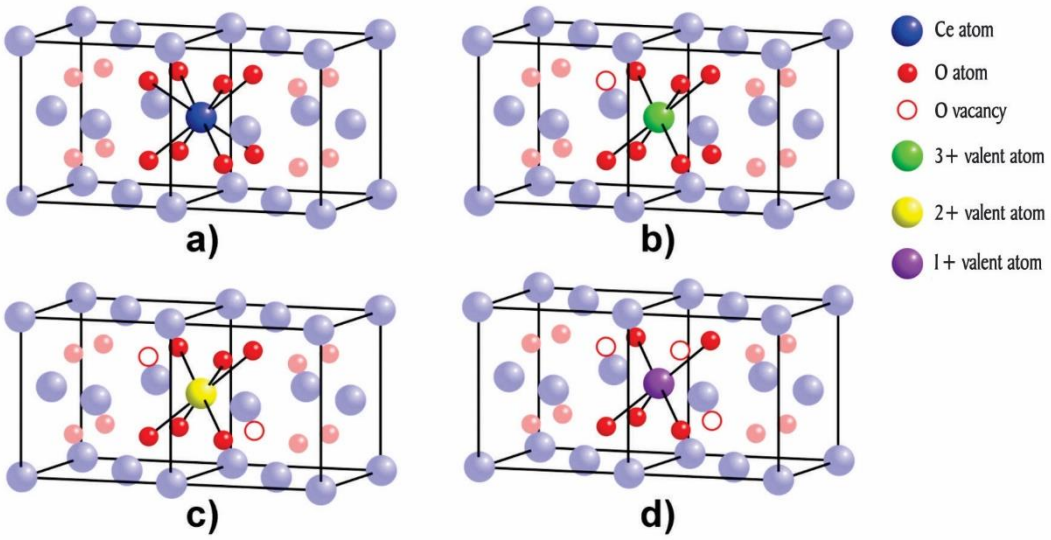

Figure 1. 11. Oxygen vacancy formation in CeO2 unit cell according to its a) neutral form, b) +1 valent, C) +2 valent and d) +3 valent atom displacement with Ce

The number of oxygen vacancies can be increased by doping ceria nanomaterials with one, two or three valent elements. Doping with other elements creates oxygen vacancy defects and changes the oxidation states in order to maintain the electroneutrality according to embedded valence state as illustrated in Figure 1. 11 [178, 179]. CeO_2 has a fluorite crystal structure with an FCC unit cell and each Ce atom accompanies 8 O atoms while each O atom is coordinated by 4 nearest neighbor Ce atoms. Multiple valencies in ceria creates an improvement of oxygen storage and release ability so that oxygen atoms diffuse more easily within the lattice to reduce or oxidize other molecules. Sudarsanam et al. reported that CuO_x-decorated CeO_2 nanocubes exhibit a higher catalytic performance for soot oxidation compared to that of pristine CeO_2 nanocubes [180] and also MnO_x/CeO_2 nanocubes exhibit a remarkable catalytic performance toward both

diesel soot oxidation and benzylamine oxidation compared to that of pure CeO_2 nanocubes [181].

Richard I. Walton discussed many different parameters, additives, dopants and solvent for the synthesis of ceria nanostructure by hydrothermal method that facilitates to control surface properties, morphologies and its composites with other elements[182]. Devaraju et al. synthesized CeO_2 hollow spheres using solvothermal reaction and they concluded that ceria exhibited better catalytic activity via the higher specific surface area and smaller crystallite size [183]. Sun et al. synthesized CeO_2 nanorods by using ethylenediamine as additive to control morphology with experimental parameters such as the solvent composition, surfactant and the cerium source precursor, and the effect of the synthesis parameter were analyzed by UV–visible adsorption and photoluminescence spectrum [184]. The reversible transformation of CeO_2 to Ce_2O_3 studied by Skorodumova et al. by using density functional theory (DFT) and they concluded that formation of oxygen vacancies, their migration and diffusion are attributed to virtual Ce^{3+} vacancy complexes [185]. A Zr–Ce–Mn–O material were prepared by Azalim et al. by sol-gel and calcination and they discovered that high concentration Mn^{4+} increased the oxygen mobility at the surface and enhanced the textural and redox properties [186]. Martínez-Arias et al. reported that the reduction and oxidation capability of CeO_2 improved in the presence of CuO in redox cycles under CO/O_2 thanks to their remarkable synergetic effect [187]. Reddy et al. demonstrated that solid solutions of ceria–zirconia exhibited high OSC in and high catalytic activity compared to bare ceria [188].

There have been only a few studies about CeO_2 so far and it has been shown to be an effective catalyst [189]. Singh et al. decorated crystalline ceria nanoparticles (CNPs) onto reduced graphene oxide (RGO) by wet chemical process and studied electron mobility throughout CNPs to rGO. According to their results, anchoring CNPs on the RGO sheets formed numerous oxygen vacant sites which enabled electron on CNP_S interaction with the localized hole on rGO [190]. Nitrogen doped reduced graphene oxide showed excellent electrocatalytic activities for oxygen reduction reaction compared to the commercial graphene oxide and carbon black as reported by Lee et al [191]

CHAPTER 2. METAL & METAL OXIDE DECORATED GRAPHENE BASED ANODES FOR LI-ION BATTERIES

2.1. Introduction

Lithium-ion batteries (LiBs) emerge as promising energy storage solutions for a range of applications, from portable electronics to the automotive and aerospace industry, thereby a high demand for LiBs with high energy/power densities as well as more sustainability arise in recent years [192]. To actualize the widespread utilization of LiBs in electric vehicles (EVs), fast charging/discharging is one of the most crucial aspects. Since the commercialization of Li-ion batteries in the 90 s, so many studies have been conducted to find a better replacement for graphite anodes to show higher rate capabilities and longer cycle life [193-195]. The commercial graphite anode demonstrates inadequate performance because of being plated with lithium dendrites at such high rates of operation, causing mass transport problems [196]. Generally, an ideal candidate for a Li-ion battery anode should have the following features simultaneously. (a) High ionic conductivity for fast solid-state diffusion of Li^+, (b) high electronic conductivity to transfer electrons to the current collector, (c) and high surface area to maximize lithiation reaction [197]. In this respect, metal and transitional metal oxide on carbon support can tailor high Li-ion storage capacities [198-200].

Graphene-based anodes may outperform in such cases due to shortened Li^+ ion transport pathways [201], yet high performance could only be achieved by specially modified graphene, as the pristine material has a high tendency towards irreversible stacking of graphene nanosheets, limiting the reversible insertion and extraction of Li^+ ions [202]. Graphene oxide (GO), which is a defective form of graphene, does not possess sufficient electronic and mechanical properties to be used alone as the anode material in LiBs [203], despite its facile producibility and excellent chemical stability [38]. A possible solution is to thermally or chemically treat the GO to remove functional groups on GO surface for boosting the conductivity, as well as the specific surface area, producing reduced graphene oxide (rGO) [204]. Another widely utilized way of further enhancing the electrochemical properties of carbon-based anode materials is to use dopants like N, B, S, and P. Nitrogen-doping of rGO can be very promising for improving the electrocatalytic activity and conductivity of the material by the provision of more electron

density and increase of unoccupied density of states as a result of electron transfer from carbon to nitrogen which is more electronegative [205, 206]. The nitrogen-doping also increases the specific surface area by bigger defect sizes and more porous structure [31]. More importantly, it supplies additional active sites for Li^+ storage [206, 207]. Furthermore, the strong interaction between the nitrogen-doped carbon lattice and lithium ions may further aid in enhanced insertion/extraction of Li^+ ions [196]. Although there are an extensive amount of studies in the literature utilizing nitrogen-doped/reduced graphene as hybrid anode materials [208-212], the studies using only the nitrogen-doped/reduced graphene oxide are rare and provides limited information about the electrochemical performance of such materials alone. A number of studies in the literature report that the nitrogen-doped graphene provides more electrocatalytic activity than non-doped graphene [213, 214]. However, only a few studies are discussing the operation at long-term and high current density, besides there is no report discussing the mechanism of capacity increasing [31, 207, 215, 216]. The effect of nitrogen doping on chemical structure as well as electronic properties of graphene sheets is well studied both theoretically and experimentally [217-219]. It is shown that pyridinic graphene has the highest capacity among all three forms of nitrogen doping for Li storage [217]. A high rate capability, as well as high reversible discharge capacity, is reported for a ca. 2 % nitrogen doped graphene anode [218]. The reason for high capacity and rate performance is attributed to change in the electronic structure of neighbor carbon atoms which gives rise to creation of active sites by increasing reactivity of the graphene sheets [219]. In this regard, NrGO or graphene oxide (GO) has been used as an auxiliary component in many anodes' formulations to improve electrode kinetics and enhance the battery performance [217-222].

Recently, TiO2-B has received much attention as an active material in Li-ion battery anodes. The reason for such attention is high rate capability, facile preparation, good chemical stability and low volume change (<3 %) during lithiation and de-lithiation [223-225]. It specifically shows higher rate capability in comparison with the other TiO_2-based materials such as anatase, and hydrogen titanates [225]. However, all polymorphs of TiO_2 have common limitations including, low solid-state diffusion of Li+ and low electronic conductivity. Another drawback of TiO_2 nanoparticles is that they tend to agglomerate during anode formation which results in lower activity of material during lithiation and de-lithiation. Agglomeration behavior and low electronic conductivity of TiO_2 have

created a necessity to increase the amount of additives like carbon black in the anode batch formula which effectively has no Li storage capacity. To overcome such shortcomings, different strategies have been employed. Various morphologies of TiO_2 have been used including nanotubes [197], nanorods [226], nanosheets [227] and nanowires [228]. Such morphologies show higher surface area and reduce diffusion distance of Li^+ leading to higher rate capability. Another strategy is to add a conductive component such as graphene or reduced graphene oxide to enhance rate performance and capacity of anodes. Good chemical stability, high surface area and preventing nanoparticle agglomeration are among the advantages of reduced graphene oxide (rGO) [229, 230].

As an attractive solution, Group IV elements (Si, Ge, Sn) offer high specific capacities (3579 $mAhg^{-1}$, 1600 $mAhg^{-1}$, 994 $mAhg^{-1}$, respectively) as LIB anodes for greater energy storage capability. In comparison to graphite, crystalline Si lattice can store severalfold more Li ions in different Li_xSi_y phases that can store up to 4.4 Li-ions per Si. However, Si also pose a serious problem of volumetric expansion upon lithiation (297 %, 270 %, 257 %, respectively) [231]. The ~300 % volumetric expansion upon every charge pulverizes the anode and results in rapidly fading capacity due to loss of electrical contact and repeated solid electrolyte interface (SEI) formation generated by reductive decomposition of the organic electrolyte on active anode surfaces [232]. Loss of contact causes irreversible lithium insertions as well as a gradual loss of Li ions to a constantly developing (unstable) SEI layer. In return, a pure Si anode is seen to suffer from a low coulombic efficiency (CE), an increased resistance for ionic flow, and a low electrical conductivity [232]. These factors contribute to a rapidly fading capacity of an otherwise energy dense anode.

Numerous ingenious composite structures of nanostructured Si and C have shown promising electrochemical properties in LIBs. These include Si nanowires [233], Si nanotubes [234, 235], and permeable SiO_x shells [236], combined with different carbon morphologies such as carbon nanotubes (CNTs) [237], electrospun carbon fibers [238], microspheres of graphene [239], and various architectures of graphene sheets [240-242]. The C-Si nanocomposite structures provide significant improvements in capacity and CE. One important study for C-Si nanocomposite structures includes Si nanoparticles in a double-shelled structure [243]. In this structure, Si particles are first surrounded by SiO_2 and then a wide carbon sphere where it lets a space for expansion. The integrated design

exhibits high mechanical strength and reversible capacity. Successful Si-based LIB anode composites aim to buffer Si expansion upon lithiation with the help of a mechanically strong, flexible and electrically conductive encapsulating framework. Graphene-based structures have been found to be useful because they have the needed mechanical strength and flexibility to withhold Si expansion upon lithiation without causing excessive damage to the anode, allow Li-ion transport with ease, and contribute to higher electrical conductivity. Reduced graphene oxide layers have in-plane carbon vacancies due to the harsh oxidizing conditions used during their syntheses. When they cover Si nanoparticles, these vacancies behave like an ion channel which is also a critical issue for Si-based materials [244-246].

While studies on graphene-silicon composites demonstrated multifold increases in capacities and good capacity retentions, many of their preparation methods are either too costly, time-consuming or complex to be deemed feasible for commercial scalability. However, two notable examples of Si-C composite anode fabrication techniques are the works of Wu et al. [247] and Chang et al. [244]. Wu J. et al. prepared multilayered silicon embedded porous carbon/graphene hybrid film by electrostatic spray deposition of alternate layers of GO and Si/multiwalled carbon nanotube/carbon black/polyvinylpyrrolidone (Si in porous carbon matrix) followed by heat treatment at 600 ºC. The resulting anode was reported to give a high specific capacity of 3114 $mAhg^{-1}$ with excellent capacity retention after 100 cycles. Another alternate layering approach was reported by Chang et al. who dip coated alternate layers of GO and Si nanoparticles (NPs) on a Ni foam. After heat treatment; specific capacity of ~2000 $mAhg^{-1}$ at 0.2 C was reported with excellent capacity retention over 300 cycles. These studies show that layering Si between graphene layers is an effective method to obtain a high-performance electrode. However, both the coating techniques used and the requirement of thermal treatment after the coating under an inert atmosphere complicate the scaling up. Therefore, a simpler method is required for the layering of the materials.

2.2. The Influence of Nitrogen Doping on Reduced Graphene Oxide as Highly Cyclable Li-ion Battery Anode with Enhanced Performance

2.2.1. Preface

In this study, as the first step, contrary to the literature where graphene oxide (GO) is generally synthesized by Hummers' or modified Hummers' method, our GO was synthesized by the improved Hummers' method. Changing the chemicals in the process alters the oxidation and doping mechanism, which is critical in electrochemical performance. The GO was thermally annealed under argon gas flow to obtain reduced graphene oxide (rGO). For nitrogen-doping, GO was directly annealed at high temperatures under ammonia and argon atmosphere as a rapid synthesis route. It should be stated that both the reduction and the nitrogen-doping of GO were employed in a single thermal annealing step. The physical as well as the electrochemical properties of NrGO were comprehensively evaluated by comparing with the rGO in order to study the doping effect of nitrogen on rGO. This study undertakes a complete evaluation of the materials' performance in terms of the high current rate and long-term operability. In this respect, we aimed to investigate the influence of nitrogen doping on LiBs performance upon cycling by comparing structural and electrochemical characterizations of NrGO to rGO. The process used for the synthesis of NrGO enabled a more open structure, letting Li^+ ions more access to doped sites (Figure 2. 1). This resulted in the highest specific capacities and stability for NrGO anodes reported in the literature. More interestingly, the sites in this NrGO improved the Li^+ intercalation, and the specific capacity increases with cycling. This study also tries to explain this extraordinary behavior of NrGO by nitrogen defects created on the graphene surface.

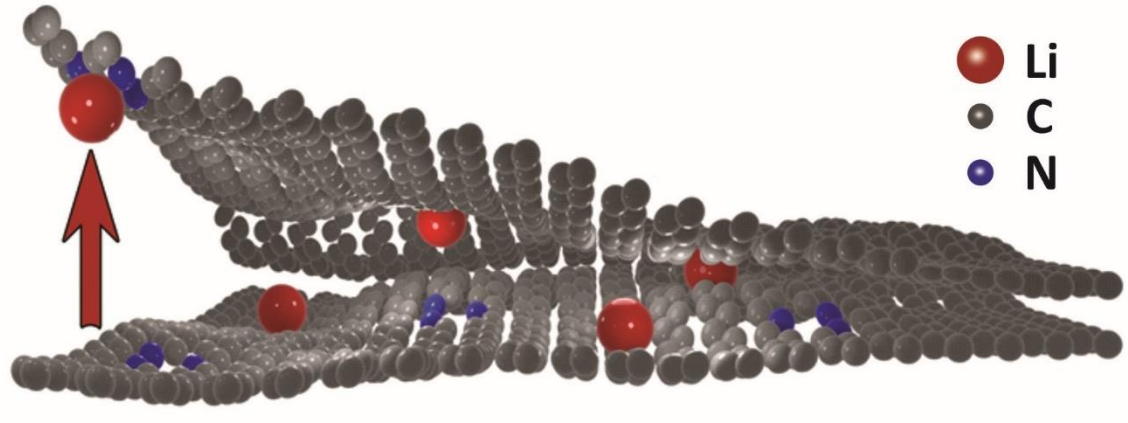

Figure 2. 1. Lithiation mechanism into graphene layers with defects due to N doping

2.2.2. Materials and Methods

2.2.2.1. Materials

Natural graphite flakes (99 %), potassium permanganate ($KMnO_4$, 99 %), sulfuric acid (H_2SO_4, 98 %), phosphoric acid (H_3PO_4, 85.0-88.0 %), hydrogen peroxide (H_2O_2, 29.0-32.0 %), hydrochloric acid (HCl, 37 %) were obtained from Sigma–Aldrich for the synthesis of graphene oxide by improved Hummers' method. N-methyl-2-pyrrolidone (NMP, 97 %) from Sigma–Aldrich and carbon black (Vulcan XC-72) from Fuel Cell Store were used for electrode preparation. 1.0 M $LiPF_6$ in EC/DEC:50/50 (v/v, battery grade) were purchased from Sigma–Aldrich as the electrolyte. All reagents used were analytical grade and used without further purification.

2.2.2.2. Graphitic oxide (GO) synthesis

The graphitic oxide was prepared by using the improved Hummers' method, as reported by Marcano et al.[47]. Initially, graphite flakes and $KMnO_4$ were mixed according to a 1:6 (w:w) ratio. Then, H_2SO_4 and H_3PO_4 emulsion with a 9:1 (v:v) ratio were poured into the mixture. The resulting slurry was mixed continuously by a stirrer at 70 rpm and kept at 50 °C for 24 hours. The synthesis is proceeded under reflux to prevent the toxic ambient and vaporization of the reactant solution. After 24 hours, a 1:20 (v:v) H_2O_2 and ice mixture was poured into the as-obtained brownish slurry, then exposed to an ice bath for cooling. Followingly, 88 mL HCl was added to deionized water, and the emulsion with a total volume of 2 L was added onto the mixture. The final suspension was kept in an ice bath for 48 hours. After this step, the slurry turned into a homogeneously dispersed, yellowish, and acidic GO suspension, which was collected by a series of centrifugation steps. Initially, the resulting suspension was centrifuged at 4750 rpm, and the supernatant was decanted away. The remaining slurry was washed sequentially by an emulsion of DI water and ethanol until the pH reached about 5.0. At the last step, the collected sample was freeze-dried for 4 days to remove the remnant water and to obtain a high specific surface area. Afterward, the GO was ready for further processing and characterizations.

2.2.2.3.Reduced graphene oxide (rGO) synthesis

In order to obtain reduced graphene oxide (rGO), the pristine GO was heated to 600 °C in a tubular furnace with a heating rate of 15 °C/min under flowing argon for 2 hours. Afterward, the system was cooled down to room temperature under the argon environment. Finally, the rGO was collected and utilized in the proceeding experiments.

2.2.2.4. Nitrogen-doped reduced graphene oxide (NrGO) synthesis

The reduction and nitrogen-doping of GO were performed via a facile thermal annealing process under ammonia environment. Firstly, graphene oxide (GO) was subjected to nitrogen under ammonia/argon gas flow at 900 °C temperature in a tubular furnace as shown in the Figure 2. 2. The sample was cooled down to room temperature after the annealing process, while argon was still flowing. As-obtained NrGO with a blackish color was collected from the furnace after the complete cooling.

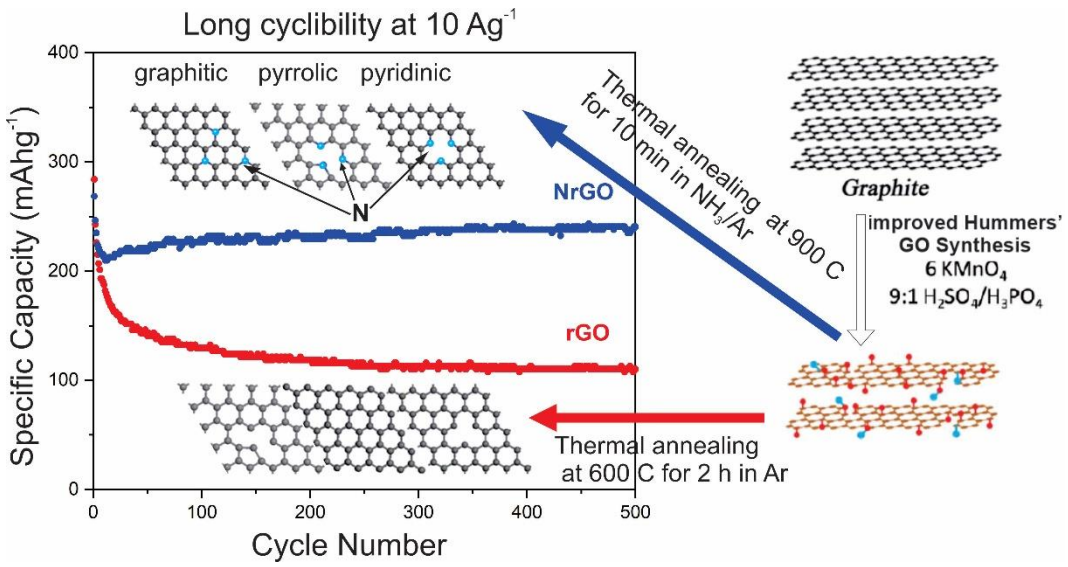

Figure 2. 2. rGO and NrGO synthesis, and battery performance comparison

2.2.2.5. Instrumentation and characterization

X-ray diffraction patterns of the powder samples were obtained by a Bruker D2 Phaser X-ray diffractometer device with a 1.540 Å Cu K_α radiation source. The data were collected from 10−90° with 0.02° 2θ step size and 1 s step time. Raman bands and modes of all graphene-based materials were analyzed by a Renishaw Raman spectrometer under

ambient conditions using a 514 nm visible laser source. Microstructural and morphological analyses of samples were monitored via a Zeiss LEO Supra 35VP Field Emission Scanning Electron Microscopy (FESEM) by a secondary electron detector at 3 kV accelerating voltage. Samples were coated with Au/Pd using the Desk V HP Denton Vacuum coating device before SEM observation. Decomposition temperatures and weight fraction of oxygenated functional groups of graphene-based materials were determined by a Netzsch STA 449C thermogravimetric analyzer (TGA) via heating from 30 to 1400 °C with a 10 °C/min heating rate within the air ambient. N_2 adsorption isotherms were investigated by a Micromeritics 3Flex Physisorption instrument at 77.3 K with relative pressure (P/P_0) of N_2 gas varying from 0 to 0.99. The complete degassing of samples proceeded at 130 °C for 24 hours prior to measurements to clean the surface from ambient gas and humidity. Specific surface area and pore size distribution analysis were obtained from the N_2 adsorption isotherms. The binding energy spectra of the samples were quantified by Thermo Fisher K-alpha X-ray Photoelectron Spectrometer (XPS) system. The spectral data were collected using a 400 elliptic radius spot size of Al K_α monochromatic source during the formation of the spectra.

2.2.2.6. Electrochemical characterization

The cyclic voltammograms (CV) were recorded by a Princeton Applied Research PARSTAT MC system. The CV data were recorded within a potential window of 0.01-3.00 V (versus Li/Li^+), and a scan rate of 0.1 mV s^{-1}. The galvanostatic charge and discharge tests were performed using an MTI 8 Channel Battery Analyzer, within a potential range of 0.01-3.00 V at different current densities, such as 0.1, 0.5, 1, 2, 5, 10 Ag^{-1} (Figure 2. 3). The electrochemical impedance spectroscopy (EIS) data collected using the PARSTAT MC system with a frequency range of 0.1 Hz to 1 MHz with a 5 mV AC amplitude.

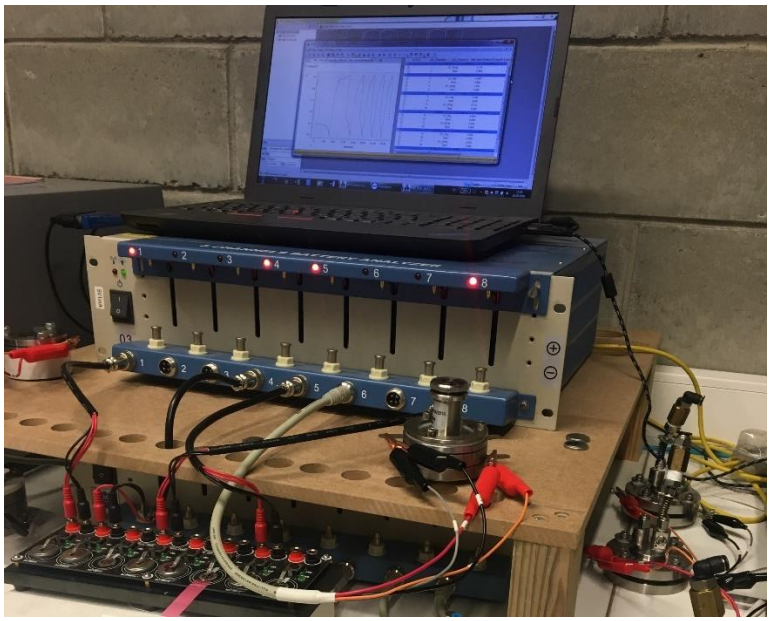

Figure 2. 3. Charge/Discharge tests by using an MTI 8 Channel Battery Analyzer

2.2.2.7. Electrode preparation and cell assembly

The slurries of rGO and NrGO were prepared by mixing and grinding the active materials with carbon black and PVDF with a weight ratio of 7:2:1. The mixture was dispersed in N-methyl pyrrolidone (NMP), followed by moderately stirring of the slurry for 24 h to obtain uniform homogeneity. The slurry was doctor bladed on a 10 μm-thick copper foil. The coated foil was dried at 120 °C for 12 h in a vacuum oven, then hot pressed to increase the bonding integrity of coating with the copper foil. Circular electrodes with 15 mm diameter were cut, and they were transferred to the glovebox (Figure 2. 4). The CR 2032 cells were assembled under glovebox, using Li chips (15 mm diameter and 0.4 mm thickness) as the counter electrode, Celgard PP as the separator, our electrodes as working electrodes and 1 M $LiPF_6$ in ethylene EC/DEC (1:1, v/v) as the electrolyte in between the electrodes. Cells were hermetically pressed and utilized for the electrochemical characterizations.

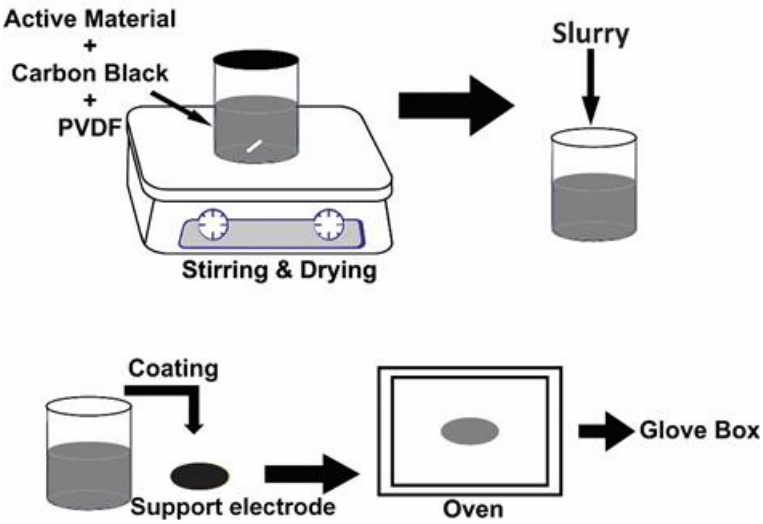

Figure 2. 4. Electrode preparation steps

2.2.3. Results and Discussion

2.2.3.1. Physical characterizations

Figure 2. 5 illustrates the crystal patterns of pristine GO, rGO, and NrGO powder samples. As can be clearly seen, the GO demonstrates a sharp peak at 11.72˚, which corresponds to (001) plane of the graphite with an interplanar distance of 7.54 Å, which is due to the oxidation of functional groups of graphite surface. The rGO exhibits two peaks at 9.27˚ ((001) plane for GO) and 25.35˚ ((002) plane for graphene), with interplanar distances of 9.53 and 3.51 Å, respectively[216]. The intense peak at 25.35˚ indicates an almost complete reduction of oxygenated functional groups on the GO surface, which is evident from the reduction of the interplanar distance to 3.51 Å. Interestingly, the peak corresponding to the (001) plane has been shifted to lower 2θ values (9.27˚) after the thermal reduction processes. This is possibly due to the expansion of the material by the reduction, which was a consequence of the gasothermal heat-treatment process. During this process, an explosive thermal reduction of the GO-based materials occurs, generally around 250 °C. Furthermore, the NrGO sample revealed two peaks centered at 11.52˚ and 26.65˚, which coincides with the interplanar distances of 7.67 and 3.34 Å, respectively [248]. The XRD of NrGO displayed that the diffraction of the (001) plane occurs in a similar position with the one in pristine GO. Still, the diffraction of the (002) plane revealed that NrGO faced more reduction, which is due to higher heat treatment

temperature resulting in more removal of oxygenated groups. The interplanar distance can vary with respect to the GO synthesis method in use. Hu et al. reported interplanar distance for (002) plane of NrGO as 3.7 Å, and Du et al. reposted it as 3.57 Å [31, 249]. The small difference can be due to the employed method since they used modified Hummer method, and we used improved Hummers' method in this study. The improved method utilizes phosphoric acid instead of using sodium nitrate as the main difference. Yet, it has proved to have a better oxidation process, which alters the interplanar distance, as reported by Marcano et al.[47].

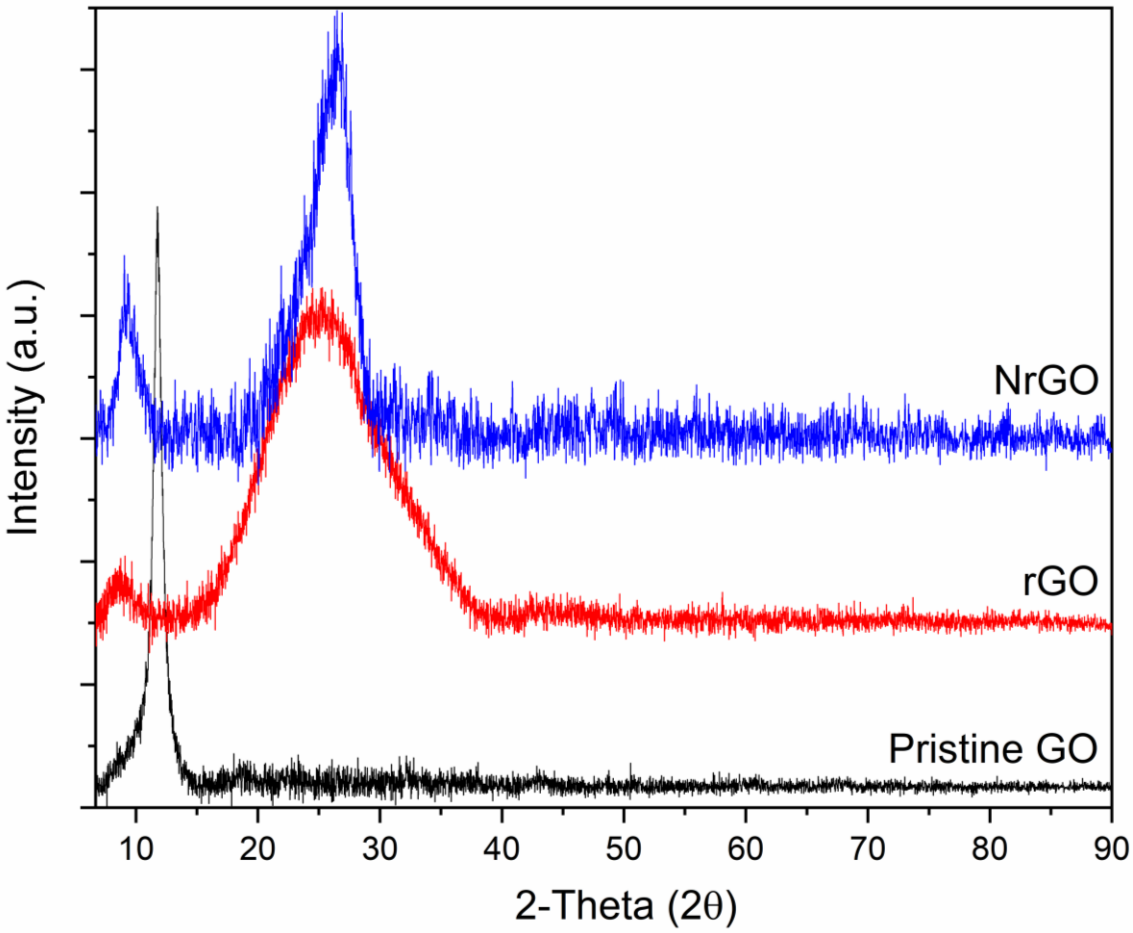

Figure 2. 5. XRD analysis of pristine GO (black), rGO (red) and NrGO (blue)

Vibrational modes of pristine GO, rGO, and NrGO were analyzed according to the Raman spectrum obtained in Figure 2. 6. As evident from Figure 2. 6, all of the samples demonstrated D- and G-peaks of graphitic carbon, which are addressed to vibrational modes of sp^3 and sp^2 hybridization of carbon-based materials, respectively. Besides, the D-peak indicates the degree of disorder resulted from defective vibrational density within the graphitic carbon. Whereas the G-peak represents stretching of carbon atoms in two-

dimensional lattice within the chains and rings of graphene layer which corresponds to E_{2g} phonons scattering centered at the Brillouin zone [250, 251]. Li^+ ion storage is directly related to defect-rich porous carbon which contributes a great number of lithium-ion storage active sites within the carbon lattice. Hence, the area (A_D/A_G) and intensity ratio (I_D/I_G) of D- to G-peak are essential in terms of explaining the functionality of carbon materials to lithium-ion battery capacity and cyclability. From Figure 2. 6, the A_D/A_G ratios of pristine GO, rGO, and NrGO samples were calculated as 1.45, 1.85, and 2.05, respectively. In addition, I_D/I_G ratios of GO, rGO, and NrGO were found to be 0.78, 0.83, and 1.10, respectively. NrGO exhibited the most defective Raman outcome over the rGO and GO samples, as proven by the A_D/A_G and I_D/I_G ratios. It can be concluded that both rGO and NrGO have a more open structure compared to GO, due to the increase in defect density in the light of Raman characterization. Lastly, NrGO has the highest sp^3 vibrational modes since nitrogen-doping of the graphene lattice created sp^3-bonded carbons to nitrogen. However, Hu et al. claimed that I_D/I_G remains same for the pristine and doped GOs, as 0.94; albeit Du et al. reported I_D/I_G ratio as 1.21 for nitrogen-doped reduced GO [31, 249]. Du et al. added melamine during GO synthesis to get nitrogen-doped GO and hydrothermally reduced it to get nitrogen-doped reduced GO so that even at a low-temperature reduction by a hydrothermal treatment may effectively provide a defective structure due to melamine. Conversely, Hu et al. reduced ammonium hydroxide included modified Hummers' GO at 1100 °C just for 30 s, which may not be enough to remove oxygen content and obtain a defective structure.

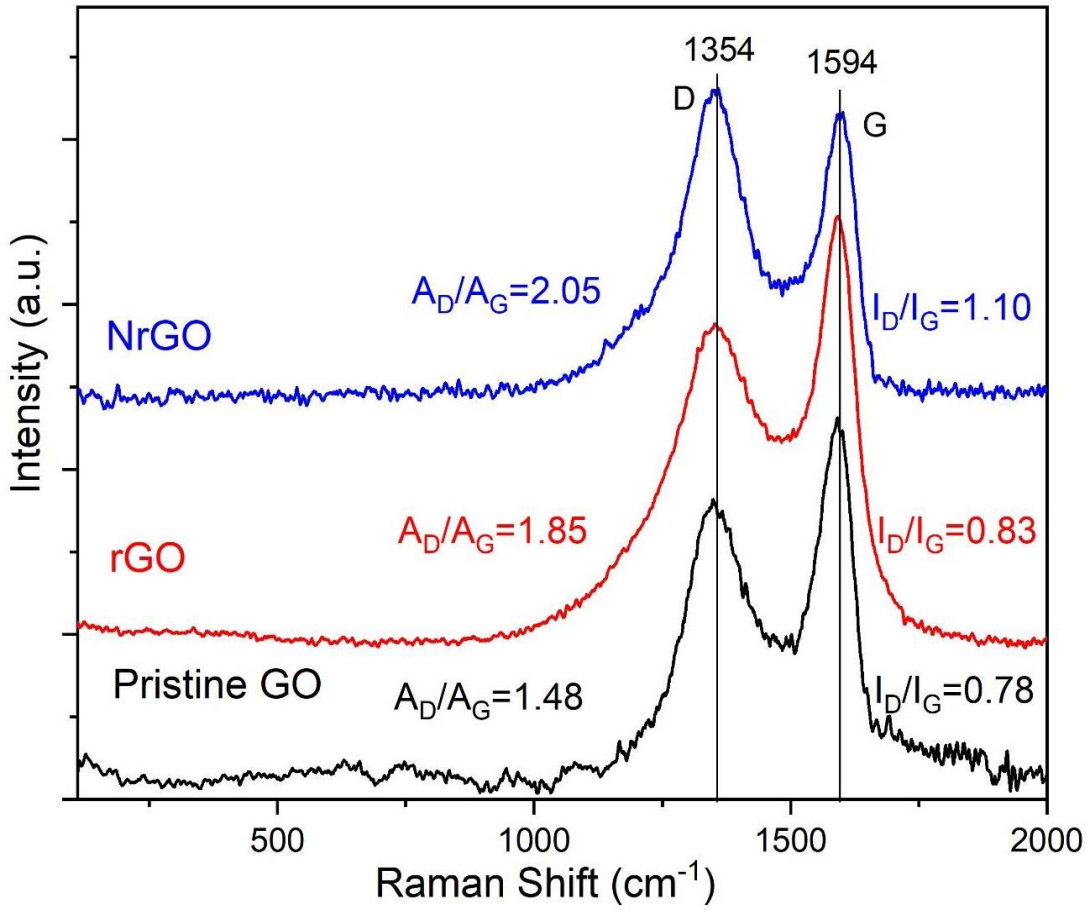

Figure 2. 6. Raman analysis of pristine GO, rGO, and NrGO

Morphological analysis of pristine GO, rGO, and NrGO was examined by FESEM, as illustrated in Figure 2. 7. According to SEM micrographs in Figure 2. 7 a & b, the GO contains large sheet-like structures. The edges and individual sheets are clearly distinguishable within the lamellar layers. The layers of GO are around 500 µm in length and 300 µm in width, with a thickness of about 0.5 to 1 µm. On the other hand, the rGO flakes showed wrinkled and curved features on their surface. Also, the SEM images in Figure 2. 7 c & d apparently demonstrate the increase of the distance between the flakes, which is consistent with the XRD result.

Moreover, the rGO displayed smaller flakes composed of thinner layers supporting the reduction process of oxygenated groups, which was also discussed in XRD and Raman analyses. Furthermore, the NrGO showed more curled, fluffed, and disordered structures compared to the rGO. It also showed more bent and thinner flakes due to heat treatment at an elevated temperature under NH_3 exposure, which results in the features observed in

Figure 2. 7 e & f. The morphologies of the GO and the reduced GO are mainly similar to previous studies in literature [126, 252].

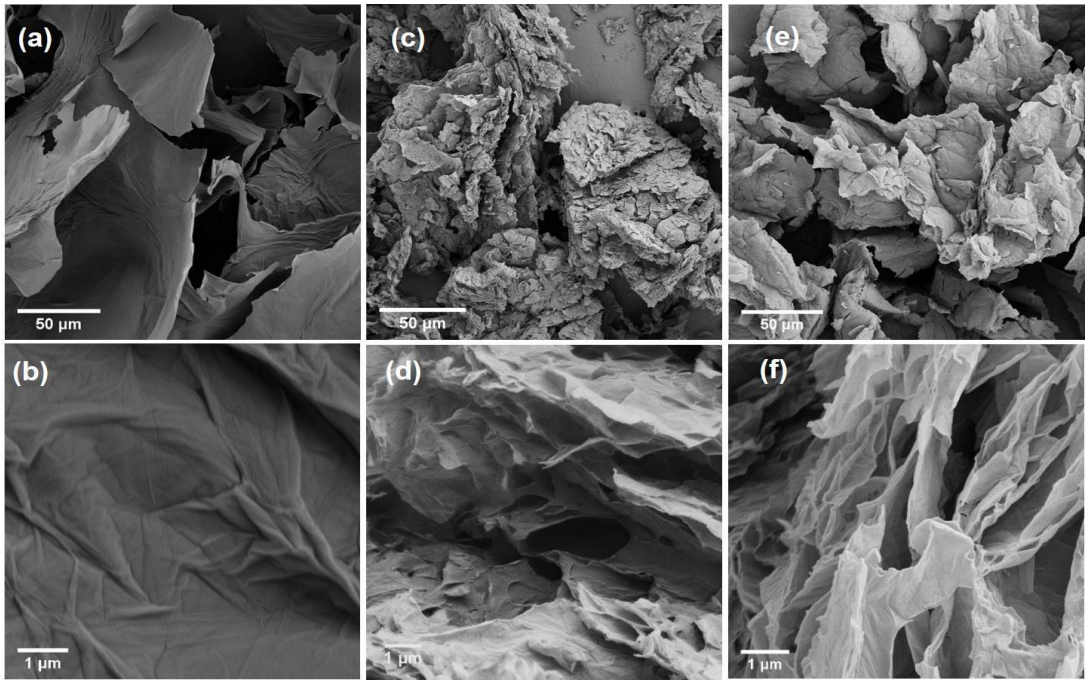

Figure 2. 7. SEM micrographs of (a, b) GO, (c, d) rGO, and (e, f) NrGO powder samples

The thermal stability of rGO and NrGO was examined by a TGA analysis (Figure 2. 8). All of the samples have mass changes over three stages. Both rGO and NrGO lose around 6 % mass below 100 °C due to the removal of the adsorbed water and surface humidity on GO flakes. On the one hand, rGO has a less steep change up to 355 °C, which corresponds to an additional mass loss of 1 %. This evidence suggests that rGO has a very small amount of unstable surface oxygenated functional groups[248]. On the other hand, NrGO showed a steeper change up to 446 °C, which is a higher temperature compared to rGO for the thermal decomposition of oxygenated surface groups on NrGO. Finally, NrGO has a higher combustion temperature of 568 °C compared to rGO's, which was 470 °C [253]. rGO might have decomposed earlier due to the expanded structure of rGO. Park et al. reported similar thermal decomposition temperature, which claims the improved thermal stability of rGO by adding intermolecular coupling agents to heal rGO and to restore the carbon network during heating [254]. Moreover, nitrogen doping probably supplied additional integrity to rGO lattice in this study and increased its thermal stability.

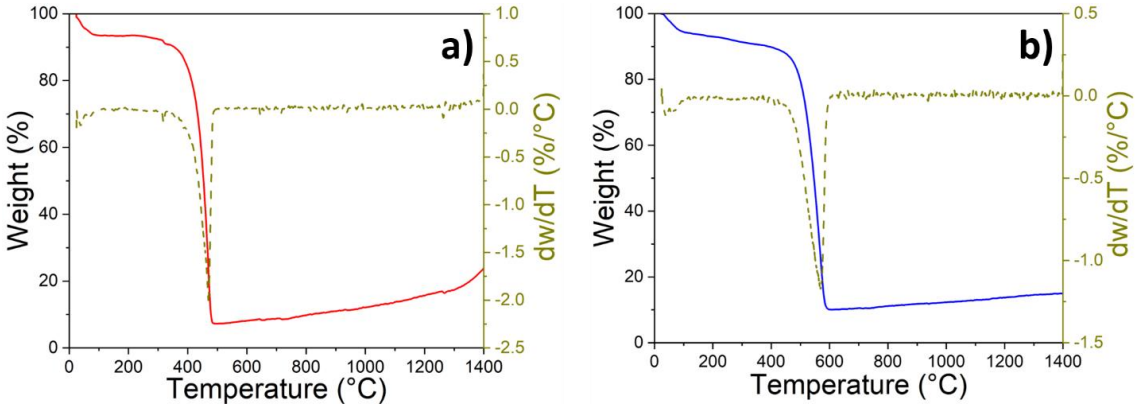

Figure 2. 8. TGA (black) and DTG (red) spectra of (a) rGO (b) NrGO powder samples.

BET isotherms and pore size distributions of rGO and NrGO are presented in Figure 2. 9. rGO showed H3, and NrGO formed H4 hysteresis loops according to IUPAC classification. According to the BET analysis, our rGO has 638.3 m^2/g specific surface area and 2.53 cm^3/g total pore volume [145]. This result was supported by SEM, XRD, and RAMAN analyses since rGO has a large interplanar distance and structural expansion. Moreover, NrGO exhibited 425.1 m^2/g specific surface area and 0.65 cm^3/g total pore volume. Pore size distribution in Figure 2. 9 b gives detailed comparisons and similarities of rGO and NrGO powders. Both powder samples have a mesoporous structure. rGO demonstrated two maxima at 2.6 and 38.6 nm, where the 2.6 nm maximum has a higher pore volume distribution. Yet, NrGO projected three maxima of average pore width pointed at 1.9, 2.4, and 5.26 nm, respectively[255]. It can be concluded that rGO has a more open structure than NrGO, whereas NrGO has narrower pores than rGO. This narrow pores of NrGO may provide better interaction with Li^+ ions during their adsorption to nitrogen groups in the graphene lattice.

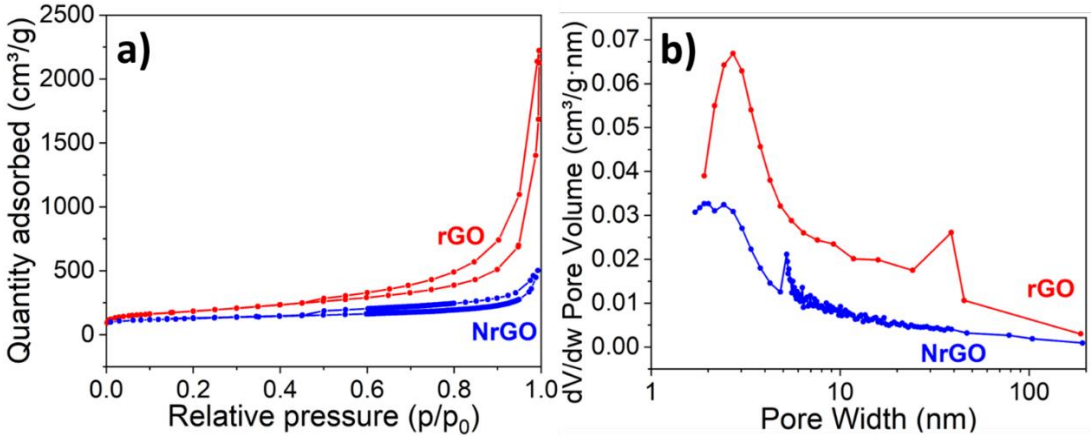

Figure 2. 9 N_2 adsorption/desorption isotherm curves (a) and BJH pore size distribution (b) for rGO (black) and NrGO (red) powder samples.

The elemental analysis of the rGO and NrGO were studied to obtain the nitrogen content and compared for carbon and oxygen-containing groups within the rGO and NrGO. Figure 2. 10 shows the general XPS surveys, C 1s and O 1s spectra of rGO and NrGO, and N 1s spectra of NrGO, which were deconvoluted by Lorentz and Gaussian functions in the Origin software. According to general survey data in Figure 2. 10 a, NrGO exhibits three peaks, namely C 1s, O 1s and N 1s centered at 285.1, 399.0, 531.7, respectively with atomic percentages of 84.9 %, 6.4 %, and 8.7 %. As expected, the rGO does not contain an N 1s peak, and it is composed of 87.4 % carbon and 12.6 % oxygen. It is clear that nitrogen was generally substituted within the oxygen sites in the rGO structure [256]. N 1s peak of NrGO, shown in Figure 2. 10 b, is deconvoluted to three main peaks, which are attributed to the graphitic/quaternary-N, pyrridonic/ pyrrolic-N, and pyridinic-N located at 401, 399.2 and 397.9 eV, respectively. The pyridinic-N and pyrrolic-N have higher occupancy over quaternary N which provides more defect rich content as supported by Raman analysis, and Xu et al. [257]. O 1s spectra of rGO and NrGO were fitted to three different curves, as shown in Figure 2. 10 c, which are assigned to oxygen signals in epoxy (C-OH), carbonyl (C=O) and carboxyl group (O=C-OH). The peak centers of C-OH, C=O, and O=C-OH for rGO were pinned at 533.5, 532.0, 530.7 eV. However, these peaks were centered at 532.5, 531.2, and 530.1 eV for NrGO. Moreover, the occupancies of epoxy and carboxyl groups in NrGO were decreased dramatically compared to the ones in rGO, which explains the removal of single-bonded oxygen after re-coordination of these sites with nitrogen due to doping process. Lastly, the C 1s spectra demonstrate 4 peaks for both rGO and NrGO separately in Figure 2. 10 d. On one hand,

the curves centered at 284.5, 285.9 286.6, 287.8 eV for rGO correspond to sp^2 hybridized carbon (C=C/C-C), the carbon in epoxy (C-O), in carbonyl (C=O), and in carboxyl (O-C=O) groups, respectively. On the other hand, NrGO C 1s spectra were split into 4 different peaks as well, which are centered at 284.5, 285.3, 286.9, and 288.4 addressing C=C/C-C, C-N, C=O, and O-C=O respectively.[258] The shift of the binding energies in the O 1s and C 1s spectra for rGO and NrGO were raised due to the higher annealing temperature of NrGO than that of rGO. As a result of that, C=O becomes unstable and creates small graphene plane between graphitic layers which act as free-electron like a set of bands corresponding to electronic excitations lying between graphite layers as studied by Ganguly et al. [259]. The effect of nitrogen doping was reflected in this analysis as displacement of C-O to C-N since single-bonded oxygen in the epoxy group is the weakest bond to be removed and then bonded to nitrogen so that C-N has the second-highest occupancy in C 1s graph [260]. Furthermore, C 1s has the highest intensity of C=C/C-C peak and slightly less intensity of oxygen-containing groups which explains the reduction process for both rGO and NrGO as similarly reported by Aliyev et al. [261].

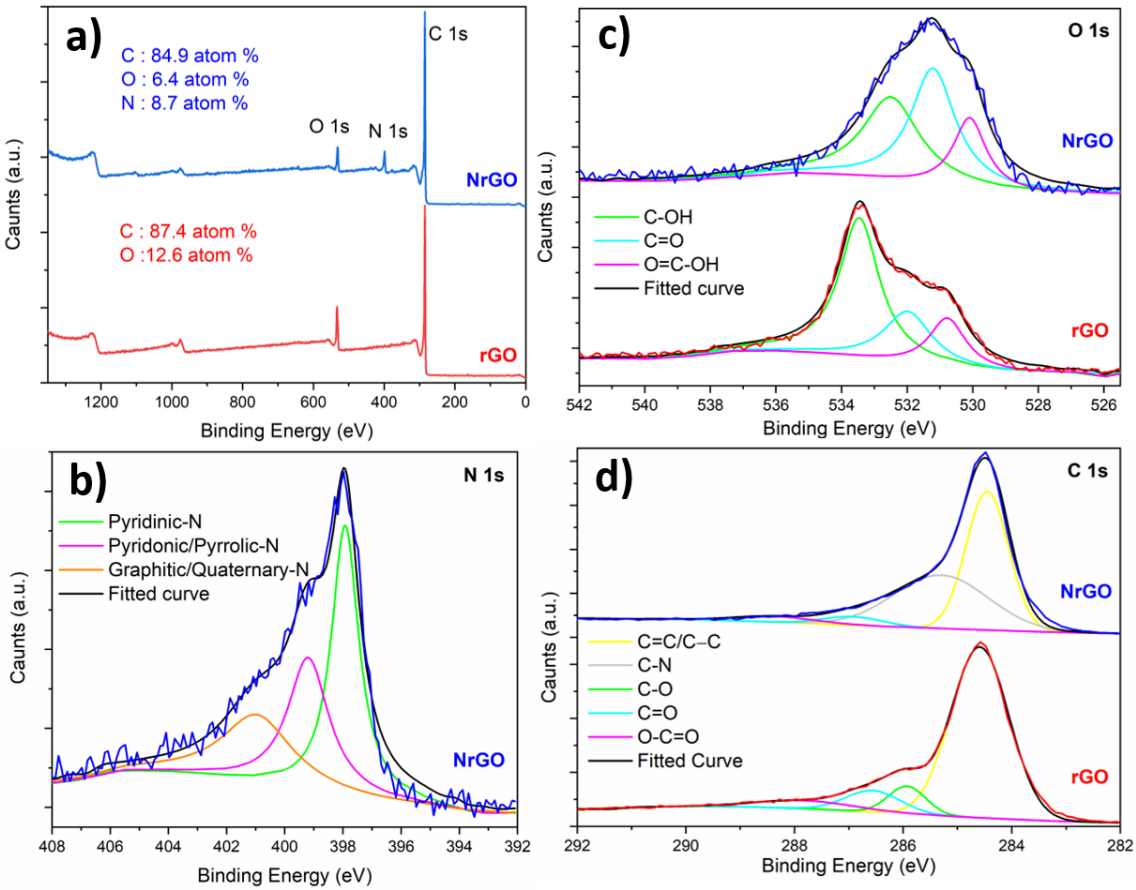

Figure 2. 10. General surveys of rGO and NrGO (a), N 1s deconvoluted spectra of NrGO (b), O 1s (c) and C 1s (d) deconvoluted spectra's of rGO and NrGO

2.2.3.2. Electrochemical Performance

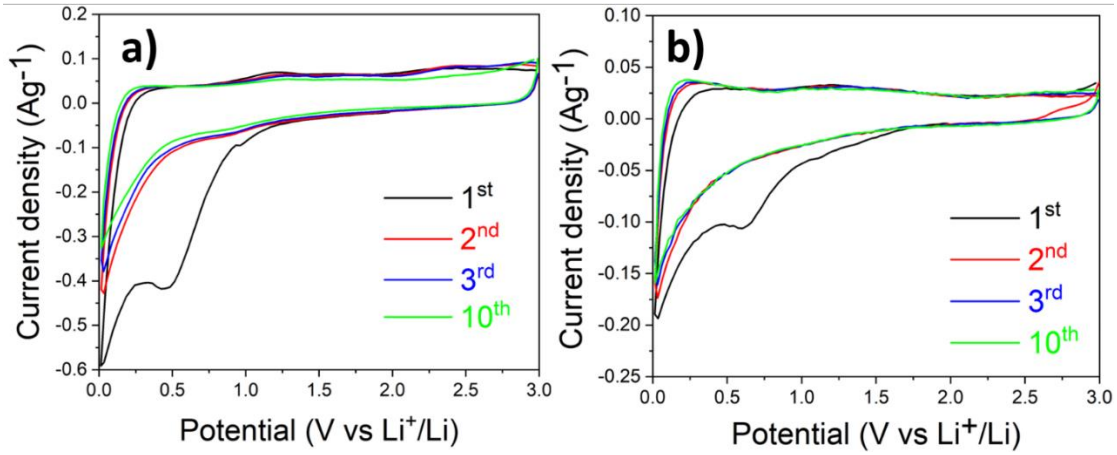

Figure 2. 11. CV profiles of (a) rGO (b) NrGO electrode at 0.1 mVs^{-1} scan rate between 0.01-3.00 V.

The cyclic voltammetry curves of rGO and NrGO electrodes are depicted in Figure 2. 11**.** The NrGO electrode exhibits a sharp peak at 0.03 V at the first cathodic scan, attributed to the Li^+ insertion into the NrGO layers [262]. In the subsequent cycles, this peak shifts closer to 0.018 V due to irreversible phase transformations occurred at the first cycle [31]. The electrolyte decomposition on the rGO electrode surface is indicated by a peak at 0.44 V, leading to the formation of lithium-containing compounds. For the NrGO electrode, this peak appears at a higher voltage, 0.60 V [263]. These two peaks vanished at the subsequent cycles, which can be explained by the further and irreversible reduction of the electrode surfaces by the ongoing electrochemical operation [264]. The Li^+ extraction from both the rGO and NrGO layers occurs around 0.25 V, represented by a shoulder at the first anodic scan [262], which shifts to lower voltages by the subsequent scans. The distinctive behavior between the electrodes at this point is, the Li^+ extraction peak of NrGO appears at increased current densities, which might be an indication of increased electrochemical activity by increased Li^+ charge storage of the NrGO electrode, together with the increased area of the CV curve in contrast to the rGO electrode at its 10^{th} cycle, which displayed a lower area. Moreover, the broad anodic peak around 1.20 V can be associated with the decomposition of the as-formed Li_2O as a component of SEI formed in the cycle during lithiation [265] as well as the Li^+ extraction reactions occurring at the functional groups of the NrGO [266]. At the subsequent cycles, the CV curves overlap, and these oxidation peaks vanish, indicating good reversibility of the electrode.

The electrochemical performances of the rGO and NrGO electrodes were first determined by galvanostatic cycling at a current density of 0.1 A g^{-1} (Figure 2. 12). Although some studies interpret the cycling rate of the graphene-based materials by C-rate using the theoretical capacity of graphite [31, 267], the performance of graphene-based materials should have better be evaluated by current density (Ag^{-1}), since the structure of such materials is different than that of graphite. This creates confusion when C-rates are compared, as graphene studies in the literature use 372 or 744 $mAhg^{-1}$ as the theoretical capacity.

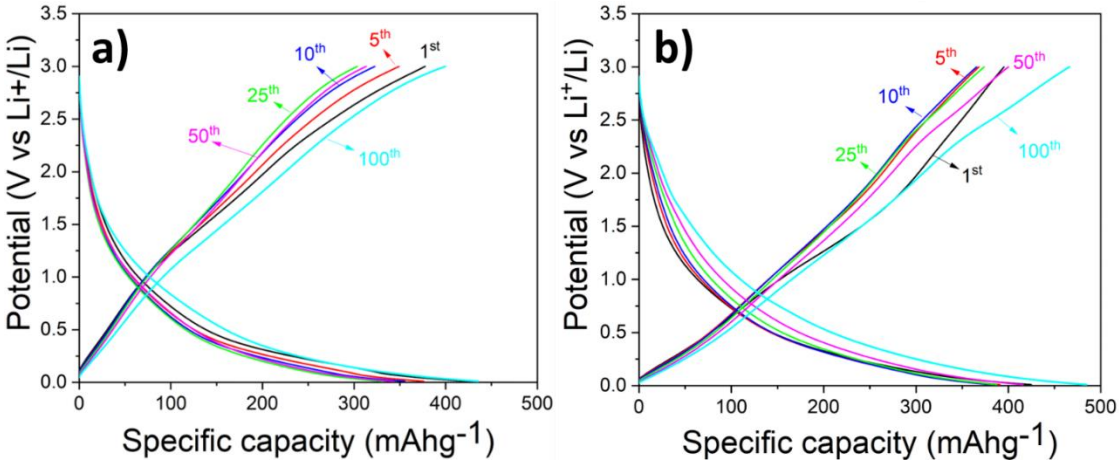

Figure 2. 12. Galvanostatic charge-discharge profiles of (a) rGO and (b) NrGO electrodes obtained at a current rate of 0.1 Ag^{-1} at their 1st, 5th, 10th, 25th, 50th and 100th cycles between a potential range of 0.01-3.0 V.

The deliverable charge/discharge profiles were obtained from the selected 1st, 5th, 10th, 25th, 50th and 100th, cycles. At the initial cycle of operation, the rGO and NrGO electrodes delivered a discharge capacity of 423.4 and 425.1 $mAhg^{-1}$, at 0.1 Ag^{-1} respectively. Although the deliverable capacities at the first cycle were similar, the capacity only reached up to 440 $mAhg^{-1}$ by the 100th cycle for the rGO electrode. Oppositely, the NrGO electrode demonstrates an increasing capacity profile, reaching beyond 488 $mAhg^{-1}$ by the same cycles of operation. The cyclability profiles at different current densities of 0.1, 1, 2, and 10 Ag^{-1} support the improving performance of the NrGO cell by 100 times cycling. However, the rGO electrodes show a gradual fading of capacity by the same amount of operation (Figure 2. 13).

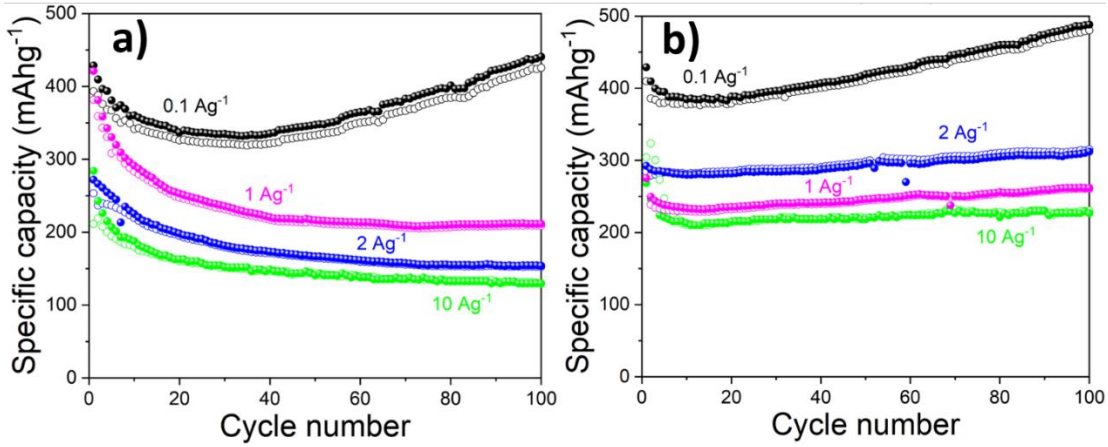

Figure 2. 13. Cycling performance of (a) rGO (b) NrGO electrodes at selected current densities of 0.1, 1, 2, and 10 Ag^{-1} for 100 cycles of operation, between 0.01-3.00 V.

At the long-term operation for 500 cycles at a high current rate (10 Ag^{-1}), the NrGO electrode outperformed, preserving 90 % of the initial delivered capacity, albeit the rGO electrode could only reach to 40 % of its initial capacity (Figure 2. 14). It is important to mention that there is no reported literature available demonstrating both of the electrode materials beyond 100 cycles of operation at such a current rate. Both of the rGO and NrGO electrodes in this study demonstrate remarkably higher capacity retention compared to literature where the retention is reported to be 38.3 and 33.9 % for rGO and NrGO electrodes, respectively, for only 60 cycles of operation [268].

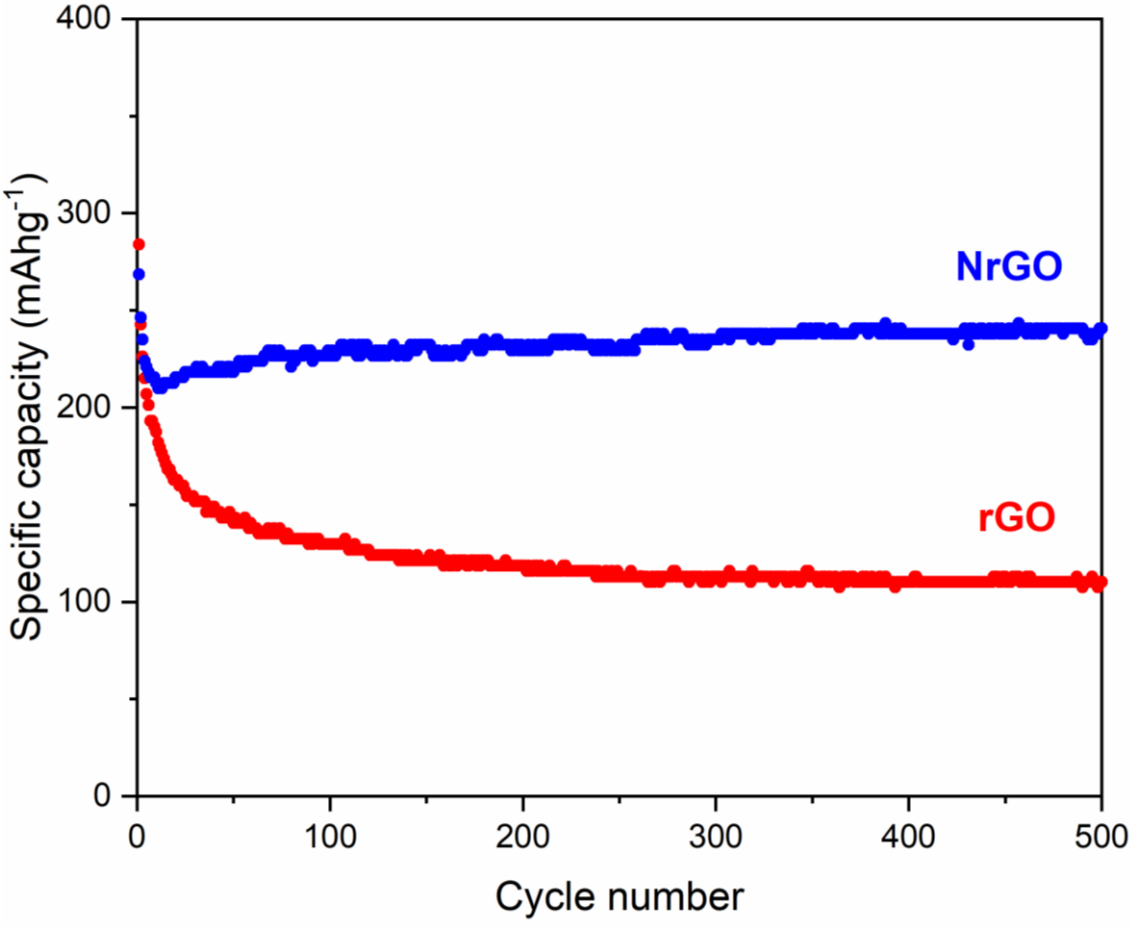

Figure 2. 14. Long-term cycling performance of the rGO and NrGO cells at a high current density of 10 Ag^{-1} for 500 cycles of operation, between 0.01-3.00 V.

To compare the rate capability performances, the rGO and NrGO electrodes were operated consecutively at current densities ranging from 0.1 to 10 Ag^{-1}, as shown in Figure 2. 15. The rGO electrode yielded deliverable discharge capacities of 306, 176, 142, 115, 85, 63 $mAhg^{-1}$ at the 20^{th} cycles of each 0.1, 0.5, 1, 2, 5, 10 Ag^{-1} current rate, respectively. As the current density was reverted back to 0.1 Ag^{-1}, the discharge capacity

was retained to be 362 $mAhg^{-1}$ by the end of the last 20 cycles. As the initial discharge capacity of the rGO electrode was 443 $mAhg^{-1}$ by the beginning of the rate capability test, the sample encountered a capacity fading of 31 % and 18 % at 0.1 Ag^{-1} and 0.5 Ag^{-1} current densities, respectively. The deliverable capacities almost remained constant during the consecutive cycles at 1, 2, 5, and 10 Ag^{-1}. Overall, the rGO electrode suffered from a capacity fading of about 19 % by the end of the total 140 cycles. Nevertheless, the NrGO electrode provided discharge capacities of 402, 311, 293, 272, 223,181 and 507 $mAhg^{-1}$ at the end of operation at 0.1, 0.5, 1, 2, 5, 10 and 0.1 Ag^{-1} current densities, respectively. NrGO displayed an initial capacity fading by the first 0.1 Ag^{-1} stage. However, during the following cycles, an increasing capacity profile was observed at each separate stage. As compared with the rGO, the NrGO electrode demonstrated better battery performance; however, there have been no previous studies to compare the differences, especially at such high current density, where most of the studies have only been carried out to a current density of up to 2 Ag^{-1} or equivalent [263]. As the NrGO cell reverted back to cycling at 0.1 Ag^{-1} rate, the cell even exceeded its initial delivered capacity, exhibiting an overall capacity gain of 11 % by the end of 140 cycles.

The remarkable performance of NrGO can be firstly attributed to higher ionic and electronic conductivity of the material over rGO [269]. Also, more wrinkled and corrugated morphology of the material may aid in enhanced charge storage as the cycle goes, which is a result of gradual wetting of the inner parts of the material by the electrolyte. Another consequence of extended electrochemical operation might be the structural reorganization of the π-π stackings of NrGO, where extra sites accessible by Li^+ ions may arise. Moreover, the surface redox reactions happening at the functional groups of the material, as evident by the CV, can further contribute to pseudo-capacitive effects to the charge storage, contributing to enhanced performance [270]. The coulombic efficiencies of both cells are almost stabilized at almost 100 % except from the first cycle, indicating the stabilized reversibility of the electrodes after the formation of the SEI layer.

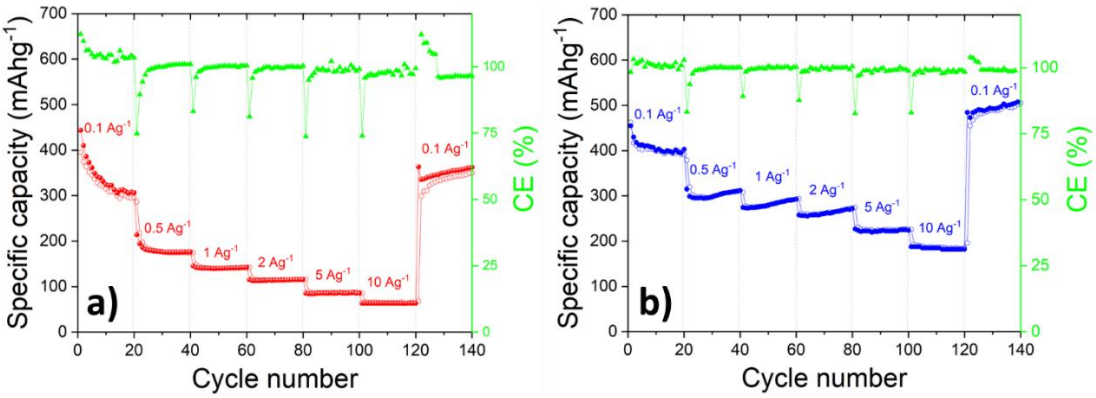

Figure 2. 15. Rate performances of (a) rGO and (b) NrGO electrodes obtained by cycling the cell at current densities 0.1, 0.5, 1, 2, 5, 10 Ag^{-1} for 20 cycles at each current density, between 0.01-3.00 V.

The Nyquist plots of rGO and NrGO batteries are compared in Figure 2. 16. The aim was to explain the relation of the impedance of the cells to electrodes kinetic, and the charge transfer resistance resulted after 500 cycles at 10 Ag^{-1}, using electrochemical impedance spectroscopy (EIS) analysis. rGO and NrGO have the same ohmic contact resistance of 3.5 ohms. The ohmic contact was shifted to 7.2 ohms in both of the battery cells. This implies that the ohmic loss can be due to electrolyte precipitations/decompositions within the contacts or direct impact of SEI formation, creating an extra resistance on the electrode surface as resulted in an increase in ohmic contact resistance. Moreover, both cells have different reflections in charge transfer resistance (R_{ct}). On the one hand, rGO showed 114.5 ohms charge transfer resistance before the cycle test, but the resistance decreased to 53.3 ohms after 500 cycles operation at 10 Ag^{-1}. On the other hand, NrGO displayed a higher R_{ct} of 144.4 ohms before cycling; however, it exhibited a lower R_{ct} than rGO after 500 cycling at 10 Ag^{-1}. Similar impedance measurements were observed in Gau et al.'s study in terms of an increase in ohmic contact resistance but a decrease in charge transfer resistance upon cycling[271]. Du et al. showed NrGO having lesser charge transfer resistance than rGO as well[31]. These findings support the increase of capacity for both cells, and EIS analysis matched with NrGO having a discharge capacity higher than rGO. NrGO has better cell kinetic, greater Li^+ ion diffusion and smaller R_{ct} so that it has faster charge transfer rate and excellent electrical conductivity compared to rGO [207, 272].

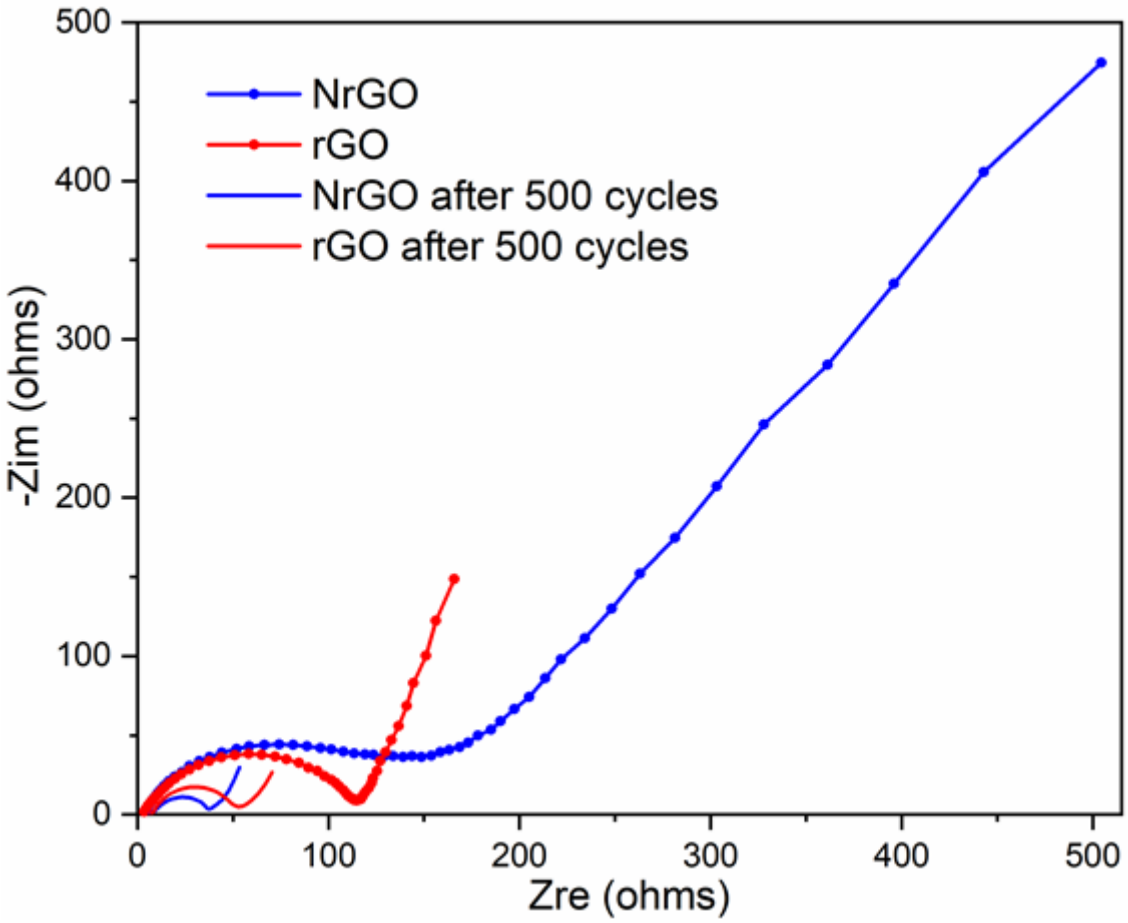

Figure 2. 16. Electrochemical impedance spectroscopy analysis of rGO and NrGO prior to the charge-discharge test and after 500 cycles at 10 Ag^{-1}

There are a couple of studies previously reported, which include GO synthesis as the first step of nitrogen doping and reduction of graphene-based materials in order to be used in LiBs. Table 2. 1 summarizes these studies in terms of current densities, delivered capacity, capacity retention, and cycling performance as well. Hu et al. fabricated GO by modified Hummers' method, then dispersed it in ammonium hydroxide solution and finally reduced it in Ar gas flow at 1100 °C for 30 s to obtain N-doped graphene. N-doped graphene as anode material for LiBs delivered 453 $mAhg^{-1}$ at 2 Ag^{-1} current density after 550 cycles with 90 % capacity retention. Moreover, they obtained a 94 % capacity conversion of 180 $mAhg^{-1}$ at 10 Ag^{-1} after 500 cycles [249]. Further, Du et al. synthesized N-doped graphene oxide by adding melamine as the nitrogen source during GO synthesis by modified Hummers' method, then hydrothermally reduced it at 180 °C for 3 hours to get N-doped reduced GO (N-rGO). They also studied the nitrogen doping effect to reduced graphene oxide by comparing their battery performance after 60 cycles at 0.037

Ag^{-1}. Their rGO, which is the melamine free sample, provided 350 $mAhg^{-1}$ with 71 % capacity reservation however, N-rGO showed higher capacity retention as 95 % of 600 $mAhg^{-1}$ discharge capacity [31]. Similarly, Fu et al. have investigated the battery performance of hydrothermally reduced GO (rGO). They produced GO by modified Hummers' method again, then dispersed this GO within ethanol and rGO, and this suspension was hydrothermally treated at 160 °C for 4 hours to have rGO. It demonstrated a reversible specific capacity of 561 $mAhg^{-1}$ at a current density of 0.1 Ag^{-1} having only 7 % capacity fading at the 50^{th} cycle [216]. As in the following work, Liu et al. have compared the graphite and reduced graphene nanosheets (rGNS) which was obtained by reducing modified Hummers' GO at 300 °C for 2 hours under a reducing atmosphere of 15 % H_2: 85 % N_2 [267]. They reported 50 % reversible capacity of 280 $mAhg^{-1}$ for rGNS after 30th cycles at 0.074 Ag^{-1} current density besides 60 % capacity retention of 200 $mAhg^{-1}$ for graphite powder after 30^{th} cycle at 0.074 Ag^{-1}. Wu et al. prepared GO by Hummers' method as different than others and then converted it to graphene using two thermal treatment steps. First, GO was expanded/exfoliated at 1050 °C under Ar flow for only 30 s. Second, resulted sample was exposed to another reduction process at 450 °C for 2 hours in H_2 and Ar atmosphere then pristine graphene was obtained in supernatant of final product after centrifugation. However, their as-called pristine graphene seems to have an oxygen content of 8.5 % over carbon having 91.5 % occupancy according to their XPS results. Finally, N-doped graphene was synthesized by thermally treating their pristine graphene at 600 °C for 2 hours in a gas mixture of NH_3 and Ar (1:2 v/v) which is similar to our nitrogen doping synthesis conditions with lower annealing temperature after processing GO with several other steps. In the conclusion of their study, the N-doped graphene sheets' battery performance was compared over pristine graphene. The N-doped graphene revealed around 827 $mAhg^{-1}$ capacity after 30th cycle at a 0.05 Ag^{-1} rate with 84 % capacity retention. Still, pristine graphene provided only 66 % of the reversible capacity of 638 $mAhg^{-1}$ after 30 cycles at 0.05 Ag^{-1} [215]. In our study, the cyclic performance of NrGO and rGO were compared at 10 Ag^{-1} for 500 cycles and 0.1 Ag^{-1} for 100 cycles. The rGO exhibited 113 $mAhg^{-1}$ capacity at 10 Ag^{-1} with the 40 % capacity retention after 500 cycles. However, it preserved 102 % of the initial capacity at 0.1 Ag^{-1} delivering 440 $mAhg^{-1}$ discharge capacity by the 100^{th} cycle. On the other hand, NrGO displayed 240 $mAhg^{-1}$ capacity with 90 % capacity retention after 500 cycles at 10 Ag^{-1}. More interestingly, our NrGO yielded 114 % retention with its increasing capacity of 488

$mAhg^{-1}$ even after 100^{th} cycle at 0.1 Ag^{-1}. It showed an excellent capacity increase with the increase in charge/discharge cycles.

Table 2. 1. Comparison of the performances of various nitrogen-doped/reduced graphene (oxide) as Li-ion battery anodes

Material	Current Density (Ag^{-1})	Capacity ($mAhg^{-1}$)	Capacity Retention (%)	Cycle No (Number)	Reference
N-doped Graphene	10	180	94	500	[249]
N-doped Graphene	2	453	90	550	[249]
RGO	0.037	350	71	60	[31]
N-RGO	0.037	600	95	60	[31]
rGO	0.1	561	93	50	[216]
Graphite Powder	0.074	200	60	30	[267]
Graphene Nanosheet	0.074	280	50	30	[267]
N-doped Graphene	0.05	827	83	30	[215]
Pristine Graphene	0.05	638	66	30	[215]
rGO	0.1	440	102	100	This study
	10	113	40	500	This study
NrGO	0.1	488	114	100	This study
	10	240	90	500	This study

In summary, the NrGO in this study was obtained by thermal annealing at elevated temperature in an Ar/NH_3 atmosphere, which is enabling the reduction and nitrogen-doping of improved Hummers' GO by a single step process. Apart from all of the abovementioned references in Table 2. 1, GO was fabricated by improved Hummers' method rather than Hummers' or modified Hummers' method. This provided more and efficient oxidation of graphite by using H_3PO_4 instead of $NaNO_3$. Therefore, the reduction of GO resulted in a more open structured material for the next steps. This is because of the process's ability to remove the C-O bond since it is the weakest bond among other oxygenated groups. Also, it has 2^{nd} higher occupancy to rank after C=C bonds according to our XPS results in Figure 2. 10**.** Thus, it provided higher electrical conductivity, which leads to better rate performance. Moreover, both samples have a high specific surface area and better pore size distribution according to our BET results. Besides, both have an excellent defect density according to our Raman results, which provide a superior number of electrochemically active sites. Hence, the enhanced cell kinetics and high battery performance were obtained due to efficient and open access of electrolyte to the electrode surface, so that resulting electrolyte/electrode interaction increased with cycling due to

the Li storage mechanism. Nevertheless, the NrGO has a constant slope of increasing capacity upon cycling at low current densities, as illustrated in Figure 2. 13. It is evident from all electrochemical characterization that the NrGO synthesized in this study becomes more electrochemically active upon lithium storage by cycling rather than rGO. This can be a result of NrGO having high structural defect density due to the nitrogen doping at the edges of layers which supply more electrochemical active site for Li to accommodate. Ma et al. studied the electronic and magnetic properties of pyridinic, pyrrolic, and graphitic defect models in graphene resulting from nitrogen doping by first-principles calculations [217]. They concluded that the pyridinic nitrogen groups are the most suitable sites for Li adsorption. The nitrogen p orbitals in these pyridinic sites hybridize with lithium p orbitals with optimum adsorption energy. Pyridinic sites form a higher electron density, and this strong electronegativity attracts the Li^+ ions more. Moreover, among nitrogen sites on graphene, the pyridinic groups are the sites that can accommodate the highest number of Li^+ ions [273]. More importantly, the distance between adsorbed lithium ions on the pyridinic sites is high enough to prevent Li clusters from forming. For pristine graphene, the Li cluster formation decreases the electrode capacity by cycling and even fails the battery after dendrite formation. For that reason, nitrogen doping enhances the Li adsorption energy and lowers the energy barrier for Li intercalation [274]. The lowering of the intercalation energy barrier has an important outcome when the nitrogen-doped graphene has an open structure. At each cycle, Li^+ ions are adsorbed on the pyridinic sites and intercalate the structure more. So after each charge/discharge cycle, by the expansion of the graphene sheets, the capacity also increases. This is the first time to show such a behavior for a nitrogen-doped graphene anode. This mechanism does not occur when the oxidation and nitrogen doping steps use mild techniques because these methods cannot create open graphene sheets. All in all, the defective layers of NrGO due to nitrogen doping become more electrochemical active with the expansion of rGO stacks so that capacity of cell increases by cycling with an approach of the theoretical capacity of graphene.

2.2.4. Conclusion

NrGO and rGO were successfully fabricated by thermal annealing of as-synthesized improved Hummers' GO in Ar/NH_3 and Ar atmosphere, respectively. The structural and electrochemical characteristics of NrGO and rGO were comprehensively compared. Nitrogen doping was proved to increase interplanar distance, enhance the defect density,

decrease pore diameter, boost structural integrity, and alter the occupancies of functional groups within GO structure over rGO. Furthermore, the high amount of pyridinic nitrogen sites within the NrGO enhanced Li storage capacity because Li^+ ions are more attracted by the strong electronegative groups, and they lower the energy barrier for Li intercalation. In light of these findings, NrGO exhibited a higher discharge capacity and better cell kinetics than rGO. In addition to that, NrGO showed the highest and increasing discharge capacity upon cycling due to its excellent electrical conductivity, the higher density of electrochemically active sites, and effective pore size distribution.Homogeneous Growth of TiO_2-Based Nanotubes on Nitrogen-Doped Reduced Graphene Oxide and Its Enhanced Performance as a Li-ion Battery Anode

2.3. Homogeneous Growth of TiO2-Based Nanotubes on Nitrogen-Doped Reduced Graphene Oxide and Its Enhanced Performance as a Li-ion Battery Anode

2.3.1. Preface

Our aim is to simultaneously enhance electronic and ionic conductivities of the active material in anode by adding a conductive component. For a stronger attachment, TiO_2-B nanotubes are hydrothermally grown on NrGO sheets in an aqueous medium. This novel 3D architecture results in a reduction of conductive additive components such as carbon black and enhances the overall performance of anode. To the best of our knowledge, such morphology and phase combination have not been reported. In this work, we combined the synergistic effects of the high ionic conductivity of nanotubular TiO_2-B phase with the good conductivity of NrGO to increase both electronic and ionic conductivity which result in high rate capability of prepared anode materials. With the channeled pathway and layered structures of TiO_2 nanotubes, Li ions transport without facing resistance and overall composite anode yield stable capacity upon cycling.

2.3.2. Experimental

2.3.2.1. Materials

Commercial anatase, sodium hydroxide (NaOH) pellets, N-Methyl-2-pyrrolidone (NMP) and polyvinylidene fluoride (PVDF) were purchased from Aldrich and used as received. GO was purchased from Grupo Antolin Ingenieria SA (Spain). Lithium hexafluorophosphate ($LiPF_6$) solution (1 M) in ethylene carbonate (EC) and dimethyl carbonate (DMC) (EC/DMC=50/50 (v/v) was purchased from Sigma-Aldrich.

2.3.2.2. Synthesis of NrGO

Nitrogen-doped reduced graphene oxide was synthesized by thermal annealing method in the presence of ammonia gas [27]. Briefly, GO powder was placed in a quartz tube furnace and was heated treated at 900 °C under ammonia and Ar atmosphere. Then, the furnace was cooled down to room temperature. The synthesized NrGO powder was collected for the characterizations and further use.

2.3.2.3. Synthesis of NrGO/TiO_2-B nanocomposite

0.2 g NrGO was dispersed in a solution of 20 mL distilled water (DW) and 10 mL dilute glycerol (50 vol.%) using probe sonication (Qsonica, Q700) for 1-hour. In another beaker, 0.3 g anatase was dispersed in 70 mL DW by stirring for 15 minutes. NrGO dispersion was added to anatase dispersion and resultant dispersion was stirred for 15 minutes, followed by 1-hour probe sonication to disperse the mixture completely. Then, 40 g NaOH pellets were gradually added to NrGO/anatase water dispersion within an hour under agitation, followed by 5 hours stirring at room temperature and 1-hour bath sonication. The resulting suspension of NrGO/anatase in NaOH solution was poured into a 150-mL Teflon lined stainless steel autoclave and heated at 130 °C inside an oven for 48 hours for hydrothermal treatment. After cooling to room temperature, autoclave content was filtered (Sartorius, Grade 393) and mildly washed to separate the solid content. Ion exchanging of H^+ with Na^+ was performed as the next step. The filtered product was poured into 1-liter DW and pH of the suspension was gradually decreased from 12 to 7 using 1 M and 0.1 M HCl solutions under constant stirring within 24 hours. This step is crucial for the formation of long hydrogen titanate nanotubes as represented in Figure 2. 17 schematically [275, 276]. The ion-exchanged suspension was filtered, followed by drying at 60 °C overnight. To convert hydrogen titanate to TiO_2-B phase, the ion-exchanged nanocomposite powder was heat treated in a tube furnace at 500 °C for 2 hours with a heating rate of 15 °C/min using Ar gas purge. The product was collected and stored for further use.

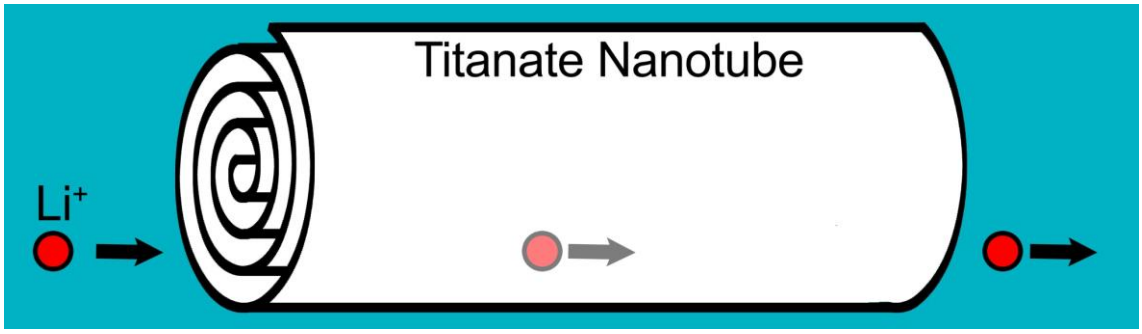

Figure 2. 17. Special morphology of titanate for lithiation mechanism

2.3.2.4. Synthesis of TiO_2-B phase

0.4 g anatase was dispersed in 100 mL DW by stirring for 15 minutes followed by probe sonication for 1 hour. 40 g NaOH pellets were gradually added to above-mentioned suspension within an hour. The dispersion was completed by 5 hours of further stirring at room temperature and 1-hour bath sonication. The resulting suspension was transferred to a 150-mL Teflon-lined stainless-steel autoclave. The autoclave was then put in a thermally insulated oil bath which was placed on a temperature-controlled heater stirrer. Hydrothermal treatment with continuous stirring was performed at 130 °C for 48 hours. The rest of procedures including washing, drying, ion exchange and heat treatment were similar to NrGO/TiO_2-B nanocomposite.

2.3.2.5. Materials characterizations

X-ray diffraction technique (XRD) (Bruker, D2 Phaser) was used to characterize phase composition and crystal structure of synthesized materials. To investigate the surface chemistry of synthesized products, X-ray photoelectron spectroscopy (XPS) (Thermo Scientific, K-Alpha) was performed using an Aluminum anode (Al K_α= 1468.3 eV) as the X-ray source and C 1s was assigned to 284.5 eV as the internal standard for peak calibration. Morphology of prepared nanocomposite was investigated by field effect scanning electron microscope (SEM) (Zeiss LEO Supra 35VP SEM-FEG). Raman spectroscopy (Renishaw, inVia) was performed using a 532-nm laser source. The surface area of materials was investigated by Brunauer-Emmett-Teller (BET) method using nitrogen adsorption and desorption isotherms (Micrometrics, 3FLEX). Pore size and pore size distribution (PSD) curves were calculated from the desorption isotherms using Barrett-Joyner-Halenda (BJH) method. Powder samples were degassed (Micrometrics, VacPrep 061) at 130 °C for 24 hours in advance. Thermogravimetric (TG) analysis was performed on a (Shimadzu, DTG-60H) from room temperature to 1000 °C with heating rate of 10 °C/min in air atmosphere. The weight percentage of TiO_2 and NrGO phases were calculated from TG curves.

2.3.2.6. Electrochemical characterizations

Electrochemical measurements were performed on a split cell battery set up (Split Flat Co. XA 201540, MTI). To make the anode, a paste composed of the active material, carbon black as a conductive additive, and polyvinylidene fluoride (PVDF) as a binder was made. All materials were well ground and mixed in an agate mortar. Then NMP was added to the powder mixture to form a paste and well mixed for 24 hours. The active material paste was painted on a clean Cu foil and was dried in vacuum oven at 120 °C overnight to extract NMP completely. Loading of the active material on the anode was about 1-2 mg/cm^2. Batteries were assembled inside an Ar-filled glove box (GP CAMPUS, Jacomex) using Li chips as the counter electrode, a porous polypropylene film (Celgrad 2400) as the separator, and 1 M lithium hexafluorophosphate ($LiPF_6$) solution in ethylene carbonate (EC) and dimethyl carbonate (DMC) (EC/DMC=50/50 (v/v)) as the electrolyte.

Galvanostatic charge/discharge cycling tests of assembled batteries were conducted on an MTI 8-channel battery analyzer set-up at a voltage range of 1-3 V versus Li/Li$^+$, using different current rates (0.1 C, 0.5 C, 1 C, and 2 C). It should be noted that here Li$^+$ insertion to / de-insertion from the anode is attributed to charge/discharge, respectively. Rate capability of the prepared anodes was characterized by charge/discharge cycling at current rates of 0.1 C, 0.5 C, 1 C, and 2 C for 10 cycles at each current rate. Coulombic efficiency was calculated at each cycle by dividing charge capacity over discharge capacity. Cyclic voltammetry (CV) (Gamry 3000 potentiostat/galvanostat/ZRA) of assembled batteries were studied before cycling at a range of 1-3 V vs. Li/Li$^+$ with a scan rate of 0.1 mV/s. All electrochemical measurements were performed at ambient temperature.

2.3.3. Results and discussion

Crystal structure of synthesized materials was investigated by XRD method and Raman spectroscopy. Figure 2. 18 illustrates XRD patterns of synthesized TB, NrGO-TB as well as NrGO. As it is shown in the figure, all main diffraction peaks can be assigned to TiO_2-B phase (JCPDS 46-1237) and anatase (JCPDS 21-1272) in both synthesized samples. It is notable that the main peak of anatase (2Θ=25.5°) overlaps with the main peak of TiO_2-B phase, but diffraction peaks at 37.8° and 48.0° correspond to anatase only, which indicates that a mixture of two phases is present in both samples. In sample NrGO-TB the broad peak at 26.5 ° is associated with the stacking of (002) planes of graphene sheets

[221, 277]. It is also noteworthy that broadening of strong diffraction peaks reveals nanostructure nature of both two samples.

The phase structure of synthesized materials was further characterized by Raman spectroscopy. Figure 2. 18 b and c depict Raman spectra of the synthesized samples. Peaks were observed at Raman shifts of 144, 196, and 638 cm^{-1} which are typical Raman peaks of TiO_2-B [278]. However, there is a discrepancy in the literature about assigning the two peaks at 400 cm^{-1} and 514.2 cm^{-1}. The peak at 514.2 cm^{-1} is assigned to the A1g mode of anatase in some studies [279], whereas it is attributed to TiO_2-B in the others [227, 278]. The peak at 400 cm-1 is also mentioned to be a unique peak of anatase [220, 278], while it is assigned to TiO_2-B by other reports [227]. Nevertheless, both phases share the strongest reflection at 144 cm^{-1} and both are present in our synthesized samples. GO phase, which is present in NrGO-TB sample (Figure 2. 18 c) shows two distinct Raman peaks at 1360 cm^{-1} due to sp^2 hybridization of carbons (D-band) and 1588 cm^{-1} due to the graphitic structure of graphene sheets (G-band) [126].

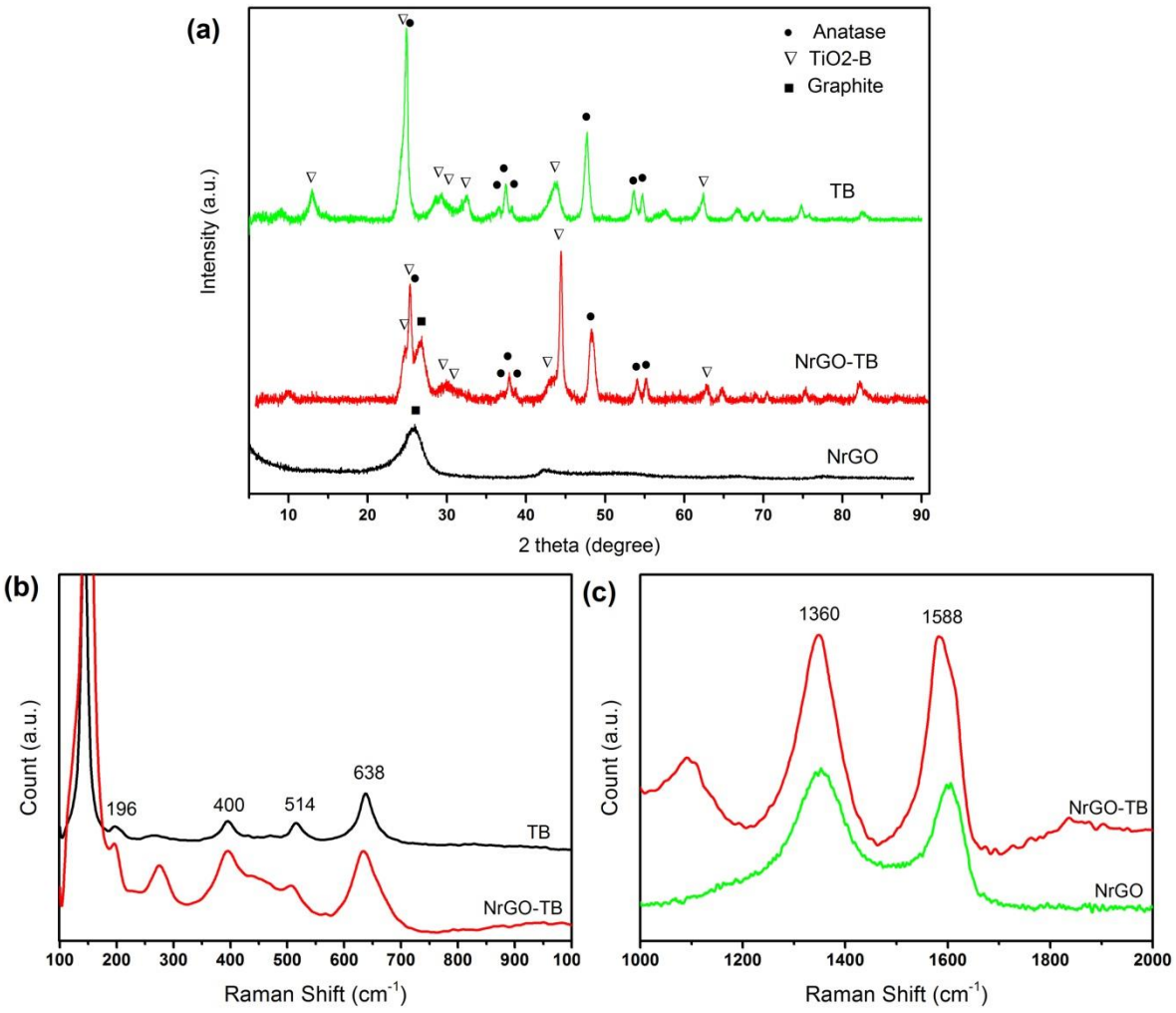

Figure 2. 18. X-ray diffraction patterns of synthesized nanocomposites(a), Raman spectroscopy of synthesized nanocomposites (b), Raman spectrum of NrGO-TB and NrGO at higher magnification.

Morphology and microstructure of NrGO, TB and NrGO/ TiO_2-B were characterized by SEM and are shown in Figure 2. 19. Synthesized NrGO particles show stacks of flat and large-size reduced graphene oxide sheets which confirms its XRD pattern (Figure 2. 18 a). As Figure 2. 19 b, c depict, stirring hydrothermal method is successfully employed to synthesize long nanotubes of TiO_2-B with diameters between 60-350 nm and length of up to 5 microns. Micrographs of NrGO-TB (Figure 2. 19 d,e) indicate growth of TiO_2-B nanotubes around NrGO particles. Comparing nanotube dimensions in NrGO-TB and TB samples (Figure 2. 19 c,e) reveals that diameter range of nanotubes in NrGO-TB is 15-23 nm which is quite smaller and more uniform than TB. This shows the effect of NrGO sheets as a substrate for heterogeneous nucleation of hydrogen titanate during

hydrothermal synthesis. In addition, thinner nanotubes show higher surface area and thus can more effectively contribute to electrochemical reactions. As it is seen, the presence of NrGO particles have also prevented agglomeration of TiO_2 nanotubes and created a porous microstructure. Besides to be a connection for TiO_2 nanotubes with NrGO particles as a substrate, it enhances transfer of electrons from TiO_2-B phase through NrGO particles toward current collectors.

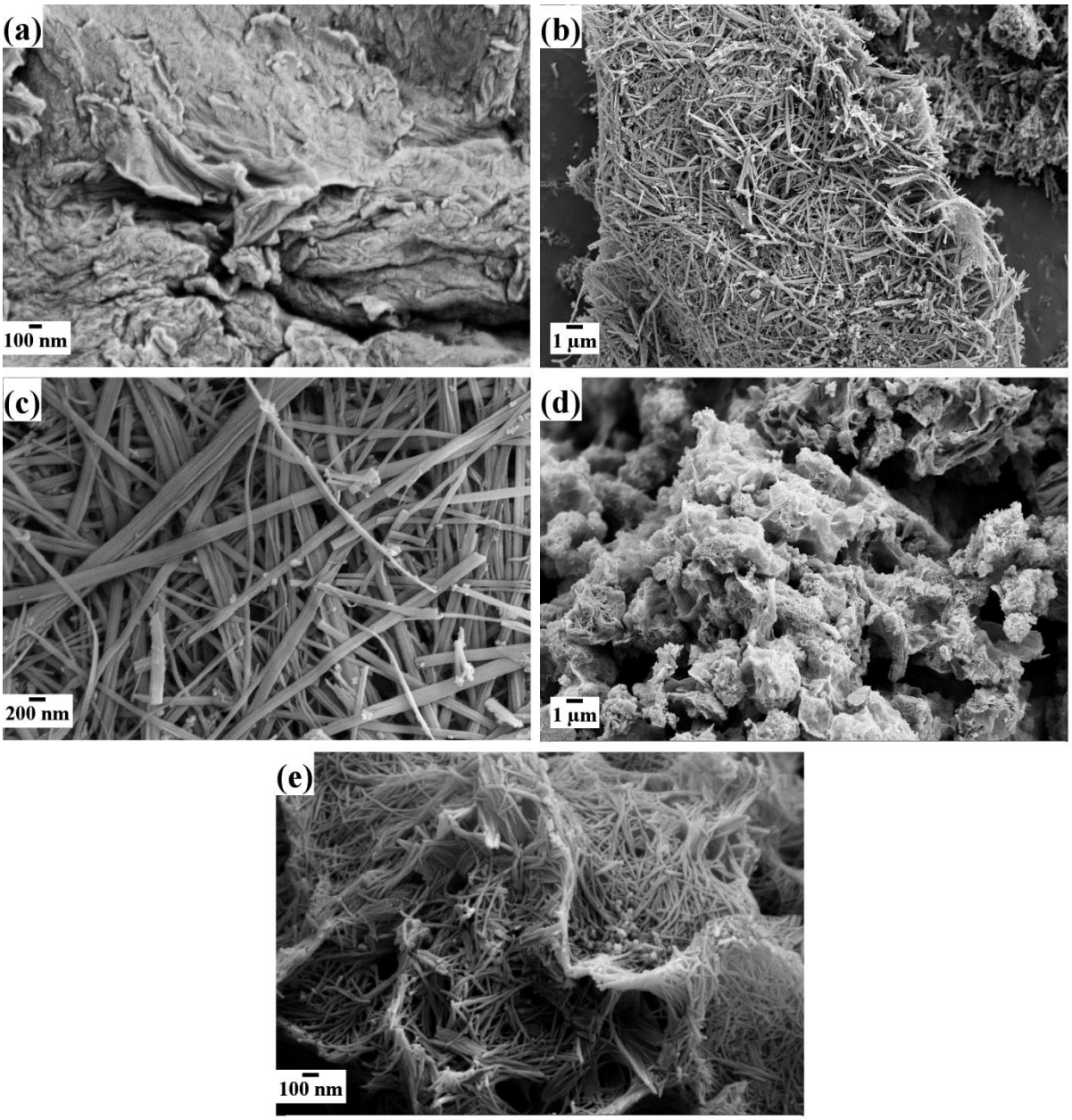

Figure 2. 19. SEM micrographs of synthesized (a) NrGO, (b, c) TB at two magnifications, (d, e) NrGO-TB at two magnifications.

Titanium-based nanotubes after their synthesis tend to stack on each other. As can be seen from Figure 2. 19 b, there is a large haystack like nanotube formation. The clump size is about 15x30x5 μm and the nanotubes have minimal bending. However, when Figure 2. 19 e is examined, the nanotubes are bending and following the natural curves of graphene sheets (Figure 2. 19 a). The curvature of pure graphene (Figure 2. 19 a) and nanotube coated graphene (Figure 2. 19 e) is in the same order of magnitude. In addition to that, when lower magnification images of these materials (Figure 2. 19 b & Figure 2. 19 c) are compared, the curvature can be seen more clearly. Moreover, when the sides of nanotube coated graphene layers are examined (Figure 2. 19 e), sheets with 100-150 nm thickness can be seen.

The precise weight ratio of NrGO and TiO_2 phases were measured by thermogravimetric analysis from room temperature up to 970 °C followed by 2 hours soaking in that temperature in an air atmosphere to completely remove the carbonaceous phase (Figure 2. 20). Accordingly, the percentage of TiO_2 phase in NrGO-TB sample was calculated as 48.9 wt. %. For every different active material, the amount of the substrate should be determined separately. In this study, we tried to optimize the amount of the nanotubes on the graphene surface. At a higher nanotube amount, we obtained a much thicker nanotube layer on graphene. This would be an undesired situation for electrical conductivity. If we assume that graphene is pure carbon and the nanotubes are pure TiO_2, then from the TGA result, for every 1 C atom there should be about 4.5 TiO_2 crystal. Since the deposited material is a layered 1D material covering a 2D substrate, this value is considerably low.

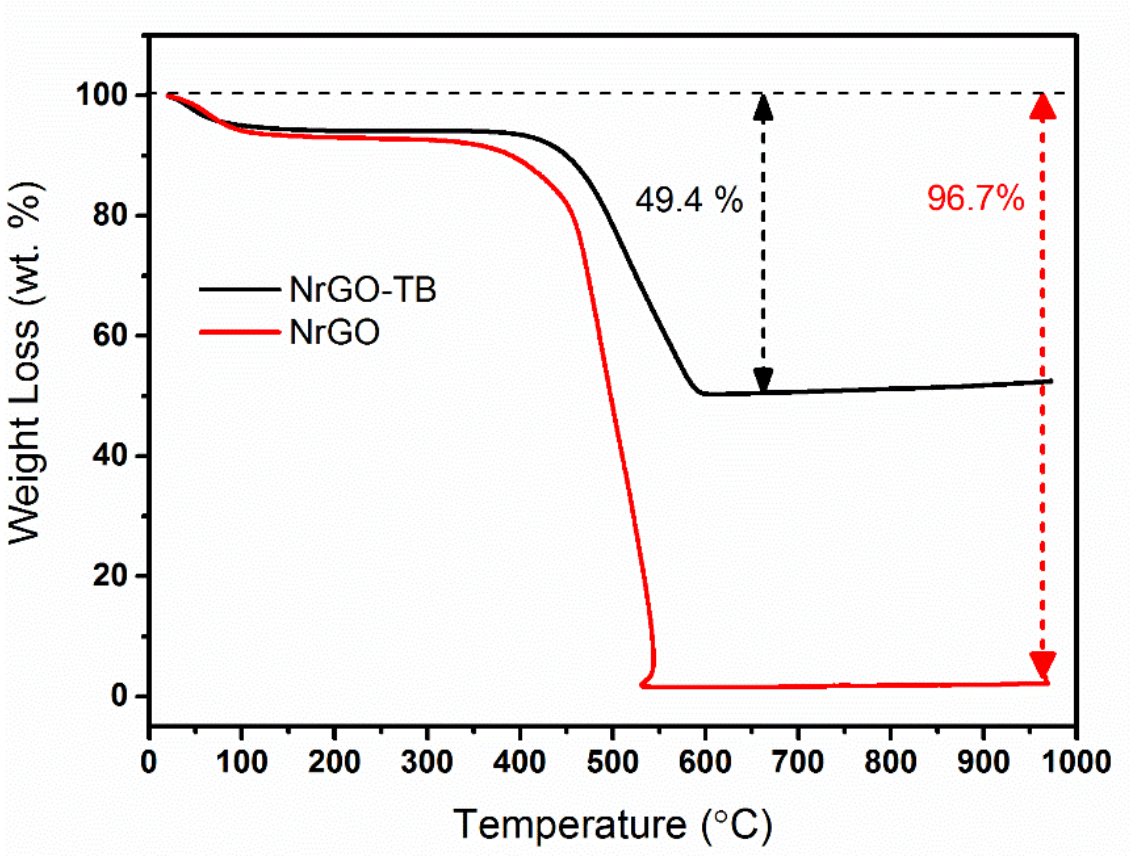

Figure 2. 20. Thermogravimetric curves of NrGO and NrGO-TB samples in air.

The surface bond structure of NrGO was investigated by XPS method. As it is shown in Figure 2. 21, all principal peaks of C, N, and O can be identified in the survey spectrum which is explained with their assignments in Table 2. 2. Accordingly, atomic percent of nitrogen atoms in NrGO was calculated as 6.3 %, which indicates a successful doping process. Percentages of nitrogen atom bondings are 47.8 %, 33.3 %, and 18.9 % for pyridinic, pyrrolic, and graphitic, respectively. It is notable that the majority of C 1s bonds correspond to graphitic C with sp^2 hybridization indicating hexagonal carbon arrangements in graphene sheets. The other two minor peaks i.e. C2 and C3 arise from the defects due to nitrogen doping or edge effect of graphene sheets [218, 280] which are ascribed to C-N and carbon-oxygen bonding arrangements, respectively [28]. The presence of O 1s peaks reveals that some oxygen-carbon compounds have remained in the sample even after thermal reduction, and this is consistent with the literature to observe 3-5 atomic % oxygen (Table 2. 2) in reduced graphene oxide [281]. The peaks at 529.85 eV (O3), 531.37 eV (O1) and 533.13 eV (O2) can be assigned to O=C-OH, C=O and C-OH, respectively [282].

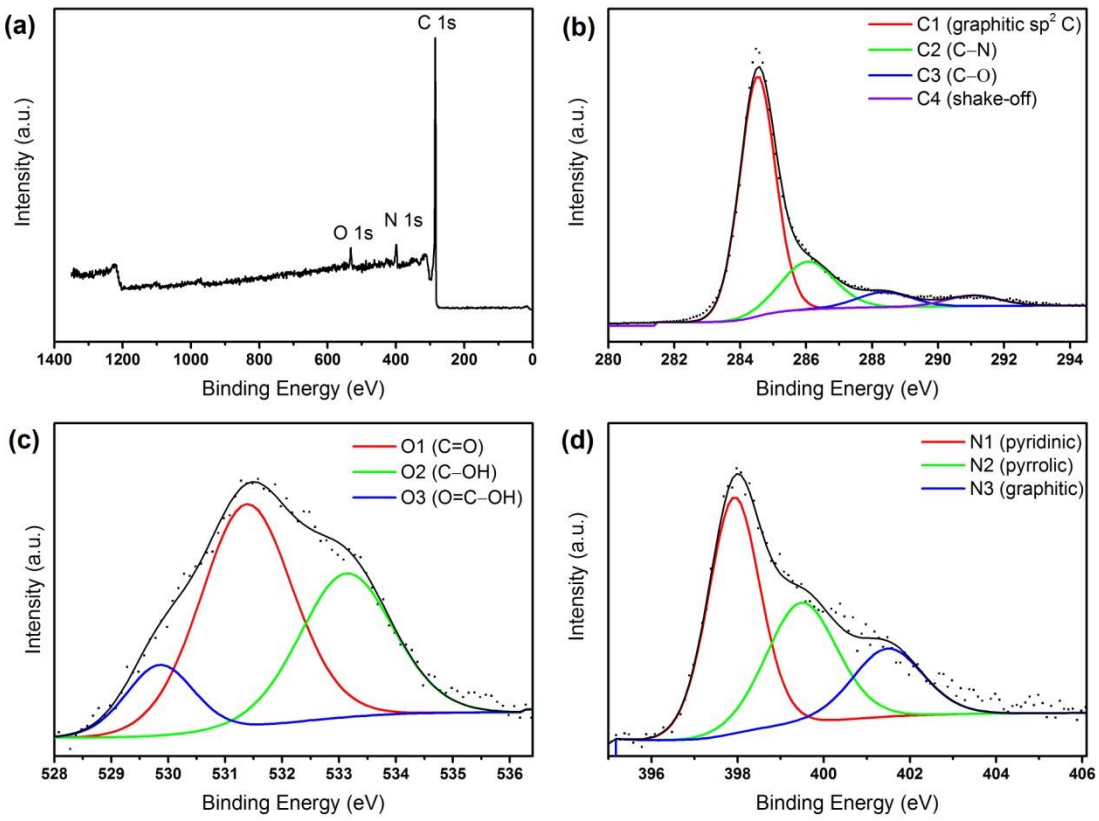

Figure 2. 21. XPS spectrum of NrGO. (a) survey spectrum, (b) C 1s, (c) O 1s and (d) N 1s.

Table 2. 2. Peak assignments, as well as the atomic percent of elements, present in NrGO according to XPS

Peak Name	Assignments	Peak Energy (eV)	Atomic %
C 1s	C1 (graphitic sp^2 C)	284.52	64.24
	C2 (C-N)	286.04	19.48
	C3 (C-O)	288.36	6.23
N 1s	N1 (pyridinic)	397.92	3.02
	N2 (pyrrolic)	399.48	2.10
	N3 (graphitic)	401.49	1.19
O 1s	O1 (C=O)	531.37	1.99
	O2 (C-OH)	533.13	1.30
	O3 (O=C-OH)	529.85	0.47

Specific surface area of synthesized materials was examined by BET method. Figure 2. 22 a illustrates nitrogen adsorption and desorption isotherms for the two synthesized samples as well as pristine NrGO. BET surface area of NrGO sheets was measured to be 239 m^2/g. such high value can be ascribed to the layered microstructure of reduced graphene oxide which introduces high free surface area. Relatively low surface area of TB (43 m^2/g) is consistent with its agglomerated microstructure (Fig. 2.b) which indicates that only nanotubular morphology is not enough for achieving high surface area. In the other word, a well dispersed and not agglomerated architecture is necessary for a high surface area which can be attained by the growth of TiO_2-B nanotubes on NrGO sheets as a substrate. As confirmed by the SEM micrographs of NrGO-TB (Figure 2. 19 d, e), high BET surface area of NrGO-TB sample (153 m^2/g) reveals a porous and not agglomerated microstructure. To guarantee fast diffusion of L^{i+} as well as high a kinetic rate of lithiation / de-lithiation reactions, a sufficiently high surface area is a crucial feature of a potential candidate for Li-ion battery anode. PSD curves in Figure 2. 22. b further confirms that conclusion. The total pore volume of NrGO, TB and NrGO-TB were measured to be about 0.20, 0.12 and 0.43 cm^2/g, respectively. This is consistent with the SEM microstructures of synthesized samples. Despite nanotubular morphology of TB, its high agglomeration nature resulted in fewer accessible pores. However, the NrGO-TB sample which benefits from both high surface area graphene sheets and TiO_2 nanotubes, shows significantly improved mesoporous structure due to well dispersion of TiO_2 nanotubes. As the PSD curves illustrate in Figure 2. 22, all samples have a mesoporous structure with a sharp peak at about 3.8 nm which can be ascribed to the inner volume of nanotubes [283, 284].

All three samples showed hysteresis loop in their adsorption/desorption isotherms (Figure 2. 22 a) which can be ascribed to a mesoporous material (type IV curve). Accordingly, the shape of hysteresis reveals information about the texture and type of pores. NrGO hysteresis belongs to H2 type while TB sample belongs to H3 type [285]. NrGO-TB resembles a combination of the H2 and H3 type as it includes both contents as well. H2 type curves are generally ascribed to material with disordered pore shape, whereas H3 type curves are attributed to materials with slit-shaped pores which can be indicative of the layered structure of nanotubes.

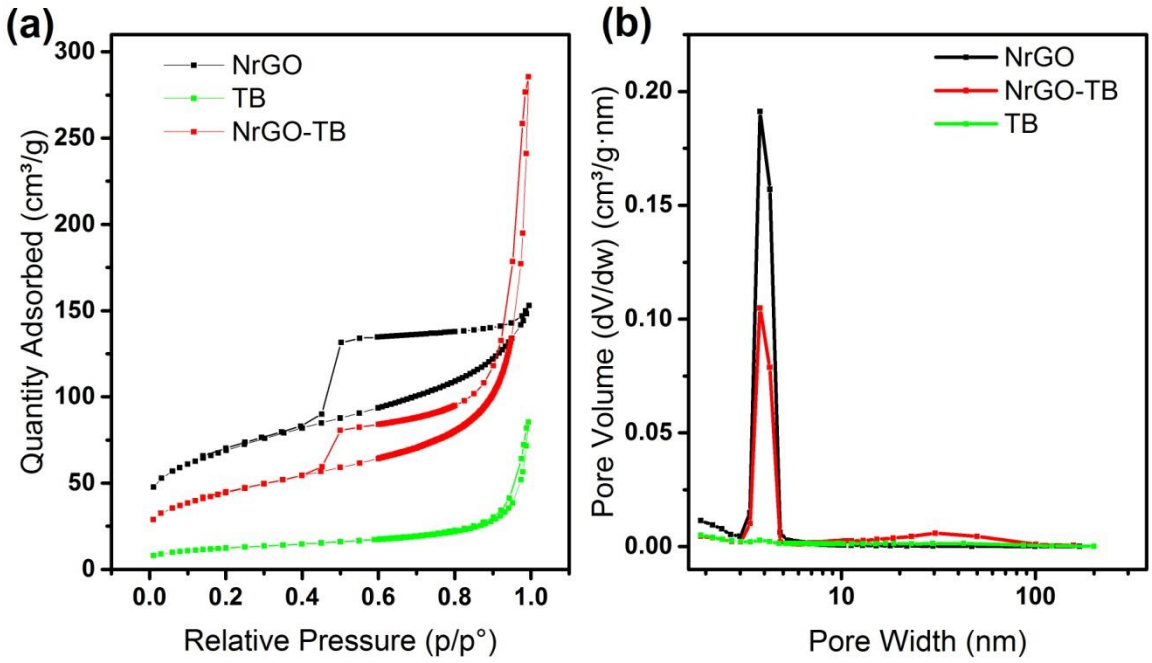

Figure 2. 22. (a) BET adsorption and desorption isotherm curves for pristine NrGO, TB, and NrGO/TIOB$_2$. (b) BJH pore size distribution for pristine NrGO, TB, and NrGO/TIOB$_2$.

Electroactivity of prepared anodes was studied by CV technique. As seen in Figure 2. 23, cyclic voltammogram of TB depicts one main cathodic peak at around 1.75 V which is attributed to Li^+ insertion into TiO_2-B phase [197], the small cathodic peak at around 2.25 V is attributed to Li^+ insertion into the small amount of anatase phase which is present in the sample (Figure 2. 18 a) [286, 287]. The same set of peaks can be characterized in NrGO-TB sample as well, with the difference that the anatase peak is more intense in NrGO-TB. This can be a result of higher anatase content in this sample. Both samples show reversible redox reactions at a scan rate of 0.1 mV/s. voltammograms of both samples illustrate broad peaks rather than sharp peaks which is another indication of pseudocapacitance mechanism of charge storage in TiO_2-B nanotubes [275, 288]. Furthermore, nanotube morphology of both samples can be distinguished from other one-dimensional nanostructures such as nanowires and nanorods by Figure 2. 23. Nanotubes of TiO_2 usually show one broad CV curve peak while the other TiO_2 one-dimensional nanostructures show a double peak at around 1.5-1.7 V vs. Li/Li^+ with a small difference (<0.1 V) [197, 289-291].

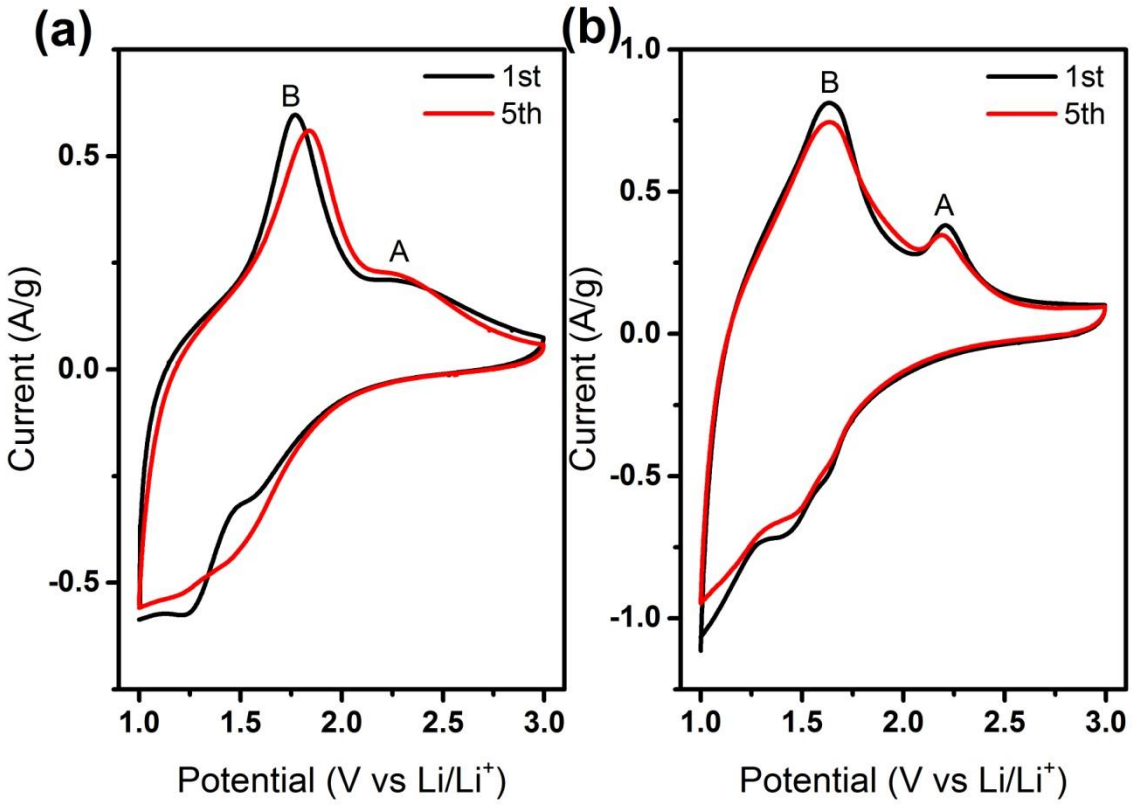

Figure 2. 23. CV of prepared anodes at a scan rate of 0.1 mV/s. (a) TB. (b) NrGO-TB. B sign denotes TiO_2-B phase and A sign denotes anatase.

The charge/discharge potential-capacity profiles of the prepared anodes are shown in Figure 2. 24 a, b. TB sample has a capacity of 138 mAh/g in the first cycle with a discharge rate of 0.1 C. However, its capacity drops to 40 mAh/g after 50 cycles, which indicates only about 29 % capacity retention. Such a behavior is observed in NrGO-TB sample as well in which it shows a capacity of 777 mAh/g at first cycle, but the capacity drops to 128 mAh/g. The high irreversible capacity for the first cycle is attributed to the reaction of surface groups of titanium oxide with the electrolyte which gives rise to decomposition of the electrolyte. That kind of capacity decay is reported for pseudocapacitive oxide materials including titanium-based oxide compounds as a common drawback due to the reaction of oxygen-containing surface groups with electrolyte at service voltage range [292]. Some of the capacity loss is due to the oxygen groups on the surface. However, the rest of the capacity comes from capacitive storage and that capacity decreases for these kinds of materials. It cannot stay above theoretical capacity. The capacity loss due to the oxygen groups can be minimized by modifying the electrolyte. The reason for better performance at current rates higher than 0.1 C can be

attributed to having more time for undergoing side reactions with electrolyte at the 0.1 C rate.

The cyclability of the prepared samples is compared in Figure 2. 24 c, d. The discharge capacities of both samples at a current rate of 0.1 C show a large decay. However, for current rates of 0.5 C and 1 C, they show relatively stable capacity for 50 cycles. The discharge capacity of NrGO-TB at 0.5 C and 1 C after 50 cycles are measured to be 220 mAh/g and 150 mAh/g, respectively. This shows a great enhancement in comparison with TB sample which shows 130 mAh/g and 100 mAh/g for 0.5 C and 1 C, respectively. The reason for this capacity enhancement can be ascribed to higher ionic and electronic conductivity of NrGO component which results in faster diffusion of Li^+ and thus higher capacities in higher current rates. Such a trend is also observed in coulombic efficiency values in Figure 2. 24. Coulombic efficiency of NrGO-TB at 0.1 C, 0.5 C, and 1 C current rates are, respectively about 25 %, 50 % and 50 % greater than that of TB which clearly shows an enhancement.

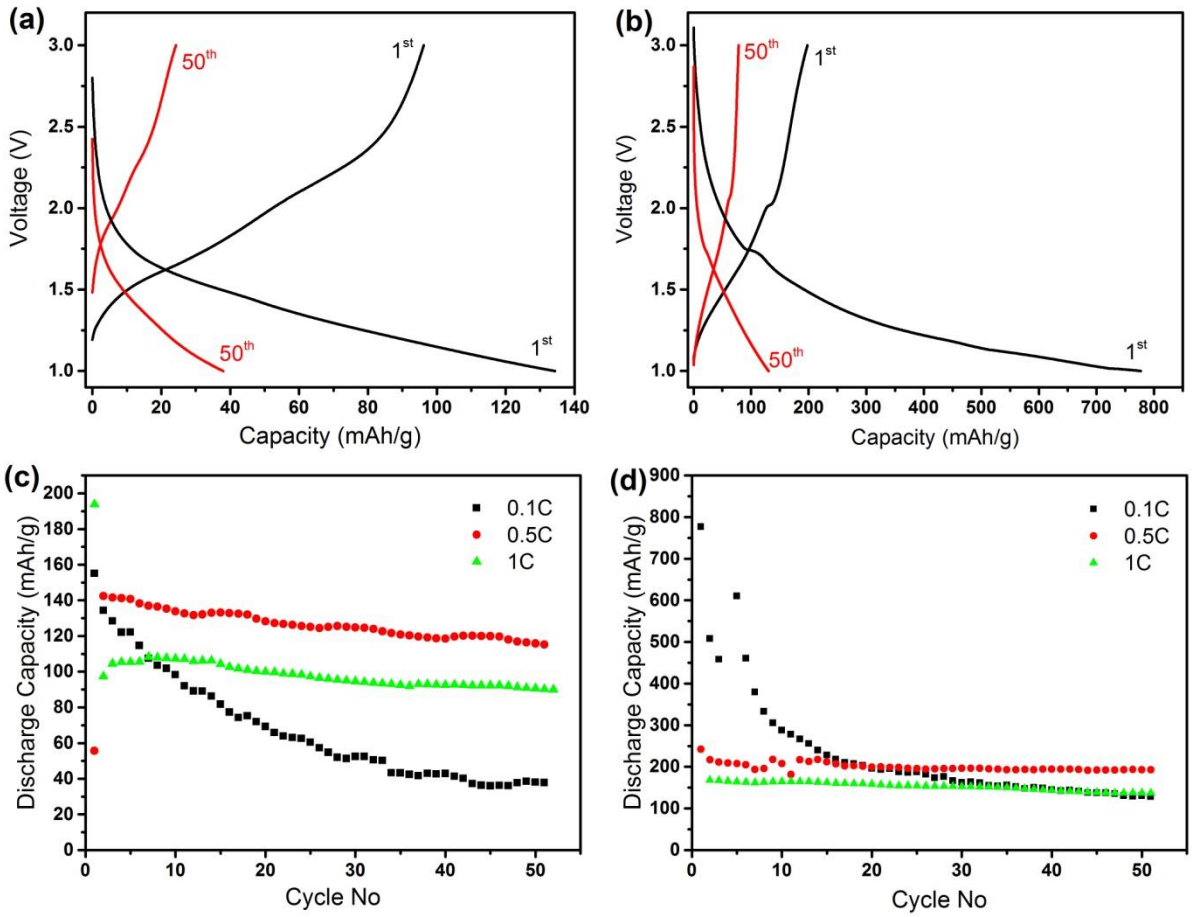

Figure 2. 24. Cycling performance of prepared anodes. (a) TB at 0.1 C. (b) NrGO-TB at 0.1 C (c) cyclability of TB at different current rates. (d) cyclability of NrGO-TB at different current rates.

In the literature, the number of NrGO supported titanium-based anode material studies is scarce. In Table 2. 3, some of those studies are compared. For all of the materials, with NrGO support, a higher capacity was obtained due to enhanced electrical conductivity and better material dispersion. In addition to that, all of the supported materials had better stability. When NrGO-TB was compared with the other samples, it had a better capacity at similar operating conditions. This difference probably comes from improved ionic conductivity inside the nanotubes.

Table 2. 3. Capacity comparison of some NrGO supported anode materials

Active Material	Capacity w/o support (mAh/g)*	Capacity w/ support (mAh/g)*	Ref.
LTO	160	170 (0.5 C)	[293]
TB	130	220 (0.5 C)	This work
TB	100	150 (1 C)	This work
LTO	105	120 (1 C)	[294]
TiO_2	60	175** (800 mA/g)	[295]

* 50th cycle
** Operating voltage: 0-3 V

Rate capability performance, as well as the coulombic efficiency of prepared battery anodes, are illustrated in Figure 2. 25. For both of the samples at an initial current rate of 0.1 C, like Figure 2. 24 c, d a decay is observed, however, in higher current rates samples show a stable discharge behavior. The rate performance of NrGO-TB sample is significantly higher than TB compared to each current rate. In the end, TB sample showed reversible discharge capacity of 68.6 mAh/g with 95 % capacity retention, while NrGO-TB sample showed reversible discharge capacity of 164.8 mAh/g with 97 % capacity retention. In fact, the presence of NrGO component in NrGO-TB sample not only increases the electronic conductivity of active material but also prevents agglomeration of TiO_2 nanotubes which greatly improve surface area and thus substantially enhances the kinetics of electrochemical reactions in the anode. Furthermore, the synergistic effect of NrGO sheets and TiO_2 nanotubes in boosting Li^+ intercalation properties plays an important role in improving electrochemical performance of anode. It is shown that both pyridinic and pyrrolic N doping structures in graphene provide interaction sites for Li^+ anchoring during intercalation [296]. In addition, NrGO sheets as a substrate demonstrate high integrity with TiO_2 nanotubes to form a unique microstructure which is stable during electrochemical cycling tests.

The N doping in this hybrid system has several effects. First of all, doping creates charged centers on the graphene surface and this facilitates homogeneous dispersion of metallic or metal oxide nanoparticles [297-299]. Both theoretical and experimental studies show that N doping can modulate the graphene structure and enhance the electrical conductivity [300, 301]. As a result, materials with N-doped graphene exhibits improved performances

in electrochemical applications. Another important effect of N doping is the creation of defects on the graphene surface which increases the wettability of the electrode with the Li electrolyte and creates active sites for Li^+ storage [302, 303].

In comparison with the reported cycling performances of TiO_2-B or anatase in the literature [304-307], our NrGO-TB sample shows enhanced or close cycling performance at similar or even higher current rates after 50 cycles which confirms the effect of NrGO sheets on improving the life cycle of anodes. These studies confirm that having some portion of anatase phase in TiO_2-B enhances the performance of the material. Moreover, dispersing the nanotubes on NrGO promotes the electron movement in the material.

There is a concern for new materials in the electric vehicles (EVs) area. Although the energy capacity is lower than graphite, lithium titanate (LTO) based anode materials are used in some commercial EVs. The manufacturers prefer these materials for their stability and fast charging capabilities. This means that there is a market for such batteries in EVs. However, we believe that titanium-based materials have a better usage in stationary systems. With their high performances at high currents, they are better match for solar cells, wind turbines and grid storage systems. For these kinds of systems, battery weight is not a big concern and being able to supply high currents is crucial. In that case, graphite cannot compete with titanium-based materials.

The strategy of growth of the main Li storing component with various morphologies on graphene sheets or nitrogen-doped graphene sheets has been successfully employed in many published papers. In this regard, not only metal oxides [220, 227, 230, 286] but also some metal sulfides such as MoS_2 and FeS_2 are anchored onto rGO and NrGO sheets and reported to enhance capacity and rate performance of Li-ion battery anodes [308, 309]. Such strategy can be proposed as a simple, fast and cost-effective material preparation method for Li-ion battery anode which is promising for scale-up.

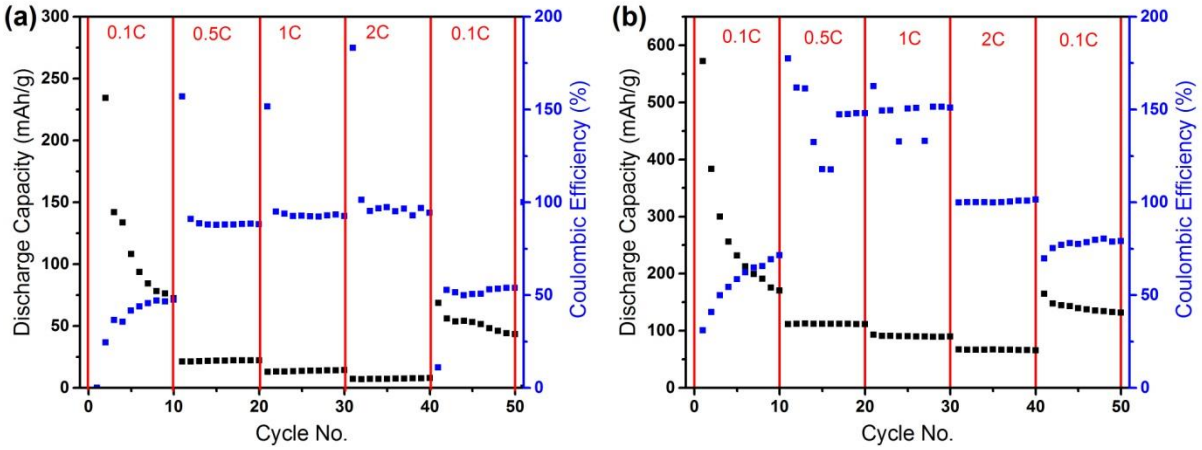

Figure 2. 25. Rate capability of (a) TB and (b) NrGO-TB battery anodes

2.3.4. Conclusions

In this work, a unique and novel combination of morphology evolution of titanium oxide and the presence of nitrogen-doped reduced graphene oxide was investigated for the first time to be used as a Li-ion battery anode. TiO_2 nanotubes with a mixture of bronze and anatase phases were grown by simple and straightforward hydrothermal method to decorate NrGO sheets following by thermal annealing. Characterized by SEM, the unique morphology of synthesized nanocomposite revealed a non-agglomerated growth of nanotubes on NrGO sheet surfaces. Here we have shown that such 3D architecture benefits electrochemical properties such as increasing the electronic and ionic conductivity of active material which finally result in a faster lithiation/de-lithiation of the anode. Compared with bare TiO_2-B, NrGO/TiO_2 anode showed superior performance in terms of rate capability and cyclability which is ascribed to the synergistic effect of nanotubular TiO_2-B phase and presence of NrGO sheets to enhance both electronic and ionic conductivity of the active material.

2.4. A Simple Spray Assisted Method to Fabricate High Performance Layered Graphene/Silicon Hybrid Anodes for Lithium-Ion Batteries

2.4.1. Preface

In this research, Si nanoparticles NPs were embedded between the top and bottom layers of thermally reduced graphene oxide (rGO) to form an rGO-Si-rGO sandwich-like structure (Figure 2. 26) using a facile and easily scalable spray and drying method for high capacity LIB anodes. The electrochemical performances of the as-prepared electrodes show excellent specific capacities with stabilized CEs. We believe that this is the first work showing the preparation of an easy and scalable process, including synthesis of chemical species and anode fabrication, for obtaining high-performance Si/graphene hybrid anodes.

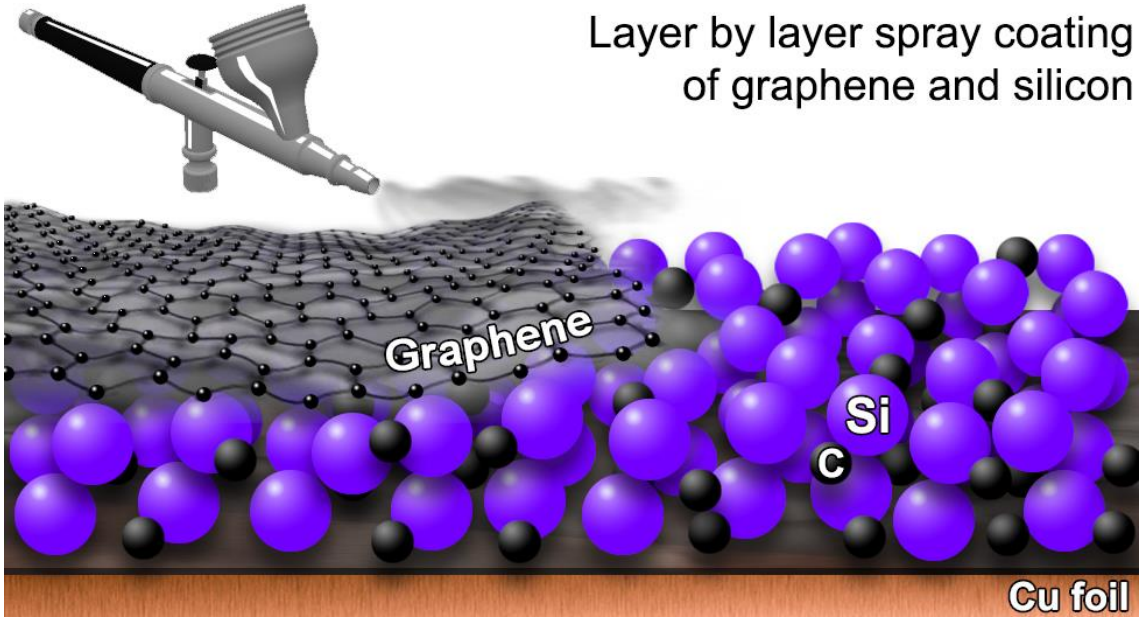

Figure 2. 26. rGO-Si-rGO sandwich like anode

2.4.2. Experimental

2.4.2.1. Materials

2.4.2.2. Synthesis of silicon nanoparticles

Si NPs were obtained by the magnesiothermic reduction of SiO_2 powder which was synthesized by the gelation of sodium metasilicate solution (AppliChem, 7.5-8.5 % Na_2O, 25.5-28.5 % SiO_2). 20 mL sodium silicate was diluted in distilled water in the ratio 1:10

by volume. 0.1 M hydrochloric acid (HCl) solution was slowly added to the silicate solution at 40 ºC until the pH reached 4 [310]. The solution was left to stir overnight at 40 ºC to obtain the silica gel which was then aged for about 48 hours. A loss in uniform fluid flow, signs of breakage planes upon shaking, and adherence of the gel particles to the apparatus walls were considered as rough criteria for successful gelation. The as-obtained wet gel was then dried in a vacuum oven (90 ºC) overnight to obtain a caky silica gel. After several washes with distilled water, the dried SiO_2 powder was finely crushed, mixed with excess Mg powder (SiO_2:Mg=1:2 wt. ratio) and heated to 670 ºC for two hours under an argon flow (40 mL/min). The resulting mixture of Si + MgO was acid washed in 1 M HCl to dissolve all the remaining unreacted Mg and MgO. The as-prepared Si powder was first sonicated in ethanol for 5 minutes, then in DI water for 10 minutes, and finally washed several times with water and dried at 90 ºC under vacuum. The last sonication and washing steps helped in preventing the spherical Si NPs from excessive agglomeration.

Next, 0.1 g of the synthesized Si was mixed with carbon black (CB) and polyvinylidene fluoride (PVDF) binder (Si:CB:PVDF=80:15:5). Fixed amounts of this powder mixture were dispersed in 35 mL of NMP to prepare Si slurry for the spray coating process. The slurries were homogenized by stirring them at 300 rpm for 24 hours at room temperature, and successively probe sonicating them for 10 minutes.

2.4.2.3. Reduction of graphene oxide

Commercial graphene oxide (GO) (GRAnPH Nanotech) was thermally reduced at 900 ºC for 10 minutes under an argon stream to obtain thermally reduced GO (rGO) [311]. To make a homogenous rGO slurry, 0.1 g of the obtained rGO powder along with PVDF (rGO:PVDF=95:5) was mixed in 10 mL N-Methyl-2-pyrrolidone (NMP), stirred overnight at 300 rpm, and probe sonicated for 10 minutes to get a homogeneously dispersed slurry.

2.4.2.4. Anode fabrication

The proposed sandwich anode structure was prepared such that Si NPs were embedded between two protective layers of rGO sheets. To do this, once the slurries were sonicated, a spray and drying setup such as shown in Figure 2. 27 was constructed. A Cu foil current

collector sheet, simultaneously heated at 50 ºC, acted as the substrate for spray deposition. Initially, a certain amount of the rGO/PVDF slurry was sprayed to form a base film of rGO sheets on the current collector. As the atomized aerosol droplets hit the substrate, the solvent quickly evaporated due to mild heating, leaving behind a thin and uniform layer of rGO with PVDF. After a layer was sprayed on the Cu foil held at 50 ºC, it was heated for 1 minute at 120 ºC to completely get rid of all traces of NMP. After the first layer of coating, another layer, this time Si/CB/PVDF slurry, was spray coated and dried following the same drying temperatures and durations as the previous layer. In the end, a topmost layer of rGO/PVDF was spray coated to envelop the Si layer. The topmost rGO coat was aimed to be thicker so that it can efficiently coat the bare Si NPs, hence not only contributing to the mechanical integrity of the anode but also serving to protect Si from direct exposure to the electrolyte, decreasing the chances of unstable SEI. It is noted that for all three successive layers, the substrate temperature was kept at 50 ºC during, and 120 ºC for 1-minute post-spray deposition. Additionally, for comparison, we also prepared the electrodes without rGO layers in the same way.

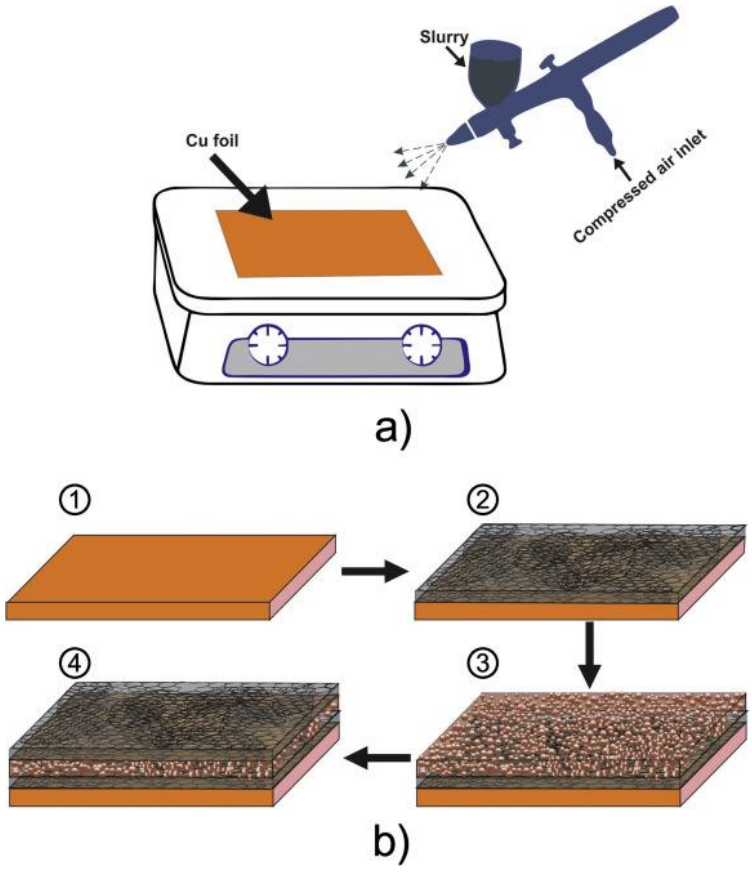

Figure 2. 27. (a) Illustration of spray deposition equipment. The temperature of the Cu foil was maintained at 50 °C during the spraying, (b) Schematic of the G-Si layered

anode fabrication. Alternate layers of rGO and Si NPs were spray deposited in this order.

2.4.2.5. Material characterization

Phase distribution and crystallinity of the Si NPs, and the degree of reduction of GO to rGO were probed using Raman spectroscopy (Renishaw in Via Reflex Raman Microscope and Spectrometer). Nd-YAG laser with a power of 0.5 mW at 532 nm was used for the data acquisition and the spectral range was kept from 5 cm^{-1} to 2000 cm^{-1}. Phase composition and crystal structure of the synthesized materials were examined with X-ray diffraction analysis (XRD; Bruker AXS GmbH D8 Advance). The measurements were collected at a 2θ range of 5-90º and the step size was set at 0.0 1 while the voltage and current values were 40kV and 40mA using Cu-K_α 1.5406 Å radiation.

The particle size of the Si NPs, and surface morphology of the second and third layers of the rGO-Si-rGO electrode were investigated with scanning electron microscopy (SEM) (Zeiss Leo Supra 35VP SEM-FEG) at a working voltage of 3 kV.

2.4.2.6. Electrochemical characterization

2032 coin cells were prepared to investigate the electrochemical properties of the rGO-Si-rGO anode as seen in Figure 2. 28. The cells were assembled in a glove box filled with pure argon (GP CAMPUS, Jacomex). Li chips were used as the counter electrode, the electrolyte was 1 M $LiPF_6$ dissolved in ethylene carbonate (EC) and dimethyl carbonate (DMC) (1:1 (v/v)), and a Celgrad 2400 film was used as the separator. The assembled cells were put to test for galvanostatic cycling (MTI 8-channel battery analyzer) from 0.01 V to 3V (vs. Li/Li^+) at 1 C and 2 C for 50 cycles. Rate capability of the Si-based electrodes was tested by charging and discharging the cells at the current density order of 0.1 C, 0.5 C, 1 C, 2 C, 5 C and 0.1 C for 10 cycles at every step. Cyclic voltammetry (CV) (PARSTAT MC system) in a potential window of 0.01 V to 3 V vs. Li/Li^+ at a scan rate of 0.1 mV/s was performed to investigate the charge and discharge profiles.

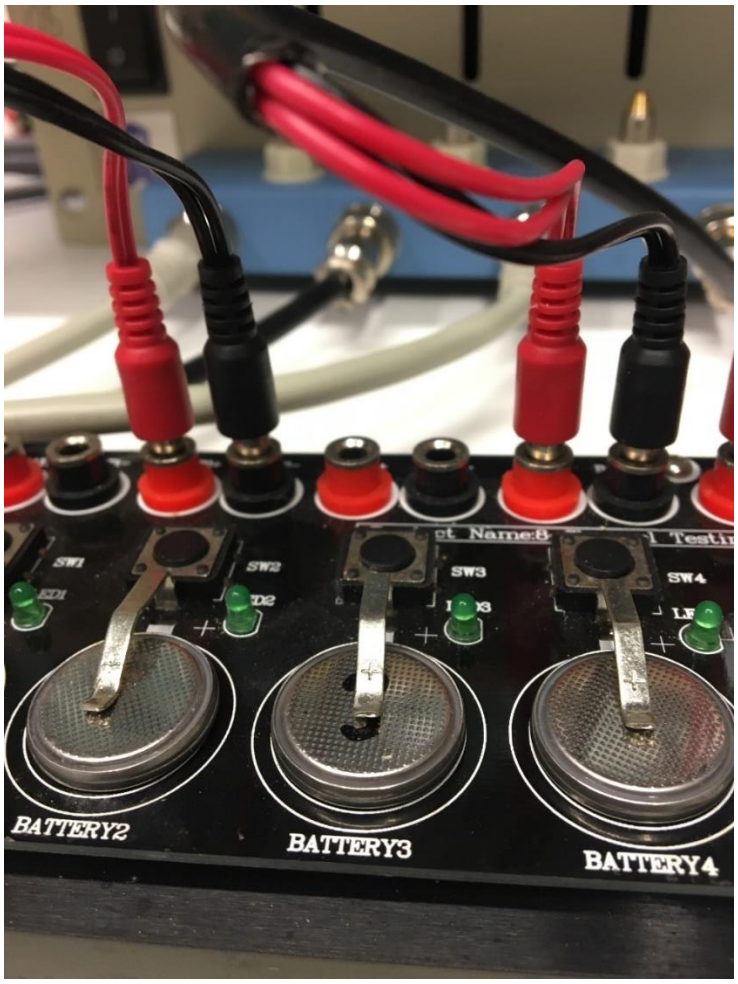

Figure 2. 28. Prepared coin cells for charge/discharge tests

2.4.3. Results and Discussion

2.4.3.1. Sample synthesis and crystal characterization

In a standard magnesiothermic reaction, SiO_2 is reduced to Si with the following reaction (1) [312]:

$$SiO_2(s) + 2Mg(g) \rightarrow Si(s) + 2MgO(s) \quad (1)$$

However, depending on the reaction conditions, some by-products that reduce the yield can also be produced. The side reactions are as follows (2) & (3) [312, 313]:

$$2Mg(g) + Si(s) \rightarrow Mg_2Si(s) \quad (2)$$

$$SiO_2(s) + 2MgO(s) \rightarrow Mg_2SiO_4(s) \quad (3)$$

Depending on the Mg:Si ratio, reaction temperature and duration, unwanted Mg_2Si and Mg_2SiO_4 by-products can form. The most reliable way to determine the purity of the final material is using XRD characterization. The reduction degree of silica particles and the purity of the Si sample was determined according to the XRD results shown in Figure 2. 29 a. At the end of the reaction before washing with the acid solution, it was noted that the sample mainly contained Si with MgO and a little portion of unreacted Mg. However, other by-products such as Mg_2Si or Mg_2SiO_4 were not detected in the medium. It is reported that at high temperatures (900 ºC) the production of these by-products can be minimized [313]. In our case, at a relatively moderate temperature of 670 ºC, Si NPs were synthesized without any unfavorable by-products from the side reactions. One factor that helps to avoid these side reactions is the particle size of the material which is a crucial parameter for this reaction. Starting the reduction process with nanosized silica helps in reducing the generation of by-products. Moreover, the Mg:Si ratio also determines the side reactions [314] as a high amount of Mg in the Mg/Si mixture leads to the formation of Mg_2Si. In conventional magnesiothermic syntheses, a bomb reactor is used [315]. This creates a relatively higher Mg gas pressure and may lead to the formation of side products. However, in our case, the magnesiothermic reaction proceeded under Ar flow in a tubular furnace. This effectively reduced the Mg pressure and eliminated the production of the side products. According to the XRD results, the Mg:Si ratio used in this study was appropriate to our Si purity requirement.

After washing with the acid solution, MgO and Mg were removed from the medium and as seen in the XRD pattern, we obtained pure Si (Figure 2. 29 a (upper pattern)). The diffraction pattern shows four sharp characteristic XRD peaks of crystalline Si at 2θ = 28.5° (111), 47.3° (220), 56.1° (311) and 69.1° (400) [316, 317]. The peak positions are in perfect agreement with the standard values of a face-centered cubic crystal structure (Fd-3m) (ICDD 01-077-2108). This type of silicon crystal is a common structure after a magnesiothermic reduction of silica [318].

The other important component in the hybrid material is rGO which was obtained by thermal reduction of GO. According to the x-ray diffraction pattern, GO has a characteristic peak at 11.2º. This peak is a result of the oxygen groups present at the carbon sheet and corresponds to the (001) peak of GO [319]. When thermally reduced at 900 °C, the (001) peak of GO disappears and a peak at 26.2º starts to appear. The corresponding peak fits the (002) peak of rGO and indicates the existence of sp^2

hybridized carbon sheets. It is concluded from the XRD pattern, that after thermal reduction, GO is successfully reduced to rGO. Since the material is used for covering the Si NPs, the number of layers stacked together into the rGO flakes is an important factor when considering an efficient coating. Using the information from the XRD results, an estimate of the number of layers can be obtained by Debye-Scherrer equations (4) & (5) [320, 321]:

$$LC = (0.89*\lambda) / (B002*\cos(\varphi 002)) \quad (4)$$

$$N = LC / d002 \quad (5)$$

In these equations, N gives the number of layers, LC is the stacking height, λ is the radiation wavelength, B002 is the FWHM (in radians), d002 is the d-spacing of the (002) planes, and φ002 is the scattering angle. According to these equations, the number of graphene planes is about 4, which is just enough for a good coating of the Si NPs.

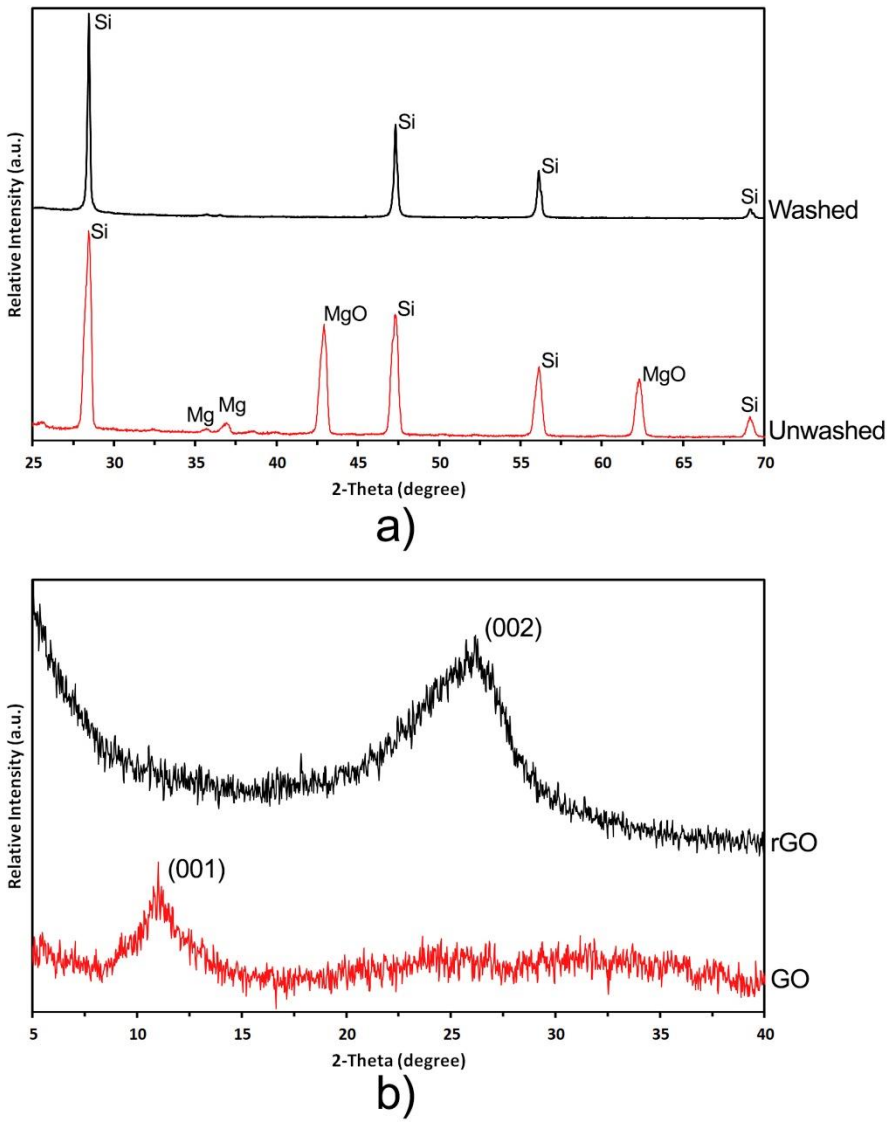

Figure 2. 29. XRD graphs of a) Si NPs before and after acid washing, b) GO and thermally reduced rGO.

Raman analysis can provide valuable information about Si and graphene-based samples. For this purpose, separate analyses were performed for Si NPs, GO and rGO. As shown in Figure 2. 30 a, a deconvolution of Raman spectrum of the synthesized Si NPs revealed two contributions: (i) a wide peak located around 507 cm^{-1} that represents a defective crystalline phase, and (ii) a sharp peak centered at 518 cm^{-1} which is attributed to the crystalline phase (the transverse optic mode) [322, 323]. In some silicon Raman spectra, a peak positioned near 480 cm^{-1} can be found. This peak is considered to be a transverse mode of amorphous silicon [324]. In our sample, no amorphous phase was present which is an expected result for a magnesiothermic synthesis. By considering the deconvolution of the spectrum, the percentage of the defective crystalline phase was found to be 52.8 %.

In effect, the defective crystalline phase comes from the nano-sized Si particles [314, 325, 326], which, by reducing the anisotropic expansion of bulk Si, can improve the resistance to pulverization [327].

In Figure 2. 30 b, the Raman spectra of GO and thermally reduced GO (rGO) are displayed. These spectra show D and G-bands that are typical of graphene-based materials and appear around 1343 and 1594 cm^{-1}, respectively [328, 329]. The G-band represents the vibration of the sp^2-hybridized carbon atoms in a two-dimensional hexagonal graphene layer. On the other hand, the D-band corresponds to the in-plane stretching modes of C-C sp^2 sites [298]. The I_D/I_G ratio provides a measure of disorder in graphene structures as the D-band essentially corresponds to a lack of long-range periodicity and defects in the structure, whereas the G-band is a characteristic Raman peak representing crystalline graphite. I_D/I_G of our GO sample is 0.91 whereas that of thermally reduced rGO is 1.02. Since the I_D/I_G can be essentially expressed as the sp^3/sp^2 carbon ratio [330], an increase in its value is associated with a decrease in crystallinity of graphitic materials. Additionally, it shows the enlargement of sp^2 domains [328]. Therefore a higher I_D/I_G ratio of thermally annealed GO indicates that some structural changes, such as disorder in the orientation of graphene layers, reduction of oxygen groups and a decrease in the number of graphene layers [331, 332] have taken place.

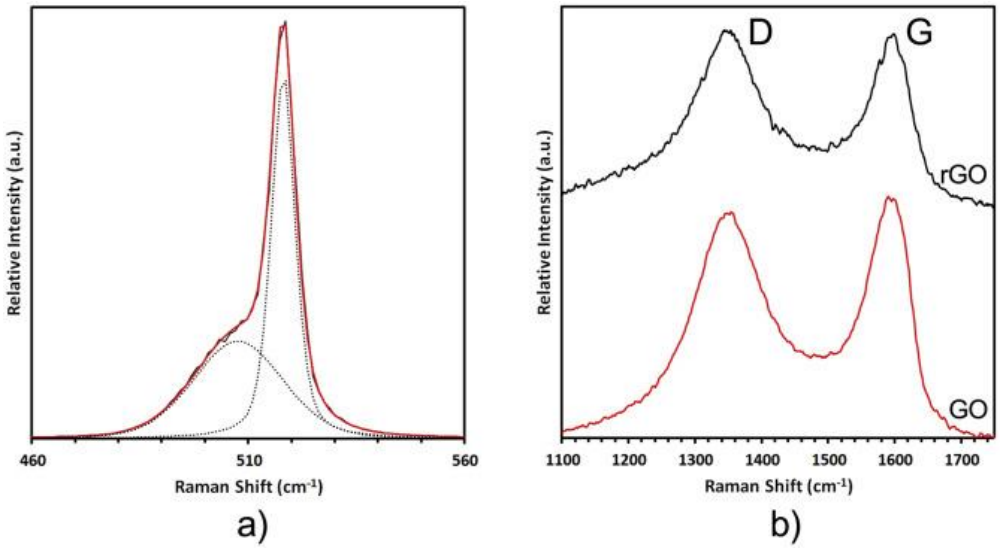

Figure 2. 30. a) Deconvoluted Raman spectra of the synthesized silicon powder, b) Raman spectra of GO (red) and rGO (black).

2.4.3.2. Morphological characterization

The hydrolysis of sodium silicate in an acidic medium is a common chemical route to obtain spherical silica nanoparticles through a gelation reaction and subsequent drying. Size and morphology of the silica nanoparticles achieved by gelation are sensitively affected by reaction conditions such as pH and temperature of gelation. Therefore, parameters such as time, temperature, pH, and stirring require close attention to synthesize the appropriate size and morphology of silica nanoparticles which are later reduced to Si NPs. After the synthesis at 40 ºC and a pH of 4, the dried SiO_2 powder consisted of agglomerated spherical particles having a diameter between 60-80 nm (Figure 2. 31 a). We obtained the most desirable size and shape of particles in the least time at a pH of 4, which is considered the optimum pH for the synthesis of smaller silica particles in an acidic medium [310]. The particle size was also found to be consistent with data from literature which provides a range of 5-2000 nm for silica particles depending on the synthesis conditions [333, 334].

After the synthesis of a dry white silica powder, the material was reduced to Si using a magnesiothermic reduction reaction. In the literature, utilizing magnesiothermic reaction for Si synthesis is a common method. In most of these studies, SiO_2 or Si is accompanied with a carbon material to overcome the drawbacks of Si. Some studies, for example, start with GO; synthesize SiO_2 on GO and finally reduce it to rGO/Si. Though this is a simple method to to obtain the hybrid material, due to sintering along the heating process, the final product may not have very small Si particles and the resulting structure contains too much graphene which hinders real-life applications. Although in these structures Si nanoparticles are supported by rGO, they are still in direct contact with the electrolytic environment, paving the way for an unstable SEI. Kannan et al. synthesized a similar material and their structure contained tightly packed Si nanoparticles with a diameter above 100 nm on graphene [335]. Even though the size of the Si nanoparticles on rGO can be reduced to 25 nm by careful modification of the synthesis conditions, the Si particles, regardless of their size, are still directly exposed to the electrolytic environment, thus after some cycles, the capacity is bound to drop [336].

The technique followed in this study was a direct reduction of SiO_2 particles. The synthesis method is fairly simple and flexible which allows an easy scale-up and also uses less graphene in the final structure. The particle size can be easily reduced with sonication

and dispersed in the medium. As expected from the method, the final product in powder form was prone to particle agglomeration, a behavior which depends on how thoroughly the synthesized particles are washed. XRD, Raman and SEM images of the powder revealed that spherical Si nanoparticles were successfully synthesized after the reduction of the silica particles (Figure 2. 29 a, Figure 2. 30 a, Figure 2. 30 b). It is noted that due to the high surface interactions, in dry form, the individual particles are agglomerated into micrometer-sized clumps. However, multiple washes with DI water followed by thorough stirring and sonication in NMP made it possible for the Si NPs to disperse uniformly into discernable spheres of sizes 30-40 nm. When suspended in NMP along with carbon black, and sprayed on a layer of rGO, the Si NPs, as seen in Figure 2. 30 c, dispersed much more efficiently into observable particles. Furthermore, since the sprayable Si NP slurry also contained CB particles, when sprayed and dried on the copper foil, they acted as barriers against re-agglomeration of Si particles upon drying. The randomly distributed carbon black particles help to prevent agglomeration after the solvent evaporates, forming a Si NP layer with scattered CB particles which also contribute in improving the electronic conductivity. To ensure that the rGO sheets and Si particles were being arranged in layers instead of mixing in a haphazard fashion, we obtained SEM images of two layered (rGO-Si) and three-layered (rGO-Si-rGO) electrodes in Figure 2. 30 c, and e respectively. The electrode with Si + CB slurry on top in Figure 2. 30 c revealed a porous layer of spherical nanoparticles with no apparent signs of the bottom rGO layer in the form of graphene sheets/flakes; as expected, micrometer-sized CB particles were also observed scattered among the Si particles. Figure 2. 30 e shows a three-layered electrode structure (rGO layer on top). Evident from its flaky appearance and the absence of spherical NPs on the surface, the last rGO film efficiently blankets Si particles of the layer below. A sandwich structure like this helps to promote a stable SEI layer as well as cushions Si expansion. It is worth noting here that the topmost rGO film was sprayed to ensure a thick enough coating that can efficiently cover all the Si NPs under it. To achieve that thickness, 1.4 and 0.7 mg/cm^2 of rGO was sprayed on the top and bottom layers respectively. In Figure 2. 30 d an rGO-Si-rGO electrode with less amount of rGO coating is shown. In this case, the surface of Si NPs is not covered completely which exposes them to the environment and provides poor protection from the effects of volumetric expansion.

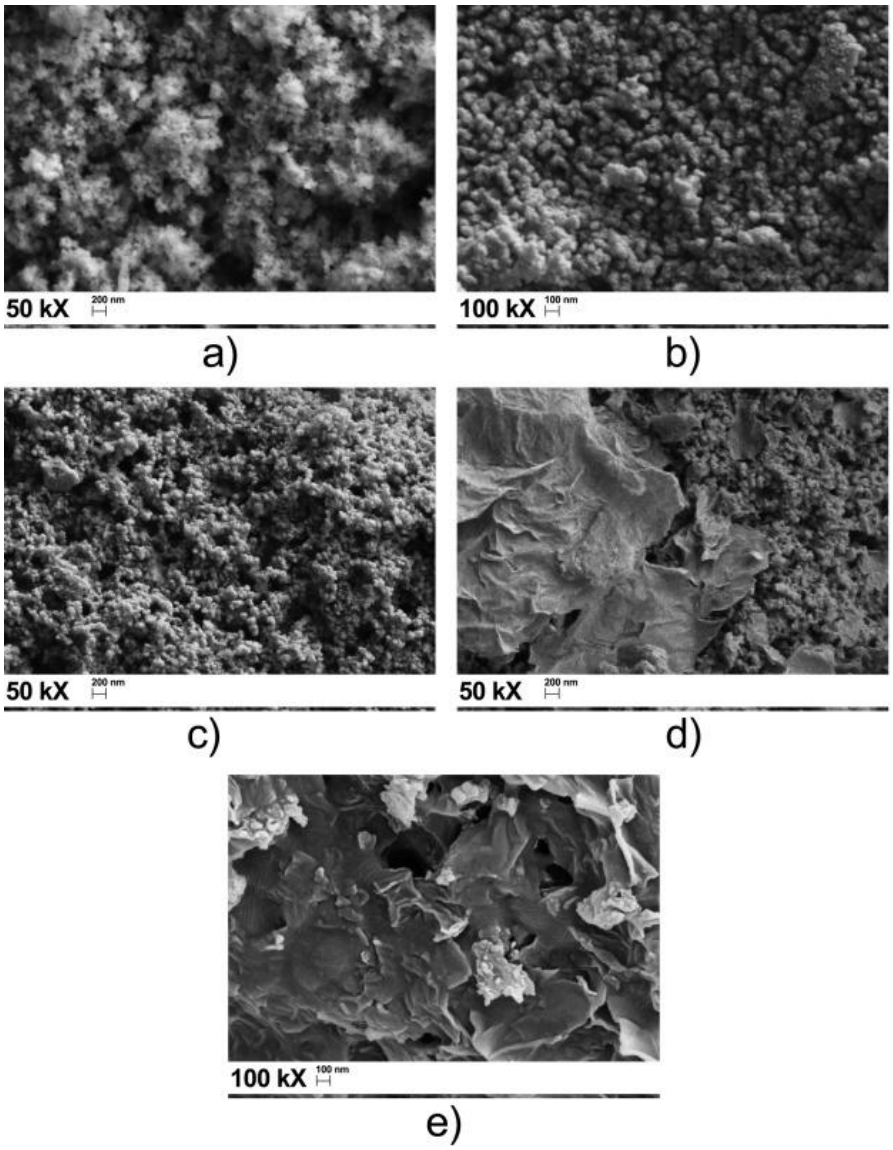

Figure 2. 31. SEM images of a) synthesized SiO_2 and, b) Si powder, c) a two-layer rGO-Si electrode with a topmost layer of Si slurry, d) three-layered rGO-Si-rGO electrode with half the amount of rGO on the top, e) three-layered rGO-Si-rGO electrode showing a thicker topmost layer of graphene completely covering the Si layer.

2.4.3.3. Electrochemical characterization

To evaluate the performance of the hybrid electrode as a Li-ion anode, we did some electrochemical characterizations. In Figure 2. 33 a the cyclic voltammograms (CV) of the rGO-Si-rGO electrode between 0.01-3.00 V vs. Li/Li^+ with a scanning rate of 0.1 mVs^{-1} is displayed. Initially, the cathodic part of the scan, an irreversible broad peak located below 1.0 V was observed. This peak disappeared after the first cycle and it is the

result of electrolyte decomposition and SEI formation [335, 337]. Although not visible in the first cycle due to this broad peak, in the following cycles a peak around 0.2 V can be seen. This peak is described as the lithiation of the Si NPs [338]. In the anodic branch, another broad peak around 0.4 V was observed and this corresponds to the delithiation of LiXSi alloy [336]. After the first cycle, the redox peaks have similar attributes, and this indicates a good reversibility of the hybrid electrode.

Figure 2. 33 b shows the 1st, 5th, and 10th charge and discharge profiles of the rGO-Si-rGO electrode at 0.1 C in the potential range of 0.01–3.0 V. The hybrid electrode shows typical Si alloying and dealloying reaction profiles. The calculated initial specific discharge and charge capacities of the hybrid electrode based on rGO and Si NPs are 2611 and 2446 mAhg^{-1}, respectively. Usually, with Si-based anodes, the initial Coulombic efficiencies are low. The reasons for low efficiencies and high capacity drops are related to highly exposed electrode surfaces and instability of the SEI layer due to the expansion [336, 339], however, when the silicon is completely covered the CE increases. Xiao et al. showed that with increasing carbon coating thickness the initial CE can reach to values above 90 % [340]. On the other hand, when the silicon particles are only supported but not covered with graphene, the initial CE can be as low as 50 % [336, 341]. The hybrid electrode prepared in this study has a graphene layer that completely covers the Si NPs. This structure facilitated in obtaining a high initial CE of 93 %. Additionally, the charge-discharge profiles do not show a significant plateau due to nano-sized and well dispersed Si particles. After the 5th and 10th cycles, the specific discharge capacities dropped to 2057 and 1967 mAhg^{-1}, respectively. When compared with similar structures, the hybrid material showed a 21 % lower irreversible capacity loss [338]. On the other hand, in the electrode without any rGO layers, the performance was considerably worse (Figure 2. 32).

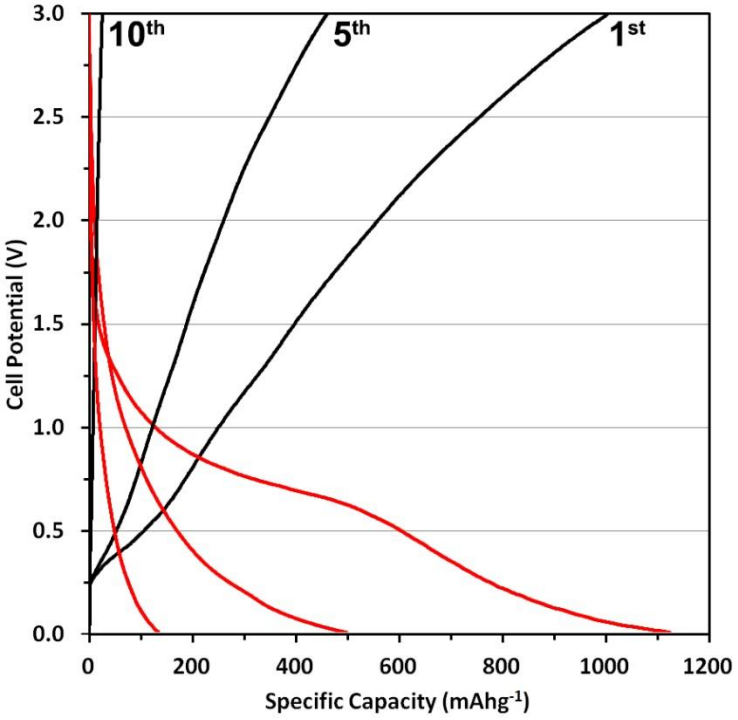

Figure 2. 32. Shows the charge-discharge profiles of bare Si electrode at the 1st, 5th, and 10th cycles.

With lower coulombic efficiency and lack of protection, the specific capacity decreased rapidly. After the 10th cycle, the bare Si cell almost failed and delivered a specific discharge capacity of 50 $mAhg^{-1}$. The complete coverage of Si NPs can prevent unstable SEI formation and Si pulverization which in return reduces irreversible capacity loss. Another factor that helps that attribute is the presence of defective crystalline Si particles which provides a better resistance against expansion.

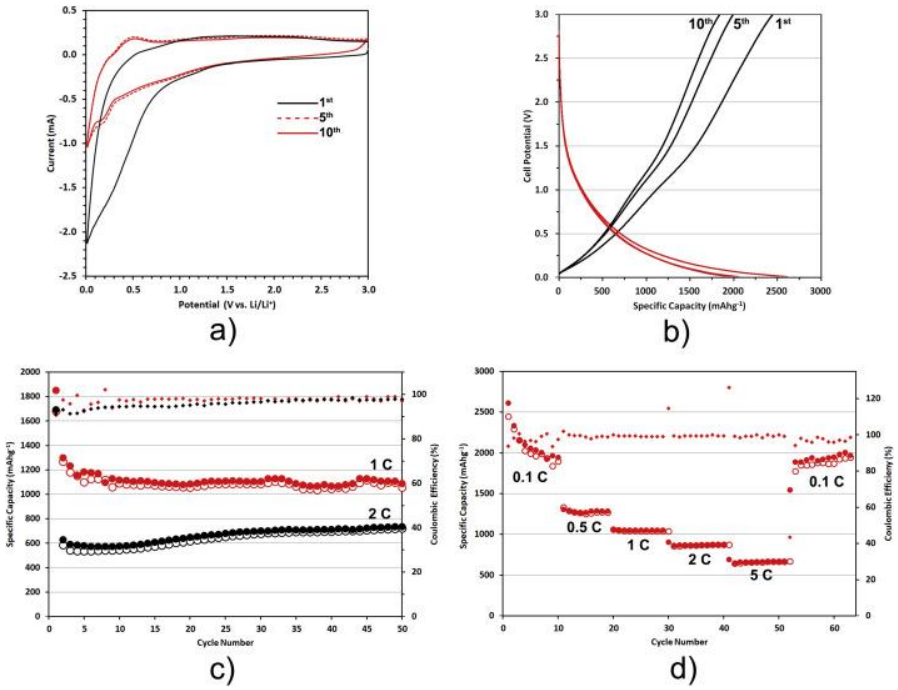

Figure 2. 33. (a) Cyclic voltammograms of the 1st, 5th and 10th cycles. (b) Charge-discharge profiles of the 1st, 5th, and 10th cycles. (c) Charge and discharge specific capacities at 1 C (red) and 2 C (black) for 50 cycles. (d) Rate capability test at 5 different current densities.

The cycling performance of the hybrid electrode was tested at 1 C and 2 C currents between 0.01 and 3 V (Figure 2. 33 c). At the first cycle, the rGO-Si-rGO electrode had a specific discharge capacity of 1853 and 1693 $mAhg^{-1}$ at 1 C and 2 C respectively (based on rGO and Si NPs). For 1C, after the 10th cycle, the capacity stayed above 1070 $mAhg^{-1}$. On the other hand, for 2 C, initially we observed a significant capacity drop but with increasing cycle number, the capacity increased and stabilized after the 40th cycle at about 720 $mAhg^{-1}$. For both of the cases, the coulombic efficiency reached 98 % after the 10th cycle. As discussed above, the complete coverage also enabled a stable SEI formation and resulted in a highly reversible electrode. Conversely, the electrode with bare Si particles showed a very mediocre result (Figure 2. 34). In 10 cycles the capacity dropped from 1123 to 50 $mAhg^{-1}$. As a matter of fact, this is a common situation for Si-containing anodes without any protective layer. The cycling performance tests prove that with a simple spray assisted layer by layer coating and drying process a very durable Si anode can be produced. In Table 2. 4, the cycling behavior of our rGO-Si-rGO hybrid structure is compared with other graphene silicon composites prepared with layering and/or spraying. All of the studies report very similar superior performances, which shows the

positive effect of layering and/or spraying has on the specific capacity. However, when the techniques are considered, most studies use either very complex or time-consuming processes. In this study, we employed a relatively easier technique that as a process can be employed in large-scale manufacturing applications with lower cost and effort.

Table 2. 4. Comparison with previous Si anode studies

Sample	Current Rate	Capacity*	Reference
Electrosprayed sandwich of Si/CNTs with rGO	0.1 A/g	900	[247]
Sprayed mixture of rGO and Si	0.2 A/g	1041	[342]
Spray pyrolized rGO and Si mixture	0.2 A/g	1000	[242]
Dip-coated alternating layers of rGO and Si	1 C	1500	[244]
Alternating rGO-Si-rGO layers	1 C	1089	This Study

*Capacities are approximate values at the 50th cycle

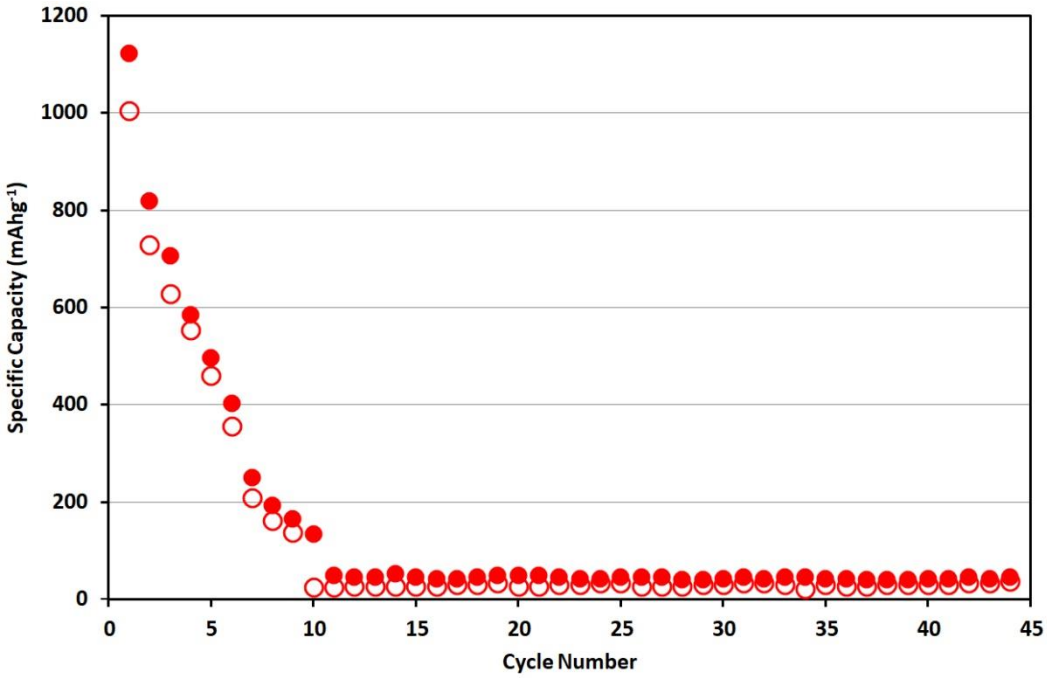

Figure 2. 34. Shows the charge and discharge cycle of bare Si at 1C

Figure 2. 33 d shows the rate capability test of the rGO-Si-rGO electrode between current rates of 0.1 C-5 C. During the first segment of the test, where the current rate is 0.1 C, the specific capacity drops from 2611 to 1945 mAhg^{-1}. After increasing the current rates to

0.5 C, 1 C, and 2 C, the specific capacities were measured as 1284, 1050, and 879 $mAhg^{-1}$, respectively. Moreover, at a current density as high as 5 C, the specific capacity stayed stable at a value of 672 $mAhg^{-1}$. After switching back to 0.1 C, the specific capacity reached 1887 $mAhg^{-1}$ (corresponds to 97 % capacity recovery). The results reveal that the hybrid has a good rate capability. Furthermore, even at high current rates, the capacities stay almost constant which is a good sign of stability showing that spray coating the Si NPs minimizes the detrimental effects of expansion. The efficient covering of Si NPs with rGO suggests that the sandwich-like anode could withstand rigorous Si expansion through varying current densities and still maintain the structural integrity, hence giving a steady and reliable performance with high capacities and stability (with CE of above 97 %).

In a spray-dried layer by layer structure such as ours where Si NPs are sandwiched between layers of rGO sheets, several factors help improve the capacity and cyclic performance. First, the entrapped Si find ample but buffered space under strong and flexible rGO sheets to allow for a less lethal expansion. Second, nanosizing Si minimizes the mechanical strain induced by volume change [231]. Third, spray coating the electrode with a controlled flow rate and a constant low heat (50 ºC), allows the droplets to spread on the substrate [343] before the solvent (NMP) evaporates. This has two effects: (a) it helps form a thin and discernable layer by layer structure as compared to other slurry coating methods (doctor blade etc.), and (b) a low controlled mass loading maximizes the utilization of active material in the anode [247], contributing positively to the total capacity.

2.4.4. Conclusion

A facile, cost-effective, and scalable anode fabrication method based on spray deposition of alternate layers is developed to fabricate stable and high capacity graphene-silicon hybrid anodes for LIBs. The presence of spherical silicon nanoparticles as the active material minimizes the destructive impact of volumetric expansion upon lithiation. Embedding these Si NPs between two layers of sprayed rGO sheets maintains the anode's structural integrity, promotes electronic and Li^+ conductivity and encourages a durable SEI layer between the electrode-electrolyte interface. The spray dried sandwich-like structure demonstrates excellent specific capacity (1089 mAh g^{-1} after 50 cycles at 1 C) and a minimum CE of 97 %. Spray drying a sandwich-like structure is a time and cost-

effective method because it utilizes the active materials efficiently in a controlled fashion. This facile method, therefore, simplifies the anode fabrication process of stable LIBs based on graphene and silicon for high capacity applications. For commercial Li-ion battery production, every step is critical and affects the cost. Especially where nanomaterial additives are involved, the production can be so costly and difficult that bulk production may not be feasible at all. From that point of view, the combination of techniques used in this study offers an applicable and comparatively cost-effective method to incorporate Si and graphene-based materials into commercial Li-ion battery anodes.

CHAPTER 3. INVESTIGATION OF LiI EFFECT ON THE BATTERY PERFORMANCE OF CEO_2 CATALYST NANORODS DECORATED NrGO AIR CATHODE FOR Li-O_2 BATTERIES

3.1. Introduction

Li-oxygen (Li-O_2) batteries are promising energy systems confronting energy challenges soon due to the gradual depletion of fossil fuels. Even though lithium-ion batteries and supercapacitors are widely commercialized energy storage systems to power portable electronic devices, they suffer from relatively lower energy and power densities to compete with any internal combustion engine. Unlike the lithium ion batteries (LiBs), they have an open-cell architecture enabling cathode active materials to receive oxygen from the ambient atmosphere and generating energy by the decomposition/formation of Li_2O_2 during charge/discharge steps. Nevertheless, all of the components of metal-air batteries are still being under development [88]. Li-O_2 batteries exhibit an ultra-high energy density to power electric vehicles and which can compete with gasoline-powered engines. Li-O_2 has a theoretical energy density of around 11 586 $Whkg^{-1}$ based on the mass of Li metal alone and 3505 $Whkg^{-1}$ with the mass of Li and Li_2O_2 for a non-aqueous battery [344, 345]. This corresponds to ten times higher energy density than conventional Li-ion batteries (LiBs) [346]. On one hand, lithium anode materials play a crucial role in lithium-oxygen battery owing to its low redox couple potential yielding high capacity and wide potential window [347]. On the other hand, sluggish reaction kinetics of oxygen evaluation reaction [98] of Li-O_2 battery leads to low round-trip efficiency, low reversibility and lack of cycle performance. The main reason for low round-trip efficiency and low reversibility of Li-O_2 batteries is that decomposition of Li_2O_2 requires high charge overpotential which induces side and parasitic reaction products lasting with gradual capacity decrease.

The performance of Li-O_2 battery rather depends on the stability of the electrolyte, reduction of overpotential between charge/discharge steps, Li anode cycle with low corrosion, and effectiveness of the catalyst material employed in air cathode for oxygen reduction. As for the electrolytes, a combination of almost all Li salts and solvents was attacked by highly reactive oxygen species ($O^{2\bullet-}$, LiO_2, O_2^{2-}, LiO_2^{-}), which severely decompose both the cathode and Li metal anode yielding insoluble passivating

precipitates (e.g. Li_2CO_3) accumulate in the electrolyte. A stable electrolyte can be constructed based on Pearson's Hard Soft Acid-Base (HSAB) theory providing explanations for the solubility of Li^+ and O_2^- species, and compatibility of solvent to Li salt [101]. Based on HSAB, two growth models - surface-growth model and solution-growth model - were offered in the literature via reasonable explanation and solid characterization to prove little details of O_2 reduction pathways to form Li_2O_2. On one hand, the surface growth model suggests that superoxide species $O_2^{\bullet-}$ and/or LiO_2 first adsorb on cathode surface then receive a second reduction reaction to form Li_2O_2 resulting in the formation of a thin film layer of non-conductive Li_2O_2 on the cathode surface with a thickness of around 10 nm and lower. On the other hand, the solution growth model proposes that LiO_2 can be generated and dissolved within the electrolyte, then undergoes chemical disproportion reaction spontaneously and finally forms large toroidal Li_2O_2 crystals around 1-2 μm size. Clearly, the solubility of LiO_2 and Li_2O_2 formation via solution growth pathway strongly increase cell capacity and cyclicity which can be achieved by wise selection and design of electrolyte with high donor number similarly reported by Johnson et al.[107]. Alternatively, dimethoxyethane (DME), dimethyl sulfoxide (DMSO) and acetonitrile (MeCN) were proved to be a good candidate as Li-O_2 batteries electrolyte solvents according to the recent researches [111]. Bruce et al. [120] reported that ether-based solvents exhibit more stability to the nucleophilic attack of superoxide species due to its long chain and lower vapor pressure. To conclude the solvents competition, tetraethylene glycol dimethyl ether (tetraglyme or TEGDME) proved to be a more stable solvent for this type of battery. Moreover, both lithium bis(fluorosulfonyl)imide (LiTFSI) and lithium trifluoromethanesulfonate (Litriflat, LiTF) were mostly employed with TEGDME solvent for the electrolyte to be used in Li-O_2 battery giving more or less similar results stability within the proper ether based electrolyte solvent [104]. Redox mediators can be described as soluble catalyst species to promote decomposition of Li_2O_2 even in the case of poor direct contact between cathode and Li_2O_2, which is assumed to be the main reason for high charge overpotential, high cell impedance and sluggish kinetics of cell chemistry. Redox mediators generally have redox potential higher than required decomposition potential of Li_2O_2 (2.96 V vs. Li^+/Li) so that they can provide required charge transfer between Li_2O_2 and cathode to reduce overpotential. So far, ferrocenes, 5-di-tert-butyl-1,4-benzoquinone (DBBQ), 2,2,6,6-tetramethyl-1-piperidinyloxy (TEMPO), dimethylphenazine (DMPZ), tetrathiafulvalene

(TTF) and lithium iodide (LiI) are proved to be a good redox mediator claiming high efficiency and rechargeability of Li-O_2 battery with substantial capacities [113-116]. Briefly, performance of Li-O_2 is increased by using a high donor numbered electrolyte compatible with anode and cathode material, an ideally reversible redox mediator (RM) within the electrolyte, and a catalyst material on the cathode.

The cathode is the main component of Li-O_2 batteries facilitated by molecular oxygen involving in oxygen reduction reaction (ORR) and oxygen evolution reaction (OER). In this regard, carbon materials were proposed to be the main materials as the catalyst to reduce oxygen and to employ high currents due to their high specific surface area, porous structure, and electronic conductivity properties, which provide great charge storage and high Li_2O_2 hosting ability. Besides, they demonstrate enhanced gravimetric energy density thanks to their low-density nature. In this aspect, carbon black, activated carbon, super P, ketjen black, reduced graphene oxide, and graphene nanoplates were studied as main catalyst materials for Li-O_2 batteries [348]. Similar to those carbonaceous materials, nitrogen-doped reduced graphene oxide (NrGO) can also supply numbers of catalytic sites and improve the catalytic activity for oxygen reduction reaction (ORR), as proved in Ping Chen et al. report [349]. Bare carbon materials tend to degrade the cathode and electrolyte by initiating parasitic products that passivate the active catalytic sites. For that reason, carbon-free materials like metal oxide catalysts and their composites with carbon materials were studied to balance reaction kinetics and decrease the parasitic reactions. Several types of carbide and transition metal oxide were reported as promising candidates' materials in the cathode, including TiC, Mo_2C, Ti_4O_7, MnO_2, Co_3O_4, Fe_3O_4, Fe_2O_3, NiO, and CuO, NiO, V_2O_5, MoO_3, Y_2O_3, RuO_2 and Ir_2O_3 as cathode catalysts for Li-O_2 batteries. Mingrui Liu et al. studied Ru loaded 3D N-doped reduced graphene oxide demonstrating high active site density and high ORR/OER activity for high-performance air cathode in Li–O_2 batteries [161, 350-355].

Ceria (CeO_2) has been partaking in numerous catalytic application such as water gas shift reactions [356], UV blocking [357], electrochromic thin films [358], UV absorbent [359], solid oxide fuel cells [360] and oxygen sensors. Ceria is a very versatile material due to its excellent redox property, providing the ability to shift easily Ce^{4+} to Ce^{3+}. This leads to a change in oxidation states and the number of oxygen vacancy defects by minimal activation energy. In this sense, ceria is both reductant and oxidant according to change in its oxidation state with respect to chemical reaction in process. Moreover, the catalytic

property of ceria is directly related to its oxygen storage capacity (OSC), which means the number of oxygen vacancies that the crystal structure can host [361]. Ceria can be synthesized with several different morphologies, such as nanocubes, nanotubes, nanorods, nanowires, microplates, and octahedra [362-364]. Ceria nanoparticles usually accommodate octahedral morphology and this morphology consist of (111) crystal plane to minimize its surface energy. On the other hand, ceria nanorods and nanocubes are enclosed by (110) and (100) planes [365]. Crystal planes define the catalytic activity because the activation energy to create oxygen vacancy on the plane surface is different for each of them due to their different cerium and oxygen distribution and oxygen mobility. Among these planes, (110) requires less activation energy to create an oxygen vacancy on the surface than (100) planes. On all these crystal planes, (111) crystal plane has the highest activation energy to create a vacancy [366]. The oxygen vacancies tend to be most abundant in nanorod form and, with its active facets, it leads to the improvement of highly efficient catalytic properties without changing the catalyst composition. According to Wu et al. [367], nanorods exhibit more oxygen vacancies than nanocubes, which is an excellent proof that ceria nanorods are the best choice for catalytic activities among its nanostructures for oxygen reduction reactions.

In this study, nitrogen-doped reduced graphene oxide (NrGO) was synthesized by thermal annealing method by processing GO at elevated temperature in ammonia and argon gas flow. Then, the CeO_2 nanorod catalysts were successfully decorated onto NrGO by a simple hydrothermal process and to the best of our knowledge it was employed as an air cathode for the first time in the Li-O_2 battery application in the literature. Moreover, CeO_2/NrGO air cathode was tested for the first time in LiTF/TEGDME electrolyte, besides LiI was exploited as a redox mediator for the first time for ceria-based air cathode performance (Figure 3. 1). In addition, we aimed to understand the synergetic effect of ceria to NrGO support in terms of battery capacity at different current densities. Furthermore, the influence of LiI on the battery capacity with the different air cathodes was investigated compared to their overpotentials values.

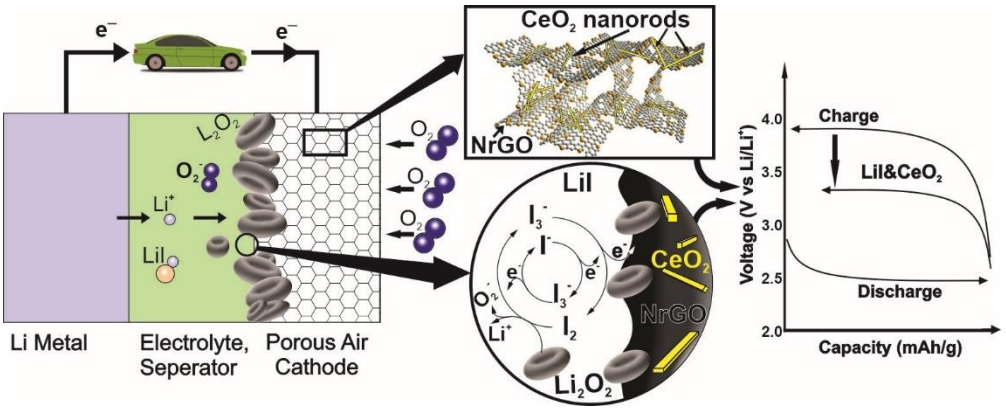

Figure 3. 1. Schematic representation of CeO_2/NrGO air cathode test in Li-O_2 battery

3.2. Experimental Procedures

3.2.1. Materials

Natural graphite flakes (99 %), potassium permanganate ($KMnO_4$, 99 %), sulfuric acid (H_2SO_4, 98 %), phosphoric acid (H_3PO_4), hydrogen peroxide(H_2O_2), hydrochloric acid (HCl, 37 %) were purchased from Sigma–Aldrich for the synthesis of graphene oxide. Cerium (III) chloride heptahydrate ($CeCl_3$ $7H_2O$, 99.99 %), sodium hydroxide (NaOH, ≥97 %), ethanol (C_2H_6O), N-methyl-2-pyrrolidone (NMP, 97 %), lithium trifluoromethanesulfonate (LiTF, 99.9 %), lithium iodide (LiI, 98 %) and tetra ethylene glycol dimethyl ether (TEGDME, 99%) were provided from Sigma–Aldrich as well for the ceria nanorods fabrication, electrolyte and electrode preparation. Carbon paper (AvCarb MGL190) and carbon black (Vulcan XC-72) were purchased from the Fuel Cell Store. A polypropylene separator (PP, Celgard) was used as the separator. All reagents used were analytical grade and employed without further purification.

3.2.2. Graphitic oxide (GO) Synthesis

The graphitic oxide was synthesized by the improved Hummers method. At the first step, graphite flakes, and $KMnO_4$ were mixed then H_2SO_4, and H_3PO_4 emulsion were poured into the mixture. This prepared mixture was continuously stirred further at 70 rpm and 50 °C for 24 hours. A reflux system was mounted to the synthesis system to avoid hazardous toxicity and evaporation of the reactant solution. A brownish slurry was obtained after this step and cooled down in an ice bath. In the next step, the slurry was introduced to the ice and H_2O_2 mixture. Then, an HCl solution was added to the slurry, and the suspension was diluted by adding DI water. The slurry was kept 48 hours in an ice bath. A well dispersed, homogenous, yellowish, acidic suspension of GO was obtained at the end of

this step. The obtained slurry was washed several times with DI water/ethanol emulsion and followed by mixing with just DI water so that pH reached around 5. Finally, the suspension was freeze-dried for four days then collected for further synthesis and characterization.

3.2.3. Nitrogen-doped reduced graphene oxide (NrGO) synthesis

NrGO was produced via using a thermal annealing method within the ammonia gas ambient at elevated temperature. The GO synthesized by the improved Hummers method was heated at 900 °C under ammonia and Ar gas flow in a tubular furnace as displayed in Figure 3. 2. The tube furnace was cooled down to room temperature under continued Ar gas flow. After cooling down, NrGO was obtained and ready for the next syntheses and characterizations.

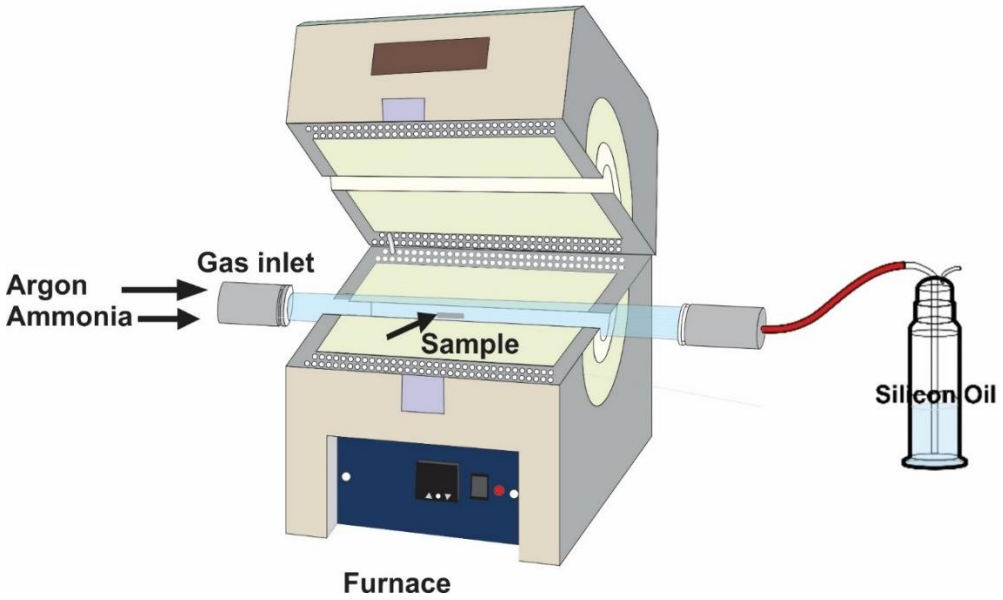

Figure 3. 2. Nitrogen doping and deucing GO by thermal annealing method.

3.2.4. CeO_2 nanorod synthesis

Cerium dioxide (CeO_2) nanorods were synthesized by hydrothermal method. Initially, 100 mL DI water was mixed with 9 M NaOH by a magnetic stirrer. Then 5 mmol of $CeCl_3.7H_2O$ was added to the mixture and stirred for 15 minutes. Subsequently, the mixture was poured into 200 mL Teflon container and sealed tightly in a stainless-steel autoclave. The hydrothermal process was conducted at 100 °C for two days. Afterwards, the sample was slowly cooled down to room temperature and washed with DI water while

filtering via a Buchner setup to reach a neutral pH value. Finally, ceria nanorods were dried for 12 h.

3.2.5. CeO_2/NrGO synthesis

Nitrogen-doped reduced graphene oxide supported cerium oxide nanorods (CeO_2/NrGO) were synthesized with another hydrothermal method. In this regard, firstly, a solution of DI water, ethanol, and NMP were prepared. Then, an NrGO mixture with 3 g/L loading was mixed. Then, CeO_2 nanorods were added to reach a 4.5 g/L loading. Finally, NaOH was added to reach 4.5 M. Afterward, the final suspension was poured into a Teflon lined stainless-steel autoclave. CeO_2/NrGO suspension was hydrothermally heated to 100 °C for 12 h. After the final product was slowly cooled down to room temperature, CeO_2/NrGO was washed with DI water until the pH value neutralized using centrifugation. Finally, ceria nanorods were dried for 12 h and prepared for further use as demonstrated in Figure 3. 3

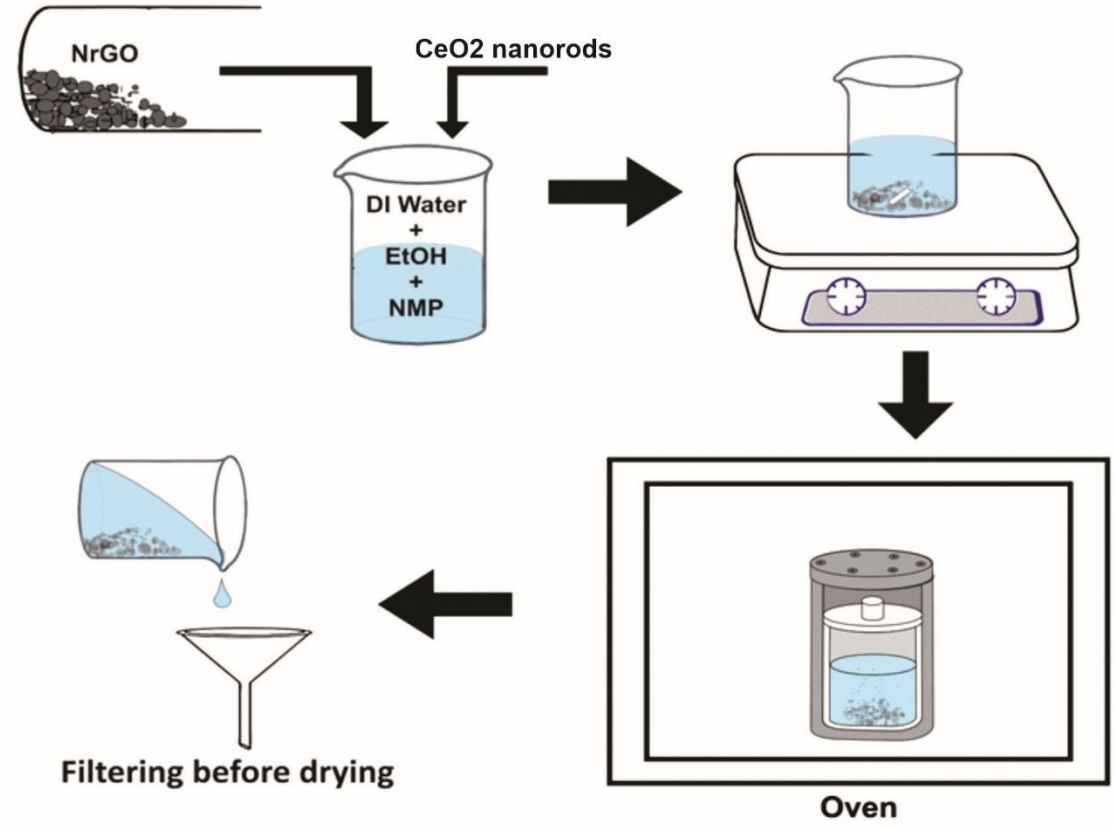

Figure 3. 3. CeO_2/NrGO synthesis by hydrothermal method.

3.2.6. Electrodes and electrolyte preparation

The slurry of active materials for electrode coating was prepared by mixing carbon black as a conductive agent, PVDF as a binder, and active material such as bare NrGO or CeO_2/NrGO in NMP. The slurry was mixed for 12 h by a magnetic stirrer. Then, the slurry was coated onto a carbon paper, and electrodes were dried for 12 h at 120 °C in a vacuum oven. The final mass of active material on the carbon paper was calculated to be 0.5-1 mg/cm^2. The electrodes were hot-pressed for better binding and evaporate of NMP. Finally, the electrodes were transferred in a glovebox for battery assembly.

The electrolyte was prepared through heating LiTF, and LiI powders at 120 °C in the glovebox. Followed by dispersion of 1 M LiTF as Li salt and 0.1 M LiI as redox mediators in TEGDME at 60 °C and leaving the setup for 12 h in the glovebox. The concentration of LiI was introduced as 0.1 M to better observe the effect of redox mediator to the battery test at the first cycles [368].

3.2.7. Battery assembly

A specially designed split cell was used for electrochemical tests that allowed oxygen flowing in and out as presented in Figure 3. 4. Li discs with 15 mm diameter and 0.4 mm thickness were used as the anode and 2 PP (Polypropylene) Celgard were utilized as separators. The cells were assembled in the order of Li chips, separator, coated carbon paper cathode, and stainless-steel mesh via soaking in the electrolyte. The battery cell was purged with pure O_2 and kept in 1 bar during the tests.

Figure 3. 4. Our own special designed Li-air battery test cells

3.2.8. Instrumentation and Characterizations

Powder samples for SEM analysis were placed on a regular conductive carbon tape and coated with Au/Pd for 80 seconds by using the Desk V HP Denton Vacuum coating device. Microstructural morphology analysis was conducted by a Zeiss LEO Supra 35VP Field Emission Scanning Electron Microscopy (FESEM). Ceria nanorods were visualized

with secondary electron detectors by an accelerating voltage of 3 kV and a working distance of about 8 mm. Nanostructural morphologies of ceria nanorods were monitored via a JOEL ARM200 cold FEG transmission electron microscopy (TEM). High-resolution images were obtained by using 200 keV accelerating voltage. The powder sample was first dispersed in DI water and ethanol mixture and dropped onto a copper grid for TEM operation. The powder XRD studies were performed by using a Bruker D2 Phaser X-ray diffractometer device with 1.540 Å Cu K_α radiation source. The diffraction patterns were obtained in the range of 10−90° with a 2θ step size of 0.02° and a step time of 1 s. Raman characterization was operated by a Renishaw Raman spectrometer with 514 nm visible laser source, and analysis was done under ambient conditions. The reported wavenumber values from the spectra are accurate with a sensitivity of 2 cm^{-1}. Decomposition and loading fraction of powders were analyzed by a Netzsch STA 449C thermogravimetric analyzer (TGA) under airflow during the test. Powders were tested to find the mass fraction of ceria to carbon materials with oxygenated functional groups. Samples were heated by 10K increments starting from 30 to 1400 °C. N_2 adsorption isotherms were determined at 77.3 K by using a Micromeritics 3Flex Physisorption instrument to measure samples' specific surface areas and pore size distributions. Bare GO, bare NrGO, bare CeO_2, and CeO_2/NrGO powders were degassed to remove unwanted humidity and surface radicals at 130 ˚C for 24 hours before measurements. Measurements were performed under the N_2 gas relative pressure (P/P_0), increasing from 0 to 0.99. Elemental analyses of powders were collected by Thermo Fisher K-alpha X-ray Photoelectron Spectrometer (XPS) System. XPS data were recorded by using a 400 elliptic radius spot size of Al K_α monochromatic source. Powder samples were placed onto double-sided copper tape on the XPS sample stage, and further spectral investigations were performed.

The data for cyclic voltammograms (CV) and electrochemical impedance spectroscopy (EIS) measurements were collected by using a Princeton Applied Research PARSTAT MC system. The CV data was recorded from 2.0 and 4.1 V (versus Li/Li^+) potential with 0.1 mV s^{-1} scan rate, and the EIS test was obtained in the frequency range of 0.1 Hz and 2 MHz with an AC amplitude of 5 mV. The galvanostatic charge and discharge tests were performed within the potential range of 2.0 and 4.1 V at a range of current densities by using an MTI 8 Channel Battery Analyzer. Specific capacities were calculated based on

the mass of active materials (bare NrGO or CeO_2/NrGO) and carbon black coating on carbon paper.

3.3. Results and Discussions

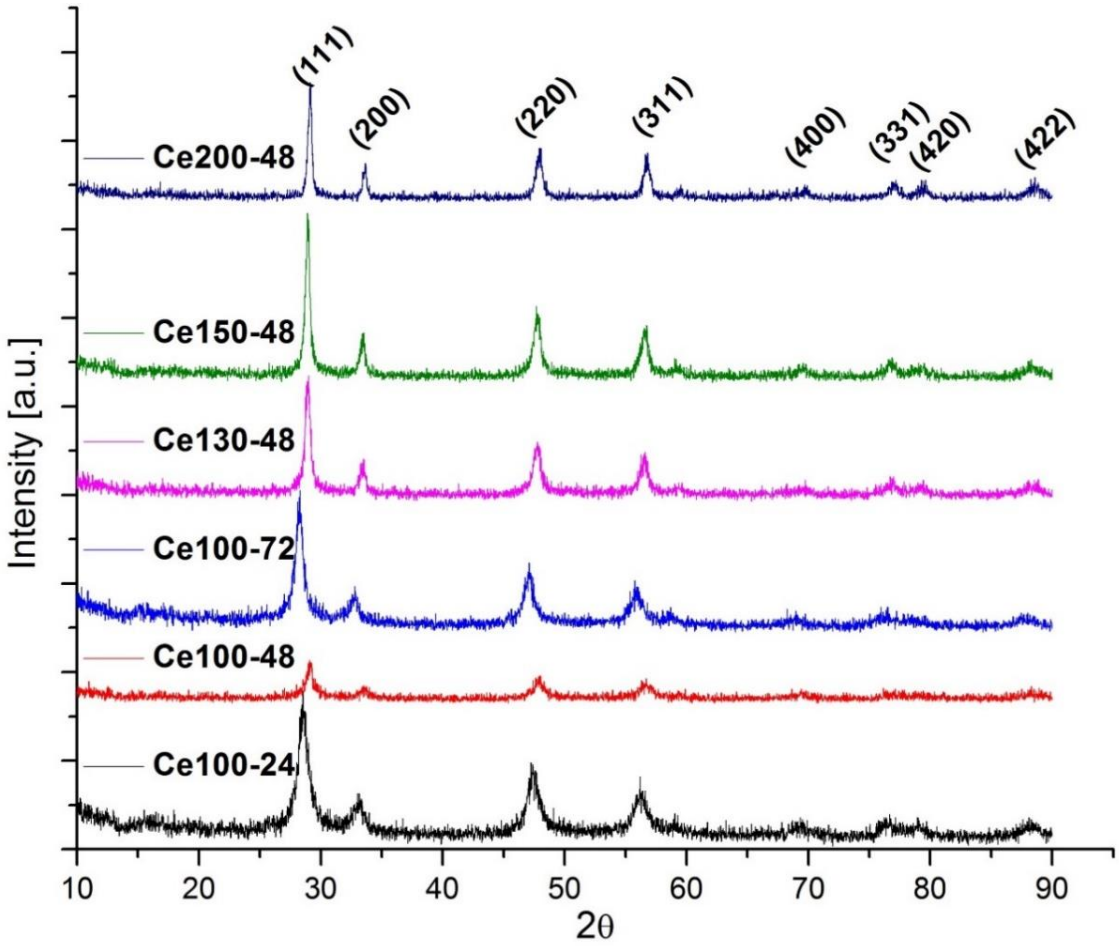

Figure 3. 5. XRD of ceria nanostructures resulting different morphologies by varying time and temperature during hydrothermal method

Time and temperature are the most effective parameters to alter the crystallography and morphology of the nanostructures in hydrothermal synthesis method. Figure 3. 5 shows the XRD analysis of ceria nanostructures synthesis via hydrothermal method by varying time and temperature. The temperature was set as 100, 130, 150 and 200 °C in different synthesis and the duration of the synthesis was changed as 1, 2 and 3 days to optimize synthesis parameters. According to results, all main peaks are consistent with ceria crystal pattern based on pdf no 01-0800. However, 2 theta peaks were slightly shifted according to the change in these two parameters implying that the interplanar distance between

crystalline planes changed. These changes revealed as the changes in morphology, distribution, structural size, agglomerations and homogeneity of nanostructures.

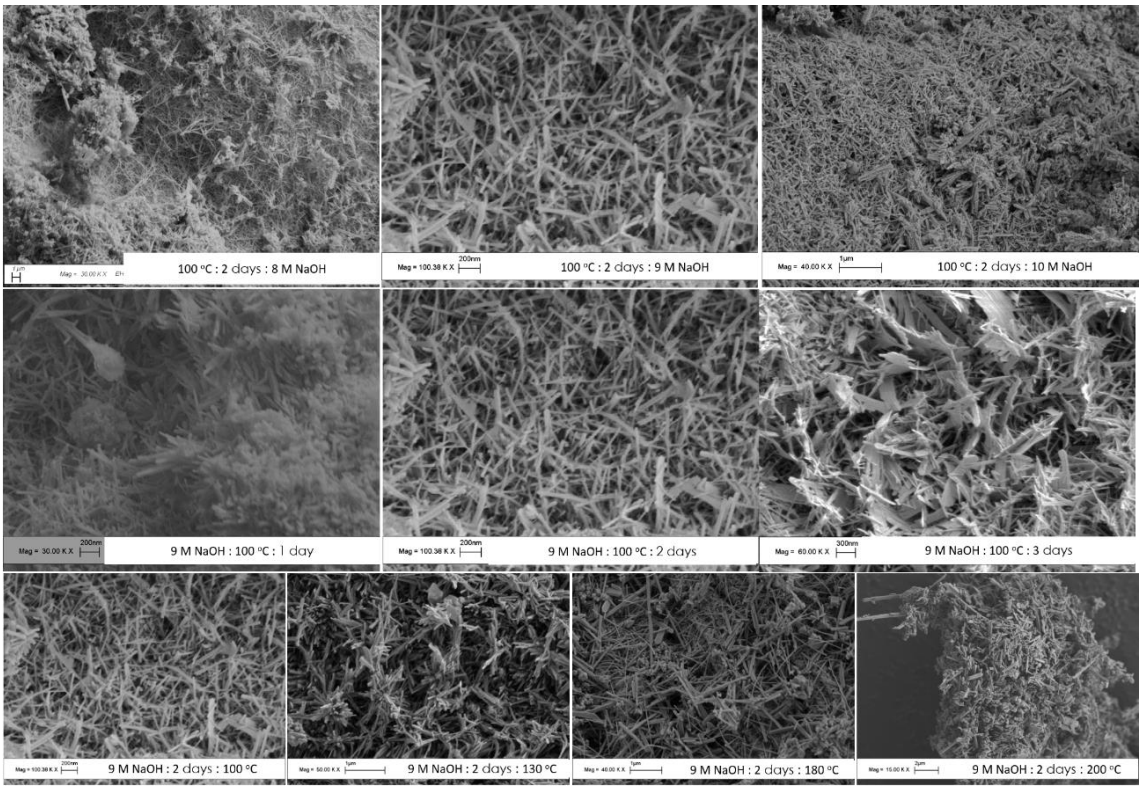

Figure 3. 6. SEM analysis of ceria nanostructures by altering temperature time and concentration of NaOH during hydrothermal method.

As three main experimental parameters of hydrothermal synthesis, the effect of time, temperature and concentration of NaOH were monitored by SEM analysis in Figure 3. 6. The overall morphology, distribution, structural size, agglomerations and homogeneity were generally compared based on the variation of each parameters to each other. In addition, the distribution of nanostructures as well as the length, width and the ratio of length to width (l/w) were reported in Table 3. 1. According to results, ceria nanorods were newly formed at 8 M NaOH concentration with additional nanoparticles and they merged via increase in concentration by 10 M. Based on NaOH concentration, 9 M was revealed the optimum concentration. Additionally, same trend was observed if the time set to 1 day or 3 days resulting initial step of nanorods formation or agglomeration of them respectively. So that, 2 days of synthesis duration was set the optimum value. According to time variation, 100 °C was set as optimum temperature because temperature rise induced bigger nanorods formation, merging or formation of other morphologies. All in all, 9 M NaOH concentration, 2 days of synthesis duration and 100 °C of synthesis

temperature were found to be optimum parameters based on nanorods formation and their homogenously distribution.

Table 3. 1. the width (nm) and length(nm) analysis of ceria nanorods based on Figure 3. 6

Label	**width**	**length**	**l/w**	**9 M NaOH & 100 °C**	**Distribution**
Ce98	35.7	480	13.4	1 day	moderate
Ce117	***23.0***	***443.0***	***19.3***	***2 days***	***good***
Ce112	35.0	818.1	23.4	3 days	bad
Label	**width**	**length**	**l/w**	**100 °C & 2 days**	**Distribution**
Ce125	19.0	604.0	31.8	8 M NaOH	nearly good
Ce117	***23.0***	***443.0***	***19.3***	***9 M NaOH***	***good***
Ce119	30.9	571.0	18.5	9 M NaOH	moderate
Ce123	43.0	477.0	11.1	9 M NaOH	moderate
Ce120	31.7	407.0	12.8	10 M NaOH	bad
Label	**width**	**length**	**l/w**	**9 M NaOH & 100 °C**	**Distribution**
Ce117	***23.0***	***443.0***	***19.3***	***100 °C***	***good***
Ce111	43.6	1471.7	33.7	130 °C	moderate
Ce118	53.6	1027.0	19.2	150 °C	moderate
Ce113	94.4	883.0	9.4	200 °C	bad

Crystal structure of bare GO, bare NrGO, bare ceria, and CeO_2/NrGO are shown in Figure 3. 7. The XRD pattern shows the characteristic peak of bare GO at 11.9˚ which is corresponding to the interplanar distance of 7.42 Å attributed to (001) plane. On the other hand, NrGO crystal pattern has both peaks of (001) planes of GO and reduced (002) planes of graphene at 11.5˚ and 26.5˚ corresponding to 7.67 Å and 3.35 Å, respectively. The decrease in interplanar space stems from the removal of functional groups such as carboxyl, hydroxyl and epoxide groups on GO lattice. NrGO clearly has both peaks implying that oxygen-containing functional groups still exist even after high-temperature

annealing of GO. This can be a result of the large agglomeration of GO particles resisting the reduction process even at high temperatures.

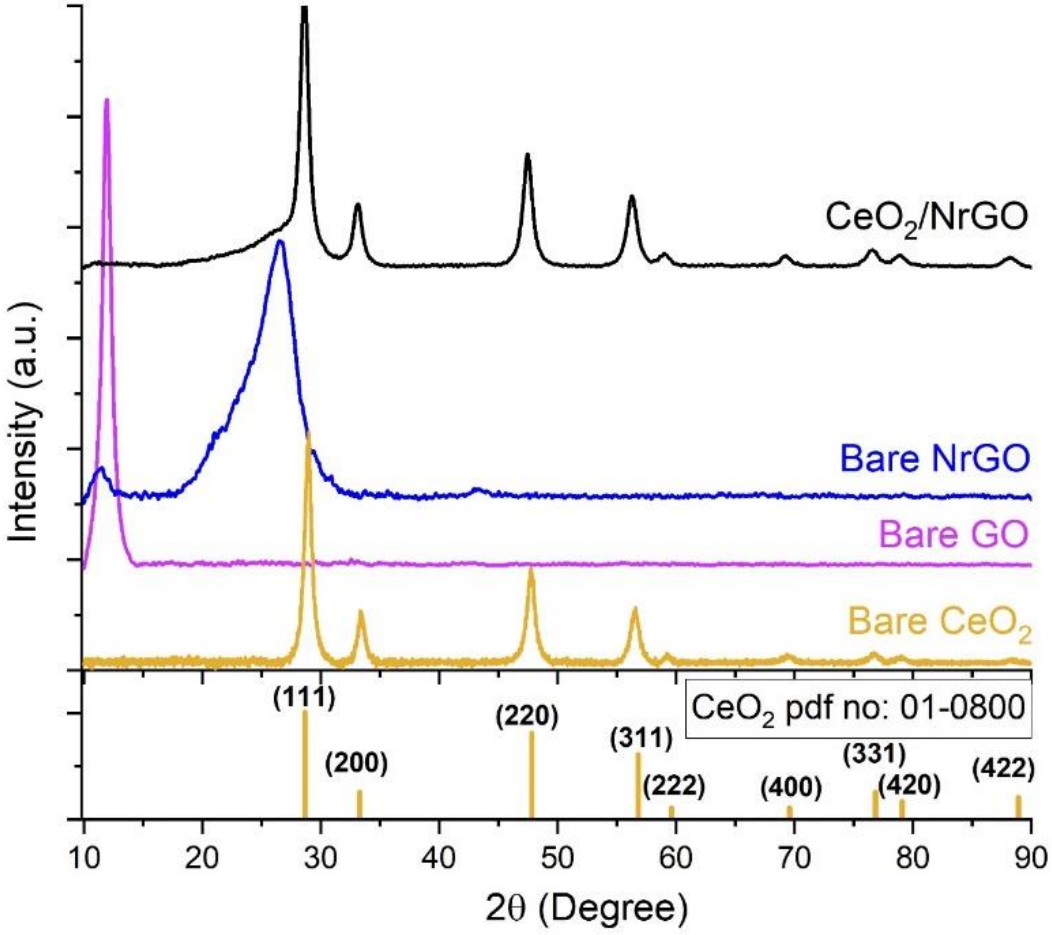

Figure 3. 7. XRD patterns of bare CeO_2, bare GO, bare NrGO, and CeO_2/NrGO

Moreover, synthesized CeO_2 nanorods have all expected peaks, and these peaks are identical to JCPDS card No. 01-0800, as shown in the graph[369]. The peaks at 28.9˚ (28.6 with NrGO due to the (002) plane of graphene), 33.4˚, 47.7˚, 56.5˚, 59.2˚, 69.4˚, 76.7˚, 79.0˚, 88.4˚two theta angles correspond to (111), (200), (220), (311), (222), (400), (331), (420) and (422), respectively. Also, the CeO_2/NrGO catalyst composite has all the expected peaks in the same pattern, which proves that CeO_2 nanorods are successfully dispersed on NrGO. For the final product, the main peaks of ceria have shifted from 28.9˚ to 28.6˚and superposed with the main peak of NrGO. This observation indicates a change in the crystallite size and signifies that the ceria nanorods have bonded to GO lattice during the graphene restacking procedure. Moreover, the (001) indexed peak of GO lattice has disappeared at the catalyst composite pattern, which offers that the ceria

nanorods have bonded to the GO active sites after the removal of the surface functional groups during the hydrothermal synthesis.

The results of a Raman spectroscopy analysis of bare GO, bare NrGO, bare ceria, and CeO_2/NrGO are shown in Figure 3. 8. On one hand, the graph shows three characteristic vibrational modes of CeO_2, which are at 245, 456, and 598 cm^{-1}. On the other hand, the spectroscopic patterns of GO and NrGO both show the characteristic D and G peaks of carbonaceous materials that correspond to sp^3 and sp^2 hybridization of carbon at 1355 and 1596 cm^{-1}, respectively [370]. Moreover, I_D/I_G (Intensity ratio of D and G peaks) and A_D/A_G (areal ratio of underneath areas of D and G curves) were calculated as 0.79 and 1.45 for GO, and as 1.10 and 2.05 for NrGO, respectively. Broadening peaks and increase in areal ratios of NrGO are direct proof of reduction of functional groups on GO surface and structural defects formation within the GO by the doping process of nitrogen. Besides, CeO_2/NrGO has both ceria and NrGO peaks, which express the existence of composite catalyst formation and strong interconnection of ceria to NrGO. CeO_2/NrGO has an even higher intensity and an areal ratio of 1.20 and 3.96, respectively, compared to bare NrGO Raman results. Besides, CeO_2 on NrGO has a broader peak at 598 cm^{-1} which indicates the formation of more O vacancies within the ceria lattice as compared to bare ceria Raman analysis result [371].

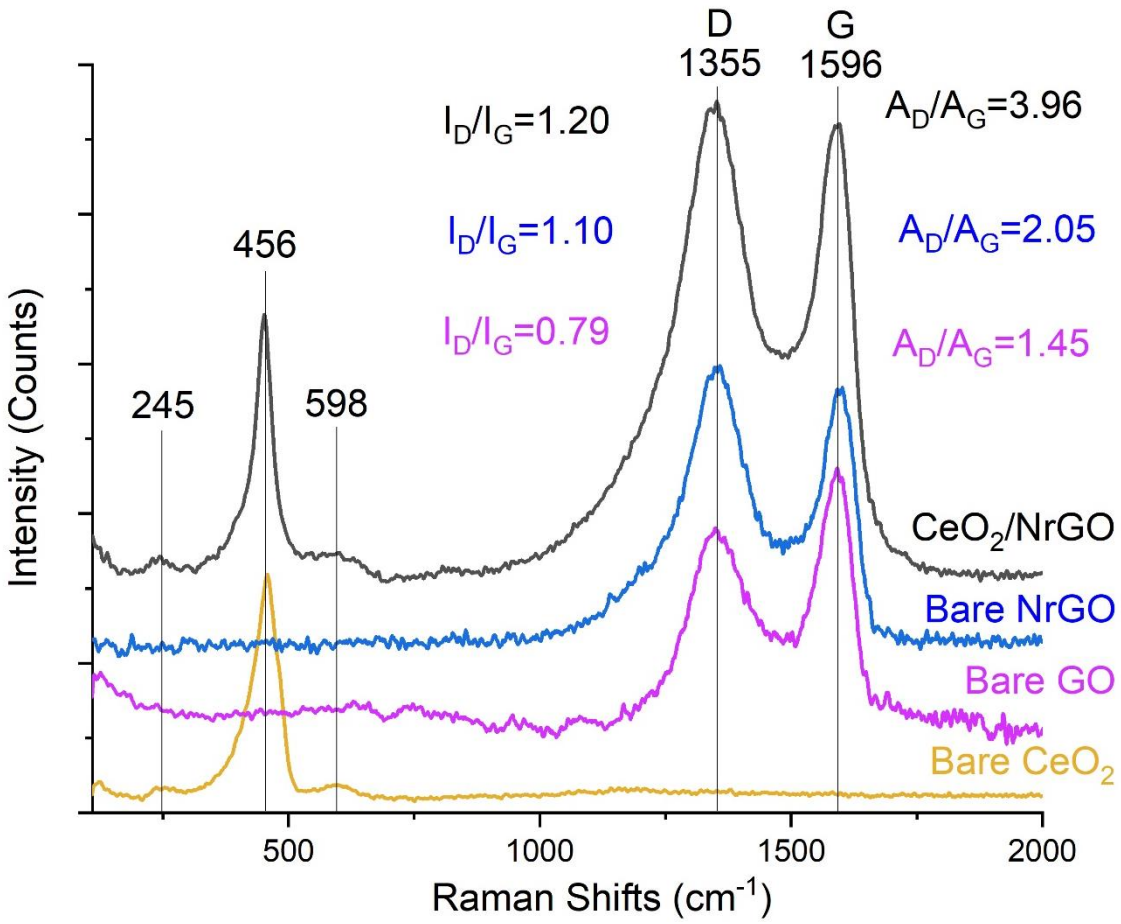

Figure 3. 8. Raman spectra of bare CeO_2, bare GO, bare NrGO, and CeO_2/NrGO

The morphological features of graphene oxides, CeO_2 nanorods on NrGO obtained by SEM analyses, and TEM image of bare CeO_2 nanorods are presented in Figure 3. 9. Bare graphene oxide generally shows large and flat platelets as large flakes. These flakes are relatively thin due to the effective reaction kinetics of $KMnO_4$ to large graphite flakes, which leads to effective oxidization of most layers within graphite agglomerates. Bare NrGO is generally wrinkled and composed of many curves on buckled flakes. The exfoliated thin flakes can be attributed to the reduction process of GO with ammonia, which results in an increase in the interspacing distance of planes of GO. The reduced functional groups cause the creation of electrostatically attractive and repulsive regions at the surface of reduced sites on GO; thus, the electrostatic interactions lead to a change in morphology by bringing more curvature on layers of GO. Moreover, the CeO_2 nanorods are observed as well-decorated on the NrGO flakes, and results are consistent with RAMAN and XRD analyses indicating a well-formed composite structure of ceria and NrGO. According to observation via SEM analysis, nanorods attach preferably on

voids or deep parts of NrGO surface. The TEM image in Figure 3. 9 (d) illustrates uniform nanorods formation of ceria, and they appear to be monodispersed with the width in the range of 30 to 40 nm.

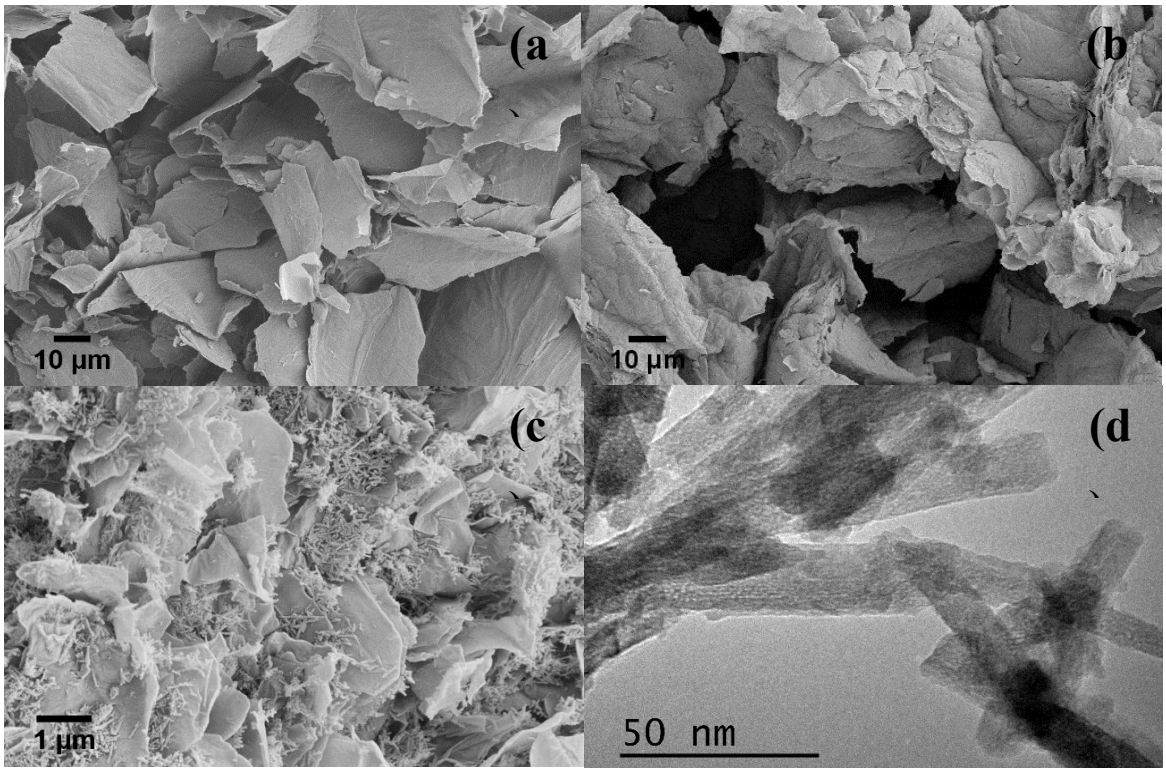

Figure 3. 9. SEM micrographs of bare GO (a), bare NrGO (b), CeO_2 nanorods on NrGO (c), and TEM image of bare CeO_2 (d)

Mass fraction of oxygenated groups, nitrogen, and ceria to reduce graphene oxide was demonstrated in Figure 3. 10 via thermogravimetric analysis. Temperature change up to 100 °C expresses the surface water content and humidity removal. Mass changes up to 450 °C exmpress that surface functional groups of rGO removed. CeO_2/NrGO and bare NrGO have different plateaus and mass fraction of oxygenated groups. CeO_2/NrGO has slightly less mass change and an additional plateau according to bare NrGO which can be assigned to extra reduction of NrGO during the hydrothermal reduction and re-coordination of extra-functional groups respectively. On the other hand, both samples have a sharp mass change between 450-600 °C. This is due to the oxidation and burning out of carbon in rGO's. Bare NrGO remained as 10 % of mass fraction after oxidation of carbon, however, mass fraction remained 52 % after oxidation of carbon in CeO_2/NrGO. 10 % of the mass is the mass of nitrogen content or some inclusions remained during GO synthesis by the Hummers method. Furthermore, 52 % mass is the mass of both ceria and

nitrogen content within the rGO's. Overall, CeO_2 mass fraction can be concluded as 42 % on NrGO which is reasonable according to observation in SEM analysis.

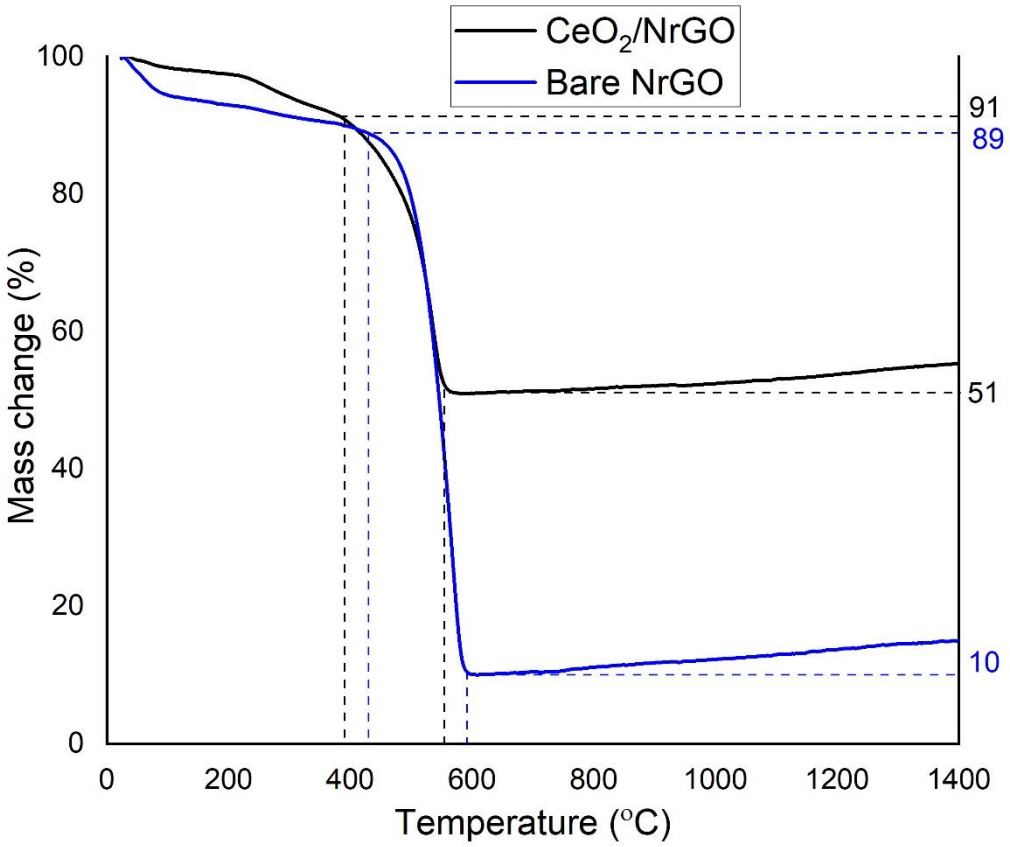

Figure 3. 10. TGA diagrams of bare NrGO and CeO_2 decorated NrGO

The BET and pore size distribution were analyzed by examining N_2 adsorption/desorption isotherms. As seen in Figure 3. 11, bare GO, bare NrGO, and CeO_2/NrGO show type IV isotherms according to their hysteresis shapes; however, bare CeO_2 demonstrates type III isotherm. All samples have a mesoporous structure according to their average pore sizes, and peak values are varying between 2.5 to 11.2 nm, as seen in Figure 3. 11 (right). On one hand, NrGO clearly has the highest specific surface area as 425.1 m^2/g, which can be attributed to the exfoliation of GO stacks via the reduction process and its textured surface as compared to that of bare GO as compared in Figure 3. 11. On the other hand, bare ceria showed the lowest surface area as 51.7 m^2/g, which is expected due to the nature of all metal oxides and similar properties are reported by Li et al. [372]. The CeO_2/NrGO has surface area value in between bare ceria and bare NrGO, which can be related to the decrease in surface wrinkles and pores. As already demonstrated in the SEM image of

Figure 3. 9(c), ceria nanorods tend to bond to high surface energy regions, which are naturally curved and porous regions.

Table 3. 2. BET analyses result of bare GO, bare NrGO, bare CeO_2, and CeO_2/NrGO

Sample Label	BET Surface Area (m^2/g)	BJH Pore Volume (cm^3/g)	BJH Average Pore Size (nm)
Bare GO	134.3	0.04	2.5
Bare NrGO	425.1	0.65	4.0
Bare CeO2	51.7	0.30	11.2
CeO2/NrGO	78.8	0.12	6.5

These results in Figure 3. 11 are also consistent with SEM analysis since the pore width distribution graph depicts the disappearance of ceria pore width peak and decrease in bare NrGO pore width peak in the case of CeO_2/NrGO . Bare NrGO has a broad range of pore volume up to 20 nm, and CeO_2/NrGO data seems to have narrower pore width with high volume, which is practical to allow electrolyte interaction with active sites in order to maintain catalytic activity and decomposition or accommodation of Li_2O_2. Both materials are good candidates as air cathode to show good catalytic activity owing to their pore size distributions.

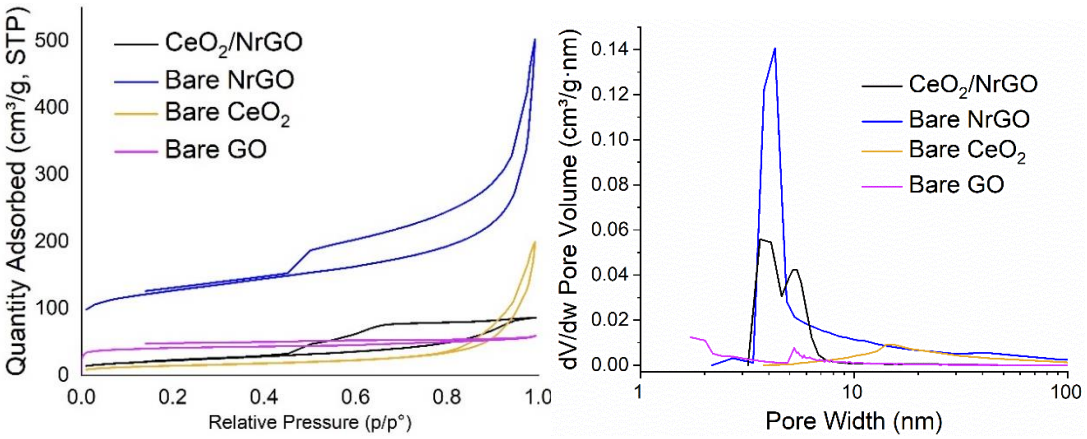

Figure 3. 11. BET N_2 adsorption isotherms (left) and corresponding pore size distribution of bare CeO_2, bare GO, bare NrGO, and CeO_2/NrGO (right)

The XPS data for NrGO decorated with CeO_2 nanorods is demonstrated and explained by fitting curves via Gaussian distribution in Figure 3. 12 (a) illustrates the full data survey throughout the spectra used to detect the general ratio of all elemental peaks compared to each other for C 1s, N 1s, O 1s, and Ce 3d allocated at 284.94, 398.9, 530.99, and 899.97 eV, respectively. Apparently, carbon has the highest presence, whereas the Ce 3d has the lowest signal in the XPS survey. As seen in Figure 3. 12 (b), the fitted curve on C 1s result shows four different deconvoluted XPS peaks that are centered at 284.5, 285.1, 286.4, and 288.8 eV arising from C=C, C-N, C-O, and O-C-O bonds respectively. Clearly, C=C has the highest ratio, while C-O and O-C-O bonds have the lowest occupancy, which confirms the reduction process by removing most of the oxygenated groups bonding to carbon. On the other hand, the presence of the C-N bonding signal in C 1s ensures that the nitrogen doping to GO lattice is consistent with XRD and Raman analysis. Figure 3. 12 (c) also provides information for four different peaks corresponding to N 1s curve fitting located at 403.1, 400.9, 399.0, and 397.9 eV, which are assigned to graphitic/quaternary-N, pyrridonic/pyrrolic-N, amino-N, and pyridinic-N respectively [373]. As figured out from XPS survey and merits of signals, nitrogen occupy 6.5 atomic % within the CeO_2/NrGO powder material. The Ce 3d XPS spectrum shows eight different deconvoluted curves whose centers are located at 917.1, 907.7, 902.6, 901.1, 898.7, 888.6, 884.9 and 882.8 eV and correspondent to U”’, U”, U’, U, V”’, V”, V’ and V respectively as seen in Figure 3. 12 (d). The U and V spectral peaks are addressed to Ce $3d_{3/2}$ and Ce $3d_{5/2}$ spin-orbit splittings, separately. The peaks satellites of V, V”, V”’, and U, U”, U”’ are associated with Ce^{4+}, and the characteristic peaks of V’, U’ are

attributed to Ce^{3+}. Remarkably, the Ce^{3+} distribution over Ce^{4+} offers an understanding of ceria having oxygen vacancies around 16 %, which is a verification of enhancement of catalytic activity and the increase in oxygen storage capacity [374].

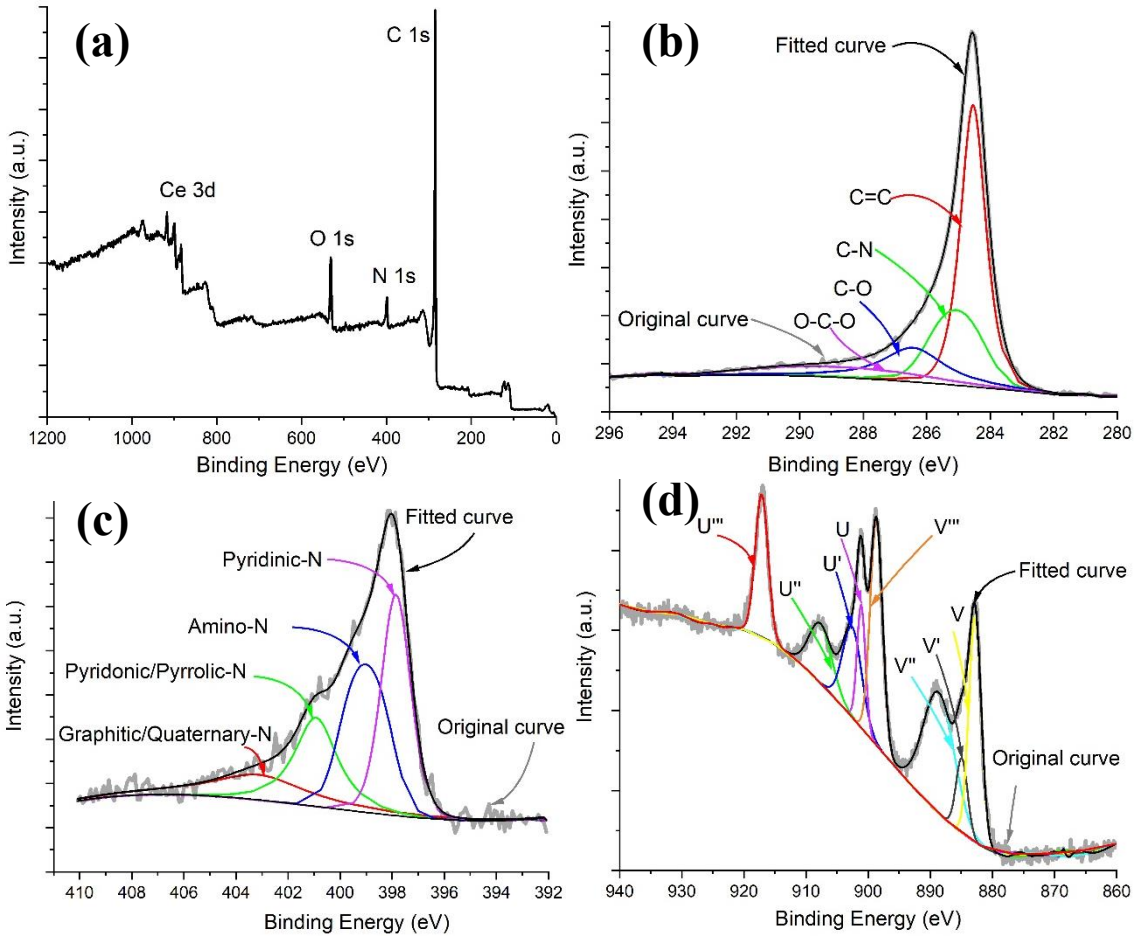

Figure 3. 12. XPS spectra of CeO_2 nanorods decorated NrGO: (a) fully scanned spectra, (b) C 1s, (c) N 1s (d) Ce 3d

Figure 3. 13 presents the results of cyclic voltammetry (CV) to analyze the electrochemical performance of NrGO with and without ceria catalyst nanorods and compare their ORR and OER process with and without oxygen gas ambient and LiI as redox mediator. CV curves are recorded from 4.1 to 2.0 V potential window with a scan rate of 0.1 mVs^{-1}. Remarkably our catalyst composite, i.e., CeO_2 nanorods decorated NrGO in electrolyte without LiI, shows no ORR and OER peaks among other CV loops under the argon gas environment and the overall area of its CV loop (green line) is smallest among others. This result is perfect proof of CeO_2/NrGO being electrocatalytically active only under the oxygen gas environment. O_2 is first adsorbed by active site of NrGO (Eq'n 1) and reduced to O_2^{*-} as presented in Eq'n 2. Adsorbed and

reduced oxygen on the cathode by carbon support changes oxygen states within the ceria (Eq'n 3). Ceria with different oxygen states reacts with new oxygen molecules to produce peroxide or superoxide (Eq'n 4) and followingly LiO_2 (Eq'n 5) or Li_2O_2 (Eq'n 6). As seen in the CV diagram, CeO_2/NrGO catalyst with non-additive electrolyte (electrolyte without LiI as redox mediator) revealed anodic and cathodic peaks at 3.20 and 2.29 V respectively under O_2 gas as pointed out in equations 4-6 (red line). This result points out 0.91 V potentials difference between anodic and cathodic peaks and indicates that our LiTF/TEGDME electrolyte has significant internal resistance even in the presence of catalyst materials. Additionally, two peaks are attributed to the decomposition and formation of Li_2O_2. Decomposition was depicted in Eq'n 7 by the oxidation reaction of Li_2O_2. On the other hand, bare NrGO and CeO_2/NrGO have anodic peaks at 3.20, 3.69, and 3.85 V indicating oxidation of Li_2O_2, I^- to I_3^- and I_3^- to I_2 conversion respectively as shown in equations 8 and 9.

$$O_2 + * \rightarrow O_2^* \qquad \textbf{(Eq'n 1)}$$

$$O_2^* + e^- \rightarrow O_2^{*-} \qquad \textbf{(Eq'n 2)}$$

$$CeO_2 \leftrightarrow CeO_{2-x} + {}^{x}/_{2}\, O_2 \qquad \textbf{(Eq'n 3)}$$

$$nCeO_{2-x} + O_2 \leftrightarrow [nCeO_{2-x}]^+ O_2^- \leftrightarrow [nCeO_{2-x}]^{2+} O_2^{2-} \qquad \textbf{(Eq'n 4)}$$

$$[nCeO_{2-x}]^+ O_2^- + Li^+ + e^- \rightarrow [CeO_2][LiO_2] \qquad \textbf{(Eq'n 5)}$$

$$[nCeO_{2-x}]^{2+} O_2^{2-} + 2Li^+ \rightarrow [CeO_2][Li_2O_2] \qquad \textbf{(Eq'n 6)}$$

$$Li_2O_2 \rightarrow 2Li^+ + O_2 + 2e^- \qquad \textbf{(Eq'n 7)}$$

$$3I^- \leftrightarrow I_3^- + 2e^- \qquad \textbf{(Eq'n 8)}$$

$$I_3^- \leftrightarrow I_2 + I^- + e^- \qquad \textbf{(Eq'n 9)}$$

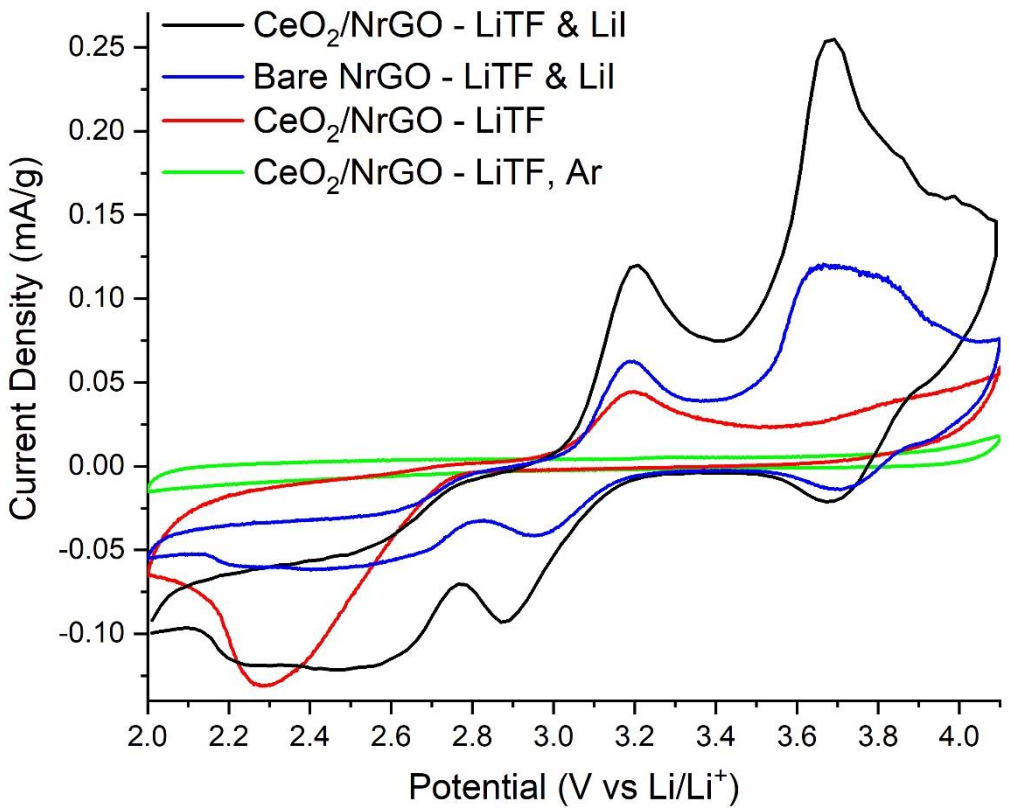

Figure 3. 13. CV curves of CeO_2 nanorods decorated NrGO in electrolyte without LiI in Ar (green) and O_2 (red), bare NrGO (blue), and CeO_2/NrGO (black) in electrolyte with LiI in O_2

Furthermore, the cathodic peaks of bare NrGO are at 3.71, 2.95, and 2.45 V (blue line), whereas the cathodic peaks of CeO_2/NrGO are at 3.67, 2.88 and 2.50 V, respectively (black line) as seen in Figure 3. 13. Peaks around 3.70 and 2.90 represent the I^- to I_3^- and I_3^- to I_2 conversion, respectively. CeO_2/NrGO catalyst tested without LiI in electrolyte and CV has one oxidation (3.20 V) and one reduction (2.29 V) peak only, however, CV data resulted in two extra peaks after addition of the LiI to the electrolyte in the CV hysteresis which are located apart from these peaks in CV. In the light of these findings, it is clear that there is no redox reaction CeO_2 and LiI. All evident in CV diagram pointed that the performance of CeO_2/NrGO catalyst with LiI as a redox mediator would result in a greater area in CV hysteresis due to the presence of more defects, active sites, and also the synergetic effect of NrGO and ceria. Thus, the performance analysis indicates that the CeO_2/NrGO and bare NrGO air cathodes have excellent electrocatalytic activity on the ORR and OER process by proving more current densities.

Charge-discharge profiles of the CeO_2/NrGO without LiI electrolyte and, bare NrGO and CeO_2/NrGO with LiI containing electrolyte, tested at 25 mA/g current density are

illustrated in Figure 3. 14 (left). The test without LiI has the highest overpotential of 1.03 V. In contrast, the sample with ceria catalyst nanorods has the lowest overpotential of 0.76 V. On the other hand, the overpotential of bare NrGO is 0.87 V in between these two cases. This observation stems from the reduction of overpotential due to utilizing efficient catalyst materials both in air cathode and electrolyte solution as the redox mediator[375, 376]. LiI additive in LiTF/TEGDME electrolyte mainly yields soluble LiO_2 with low discharge overpotential then disproportionated to the large Li_2O_2 particles away from the cathode surface, which obeys the solution growth mechanism of Li_2O_2. Bare NrGO and CeO_2/NrGO with LiI containing electrolyte both show discharge plateaus at 2.7 V, and the plateau of oxidation of Li_2O_2 are at 3.60 and 3.45 V, respectively.

The lowering of oxidation potential for Li_2O_2 is a direct indication of catalytic activity of ceria over NrGO, which addresses the fast transition between Ce^{4+} to Ce^{3+} and the existence of oxygen vacancies to enhance OER [377, 378]. It is seen that the presence of LiI reduces the oxidation potential of Li_2O_2 and decomposes Li_2O_2 at a higher discharge potential as similar effect as ceria. Moreover, the NrGO supported ceria nanorods catalyst showed the highest capacity as 5040 mAh/g based on the mass of CeO_2/NrGO and carbon black on air cathodes. Followingly, CeO_2/NrGO without LiI and bare NrGO with LiI yielded discharge capacities of 2250 and 2113 mAh/g, respectively [379, 380]. CeO_2/NrGO test without LiI has higher discharge capacity over bare NrGO test with LiI even though bare NrGO has higher pore volume, variety of pore size, and contribution of redox mediator which proves ceria contribution as oxygen buffer and superior electrocatalyst effect on cell capacity. Electrocatalytic activity of ceria nanorods on NrGO support improves decomposition and formation of Li_2O_2, resulting in an increase in cell capacity by the accommodation of a high number of Li_2O_2 on defects and active sites of NrGO surface by exploiting mesoporous volume and narrow pore size distribution. Previously, sp^3 hybridized carbon was reported to be less stable with respect to sp^2 hybridized carbon so that peroxide-containing species bond with unsaturated C=C bonds and new epoxy groups (C=O group) form as the final product on carbon. Moreover, LiI depicts more influence on cell capacity and reduction of overpotential due to the more significant interaction of electrolyte to air cathode which consists of NrGO with high electronic conductivity and numerous active and defect sites and ceria with great catalytic activity. Wang et al. reported that cerium triflate ($Ce(CF_3SO_3)_3$) can be used as scavengers to inhibit the superoxide attack to electrolyte and prevent electrolyte decomposition

resulting 35% increase in battery capacity [381]. Ceria and LiI catalytic combination might reduce the nucleophilic attack of oxide radical so that Li-O_2 cell demonstrated lower overpotential and higher capacity [382].

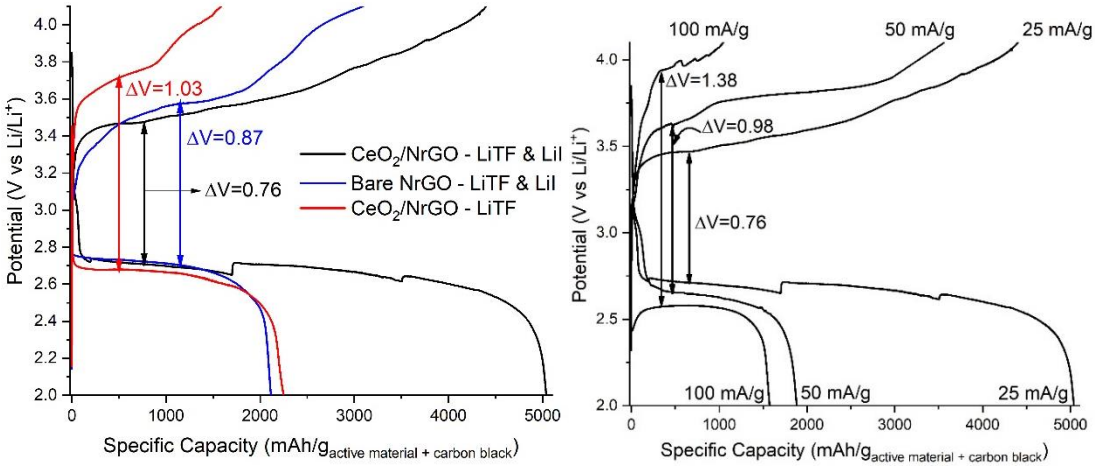

Figure 3. 14. Charge-discharge profiles of CeO_2 nanorods decorated NrGO without LiI, both bare NrGO and CeO_2/NrGO with LiI at 25 mA/g (left), specific capacity versus potential of NrGO supported CeO_2 at 25, 50, and 100 mA/g (right)

NrGO supported ceria catalyst nanorods are tested with current densities as 25, 50, and 100 mA/g via LiI and LiTF in TEGDME electrolyte, as illustrated in Figure 3. 14 (right). The overpotential values (ΔV) are determined at first platue of the charging process right before the change in the slope which express the location of the first mina of the derivation and oxidation of Li according to CV diagram. Discharge capacities under 25, 50, and 100 mA/g current densities were obtained as 5040, 1883, and 1573 mAh/g with their overpotential as 0.76, 0.98, and 1.38 V, respectively [383]. Despite the decrease in discharge potentials for Li_2O_2, its oxidation potentials constantly increase with the rise of current density. Therefore, as seen in Figure 3. 14, the gap between the charge and discharge plateaus becomes wider. This result demonstrates that change in the current density of Li-air batteries directly alters the charge overpotential, which influences the kinetics of the formation of the discharge product and discharge capacity. This outcome may offer that increase in current density may elevate the decomposition/formation of Li_2O_2 within the pores of air cathode with an increase in cell polarization as a result of losing electrolyte channels by blocking oxygen flow or precipitation of irreversible discharge products on pores. This observation is consistent with the study conducted by Adams et al. [384].

Ceria and its combinations with other materials have been reported for Li-O_2 batteries, as seen in Table 3. 3. Lin et al. compared different morphologies of ceria affecting ORR processes and the capacity of Li-O_2 cell as 2128 mAh/g at 0.05 mA/cm^2 [377]. Graphene/doped ceria nanoblend air cathode was fabricated by Ahn et al. showing a cell capacity of 3254 mAh/g at 0.2 mA/cm^2 [385]. Yuexing Jiang et al. fabricated ceria microspheres on self-standing graphene foam, releasing a high capacity of 3250 mAhg^{-1} at a current density of 200 mAg^{-1} [386]. Yang et al. analyzed the nucleation, growth, and decomposition of Li_2O_2 on CeO_2/CNT electrodes in his research [387]. Kalubarme et al. presented the enhancement of battery capacity via an increase in catalytic activity by doping ceria with Zr and Zn in their researches yielding 8435 mAh/g at 0.1 mA/cm^2 [388]. Y. Zhu et al. explored MnO_x decorated CeO_2 nanorods and bare CeO_2 nanorods as highly active cathode catalysts for lithium-air batteries, which showed enhanced electrochemical performances resulting 2617 mAh/g and 1538 mAh/g at 100 mA/g respectively [389]. Even though results varied in capacity according to the composition of ceria with carbon materials of interest, CeO_2/NrGO air cathode in this study yielded a very high capacity similar to reported results. In addition to that, for the first time, NrGO supported ceria nanorods were introduced to the literature. Besides, the LiI effect study is the first ever with this novel catalyst. Thanks to synergetic effect of LiI to overall cell and ceria on NrGO support, it revealed 5040 mAh/g discharge capacity at 25 mA/g current density with 0.76 V overpotential.

Table 3. 3. Cerium based catalyst data from the literature for Li-air battery applications

Material	Electrolyte	Overpotential (V)	Current Density	Capacity (mAh/g)	References
CeO_2 nanoparticles	1 M LiPF6/PC:DMC-1:1 w/w	NA	0.05 mA/cm^2	2128	[377]
Graphene/doped ceria NP	1M LiTFSI/TEGDME	0.9	0.2 mA/cm^2	3254	[385]
C-CeO_2@GF	1M LiTFSI/DMSO	1.5	0.4 mA/cm^2	3250	[386]
CeO_2 NP/CNT	0.5 M LiClO4/TEGDME	1	20 mA/g	2000	[387]
Zr doped ceria NP	1M LiTFSI/TEGDME	NA	0.1 mA/cm^2	8435	[388]
MnOx@CeO_2 nanorods	1M LiTFSI/TEGDME	1	100 mA/g	2617	[389]
CeO_2 nanorods	1M LiTFSI/TEGDME	1	100 mA/g	1538	[389]
CeO_2 nanorods/NrGO	1M LiTF/TEGDME & 0.1 M LiI	0.76	25 mA/g	5040	this study
CeO_2 nanorods/NrGO	1M LiTF/TEGDME & 0.1 M LiI	1.15	50 mA/g	1883	this study

Electrochemical impedance spectroscopy analysis of CeO_2/NrGO air cathode before and after the charge-discharge test is shown in Figure 3. 15 (left). Li-O_2 cathode before the test has an ohmic contact of 31 ohms and charge transfer resistance is 400 ohms while after charge-discharge test, it possesses an ohmic contact of 25 ohms and a charge transfer resistance of 241 ohms. As seen in Figure 3. 15, air cathode after the charge-discharge test has less ohmic contact and internal resistance as compared to air cathode prior to the test. This observation indicates that LiTF and LiI dissociate and increase the mobility of their ions, which results in better conductivity [390]. Similarly, LiTF does not contain HF bonds; therefore, as the charge/discharge cycles and the interaction between TEGDME and the air electrode increase, electrolyte resistance decreases accordingly. Choi et al. also reported such an observation for Li/ Pyrite battery system [391]. Another point seen in Figure 3. 15 is that the air cathode shows an extra semicircle after charge/discharge tests. This semicircle can be attributed to the resistance of the newly created interface due to Li_2O_2 formation, which is in accordance with the findings presented in a study by

Mirzaeian&Hall [392]. Remarkably, the extra resistance of Li_2O_2 formation does not affect the overall decrease in the charge transfer resistance. As shown in the SEM image of Figure 3. 15 (right) Li_2O_2 is formed on CeO_2/NrGO air cathode after the charge-discharge test. As indicated in the SEM image, Li_2O_2 is formed in the form of big particles rather than thin film covering the surface of the air electrode, implying to solution growth mechanism of Li_2O_2. According to an investigation by Adams et al. [384], these particles have a bulk size of 200 nm, which is consistent with the observation in this study as well.

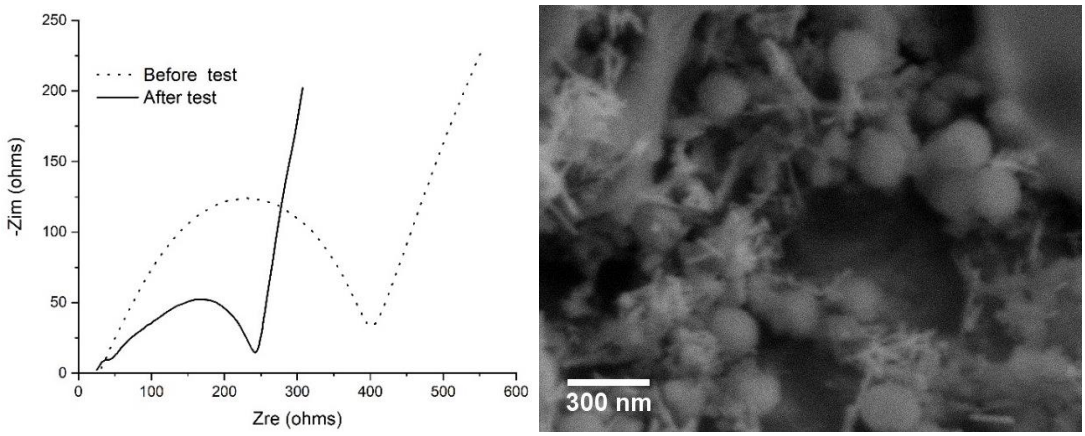

Figure 3. 15. EIS analysis of CeO_2/NrGO air cathode before and after charge-discharge test (left), and SEM analysis of air electrode to observe Li_2O_2 formation (right)

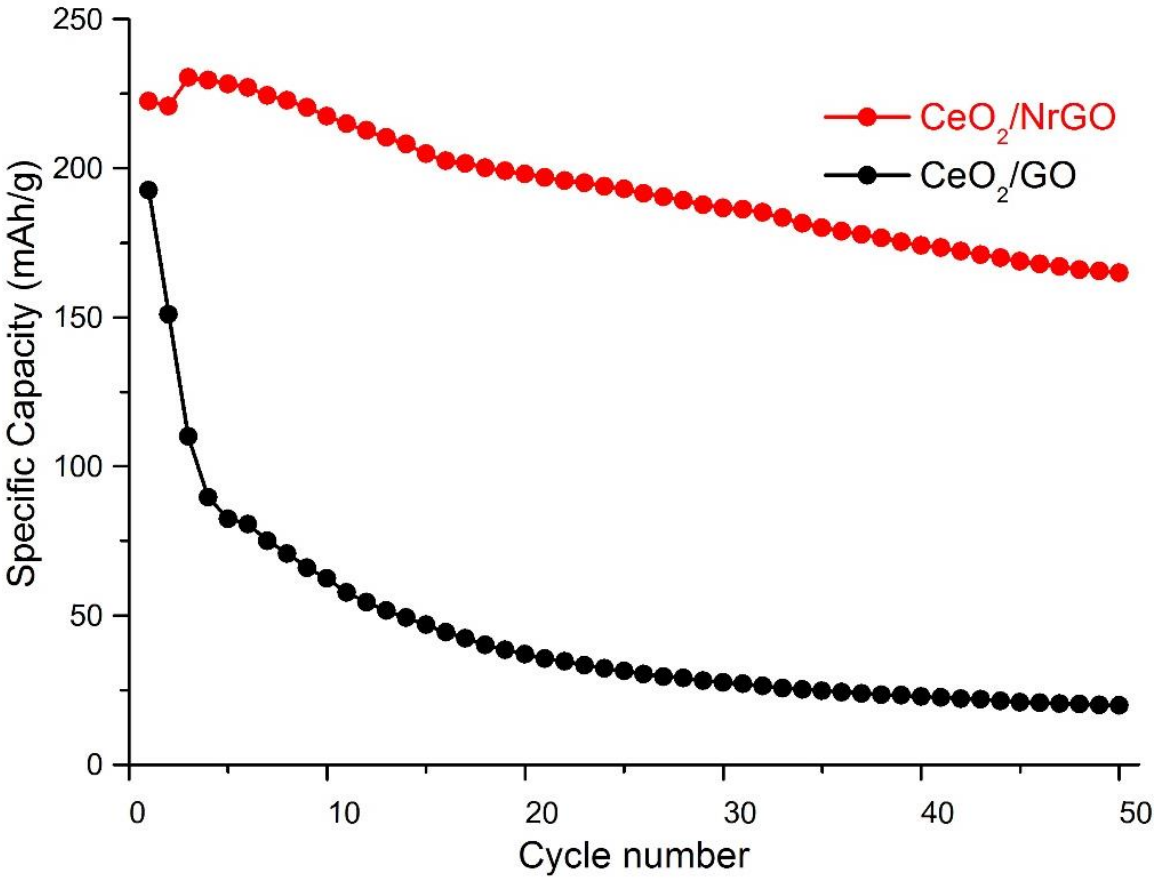

Figure 3. 16. A cycling comparison of CeO_2/GO and CeO_2/NrGO at 350 mAg^{-1} current density

A comparison of GO and NrGO as support materials for ceria nanorods were established by performing a cycling performance up to 50 cycles as shown in Figure 3. 16. CeO_2/GO showed a huge capacity drop over cycling due to the insulating nature of GO. Based on this comparison GO was not preferred as support material for this study. Apparently, NrGO demonstrated synergetic effect and cell kinetics better than GO for ceria nanorods via providing only 25 % capacity fading over 50 cycles. Even though, our Li-O_2 battery cell displayed a reasonable capacity fading and a working cell over 50 cycles, it showed a capacity of 168 $mAhg^{-1}$ which does not match the energy merit of this battery. For that reason, electrolyte and catalyst properties need to enhance for cycling performance.

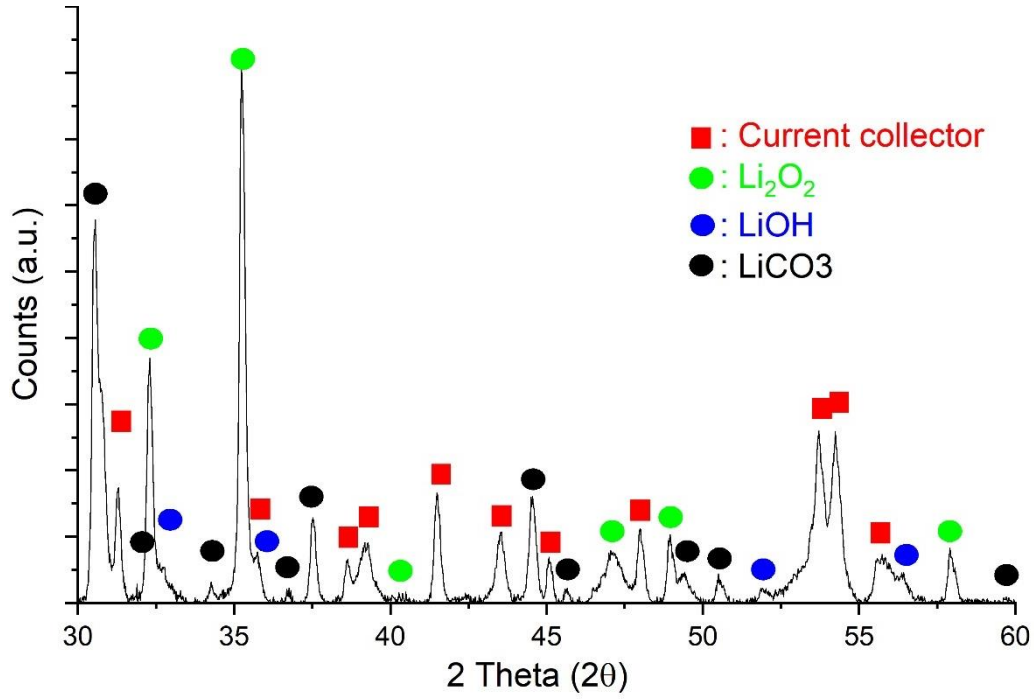

Figure 3. 17. XRD analysis of CeO_2/NrGO electrode after discharge test

CeO_2/NrGO electrode was washed with bare TEGDME and dried overnight for XRD analysis. XRD analysis in Figure 3. 17 pointed out all side products not only Li_2O_2 but also $LiCO_3$ an LiOH formation. The formation of LiOH and $LiCO_3$ is the limiting factor for low cycling performance so that a better combination of electrolyte and catalyst is required. These irreversible side products passivate the electrode surface and tremendously decreased the capacity.

In summary, the crystallinity and morphology of discharge product are affected by various cell parameters, including stability of electrolyte, mass transport of O_2^- and Li^+, purity and partial pressure of oxygen, nucleation and decomposition rate, the functionality of catalyst and carbon material and their interaction at the atomistic level due to the complex three-phase-boundary (i.e., electrolyte-gas-solid electrode) condition [96, 97, 393]. Moreover, current density and cathode adsorption strength were found to alternate reaction pathway and change growth mechanism [384, 394]. In this respect, catalyst materials in air cathode and soluble catalyst materials within the electrolyte as redox mediators promote solution growth mechanism and enhance the solubility of O_2^- and LiO_2[117]. Despite all, these achievements are inadequate to explain the intrinsic mechanism that includes charge and discharge process and their side products in detail [395].

3.4. Conclusion

GO was synthesized by improved Hummers method, then thermally converted to NrGO under Ar and NH_3 gas flow. Then, CeO_2 nanorods were synthesized and decorated onto NrGO by a hydrothermal method. The CeO_2/NrGO catalyst material was tested in LiTF/TEGDME electrolyte containing LiI as the redox mediator to study Li-O_2 battery and its electrochemical performance. Results showed that CeO_2/NrGO catalyst has a higher discharge capacity and lower overpotential with respect to the bare NrGO catalyst. Another confirmation is that CeO_2/NrGO demonstrated lower overpotential in the electrolyte containing LiI as redox mediator over the electrolyte without LiI. Overpotential of CeO_2/NrGO air cathode increased with the increase in applied current density. All evidence in this study pointed out that CeO_2 catalyst nanorods have a synergetic effect with NrGO on ORR and OER. CeO_2/NrGO catalyst air cathode exhibited a high capacity of 5040 mAh/g. All in all, CeO_2/NrGO catalyst material proved to be a very promising cathode material for the Li-O_2 battery application and LiI effectively reduced overpotential.

CHAPTER 4. GENERAL CONCLUSION

Rechargeable batteries have found vast applications emerging high energy and power densities to meet energy demands for electronics, electric vehicles, as well as large-scale application. Thus, it's obvious that the adaption of high capacity electrode materials is an essential factor to the effective development of a high energy density battery. Therefore, extensive research efforts are made to modify the chemistries of the anode, cathode, and electrolyte to obtain higher energy storage capabilities. In this study, N doped reduced graphene oxide, TiO_2-B nanotubes and sandwich like rGO-Si-rGO materials were used to find better energy merits in anode for LiBs, Moreover, highly active CeO_2 nanorods decorated NrGO were used as porous air cathode for Li-O_2 batteries as next generation energy storage technology.

In the first part of this study, The GO was synthesized as starting material by improved Hummers' method, which offers better product quality compared to other studies that generally use Hummers' or modified Hummers' methods. The nitrogen-doping and reduction of GO were carried out by a single step through thermal annealing at high temperature within Ar/NH_3 atmosphere. rGO was fabricated as control sample to compare the difference in electrochemical performance of the rGO and NrGO electrodes including high current rate testing and long-term operability. The improved Hummers' method and annealing with NH_3 yielded a more open structure with nitrogen sites suitable for enhanced Li intercalation. As-synthesized rGO has delivered 113 $mAhg^{-1}$ capacity at 10 Ag^{-1} after 500 cycles of operation, retaining only 40 % of the initial capacity. Conversely, our NrGO electrodes exhibited a reversible capacity of 240 $mAhg^{-1}$, with 90 % capacity retention at the same operation conditions, which is so far the best result achieved among graphene oxide-based anodes at this current density in the literature. In contrast to rGO, NrGO cells exhibited a gradually increasing capacity profile, reaching up to 114 % of the initial capacity at 0.1, 1, 2, and 10 Ag^{-1} current densities. Results showed that high occupancy of pyridinic N within NrGO enhanced battery performance and cell kinetics upon cycling. Furthermore, the remarkable long-time performance opens the possibility to use NrGO based materials as suitable Li-ion battery anode materials.

In the second part of this study, a simple and scalable hydrothermal method was used to decorate titanate nanotubes on the NrGO sheets for the purpose of achieving high rate capabilities with high capacity upon battery cycling. Followingly, titanate nanotubes were

converted to a mixed phase of TiO_2-B and anatase (TB) using thermal annealing method. The final product was yielded 150 $mAhg^{-1}$ capacity at 1C current rate at 50^{th} cycles with a stable cycling performance. The promising capacity of synthesized NrGO-TB was attributed to the unique and novel microstructure of NrGO-TB in which long nanotubes of TiO_2 have been grown on the surface of NrGO sheets. Such architecture synergistically reduces the solid-state diffusion distance of Li^+ and increase electronic conductivity of the anode. Due to chemical and structural stability of TiO_2 nanotubes, neither volume expansion nor capacity fading were observed even at high current rate. This composition can be used in a grid system to deliver a stable capacity exploiting higher current density.

In the third part of this study, Si was aimed to employ as anode materials even though it has large volumetric expansion upon lithiation which causes irreversible damage to the anode structure and promotes an unstable solid electrolyte interface (SEI) leading rapid capacity drop. To avoid the large volumetric expansion, a sandwich-like architecture was developed to Incorporate Si in anode to achieve high capacity. The rGO sheets were employed to wrap Si to avoid the detrimental effects of expansion during the reaction with Li. For this purpose, a simple spraying and drying method was developed to prepare layer by layer of rGO-Si-rGO anode in which Si nanoparticles were synthesized by the magnesiothermic reduction of SiO_2 nanoparticles and rGO sheets were obtained by thermal annealing method. The sprey-dry method enables user friendly large-scale manufacturing without using complicated chemical process that can be used in scale-up mass production of anode materials. The sandwich-like rGO-Si-rGO anode exhibited a high specific capacity of 1089 $mAhg^{-1}$ at 1C with 97% coulombic efficiency after 50 cycles and a stable cycling performance at current densities up to 5C shows. By the battery testing, the volume expansion of Si containing anode was successfully evaded.

In the last part of this study, already synthesized NrGO via thermal annealing method decorated with CeO_2 nanorods to be used as efficient catalyst material for oxygen reduction in porous air cathode for Li-air batteries in which LiI was employed as redox mediator. The impact of CeO_2 catalyst nanorods decorated NrGO on the capacity and overpotential was studied by comparing results to the bare NrGO tests. In addition, the synergetic effect of CeO_2/NrGO and LiI as redox mediator were examined according to the overpotential and capacity values. Moreover, the change in overpotential was compared by the increase in applied current density. Finally, the effect of LiI on ORR and

OER was investigated. The NrGO exhibited excellent electrical conductivity, high specific surface area, and chemical stability besides it contributed battery performance as support materials and catalyst material. Furthermore, CeO_2 nanorods provided oxygen storage capacity that promotes O_2 reduction based on its low energy transition need between its Ce^{+3} to Ce^{+4} oxygen states and catalytic activity. Additive LiI reduced the overpotential value up to 0.78V, and CeO_2/NrGO air cathode displayed a maximum capacity of 5040 $mAhg^{-1}$ at 25 mAg^{-1} current density. Additionally, increase in current density increased the overpotential value. The results conveyed that our novel catalyst hybrid composite of CeO_2 nanorods decorated NrGO and LiI directly increased the electrochemical performance of Li-O_2 battery.

All in all, Li-O_2 batteries are predicted as the future battery technology for vehicle electrification due to their superior theoretical energy density and specific capacity. However, they suffer from low cycle performance, irreversible side products, and low round-trip efficiency which stem from high overpotential between charge and discharge potential. Moreover, catalyst materials and active lithium salts within a stable electrolyte solvent are still under development to enhance Li-O_2 batteries performance and to commercialized them. Similarly, cathode materials with low practical capacity in LiBs are restricting the overall cell capacity even though there are several alternative anode materials reveling high capacity compared to graphite. This thesis reports simple-scalable methods to fabricate electrode materials by for batteries yielding high capacity at high current rates with stable cyclicity at long term operations. Lastly, this thesis offers advanced electrode materials for high performance Li-ion and Li-O_2 batteries to contribute solutions for future energy problems.

•

REFERENCES

1. Xu, K. and A. von Cresce, *Interfacing electrolytes with electrodes in Li ion batteries.* Journal of Materials Chemistry, 2011. **21**(27).
2. Shao, Y., et al., *Design and Mechanisms of Asymmetric Supercapacitors.* Chemical Reviews, 2018. **118**(18): p. 9233-9280.
3. Cheng, F. and J. Chen, *Metal-air batteries: from oxygen reduction electrochemistry to cathode catalysts.* Chem Soc Rev, 2012. **41**(6): p. 2172-92.
4. Linden, D. *Handbook of batteries*. in *Fuel and energy abstracts*. 1995.
5. Chen, J., *Recent Progress in Advanced Materials for Lithium Ion Batteries.* Materials (Basel), 2013. **6**(1): p. 156-183.
6. Wu, C., et al., *A review on fault mechanism and diagnosis approach for Li-Ion batteries.* J. Nanomaterials, 2015. **2015**: p. Article 8.
7. Besenhard, J.O., *Handbook of battery materials*. 2008: John Wiley & Sons.
8. Jiang, H., et al., *Li-Ion solvation in propylene carbonate electrolytes determined by molecular rotational measurements.* Physical Chemistry Chemical Physics, 2019. **21**(20): p. 10417-10422.
9. Hou, T., et al., *The influence of FEC on the solvation structure and reduction reaction of LiPF6/EC electrolytes and its implication for solid electrolyte interphase formation.* Nano Energy, 2019. **64**: p. 103881.
10. Lu, J., et al., *High-performance anode materials for rechargeable lithium-ion batteries.* Electrochemical Energy Reviews, 2018. **1**(1): p. 35-53.
11. Yoo, H.D., et al., *On the challenge of developing advanced technologies for electrochemical energy storage and conversion.* Materials Today, 2014. **17**(3): p. 110-121.
12. Lee, W., et al., *Advances in the cathode materials for lithium rechargeable batteries.* Angewandte Chemie International Edition, 2020. **59**(7): p. 2578-2605.
13. Yiğitalp, A., et al., *Nafion-coated LiNi0.80Co0.15Al0.05O2 (NCA) cathode preparation and its influence on the Li-ion battery cycle performance.* Energy Storage. **n/a**(n/a): p. e154.
14. Abu-Lebdeh, Y. and I. Davidson, *Nanotechnology for lithium-ion batteries*. 2012: Springer Science & Business Media.
15. Wakihara, M., *Recent developments in lithium ion batteries.* Materials Science and Engineering: R: Reports, 2001. **33**(4): p. 109-134.
16. Asenbauer, J., et al., *The success story of graphite as a lithium-ion anode material – fundamentals, remaining challenges, and recent developments including silicon (oxide) composites.* Sustainable Energy & Fuels, 2020.
17. Delhaes, P., *Carbon-based solids and materials*. 2013: John Wiley & Sons.
18. Yoo, E., et al., *Large reversible Li storage of graphene nanosheet families for use in rechargeable lithium ion batteries.* Nano letters, 2008. **8**(8): p. 2277-2282.
19. Guo, P., H. Song, and X. Chen, *Electrochemical performance of graphene nanosheets as anode material for lithium-ion batteries.* Electrochemistry Communications, 2009. **11**(6): p. 1320-1324.
20. Wang, C., et al., *Electrochemical properties of graphene paper electrodes used in lithium batteries.* Chemistry of Materials, 2009. **21**(13): p. 2604-2606.
21. Abouimrane, A., et al., *Non-Annealed Graphene Paper as a Binder-Free Anode for Lithium-Ion Batteries.* The Journal of Physical Chemistry C, 2010. **114**(29): p. 12800-12804.
22. Ellis, B.L., K.T. Lee, and L.F. Nazar, *Positive Electrode Materials for Li-Ion and Li-Batteries.* Chemistry of Materials, 2010. **22**(3): p. 691-714.

23. Yang, S.-Y., et al., *Design and tailoring of a hierarchical graphene-carbon nanotube architecture for supercapacitors.* Journal of Materials Chemistry, 2011. **21**(7): p. 2374-2380.
24. Ji, Z., et al., *Facile synthesis of reduced graphene oxide/CeO2 nanocomposites and their application in supercapacitors.* Ceramics International, 2015. **41**(7): p. 8710-8716.
25. Liu, Y., R. Wang, and X. Yan, *Synergistic Effect between Ultra-Small Nickel Hydroxide Nanoparticles and Reduced Graphene Oxide sheets for the Application in High-Performance Asymmetric Supercapacitor.* Scientific reports, 2015. **5**: p. 11095-11095.
26. Channu, V., R. Bobba, and R. Holze, *Graphite and graphene oxide electrodes for lithium ion batteries.* Colloids and Surfaces A: Physicochemical and Engineering Aspects, 2013. **436**: p. 245-251.
27. Li, X., et al., *Simultaneous Nitrogen Doping and Reduction of Graphene Oxide.* Journal of the American Chemical Society, 2009. **131**(43): p. 15939-15944.
28. Xing, Z., et al., *One-pot hydrothermal synthesis of Nitrogen-doped graphene as high-performance anode materials for lithium ion batteries.* Scientific Reports, 2016. **6**: p. 26146.
29. Wan, L., et al., *Graphene nanosheets based on controlled exfoliation process for enhanced lithium storage in lithium-ion battery.* Diamond and Related Materials, 2011. **20**(5): p. 756-761.
30. Fu, C., et al., *Synthesis and properties of nitrogen-doped graphene as anode materials for lithium-ion batteries.* Int. J. Electrochem. Sci, 2016. **11**: p. 3876-3886.
31. Du, M., et al., *Synthesis of nitrogen-doped reduced graphene oxide directly from nitrogen-doped graphene oxide as a high-performance lithium ion battery anode.* RSC Adv., 2014. **4**(80): p. 42412-42417.
32. Hummers Jr, W.S. and R.E. Offeman, *Preparation of graphitic oxide.* Journal of the american chemical society, 1958. **80**(6): p. 1339-1339.
33. Zhou, X. and Z. Liu. *Graphene foam as an anode for high-rate Li-ion batteries*. in *IOP Conference Series: Materials Science and Engineering*. 2011.
34. Ji, H., et al., *Ultrathin graphite foam: a three-dimensional conductive network for battery electrodes.* Nano letters, 2012. **12**(5): p. 2446-2451.
35. Ojha, K., O. Anjaneyulu, and A.K. Ganguli, *Graphene-based hybrid materials: synthetic approaches and properties.* Curr Sci, 2014. **107**: p. 397-418.
36. Thema, F., et al., *Synthesis and characterization of graphene thin films by chemical reduction of exfoliated and intercalated graphite oxide.* Journal of chemistry, 2013. **2013**.
37. Zhu, Y., et al., *Graphene and graphene oxide: synthesis, properties, and applications.* Advanced materials, 2010. **22**(35): p. 3906-3924.
38. Zhang, J., et al., *Graphite/graphene oxide composite as high capacity and binder-free anode material for lithium ion batteries.* Journal of Power Sources, 2013. **241**: p. 619-626.
39. Zhang, J., et al., *High-capacity graphene oxide/graphite/carbon nanotube composites for use in Li-ion battery anodes.* Carbon, 2014. **74**: p. 153-162.
40. Mo, R., et al., *Ultradispersed nanoarchitecture of LiV 3 O 8 nanoparticle/reduced graphene oxide with high-capacity and long-life lithium-ion battery cathodes.* Scientific reports, 2016. **6**: p. 19843.
41. Liang, J., et al., *Flexible free-standing graphene/SnO2 nanocomposites paper for Li-ion battery.* ACS applied materials & interfaces, 2012. **4**(11): p. 5742-5748.
42. Yu, A., et al., *Free-standing layer-by-layer hybrid thin film of graphene-MnO2 nanotube as anode for lithium ion batteries.* The Journal of Physical Chemistry Letters, 2011. **2**(15): p. 1855-1860.

43. Wang, R., et al., *Flexible free-standing hollow Fe 3 O 4/graphene hybrid films for lithium-ion batteries.* Journal of Materials Chemistry A, 2013. **1**(5): p. 1794-1800.
44. Wang, B., et al., *Adaptable silicon-carbon nanocables sandwiched between reduced graphene oxide sheets as lithium ion battery anodes.* ACS Nano, 2013. **7**(2): p. 1437-45.
45. Staudenmaier, L., *Verfahren zur darstellung der graphitsäure.* Berichte der deutschen chemischen Gesellschaft, 1898. **31**(2): p. 1481-1487.
46. Kovtyukhova, N.I., et al., *Layer-by-layer assembly of ultrathin composite films from micron-sized graphite oxide sheets and polycations.* Chemistry of materials, 1999. **11**(3): p. 771-778.
47. Marcano, D.C., et al., *Improved Synthesis of Graphene Oxide.* ACS Nano, 2010. **4**(8): p. 4806-4814.
48. Ghobadi, S., et al., *Graphene-reinforced poly (vinyl alcohol) electrospun fibers as building blocks for high performance nanocomposites.* RSC advances, 2015. **5**(103): p. 85009-85018.
49. Sun, J., et al., *Nitrogen-doped holey graphene foams for high-performance lithium storage.* RSC advances, 2015. **5**(111): p. 91114-91119.
50. Yang, Z., et al., *Nanostructures and lithium electrochemical reactivity of lithium titanites and titanium oxides: A review.* Journal of Power Sources, 2009. **192**(2): p. 588-598.
51. Yarali, M., et al., *The effect of pH on the interlayer distances of elongated titanate nanotubes and their use as a Li-ion battery anode.* Nanotechnology, 2015. **27**(1): p. 015401.
52. Yarali, M., et al., *Expansion of titanate nanotubes by the use of a surfactant and its improved performance as an anode in Li-ion batteries.* Electrochimica Acta, 2016. **220**: p. 453-464.
53. Dylla, A.G., J.A. Lee, and K.J. Stevenson, *Influence of mesoporosity on lithium-ion storage capacity and rate performance of nanostructured TiO2 (B).* Langmuir, 2012. **28**(5): p. 2897-2903.
54. Etacheri, V., et al., *Mesoporous TiO 2–B microflowers composed of (1 1 [combining macron] 0) facet-exposed nanosheets for fast reversible lithium-ion storage.* Journal of Materials Chemistry A, 2013. **1**(39): p. 12028-12032.
55. Hu, T., et al., *Flexible free-standing graphene–TiO2 hybrid paper for use as lithium ion battery anode materials.* Carbon, 2013. **51**: p. 322-326.
56. Menéndez, R., et al., *Self-organized amorphous titania nanotubes with deposited graphene film like a new heterostructured electrode for lithium ion batteries.* Journal of Power Sources, 2014. **248**: p. 886-893.
57. Hou, J., et al., *Graphene–TiO2 (B) nanowires composite material: synthesis, characterization and application in lithium-ion batteries.* Materials Letters, 2013. **100**: p. 173-176.
58. Tao, H.-C., et al., *In situ synthesis of TiO2–graphene nanosheets composites as anode materials for high-power lithium ion batteries.* Electrochimica acta, 2012. **69**: p. 328-333.
59. Wang, J., et al., *Fast lithium-ion insertion of TiO2 nanotube and graphene composites.* Electrochimica acta, 2013. **88**: p. 847-857.
60. Wang, J., et al., *A facile one-pot synthesis of TiO2/nitrogen-doped reduced graphene oxide nanocomposite as anode materials for high-rate lithium-ion batteries.* Electrochimica Acta, 2014. **133**: p. 209-216.
61. Zhang, Z., et al., *One-pot solvothermal synthesis of graphene-supported TiO2 (B) nanosheets with enhanced lithium storage properties.* Journal of colloid and interface science, 2013. **409**: p. 38-42.
62. Cai, D., et al., *High rate capability of TiO2/nitrogen-doped graphene nanocomposite as an anode material for lithium–ion batteries.* Journal of alloys and compounds, 2013. **561**: p. 54-58.

63. Gan, Y., et al., *Hybrid nanoarchitecture of rutile TiO2 nanoneedle/graphene for advanced lithium-ion batteries.* Solid State Ionics, 2015. **269**: p. 44-50.
64. Dong, L., et al., *Hydrothermal synthesis of mixed crystal phases TiO2–reduced graphene oxide nanocomposites with small particle size for lithium ion batteries.* international journal of hydrogen energy, 2014. **39**(28): p. 16116-16122.
65. Li, X., et al., *Graphene nanoscrolls encapsulated TiO2 (B) nanowires for lithium storage.* Journal of Power Sources, 2014. **268**: p. 372-378.
66. Qin, G., H. Zhang, and C. Wang, *Ultrasmall TiO2 nanoparticles embedded in nitrogen doped porous graphene for high rate and long life lithium ion batteries.* Journal of Power Sources, 2014. **272**: p. 491-500.
67. Xiu, Z., et al., *Graphene-bonded and-encapsulated mesoporous TiO2 microspheres as a high-performance anode material for lithium ion batteries.* Journal of Power Sources, 2015. **287**: p. 334-340.
68. Adschiri, T., et al., *Hydrothermal synthesis of metal oxide nanoparticles at supercritical conditions.* Journal of Nanoparticle Research, 2001. **3**(2-3): p. 227-235.
69. Hayashi, H. and Y. Hakuta, *Hydrothermal synthesis of metal oxide nanoparticles in supercritical water.* Materials, 2010. **3**(7): p. 3794-3817.
70. Larcher, D., et al., *Recent findings and prospects in the field of pure metals as negative electrodes for Li-ion batteries.* Journal of Materials Chemistry, 2007. **17**(36): p. 3759-3772.
71. Chan, C.K., et al., *High-performance lithium battery anodes using silicon nanowires.* Nature nanotechnology, 2008. **3**(1): p. 31-35.
72. Kim, H., et al., *A critical size of silicon nano-anodes for lithium rechargeable batteries.* Angewandte Chemie International Edition, 2010. **49**(12): p. 2146-2149.
73. He, W., et al., *A facile in situ synthesis of nanocrystal-FeSi-embedded Si/SiOx anode for long-cycle-life lithium ion batteries.* Energy Storage Materials, 2017. **8**: p. 119-126.
74. Chabot, V., et al., *Graphene wrapped silicon nanocomposites for enhanced electrochemical performance in lithium ion batteries.* Electrochimica Acta, 2014. **130**: p. 127-134.
75. Fan, Y., et al., *High performance lithium ion battery anodes based on carbon nanotube–silicon core–shell nanowires with controlled morphology.* Carbon, 2013. **59**: p. 264-269.
76. Luo, J., et al., *Crumpled graphene-encapsulated Si nanoparticles for lithium ion battery anodes.* The journal of physical chemistry letters, 2012. **3**(13): p. 1824-1829.
77. Luo, Z., et al., *Si nanoparticles/graphene composite membrane for high performance silicon anode in lithium ion batteries.* Carbon, 2016. **98**: p. 373-380.
78. Liu, N., et al., *A pomegranate-inspired nanoscale design for large-volume-change lithium battery anodes.* Nature nanotechnology, 2014. **9**(3): p. 187-192.
79. Liu, N., et al., *A yolk-shell design for stabilized and scalable Li-ion battery alloy anodes.* Nano letters, 2012. **12**(6): p. 3315-3321.
80. Ru, Y., et al., *Facile fabrication of yolk–shell structured porous Si–C microspheres as effective anode materials for Li-ion batteries.* Rsc Advances, 2014. **4**(1): p. 71-75.
81. Jiang, J., et al., *Putting Nanoarmors on Yolk–Shell Si@ C Nanoparticles: a reliable engineering way to build better Si-based anodes for Li-ion batteries.* ACS applied materials & interfaces, 2018. **10**(28): p. 24157-24163.
82. Guo, S., et al., *Tunable synthesis of yolk–shell porous silicon@ carbon for optimizing Si/C-based anode of lithium-ion batteries.* ACS applied materials & interfaces, 2017. **9**(48): p. 42084-42092.
83. Huang, X., et al., *HF-free synthesis of Si/C yolk/shell anodes for lithium-ion batteries.* Journal of Materials Chemistry A, 2018. **6**(6): p. 2593-2599.

84. Entwistle, J., A. Rennie, and S. Patwardhan, *A review of magnesiothermic reduction of silica to porous silicon for lithium-ion battery applications and beyond.* Journal of Materials Chemistry A, 2018. **6**(38): p. 18344-18356.
85. Huang, X., et al., *Synthesis of Porous Si/C Composite Nanosheets from Vermiculite with a Hierarchical Structure as a High-Performance Anode for Lithium-Ion Battery.* ACS applied materials & interfaces, 2019. **11**(30): p. 26854-26862.
86. Gao, P., et al., *Porous silicon from the magnesiothermic reaction as a high-performance anode material for lithium ion battery applications.* Electrochimica Acta, 2017. **228**: p. 545-552.
87. Xing, Z., J. Lu, and X. Ji, *A brief review of metallothermic reduction reactions for materials preparation.* Small Methods, 2018. **2**(12): p. 1800062.
88. Kar, M., et al., *Ionic liquid electrolytes as a platform for rechargeable metal–air batteries: a perspective.* Physical chemistry chemical physics, 2014. **16**(35): p. 18658-18674.
89. Semkow, K.W. and A.F. Sammells, *A lithium oxygen secondary battery.* Journal of the Electrochemical Society, 1987. **134**: p. 2084.
90. Abraham, K. and Z. Jiang, *A polymer electrolyte-based rechargeable lithium/oxygen battery.* Journal of The Electrochemical Society, 1996. **143**(1): p. 1-5.
91. Ogasawara, T., et al., *Rechargeable Li2O2 Electrode for Lithium Batteries.* Journal of the American Chemical Society, 2006. **128**(4): p. 1390-1393.
92. Read, J., *Characterization of the Lithium/Oxygen Organic Electrolyte Battery.* Journal of The Electrochemical Society, 2002. **149**(9).
93. Read, J., et al., *Oxygen Transport Properties of Organic Electrolytes and Performance of Lithium/Oxygen Battery.* Journal of The Electrochemical Society, 2003. **150**(10).
94. Lee, J.S., et al., *Metal–air batteries with high energy density: Li–air versus Zn–air.* Advanced Energy Materials, 2011. **1**(1): p. 34-50.
95. Zhong, L., et al., *In situ transmission electron microscopy observations of electrochemical oxidation of Li2O2.* Nano letters, 2013. **13**(5): p. 2209-2214.
96. Gallant, B.M., et al., *Influence of Li2O2 morphology on oxygen reduction and evolution kinetics in Li–O2 batteries.* Energy & Environmental Science, 2013. **6**(8).
97. Xie, J., et al., *Achieving Low Overpotential Li-O(2) Battery Operations by Li(2)O(2) Decomposition through One-Electron Processes.* Nano Lett, 2015. **15**(12): p. 8371-6.
98. Song, S., et al., *Complete decomposition of Li2CO3 in Li–O2 batteries using Ir/B4C as noncarbon-based oxygen electrode.* Nano letters, 2017. **17**(3): p. 1417-1424.
99. Lee, D.J., et al., *Sustainable redox mediation for lithium–oxygen batteries by a composite protective layer on the lithium-metal anode.* Advanced Materials, 2016. **28**(5): p. 857-863.
100. Black, R., et al., *Screening for superoxide reactivity in Li-O2 batteries: effect on Li2O2/LiOH crystallization.* Journal of the American Chemical Society, 2012. **134**(6): p. 2902-2905.
101. Viswanathan, V., et al., *Li-O2 Kinetic Overpotentials: Tafel Plots from Experiment and First-Principles Theory.* J Phys Chem Lett, 2013. **4**(4): p. 556-60.
102. Lu, J., et al., *Aprotic and aqueous Li-O(2) batteries.* Chem Rev, 2014. **114**(11): p. 5611-40.
103. Lu, J., et al., *Aprotic and aqueous Li–O2 batteries.* Chemical reviews, 2014. **114**(11): p. 5611-5640.
104. Nasybulin, E., et al., *Effects of Electrolyte Salts on the Performance of Li–O2 Batteries.* The Journal of Physical Chemistry C, 2013. **117**(6): p. 2635-2645.
105. Xu, W., et al., *Effects of nonaqueous electrolytes on the performance of lithium/air batteries.* Journal of The Electrochemical Society, 2010. **157**(2): p. A219-A224.
106. Xu, W., et al., *The stability of organic solvents and carbon electrode in nonaqueous Li-O2 batteries.* Journal of Power Sources, 2012. **215**: p. 240-247.

107. Johnson, L., et al., *The role of LiO 2 solubility in O 2 reduction in aprotic solvents and its consequences for Li–O 2 batteries.* Nature chemistry, 2014. **6**(12): p. 1091.
108. Elia, G., et al., *An advanced lithium–air battery exploiting an ionic liquid-based electrolyte.* Nano letters, 2014. **14**(11): p. 6572-6577.
109. Xu, W., et al., *Reaction mechanisms for the limited reversibility of Li–O2 chemistry in organic carbonate electrolytes.* Journal of Power Sources, 2011. **196**(22): p. 9631-9639.
110. Xu, W., et al., *Investigation on the charging process of Li2O2-based air electrodes in Li–O2 batteries with organic carbonate electrolytes.* Journal of Power Sources, 2011. **196**(8): p. 3894-3899.
111. Sharon, D., et al., *Oxidation of dimethyl sulfoxide solutions by electrochemical reduction of oxygen.* The Journal of physical chemistry letters, 2013. **4**(18): p. 3115-3119.
112. Lim, H.-D., et al., *Rational design of redox mediators for advanced Li–O 2 batteries.* Nature Energy, 2016. **1**(6): p. 1-9.
113. Bergner, B.J., et al., *How To Improve Capacity and Cycling Stability for Next Generation Li–O2 Batteries: Approach with a Solid Electrolyte and Elevated Redox Mediator Concentrations.* ACS Applied Materials & Interfaces, 2016. **8**(12): p. 7756-7765.
114. Lim, H.-D., et al., *Rational design of redox mediators for advanced Li–O2 batteries.* Nature Energy, 2016. **1**(6): p. 16066.
115. Chen, Y., et al., *Charging a Li–O2 battery using a redox mediator.* Nature Chemistry, 2013. **5**(6): p. 489-494.
116. Kwak, W.-J., et al., *Understanding the behavior of Li–oxygen cells containing LiI.* Journal of Materials Chemistry A, 2015. **3**(16): p. 8855-8864.
117. Aetukuri, N.B., et al., *Solvating additives drive solution-mediated electrochemistry and enhance toroid growth in non-aqueous Li-O(2) batteries.* Nat Chem, 2015. **7**(1): p. 50-6.
118. Shui, J.-L., et al., *Reversibility of anodic lithium in rechargeable lithium–oxygen batteries.* Nature communications, 2013. **4**: p. 2255.
119. Liu, Q.C., et al., *Artificial protection film on lithium metal anode toward long-cycle-life lithium–oxygen batteries.* Advanced Materials, 2015. **27**(35): p. 5241-5247.
120. Freunberger, S.A., et al., *The lithium–oxygen battery with ether-based electrolytes.* Angewandte Chemie International Edition, 2011. **50**(37): p. 8609-8613.
121. Xiao, J., et al., *Optimization of air electrode for Li/air batteries.* Journal of The Electrochemical Society, 2010. **157**(4): p. A487.
122. Beattie, S., D. Manolescu, and S. Blair, *High-capacity lithium–air cathodes.* Journal of the Electrochemical Society, 2008. **156**(1): p. A44.
123. Zhang, S.S., D. Foster, and J. Read, *Discharge characteristic of a non-aqueous electrolyte Li/O2 battery.* Journal of Power Sources, 2010. **195**(4): p. 1235-1240.
124. Zhang, S.S., K. Xu, and J. Read, *A non-aqueous electrolyte for the operation of Li/air battery in ambient environment.* Journal of Power Sources, 2011. **196**(8): p. 3906-3910.
125. Zhang, S.S., X. Ren, and J. Read, *Heat-treated metal phthalocyanine complex as an oxygen reduction catalyst for non-aqueous electrolyte Li/air batteries.* Electrochimica Acta, 2011. **56**(12): p. 4544-4548.
126. Stankovich, S., et al., *Synthesis of graphene-based nanosheets via chemical reduction of exfoliated graphite oxide.* Carbon, 2007. **45**(7): p. 1558-1565.
127. Xiao, J., et al., *Hierarchically porous graphene as a lithium–air battery electrode.* Nano letters, 2011. **11**(11): p. 5071-5078.
128. Li, Y., et al., *Superior energy capacity of graphene nanosheets for a nonaqueous lithium-oxygen battery.* Chemical Communications, 2011. **47**(33): p. 9438-9440.
129. Sun, B., et al., *Graphene nanosheets as cathode catalysts for lithium-air batteries with an enhanced electrochemical performance.* Carbon, 2012. **50**(2): p. 727-733.

130. Wang, B., et al., *Mn3O4 nanoparticles embedded into graphene nanosheets: preparation, characterization, and electrochemical properties for supercapacitors.* Electrochimica Acta, 2010. **55**(22): p. 6812-6817.
131. Wang, L., et al., *CoMn2O4 spinel nanoparticles grown on graphene as bifunctional catalyst for lithium-air batteries.* Journal of The Electrochemical Society, 2011. **158**(12): p. A1379.
132. Wang, S., et al., *Oxygen-enriched carbon material for catalyzing oxygen reduction towards hybrid electrolyte Li-air battery.* Journal of Materials Chemistry, 2012. **22**(39): p. 21051-21056.
133. Cao, Y., et al., *α-MnO 2 nanorods grown in situ on graphene as catalysts for Li–O 2 batteries with excellent electrochemical performance.* Energy & Environmental Science, 2012. **5**(12): p. 9765-9768.
134. Wu, Z.-S., et al., *Graphene Anchored with Co3O4 Nanoparticles as Anode of Lithium Ion Batteries with Enhanced Reversible Capacity and Cyclic Performance.* ACS Nano, 2010. **4**(6): p. 3187-3194.
135. Kim, H., et al., *Highly reversible Co3O4/graphene hybrid anode for lithium rechargeable batteries.* Carbon, 2011. **49**(1): p. 326-332.
136. Paek, S.M., E. Yoo, and I. Honma, *Enhanced cyclic performance and lithium storage capacity of SnO2/graphene nanoporous electrodes with three-dimensionally delaminated flexible structure.* Nano Lett, 2009. **9**(1): p. 72-5.
137. Ding, S., et al., *SnO 2 nanosheets grown on graphene sheets with enhanced lithium storage properties.* Chemical Communications, 2011. **47**(25): p. 7155-7157.
138. Lim, H.-D., et al., *Mechanism of Co3O4/graphene catalytic activity in Li–O2 batteries using carbonate based electrolytes.* Electrochimica Acta, 2013. **90**: p. 63-70.
139. Wang, H., et al., *Rechargeable Li–O 2 batteries with a covalently coupled MnCo 2 O 4–graphene hybrid as an oxygen cathode catalyst.* Energy & Environmental Science, 2012. **5**(7): p. 7931-7935.
140. Cheng, H. and K. Scott, *Carbon-supported manganese oxide nanocatalysts for rechargeable lithium–air batteries.* Journal of Power Sources, 2010. **195**(5): p. 1370-1374.
141. Yang, X.-h., P. He, and Y.-y. Xia, *Preparation of mesocellular carbon foam and its application for lithium/oxygen battery.* Electrochemistry Communications, 2009. **11**(6): p. 1127-1130.
142. Zheng, J., et al., *Theoretical energy density of Li–air batteries.* Journal of the Electrochemical Society, 2008. **155**(6): p. A432.
143. Wang, Z.-L., et al., *Graphene Oxide Gel-Derived, Free-Standing, Hierarchically Porous Carbon for High-Capacity and High-Rate Rechargeable Li-O2 Batteries.* Advanced Functional Materials, 2012. **22**(17): p. 3699-3705.
144. Sergeev, A.V., et al., *Effects of cathode and electrolyte properties on lithium–air battery performance: Computational study.* Journal of Power Sources, 2015. **279**: p. 707-712.
145. Storm, M.M., et al., *Reduced graphene oxide for Li–air batteries: The effect of oxidation time and reduction conditions for graphene oxide.* Carbon, 2015. **85**: p. 233-244.
146. Adhikari, B., A. Biswas, and A. Banerjee, *Graphene oxide-based hydrogels to make metal nanoparticle-containing reduced graphene oxide-based functional hybrid hydrogels.* ACS applied materials & interfaces, 2012. **4**(10): p. 5472-5482.
147. Chabot, V., et al., *A review of graphene and graphene oxide sponge: material synthesis and applications to energy and the environment.* Energy & Environmental Science, 2014. **7**(5): p. 1564-1596.
148. Wang, H., et al., *Three dimensional graphene based materials: Synthesis and applications from energy storage and conversion to electrochemical sensor and environmental remediation.* Adv Colloid Interface Sci, 2015. **221**: p. 41-59.

149. Lei, Y., et al., *Synthesis of three-dimensional graphene oxide foam for the removal of heavy metal ions.* Chemical Physics Letters, 2014. **593**: p. 122-127.
150. Peng, Z., et al., *A reversible and higher-rate Li-O2 battery.* Science, 2012. **337**(6094): p. 563-566.
151. Liang, Y., et al., *Co 3 O 4 nanocrystals on graphene as a synergistic catalyst for oxygen reduction reaction.* Nature materials, 2011. **10**(10): p. 780-786.
152. Cheng, F., et al., *Functional materials for rechargeable batteries.* Advanced Materials, 2011. **23**(15): p. 1695-1715.
153. Cheng, F. and J. Chen, *Metal–air batteries: from oxygen reduction electrochemistry to cathode catalysts.* Chemical Society Reviews, 2012. **41**(6): p. 2172-2192.
154. Li, F., T. Zhang, and H. Zhou, *Challenges of non-aqueous Li–O 2 batteries: electrolytes, catalysts, and anodes.* Energy & Environmental Science, 2013. **6**(4): p. 1125-1141.
155. Ryu, W.-H., et al., *Bifunctional Composite Catalysts Using Co3O4 Nanofibers Immobilized on Nonoxidized Graphene Nanoflakes for High-Capacity and Long-Cycle Li–O2 Batteries.* Nano Letters, 2013. **13**(9): p. 4190-4197.
156. Shao, Y., et al., *Making Li-air batteries rechargeable: Material challenges.* Advanced Functional Materials, 2013. **23**(8): p. 987-1004.
157. Shao, Y., et al., *Electrocatalysts for Nonaqueous Lithium–Air Batteries: Status, Challenges, and Perspective.* ACS Catalysis, 2012. **2**(5): p. 844-857.
158. Oh, S.H., et al., *Synthesis of a metallic mesoporous pyrochlore as a catalyst for lithium–O2 batteries.* Nature Chemistry, 2012. **4**(12): p. 1004-1010.
159. Débart, A., et al., *α-MnO2 nanowires: A catalyst for the O2 electrode in rechargeable lithium batteries.* Angewandte Chemie International Edition, 2008. **47**(24): p. 4521-4524.
160. Truong, T.T., et al., *Morphological and crystalline evolution of nanostructured MnO2 and its application in lithium–air batteries.* ACS nano, 2012. **6**(9): p. 8067-8077.
161. Black, R., et al., *The role of catalysts and peroxide oxidation in lithium-oxygen batteries.* Angew Chem Int Ed Engl, 2013. **52**(1): p. 392-6.
162. Zhang, Z., et al., *A composite of Co nanoparticles highly dispersed on N-rich carbon substrates: an efficient electrocatalyst for Li–O 2 battery cathodes.* Chemical communications, 2014. **50**(7): p. 776-778.
163. Kim, Y.J., et al., *Reduction of charge and discharge polarization by cobalt nanoparticles-embedded carbon nanofibers for Li–O2 batteries.* ChemSusChem, 2015. **8**(15): p. 2496-2502.
164. Vilé, G., et al., *Opposite face sensitivity of CeO2 in hydrogenation and oxidation catalysis.* Angewandte Chemie International Edition, 2014. **53**(45): p. 12069-12072.
165. Chen, G., et al., *Facile and mild strategy to construct mesoporous CeO2–CuO nanorods with enhanced catalytic activity toward CO oxidation.* ACS applied materials & interfaces, 2015. **7**(42): p. 23538-23544.
166. Deori, K., C. Kalita, and S. Deka, *(100) surface-exposed CeO2 nanocubes as an efficient heterogeneous catalyst in the tandem oxidation of benzyl alcohol, para-chlorobenzyl alcohol and toluene to the corresponding aldehydes selectively.* Journal of Materials Chemistry A, 2015. **3**(13): p. 6909-6920.
167. Wu, X., et al., *Effects of adsorbed and gaseous NOx species on catalytic oxidation of diesel soot with MnOx–CeO2 mixed oxides.* Applied Catalysis B: Environmental, 2010. **96**(1): p. 101-109.
168. Carrettin, S., et al., *Nanocrystalline CeO2 Increases the Activity of Au for CO Oxidation by Two Orders of Magnitude.* Angewandte Chemie International Edition, 2004. **43**(19): p. 2538-2540.
169. Laosiripojana, N. and S. Assabumrungrat, *Catalytic dry reforming of methane over high surface area ceria.* Applied Catalysis B: Environmental, 2005. **60**(1-2): p. 107-116.

170. Cargnello, M., et al., *Exceptional activity for methane combustion over modular Pd@ CeO2 subunits on functionalized Al2O3.* Science, 2012. **337**(6095): p. 713-717.
171. Stefanik, T.S. and H.L. Tuller, *Ceria-based gas sensors.* Journal of the European ceramic society, 2001. **21**(10-11): p. 1967-1970.
172. Sharma, S., et al., *CO2 methanation on Ru-doped ceria.* Journal of Catalysis, 2011. **278**(2): p. 297-309.
173. Palma, V., et al., *Oxidative steam reforming of ethanol on mesoporous silica supported PtNi/CeO2 catalysts.* International Journal of Hydrogen Energy, 2017. **42**(3): p. 1598-1608.
174. Zhang, D., et al., *Shape-controlled synthesis and catalytic application of ceria nanomaterials.* Dalton transactions, 2012. **41**(48): p. 14455-14475.
175. Bao, H., et al., *Compositions, structures, and catalytic activities of CeO2@ Cu2O nanocomposites prepared by the template-assisted method.* Langmuir, 2014. **30**(22): p. 6427-6436.
176. Maksimchuk, P., A.A. Masalov, and Y. Malyukin, *Spectroscopically Detected Formation of Oxygen Vacancies in Nano-Crystalline CeO2 – x.* Journal of Nano- and Electronic Physics, 2013. **5**.
177. Choudhury, B., P. Chetri, and A. Choudhury, *Oxygen defects and formation of Ce 3+ affecting the photocatalytic performance of CeO 2 nanoparticles.* RSC Advances, 2014. **4**(9): p. 4663-4671.
178. Wang, X., et al., *Synthesis and shape-dependent catalytic properties of CeO 2 nanocubes and truncated octahedra.* CrystEngComm, 2012. **14**(22): p. 7579-7582.
179. Blanco, G., et al., *Preparation and characterization of Ce□Mn□O composites with applications in catalytic wet oxidation processes.* Surface and Interface Analysis, 2004. **36**(8): p. 752-755.
180. Putla, S., et al., *MnO(x) Nanoparticle-Dispersed CeO2 Nanocubes: A Remarkable Heteronanostructured System with Unusual Structural Characteristics and Superior Catalytic Performance.* ACS Appl Mater Interfaces, 2015. **7**(30): p. 16525-35.
181. Sudarsanam, P., et al., *Designing CuOx Nanoparticles-Decorated CeO2 Nanocubes for Catalytic Soot Oxidation: Role of Nano-interface in the Catalytic Performance of Hetero-structured Nanomaterials.* Langmuir : the ACS journal of surfaces and colloids, 2016. **32**.
182. Walton, R.I., *Solvothermal synthesis of cerium oxides.* Progress in Crystal Growth and Characterization of Materials, 2011. **57**(4): p. 93-108.
183. Devaraju, M.K., et al., *A rapid solvothermal synthesis of cerium oxide hollow spheres and characterization.* Journal of Solid State Chemistry, 2012. **194**: p. 43-47.
184. Sun, C., et al., *Controlled synthesis of CeO2 nanorods by a solvothermal method.* Nanotechnology, 2005. **16**(9): p. 1454.
185. Skorodumova, N., et al., *Quantum origin of the oxygen storage capability of ceria.* Physical Review Letters, 2002. **89**(16): p. 166601.
186. Azalim, S., et al., *Removal of oxygenated volatile organic compounds by catalytic oxidation over Zr–Ce–Mn catalysts.* Journal of hazardous materials, 2011. **188**(1-3): p. 422-427.
187. Martínez-Arias, A., et al., *Comparative study on redox properties of nanosized CeO2 and CuO/CeO2 under CO/O2.* Journal of Catalysis, 2006. **240**(1): p. 1-7.
188. Reddy, B.M., et al., *Highly dispersed ceria and ceria–zirconia nanocomposites over silica surface for catalytic applications.* Catalysis Today, 2009. **141**(1-2): p. 109-114.
189. Lin, X., et al., *Cerium oxides as oxygen reduction catalysts for lithium-air batteries.* Int. J. Electrochem. Sci, 2012. **7**: p. 9550-9559.
190. Joung, D., et al., *Anchoring ceria nanoparticles on reduced graphene oxide and their electronic transport properties.* The Journal of Physical Chemistry C, 2011. **115**(50): p. 24494-24500.

191. Lee, C.-H., et al., *Nitrogen-doped and simultaneously reduced graphene oxide with superior dispersion as electrocatalysts for oxygen reduction reaction.* Materials Research Bulletin, 2014. **59**: p. 145-149.
192. Kim, T., et al., *Lithium-ion batteries: outlook on present, future, and hybridized technologies.* Journal of Materials Chemistry A, 2019. **7**(7): p. 2942-2964.
193. Palacín, M.R. and A. de Guibert, *Why do batteries fail?* Science, 2016. **351**(6273).
194. Goodenough, J.B. and Y. Kim, *Challenges for Rechargeable Li Batteries.* Chemistry of Materials, 2010. **22**(3): p. 587-603.
195. Liu, H.W., et al., *Bridging Covalently Functionalized Black Phosphorus on Graphene for High-Performance Sodium-Ion Battery.* Acs Applied Materials & Interfaces, 2017. **9**(42): p. 36849-36856.
196. Mao, Y., et al., *Lithium storage in nitrogen-rich mesoporous carbon materials.* Energy & Environmental Science, 2012. **5**(7).
197. Tang, Y., et al., *Mechanical Force-Driven Growth of Elongated Bending TiO2-based Nanotubular Materials for Ultrafast Rechargeable Lithium Ion Batteries.* Advanced Materials, 2014. **26**(35): p. 6111-6118.
198. Goriparti, S., et al., *Review on recent progress of nanostructured anode materials for Li-ion batteries.* Journal of Power Sources, 2014. **257**(Supplement C): p. 421-443.
199. Zhang, Y.Q., et al., *On-site evolution of ultrafine ZnO nanoparticles from hollow metal organic frameworks for advanced lithium ion battery anodes.* Journal of Materials Chemistry A, 2017. **5**(43): p. 22512-22518.
200. Li, Z., et al., *LDHs derived nanoparticle-stacked metal nitride as interlayer for long-life lithium sulfur batteries.* Science Bulletin, 2018. **63**(3): p. 169-175.
201. Chen, X.C., et al., *A graphene-based nanostructure with expanded ion transport channels for high rate Li-ion batteries.* Chem Commun (Camb), 2012. **48**(47): p. 5904-6.
202. Mo, R., et al., *High-quality mesoporous graphene particles as high-energy and fast-charging anodes for lithium-ion batteries.* Nat Commun, 2019. **10**(1): p. 1474.
203. Zhang, Y., et al., *Lithiation-Aided Conversion of End-of-Life Lithium-Ion Battery Anodes to High-Quality Graphene and Graphene Oxide.* Nano Lett, 2019. **19**(1): p. 512-519.
204. Kim, S.D., et al., *Additive-free electrode fabrication with reduced graphene oxide using supersonic kinetic spray for flexible lithium-ion batteries.* Carbon, 2018. **139**: p. 195-204.
205. Geng, D., et al., *Nitrogen doping effects on the structure of graphene.* Applied Surface Science, 2011. **257**(21): p. 9193-9198.
206. Yang, S., et al., *Graphene-Based Carbon Nitride Nanosheets as Efficient Metal-Free Electrocatalysts for Oxygen Reduction Reactions.* Angewandte Chemie International Edition, 2011. **50**(23): p. 5339-5343.
207. Wang, H., et al., *Nitrogen-doped graphene nanosheets with excellent lithium storage properties.* Journal of Materials Chemistry, 2011. **21**(14).
208. Mo, R., et al., *3D nitrogen-doped graphene foam with encapsulated germanium/nitrogen-doped graphene yolk-shell nanoarchitecture for high-performance flexible Li-ion battery.* Nature Communications, 2017. **8**(1): p. 13949.
209. Jiang, Y., et al., *Ultrasmall SnS2 nanoparticles anchored on well-distributed nitrogen-doped graphene sheets for Li-ion and Na-ion batteries.* Journal of Materials Chemistry A, 2016. **4**(27): p. 10719-10726.
210. Chang, Y., et al., *Synthesis of 3D nitrogen-doped graphene/Fe3O4 by a metal ion induced self-assembly process for high-performance Li-ion batteries.* Journal of Materials Chemistry A, 2013. **1**(46): p. 14658-14665.
211. Qi, H., et al., *High Pseudocapacitance in FeOOH/rGO Composites with Superior Performance for High Rate Anode in Li-Ion Battery.* ACS Applied Materials & Interfaces, 2016. **8**(51): p. 35253-35263.

212. Li, J., et al., *N-doped TiO2/rGO hybrids as superior Li-ion battery anodes with enhanced Li-ions storage capacity.* Journal of Alloys and Compounds, 2019. **784**: p. 165-172.
213. Gomez-Martin, A., et al., *An electrochemical evaluation of nitrogen-doped carbons as anodes for lithium ion batteries.* Carbon, 2020. **164**: p. 261-271.
214. Wang, L., Z. Sofer, and M. Pumera, *Will Any Crap We Put into Graphene Increase Its Electrocatalytic Effect?* ACS Nano, 2020. **14**(1): p. 21-25.
215. Wu, Z.-S., et al., *Doped Graphene Sheets As Anode Materials with Superhigh Rate and Large Capacity for Lithium Ion Batteries.* ACS Nano, 2011. **5**(7): p. 5463-5471.
216. Fu, C., et al., *Evaluation and Characterization of Reduced Graphene Oxide Nanosheets as Anode Materials for Lithium-Ion Batteries.* International Journal of Electrochemical Science, 2013. **8**: p. 6269-6280.
217. Ma, C., X. Shao, and D. Cao, *Nitrogen-doped graphene nanosheets as anode materials for lithium ion batteries: a first-principles study.* Journal of Materials Chemistry, 2012. **22**(18): p. 8911-8915.
218. Wang, H., et al., *Nitrogen-doped graphene nanosheets with excellent lithium storage properties.* Journal of Materials Chemistry, 2011. **21**(14): p. 5430-5434.
219. Wang, H., T. Maiyalagan, and X. Wang, *Review on Recent Progress in Nitrogen-Doped Graphene: Synthesis, Characterization, and Its Potential Applications.* ACS Catalysis, 2012. **2**(5): p. 781-794.
220. Wang, J., et al., *A facile one-pot synthesis of TiO2/nitrogen-doped reduced graphene oxide nanocomposite as anode materials for high-rate lithium-ion batteries.* Electrochimica Acta, 2014. **133**(Supplement C): p. 209-216.
221. Cai, D., et al., *High rate capability of TiO2/nitrogen-doped graphene nanocomposite as an anode material for lithium–ion batteries.* Journal of Alloys and Compounds, 2013. **561**(Supplement C): p. 54-58.
222. Ghobadi, S., et al., *Green Composite Papers via Use of Natural Binders and Graphene for PEM Fuel Cell Electrodes.* ACS Sustainable Chemistry & Engineering, 2017. **5**(9): p. 8407-8415.
223. Xiang, G., et al., *Large-scale synthesis of metastable TiO2(B) nanosheets with atomic thickness and their photocatalytic properties.* Chemical Communications, 2010. **46**(36): p. 6801-6803.
224. Dylla, A.G., J.A. Lee, and K.J. Stevenson, *Influence of Mesoporosity on Lithium-Ion Storage Capacity and Rate Performance of Nanostructured TiO2(B).* Langmuir, 2012. **28**(5): p. 2897-2903.
225. Etacheri, V., et al., *Mesoporous TiO2-B microflowers composed of (1 [1 with combining macron] 0) facet-exposed nanosheets for fast reversible lithium-ion storage.* Journal of Materials Chemistry A, 2013. **1**(39): p. 12028-12032.
226. Gao, L., et al., *TiO2 mesoporous microspheres with nanorod structure: facile synthesis and superior electrochemical performance.* Electrochimica Acta, 2014. **120**: p. 231-239.
227. Etacheri, V., J.E. Yourey, and B.M. Bartlett, *Chemically Bonded TiO2–Bronze Nanosheet/Reduced Graphene Oxide Hybrid for High-Power Lithium Ion Batteries.* ACS Nano, 2014. **8**(2): p. 1491-1499.
228. Goriparti, S., et al., *Direct Synthesis of Carbon-Doped TiO2–Bronze Nanowires as Anode Materials for High Performance Lithium-Ion Batteries.* ACS Applied Materials & Interfaces, 2015. **7**(45): p. 25139-25146.
229. Qiu, J., et al., *Photocatalytic Synthesis of TiO2 and Reduced Graphene Oxide Nanocomposite for Lithium Ion Battery.* ACS Applied Materials & Interfaces, 2012. **4**(7): p. 3636-3642.
230. Wang, D., et al., *Self-Assembled TiO2–Graphene Hybrid Nanostructures for Enhanced Li-Ion Insertion.* ACS Nano, 2009. **3**(4): p. 907-914.

231. Li, S.L., et al., *Comparison of Si/C, Ge/C and Sn/C composite nanofiber anodes used in advanced lithium-ion batteries.* Solid State Ionics, 2014. **254**: p. 17-26.
232. Liu, N., et al., *A Yolk-Shell Design for Stabilized and Scalable Li-Ion Battery Alloy Anodes.* Nano Letters, 2012. **12**(6): p. 3315-3321.
233. Chan, C.K., et al., *High-performance lithium battery anodes using silicon nanowires.* Nature Nanotechnology, 2008. **3**(1): p. 31-35.
234. Szczech, J.R. and S. Jin, *Nanostructured silicon for high capacity lithium battery anodes.* Energy & Environmental Science, 2011. **4**(1): p. 56-72.
235. Wen, Z.H., et al., *Silicon nanotube anode for lithium-ion batteries.* Electrochemistry Communications, 2013. **29**: p. 67-70.
236. Wu, H., et al., *Stable cycling of double-walled silicon nanotube battery anodes through solid-electrolyte interphase control.* Nature Nanotechnology, 2012. **7**(5): p. 309-314.
237. Cui, L.F., et al., *Light-Weight Free-Standing Carbon Nanotube-Silicon Films for Anodes of Lithium Ion Batteries.* Acs Nano, 2010. **4**(7): p. 3671-3678.
238. Ji, L.W. and X.W. Zhang, *Electrospun carbon nanofibers containing silicon particles as an energy-storage medium.* Carbon, 2009. **47**(14): p. 3219-3226.
239. Park, S.H., et al., *Spray-Assisted Deep-Frying Process for the In Situ Spherical Assembly of Graphene for Energy-Storage Devices.* Chemistry of Materials, 2015. **27**(2): p. 457-465.
240. Luo, J.Y., et al., *Crumpled Graphene-Encapsulated Si Nanoparticles for Lithium Ion Battery Anodes.* Journal of Physical Chemistry Letters, 2012. **3**(13): p. 1824-1829.
241. Gan, L., et al., *A facile synthesis of graphite/silicon/graphene spherical composite anode for lithium-ion batteries.* Electrochimica Acta, 2013. **104**: p. 117-123.
242. Kim, S.K., et al., *One-Step Formation of Silicon-Graphene Composites from Silicon Sludge Waste and Graphene Oxide via Aerosol Process for Lithium Ion Batteries.* Scientific Reports, 2016. **6**.
243. Liu, Y.J., et al., *An All-Integrated Anode via Interlinked Chemical Bonding between Double-Shelled-Yolk-Structured Silicon and Binder for Lithium-Ion Batteries.* Advanced Materials, 2017. **29**(44).
244. Chang, J.B., et al., *Multilayered Si Nanoparticle/Reduced Graphene Oxide Hybrid as a High-Performance Lithium-Ion Battery Anode.* Advanced Materials, 2014. **26**(5): p. 758-764.
245. Zhao, X., et al., *In-Plane Vacancy-Enabled High-Power Si-Graphene Composite Electrode for Lithium-Ion Batteries.* Advanced Energy Materials, 2011. **1**(6): p. 1079-1084.
246. An, G.H., H. Kim, and H.J. Ahn, *Improved Ionic Diffusion through the Mesoporous Carbon Skin on Silicon Nanoparticles Embedded in Carbon for Ultrafast Lithium Storage.* Acs Applied Materials & Interfaces, 2018. **10**(7): p. 6235-6244.
247. Wu, J.X., et al., *Multilayered silicon embedded porous carbon/graphene hybrid film as a high performance anode.* Carbon, 2015. **84**: p. 434-443.
248. Syed, N., N. Sharma, and L. Kumar, *Synthesis of Graphene Oxide (GO) by Modified Hummers Method and Its Thermal Reduction to Obtain Reduced Graphene Oxide (rGO) * Open Access.* Graphene, 2017. **6**: p. 1-18.
249. Hu, T., et al., *Rapid synthesis of nitrogen-doped graphene for a lithium ion battery anode with excellent rate performance and super-long cyclic stability.* Physical Chemistry Chemical Physics, 2014. **16**(3): p. 1060-1066.
250. Kaniyoor, A. and R. Sundara, *A Raman spectroscopic investigation of graphite oxide derived graphene.* AIP Advances, 2012. **2**: p. 032183-032183.
251. Beams, R., L. Gustavo Cançado, and L. Novotny, *Raman characterization of defects and dopants in graphene.* Journal of Physics: Condensed Matter, 2015. **27**(8): p. 083002.

252. Zhou, Y., et al., *Hydrothermal Dehydration for the "Green" Reduction of Exfoliated Graphene Oxide to Graphene and Demonstration of Tunable Optical Limiting Properties.* Chemistry of Materials, 2009. **21**(13): p. 2950-2956.
253. Chen, W., L. Yan, and P.R. Bangal, *Preparation of graphene by the rapid and mild thermal reduction of graphene oxide induced by microwaves.* Carbon, 2010. **48**(4): p. 1146-1152.
254. Park, O.-K., et al., *Defect healing of reduced graphene oxide via intramolecular cross-dehydrogenative coupling.* Nanotechnology, 2013. **24**(18): p. 185604.
255. Bharathidasan, P., S. Devaraj, and S.R. Sivakkumar, *The capacitance properties of nitrogen doped reduced graphene oxide obtained by using commercial protein powder as a nitrogen dopant.* Journal of Solid State Electrochemistry, 2020. **24**(5): p. 1095-1103.
256. Zheng, Y., et al., *Two-Step Boron and Nitrogen Doping in Graphene for Enhanced Synergistic Catalysis.* Angewandte Chemie International Edition, 2013. **52**(11): p. 3110-3116.
257. Xu, Y., et al., *Highly nitrogen doped carbon nanofibers with superior rate capability and cyclability for potassium ion batteries.* Nature Communications, 2018. **9**(1): p. 1720.
258. Chen, C., et al., *Reduction of graphene oxide by an in-situ photoelectrochemical method in a dye-sensitized solar cell assembly.* Nanoscale Research Letters, 2012. **7**(1): p. 101.
259. Ganguly, A., et al., *Probing the Thermal Deoxygenation of Graphene Oxide Using High-Resolution In Situ X-ray-Based Spectroscopies.* The Journal of Physical Chemistry C, 2011. **115**(34): p. 17009-17019.
260. Saha, D., et al., *CO2 capture in lignin-derived and nitrogen-doped hierarchical porous carbons.* Carbon, 2017. **121**: p. 257-266.
261. Aliyev, E., et al., *Structural Characterization of Graphene Oxide: Surface Functional Groups and Fractionated Oxidative Debris.* Nanomaterials (Basel), 2019. **9**(8).
262. Reddy, A.L., et al., *Synthesis of nitrogen-doped graphene films for lithium battery application.* ACS Nano, 2010. **4**(11): p. 6337-42.
263. Xu, B., et al., *Lithium-storage Properties of Gallic Acid-Reduced Graphene Oxide and Silicon-Graphene Composites.* Electrochimica Acta, 2016. **212**: p. 473-480.
264. Zhao, C., et al., *Reduction of graphene oxide in Li-ion batteries.* Journal of Materials Chemistry A, 2015. **3**(36): p. 18360-18364.
265. Wang, J., et al., *Copper ferrites@ reduced graphene oxide anode materials for advanced lithium storage applications.* Scientific reports, 2017. **7**(1): p. 1-12.
266. Xiao, M., et al., *Tailoring nitrogen content in doped carbon by a facile synthesis with ionic liquid precursors for lithium ion batteries.* Applied Surface Science, 2019. **494**: p. 532-539.
267. Liu, W.-R., et al., *Characterization and electrochemical behavior of graphene-based anode for Li-ion batteries.* The Open Materials Science Journal, 2011. **5**(1).
268. Du, M., et al., *Synthesis of nitrogen-doped reduced graphene oxide directly from nitrogen-doped graphene oxide as a high-performance lithium ion battery anode.* RSC Advances, 2014. **4**(80): p. 42412-42417.
269. Namsar, O., et al., *Improved electrochemical performance of anode materials for high energy density lithium-ion batteries through Sn(SnO2)–SiO2/graphene-based nanocomposites prepared by a facile and low-cost approach.* Sustainable Energy & Fuels, 2020.
270. Nolan, H., et al., *Nitrogen-doped reduced graphene oxide electrodes for electrochemical supercapacitors.* Phys Chem Chem Phys, 2014. **16**(6): p. 2280-4.
271. Guo, W., et al., *Growth of Highly Nitrogen-Doped Amorphous Carbon for Lithium-ion Battery Anode.* Electrochimica Acta, 2016. **188**: p. 414-420.
272. Li, X., et al., *Superior cycle stability of nitrogen-doped graphene nanosheets as anodes for lithium ion batteries.* Electrochemistry Communications, 2011. **13**(8): p. 822-825.

273. Guo, L., et al., *Nitrogen-doped porous carbon spheres anchored with Co3O4 nanoparticles as high-performance anode materials for lithium-ion batteries.* Electrochimica Acta, 2016. **187**: p. 234-242.
274. Jiang, Z.-J. and Z. Jiang, *Fabrication of Nitrogen-Doped Holey Graphene Hollow Microspheres and Their Use as an Active Electrode Material for Lithium Ion Batteries.* ACS Applied Materials & Interfaces, 2014. **6**(21): p. 19082-19091.
275. Yarali, M., et al., *Expansion of titanate nanotubes by the use of a surfactant and its improved performance as an anode in Li-ion batteries.* Electrochimica Acta, 2016. **220**: p. 453-464.
276. Miad, Y., et al., *The effect of pH on the interlayer distances of elongated titanate nanotubes and their use as a Li-ion battery anode.* Nanotechnology, 2016. **27**(1): p. 015401.
277. Li, N., et al., *Battery Performance and Photocatalytic Activity of Mesoporous Anatase TiO2 Nanospheres/Graphene Composites by Template-Free Self-Assembly.* Advanced Functional Materials, 2011. **21**(9): p. 1717-1722.
278. Tang, Y., et al., *TiO2(B) nanowire arrays on Ti foil substrate as three-dimensional anode for lithium-ion batteries.* Electrochimica Acta, 2016. **195**(Supplement C): p. 27-33.
279. Yan, X., et al., *Effect of Anatase TiO2 on Electrochemical Properties of Elongated Bending TiO2-Bronze nanowires for Lithium Ion Batteries.* Electrochimica Acta, 2016. **191**(Supplement C): p. 661-668.
280. Wei, D., et al., *Synthesis of N-Doped Graphene by Chemical Vapor Deposition and Its Electrical Properties.* Nano Letters, 2009. **9**(5): p. 1752-1758.
281. Jun, G.H., et al., *Enhanced conduction and charge-selectivity by N-doped graphene flakes in the active layer of bulk-heterojunction organic solar cells.* Energy & Environmental Science, 2013. **6**(10): p. 3000-3006.
282. Yang, D., et al., *Chemical analysis of graphene oxide films after heat and chemical treatments by X-ray photoelectron and Micro-Raman spectroscopy.* Carbon, 2009. **47**(1): p. 145-152.
283. Hernández-Hipólito, P., et al., *Novel heterogeneous basic catalysts for biodiesel production: Sodium titanate nanotubes doped with potassium.* Catalysis Today, 2015. **250**(Supplement C): p. 187-196.
284. Morgado, E., et al., *Characterization of Nanostructured Titanates Obtained by Alkali Treatment of TiO2-Anatases with Distinct Crystal Sizes.* Chemistry of Materials, 2007. **19**(4): p. 665-676.
285. ALOthman, Z., *A Review: Fundamental Aspects of Silicate Mesoporous Materials.* Materials, 2012. **5**(12): p. 2874.
286. Chen, C., et al., *TiO2–B Nanosheets/Anatase Nanocrystals Co-Anchored on Nanoporous Graphene: In Situ Reduction–Hydrolysis Synthesis and Their Superior Rate Performance as an Anode Material.* Chemistry – A European Journal, 2014. **20**(5): p. 1383-1388.
287. Zukalová, M., et al., *Pseudocapacitive Lithium Storage in TiO2(B).* Chemistry of Materials, 2005. **17**(5): p. 1248-1255.
288. Li, J., Z. Tang, and Z. Zhang, *Pseudocapacitive characteristic of lithium ion storage in hydrogen titanate nanotubes.* Chemical Physics Letters, 2006. **418**(4): p. 506-510.
289. Zhang, H., et al., *Electrochemical lithium storage of sodium titanate nanotubes and nanorods.* Electrochimica Acta, 2008. **53**(24): p. 7061-7068.
290. Kavan, L., et al., *Lithium Storage in Nanostructured TiO2 Made by Hydrothermal Growth.* Chemistry of Materials, 2004. **16**(3): p. 477-485.
291. Armstrong, A.R., et al., *Lithium-Ion Intercalation into TiO2-B Nanowires.* Advanced Materials, 2005. **17**(7): p. 862-865.

292. Augustyn, V., P. Simon, and B. Dunn, *Pseudocapacitive oxide materials for high-rate electrochemical energy storage.* Energy & Environmental Science, 2014. **7**(5): p. 1597-1614.
293. Yu, Z.H., L. Wang, and L.H. Jiang, *Design and synthesis of N-doped graphene sheets loaded with Li4Ti5O12 nanocrystals as advanced anode material for Li-ion batteries.* Ceramics International, 2016. **42**(14): p. 16031-16039.
294. Wei, A.J., et al., *Enhanced electrochemical performance of a LTO/N-doped graphene composite as an anode material for Li-ion batteries.* Solid State Ionics, 2017. **311**: p. 98-104.
295. Jiang, S., et al., *Enhanced conductivity and electrochemical performance of conformal mesoporous N/C co-decorated TiO2-RGO composites for lithium ion batteries.* Journal of Alloys and Compounds, 2017. **710**: p. 784-793.
296. Xu, H., L. Ma, and Z. Jin, *Nitrogen-doped graphene: Synthesis, characterizations and energy applications.* Journal of Energy Chemistry, 2018. **27**(1): p. 146-160.
297. Zhang, L.S., et al., *Identification of the nitrogen species on N-doped graphene layers and Pt/NG composite catalyst for direct methanol fuel cell.* Physical Chemistry Chemical Physics, 2010. **12**(38): p. 12055-12059.
298. Gohari-Bajestani, Z., et al., *Synthesis of anatase TiO2 with exposed (001) facets grown on N-doped reduced graphene oxide for enhanced hydrogen storage.* International Journal of Hydrogen Energy, 2017. **42**(9): p. 6096-6103.
299. Pan, D.H., et al., *In situ fabrication of nickel based oxide on nitrogen-doped graphene for high electrochemical performance supercapacitors.* Chemical Physics Letters, 2017. **685**: p. 457-464.
300. Lherbier, A., et al., *Charge transport in chemically doped 2D graphene.* Physical Review Letters, 2008. **101**(3).
301. Moon, I.K., et al., *Highly Elastic and Conductive N-Doped Monolithic Graphene Aerogels for Multifunctional Applications.* Advanced Functional Materials, 2015. **25**(45): p. 6976-6984.
302. Wu, Z.S., et al., *Doped Graphene Sheets As Anode Materials with Superhigh Rate and Large Capacity for Lithium Ion Batteries.* Acs Nano, 2011. **5**(7): p. 5463-5471.
303. Yu, H., et al., *Green Synthesis of Porous Three-Dimensional Nitrogen-Doped Graphene Foam for Electrochemical Applications.* Acs Applied Materials & Interfaces, 2016. **8**(4): p. 2505-2510.
304. Kim, B.-R., et al., *Effect of anatase phase on electrochemical properties of the TiO2(B) negative electrode for lithium-ion battery application.* Current Applied Physics, 2013. **13**(Supplement 2): p. S148-S151.
305. Lee, J., et al., *Electrochemical Investigations on TiO2-B Nanowires as a Promising High Capacity Anode for Sodium-ion Batteries.* Electrochimica Acta, 2016. **200**: p. 21-28.
306. Yang, Z.G., et al., *Electrochemical Energy Storage for Green Grid.* Chemical Reviews, 2011. **111**(5): p. 3577-3613.
307. Mason, C.W., et al., *Interconnected nanofibrous titanium dioxide bronze: an emerging lithium ion anode material for high rate performance.* RSC Advances, 2013. **3**(9): p. 2935-2941.
308. Qiu, W., et al., *L-Cysteine-Assisted Synthesis of Cubic Pyrite/Nitrogen-Doped Graphene Composite as Anode Material for Lithium-ion Batteries.* Electrochimica Acta, 2014. **137**(Supplement C): p. 197-205.
309. Xia, S., et al., *Ultrathin MoS2 nanosheets tightly anchoring onto nitrogen-doped graphene for enhanced lithium storage properties.* Chemical Engineering Journal, 2018. **332**(Supplement C): p. 431-439.

310. Shekarriz, M., et al., *Systematic synthesis of high surface area silica nanoparticles in the sol-gel condition by using the central composite design (CCD) method.* Canadian Journal of Chemical Engineering, 2014. **92**(5): p. 828-834.
311. Bajestani, Z.G., A. Yurum, and Y. Yurum, *Decoration of graphene sheets with Pd/Al2O3 hybrid particles for hydrogen storage applications.* International Journal of Hydrogen Energy, 2016. **41**(23): p. 9810-9818.
312. Richman, E.K., et al., *Ordered mesoporous silicon through magnesium reduction of polymer templated silica thin films.* Nano Letters, 2008. **8**(9): p. 3075-3079.
313. Cho, W.C., et al., *5L-Scale Magnesio-Milling Reduction of Nanostructured SiO2 for High Capacity Silicon Anodes in Lithium-Ion Batteries.* Nano Letters, 2016. **16**(11): p. 7261-7269.
314. Wissel, K., et al., *Synthesis of 3D silicon with tailored nanostructure: Influence of morphology on the electrochemical properties.* Solid State Ionics, 2017. **302**: p. 180-185.
315. Chen, W., et al., *Mesoporous Silicon Anodes Prepared by Magnesiothermic Reduction for Lithium Ion Batteries.* Journal of the Electrochemical Society, 2011. **158**(9): p. A1055-A1059.
316. Kim, K.H., et al., *Complete magnesiothermic reduction reaction of vertically aligned mesoporous silica channels to form pure silicon nanoparticles.* Scientific Reports, 2015. **5**.
317. Ju, H.M., S.H. Choi, and S.H. Huh, *X-ray Diffraction Patterns of Thermally-reduced Graphenes.* Journal of the Korean Physical Society, 2010. **57**(6): p. 1649-1652.
318. Li, Q., L.W. Yin, and X.P. Gao, *Reduction chemical reaction synthesized scalable 3D porous silicon/carbon hybrid architectures as anode materials for lithium ion batteries with enhanced electrochemical performance.* Rsc Advances, 2015. **5**(45): p. 35598-35607.
319. Yuksel, R., et al., *All-carbon hybrids for high performance supercapacitors.* International Journal of Energy Research, 2018. **42**(11): p. 3575-3587.
320. Yang, S., et al., *Research on the icephobic properties of fluoropolymer-based materials.* Applied Surface Science, 2011. **257**(11): p. 4956-4962.
321. Baysal, M., et al., *Structure of some western Anatolia coals investigated by FTIR, Raman, C-13 solid state NMR spectroscopy and X-ray diffraction.* International Journal of Coal Geology, 2016. **163**: p. 166-176.
322. Diaz-Torres, E., et al., *Formation and characterization of porous silicon films obtained by catalyzed vapor-chemical etching.* Materials Science in Semiconductor Processing, 2015. **40**: p. 533-538.
323. Tseng, M.C., et al., *Silicon films deposited on flexible substrate by hot-wire chemical-vapor deposition.* Vacuum, 2015. **118**: p. 109-112.
324. Droz, C., et al., *Relationship between Raman crystallinity and open-circuit voltage in microcrystalline silicon solar cells.* Solar Energy Materials and Solar Cells, 2004. **81**(1): p. 61-71.
325. Guo, M.Y., et al., *Fabrication of high surface area mesoporous silicon via magnesiothermic reduction for drug delivery.* Microporous and Mesoporous Materials, 2011. **142**(1): p. 194-201.
326. Gao, P.B., et al., *Porous silicon from the magnesiothermic reaction as a high-performance anode material for lithium ion battery applications.* Electrochimica Acta, 2017. **228**: p. 545-552.
327. Han, Y., et al., *An amorphous Si material with a sponge-like structure as an anode for Li-ion and Na-ion batteries.* Nanoscale, 2018. **10**(7): p. 3153-3158.
328. Pei, S.F. and H.M. Cheng, *The reduction of graphene oxide.* Carbon, 2012. **50**(9): p. 3210-3228.

329. Pandit, B., et al., *Changes in physical properties of graphene oxide with thermal reduction.* Journal of the Korean Physical Society, 2017. **71**(3): p. 156-160.
330. Ferrari, A.C. and J. Robertson, *Interpretation of Raman spectra of disordered and amorphous carbon.* Physical Review B, 2000. **61**(20): p. 14095-14107.
331. Cancado, L.G., et al., *General equation for the determination of the crystallite size L-a of nanographite by Raman spectroscopy.* Applied Physics Letters, 2006. **88**(16).
332. Gayathri, S., et al., *Synthesis of few layer graphene by direct exfoliation of graphite and a Raman spectroscopic study.* Aip Advances, 2014. **4**(2).
333. Finnie, K.S., et al., *Formation of silica nanoparticles in microemulsions.* Langmuir, 2007. **23**(6): p. 3017-3024.
334. Zulfiqar, U., T. Subhani, and S.W. Husain, *Synthesis of silica nanoparticles from sodium silicate under alkaline conditions.* Journal of Sol-Gel Science and Technology, 2016. **77**(3): p. 753-758.
335. Kannan, A.G., et al., *Silicon nanoparticles grown on a reduced graphene oxide surface as high-performance anode materials for lithium-ion batteries.* Rsc Advances, 2016. **6**(30): p. 25159-25166.
336. Chen, Y.F., et al., *Firmly bonded graphene-silicon nanocomposites as high-performance anode materials for lithium-ion batteries.* Rsc Advances, 2015. **5**(57): p. 46173-46180.
337. Hou, J.H., et al., *Hierarchical Porous Nitrogen-Doped Carbon Nanosheets Derived from Silk for Ultrahigh-Capacity Battery Anodes and Supercapacitors.* Acs Nano, 2015. **9**(3): p. 2556-2564.
338. Greco, E., et al., *Few-layer graphene improves silicon performance in Li-ion battery anodes.* Journal of Materials Chemistry A, 2017. **5**(36): p. 19306-19315.
339. Beattie, S.D., et al., *Understanding capacity fade in silicon based electrodes for lithium-ion batteries using three electrode cells and upper cut-off voltage studies.* Journal of Power Sources, 2016. **302**: p. 426-430.
340. Xiao, C., et al., *Walnut-structure Si–G/C materials with high coulombic efficiency for long-life lithium ion batteries.* Rsc Advances, 2018. **8**(48): p. 27580-27586.
341. Chen, D., et al., *Facile synthesis of graphene-silicon nanocomposites with an advanced binder for high-performance lithium-ion battery anodes.* Solid State Ionics, 2014. **254**: p. 65-71.
342. Pan, Q.R., et al., *Micro-sized spherical silicon@carbon@graphene prepared by spray drying as anode material for lithium-ion batteries.* Journal of Alloys and Compounds, 2017. **723**: p. 434-440.
343. Li, X.F., et al., *Three-Dimensional Porous Core-Shell Sn@Carbon Composite Anodes for High-Performance Lithium-Ion Battery Applications.* Advanced Energy Materials, 2012. **2**(2): p. 238-244.
344. Bruce, P., et al., *O2 and Li-S batteries with high energy density.* Nat. Mater, 2012. **11**: p. 19-29.
345. Chang, Z.-w., et al., *Recent Progress on Stability Enhancement for Cathode in Rechargeable Non-Aqueous Lithium-Oxygen Battery.* Advanced Energy Materials, 2015. **5**(21).
346. Etacheri, V., et al., *Challenges in the development of advanced Li-ion batteries: a review.* Energy & Environmental Science, 2011. **4**(9): p. 3243-3262.
347. Zhang, K., et al., *Recent developments of the lithium metal anode for rechargeable non-aqueous batteries.* Advanced Energy Materials, 2016. **6**(20): p. 1600811.
348. Ma, Z., et al., *A review of cathode materials and structures for rechargeable lithium–air batteries.* Energy & Environmental Science, 2015. **8**(8): p. 2144-2198.
349. Chen, P., et al., *A nitrogen-doped graphene/carbon nanotube nanocomposite with synergistically enhanced electrochemical activity.* Adv Mater, 2013. **25**(23): p. 3192-6.

350. Liu, M., et al., *Rationally Designed Three-Dimensional N-Doped Graphene Architecture Mounted with Ru Nanoclusters as a High-Performance Air Cathode for Lithium–Oxygen Batteries.* ACS Sustainable Chemistry & Engineering, 2020. **8**(15): p. 6109-6117.
351. Park, C.S., K.S. Kim, and Y.J. Park, *Carbon-sphere/Co3O4 nanocomposite catalysts for effective air electrode in Li/air batteries.* Journal of Power Sources, 2013. **244**: p. 72-79.
352. Kim, D.S. and Y.J. Park, *Ketjen black/Co3O4 nanocomposite prepared using polydopamine pre-coating layer as a reaction agent: Effective catalyst for air electrodes of Li/air batteries.* Journal of Alloys and Compounds, 2013. **575**: p. 319-325.
353. Riaz, A., et al., *Carbon-free cobalt oxide cathodes with tunable nanoarchitectures for rechargeable lithium–oxygen batteries.* Chemical Communications, 2013. **49**(53): p. 5984-5986.
354. Tu, F., et al., *Mushroom-like Au/NiCo 2 O 4 nanohybrids as high-performance binder-free catalytic cathodes for lithium–oxygen batteries.* Journal of Materials Chemistry A, 2015. **3**(10): p. 5714-5721.
355. Li, Y., et al., *Synthesis of ordered mesoporous NiCo2O4 via hard template and its application as bifunctional electrocatalyst for Li-O2 batteries.* Electrochimica Acta, 2014. **129**: p. 14-20.
356. Kim, C.H. and L.T. Thompson, *On the importance of nanocrystalline gold for Au/CeO2 water-gas shift catalysts.* Journal of Catalysis, 2006. **244**(2): p. 248-250.
357. Kempaiah, D.M., S. Yin, and T. Sato, *A facile and quick solvothermal synthesis of 3D microflower CeO2 and Gd:CeO2 under subcritical and supercritical conditions for catalytic applications.* CrystEngComm, 2011. **13**(3): p. 741-746.
358. Özer, N., *Optical properties and electrochromic characterization of sol–gel deposited ceria films.* Solar Energy Materials and Solar Cells, 2001. **68**(3): p. 391-400.
359. Morimoto, T., H. Tomonaga, and A. Mitani, *Ultraviolet ray absorbing coatings on glass for automobiles.* Thin Solid Films, 1999. **351**: p. 61-65.
360. Adijanto, L., et al., *Synthesis and Stability of Pd@CeO2 Core–Shell Catalyst Films in Solid Oxide Fuel Cell Anodes.* ACS Catalysis, 2013. **3**(8): p. 1801-1809.
361. Campbell, C.T. and C.H. Peden, *Chemistry. Oxygen vacancies and catalysis on ceria surfaces.* Science, 2005. **309**(5735): p. 713-4.
362. Trovarelli, A., *Catalysis by Ceria and Related Materials*. Catalysis by Ceria and Related Materials.
363. González-Rovira, L., et al., *Single-Step Process To Prepare CeO2 Nanotubes with Improved Catalytic Activity.* Nano Letters, 2009. **9**(6): p. 2511-2511.
364. Sun, C., H. Li, and L. Chen, *Nanostructured ceria-based materials: synthesis, properties, and applications.* Energy & Environmental Science, 2012. **5**(9): p. 8475-8505.
365. Sayle, D.C., S.A. Maicaneanu, and G.W. Watson, *Atomistic models for CeO2 (111),(110), and (100) nanoparticles, supported on yttrium-stabilized zirconia.* Journal of the American Chemical Society, 2002. **124**(38): p. 11429-11439.
366. Jiang, Y., J.B. Adams, and M. van Schilfgaarde, *Density-functional calculation of CeO2 surfaces and prediction of effects of oxygen partial pressure and temperature on stabilities.* J Chem Phys, 2005. **123**(6): p. 64701.
367. Wu, Z., et al., *Probing Defect Sites on CeO2 Nanocrystals with Well-Defined Surface Planes by Raman Spectroscopy and O2 Adsorption.* Langmuir, 2010. **26**(21): p. 16595-16606.
368. Yu, M., et al., *Integrating a redox-coupled dye-sensitized photoelectrode into a lithium–oxygen battery for photoassisted charging.* Nature communications, 2014. **5**: p. 5111.
369. Rezvani, E., et al., *Synthesis, First-Principle Simulation, and Application of Three-Dimensional Ceria Nanoparticles/Graphene Nanocomposite for Non-Enzymatic Hydrogen Peroxide Detection.* Journal of The Electrochemical Society, 2019. **166**(5): p. H3167-H3174.

370. Gohari-Bajestani, Z., et al., *Synthesis of anatase TiO2 with exposed (001) facets grown on N-doped reduced graphene oxide for enhanced hydrogen storage.* International Journal of Hydrogen Energy, 2017. **42**(9): p. 6096-6103.
371. Meng, F. and L. Wang, *Hydrothermal synthesis of monocrystalline CeO2 nanopoles and their room temperature ferromagnetism.* Materials Letters, 2013. **100**: p. 86-88.
372. Li, X., et al., *Three-dimensional graphene network supported ultrathin CeO2 nanoflakes for oxygen reduction reaction and rechargeable metal-air batteries.* Electrochimica Acta, 2018. **263**: p. 561-569.
373. Saha, D. and M.J. Kienbaum, *Role of oxygen, nitrogen and sulfur functionalities on the surface of nanoporous carbons in CO2 adsorption: A critical review.* Microporous and Mesoporous Materials, 2019. **287**: p. 29-55.
374. Jiang, Y., et al., *In-Situ Growth of CeO2 Nanoparticles on N-doped Reduced Graphene Oxide for Anchoring Li2O2 Formation in Lithium-Oxygen Batteries.* Electrochimica Acta, 2016. **210**: p. 712-719.
375. Liang, Z. and Y.-C. Lu, *Critical Role of Redox Mediator in Suppressing Charging Instabilities of Lithium–Oxygen Batteries.* Journal of the American Chemical Society, 2016. **138**(24): p. 7574-7583.
376. Lim, H.D., et al., *Superior rechargeability and efficiency of lithium-oxygen batteries: hierarchical air electrode architecture combined with a soluble catalyst.* Angew Chem Int Ed Engl, 2014. **53**(15): p. 3926-31.
377. Lin, X., et al., *Cerium Oxides as Oxygen Reduction Catalysts for Lithium-Air Batteries.* International Journal of Electrochemical Science, 2012. **7**: p. 9550-9559.
378. Kundu, D., et al., *A Highly Active Low Voltage Redox Mediator for Enhanced Rechargeability of Lithium–Oxygen Batteries.* ACS Central Science, 2015. **1**(9): p. 510-515.
379. Zhu, Y.G., et al., *Dual redox catalysts for oxygen reduction and evolution reactions: towards a redox flow Li–O 2 battery.* Chemical Communications, 2015. **51**(46): p. 9451-9454.
380. Zhang, T., et al., *A self-defense redox mediator for efficient lithium–O2 batteries.* Energy & Environmental Science, 2016. **9**(3): p. 1024-1030.
381. Wang, Z., et al., *Cerium triflate as superoxide radical scavenger to improve cycle life of LiO2 battery.* Journal of Power Sources, 2019. **414**: p. 327-332.
382. Landa-Medrano, I., et al., *Redox mediators: a shuttle to efficacy in metal–O 2 batteries.* Journal of Materials Chemistry A, 2019. **7**(15): p. 8746-8764.
383. Ko, Y., et al., *A comparative kinetic study of redox mediators for high-power lithium–oxygen batteries.* Journal of Materials Chemistry A, 2019. **7**(11): p. 6491-6498.
384. Adams, B.D., et al., *Current density dependence of peroxide formation in the Li–O2 battery and its effect on charge.* Energy & Environmental Science, 2013. **6**(6).
385. Ahn, C.-H., et al., *Graphene/doped ceria nano-blend for catalytic oxygen reduction in non-aqueous lithium-oxygen batteries.* Electrochimica Acta, 2014. **117**: p. 18-25.
386. Jiang, Y., et al., *Graphene Foam Decorated with Ceria Microspheres as a Flexible Cathode for Foldable Lithium-Air Batteries.* ChemCatChem, 2017. **9**(22): p. 4231-4237.
387. Yang, C., et al., *Unexpected Li2O2 Film Growth on Carbon Nanotube Electrodes with CeO2 Nanoparticles in Li–O2 Batteries.* Nano Letters, 2016. **16**(5): p. 2969-2974.
388. Kalubarme, R., et al., *Nanostructured doped ceria for catalytic oxygen reduction and Li2O2 oxidation in non-aqueous electrolytes.* J. Mater. Chem. A, 2014. **2**.
389. Zhu, Y., et al., *MnOx decorated CeO2 nanorods as cathode catalyst for rechargeable lithium–air batteries.* Journal of Materials Chemistry A, 2015. **3**(25): p. 13563-13567.
390. Tułodziecki, M., et al., *The role of iodide in the formation of lithium hydroxide in lithium–oxygen batteries.* Energy & Environmental Science, 2017. **10**(8): p. 1828-1842.

391. Choi, J.W., et al., *Effect of Various Lithium Salts in TEGDME Based Electrolyte for Li/Pyrite Battery.* Solid State Phenomena, 2007. **124-126**: p. 971-974.
392. Mirzaeian, M. and P.J. Hall, *Characterizing capacity loss of lithium oxygen batteries by impedance spectroscopy.* Journal of Power Sources, 2010. **195**(19): p. 6817-6824.
393. Lau, K., et al., *Theoretical exploration of various lithium peroxide crystal structures in a Li-air battery.* Energies, 2015. **8**(1): p. 529-548.
394. Xu, J.J., et al., *Tailoring deposition and morphology of discharge products towards high-rate and long-life lithium-oxygen batteries.* Nat Commun, 2013. **4**: p. 2438.
395. Geng, D., et al., *From Lithium-Oxygen to Lithium-Air Batteries: Challenges and Opportunities.* Advanced Energy Materials, 2016. **6**(9): p. 1502164.